3D SEISMIC ANALYSIS OF THE GEOMETRY AND DEVELOPMENT OF A DEEP WATER FOLD AND THRUST BELT

SIMON MARK HIGGINS

Submitted in partial fulfilment of the requirements for the degree of Ph.D

Cardiff University

December 2007

ProQuest LLC
789 East Eisenhower Parkway
P.O. Box 1346
Ann Arbor, MI 48106-1346

DECLARATION

This work has not previously been accepted in substance for any degree and is not concurrently submitted in candidature for any degree.

Signed ..... (candidate) Date 18/12/2007

STATEMENT 1

This thesis is being submitted in partial fulfillment of the requirements for the degree of PhD .

Signed ..... (candidate) Date 18/12/2007

STATEMENT 2

This thesis is the result of my own independent work/investigation, except where otherwise stated.
Other sources are acknowledged by explicit references.

Signed ..... (candidate) Date 18/12/2007

STATEMENT 3

I hereby give consent for my thesis, if accepted, to be available for photocopying and for inter-library loan, and for the title and summary to be made available to outside organisations.

Signed ..... (candidate) Date 18/12/2007

STATEMENT 4: PREVIOUSLY APPROVED BAR ON ACCESS

I hereby give consent for my thesis, if accepted, to be available for photocopying and for inter-library loans after expiry of a bar on access previously approved by the Graduate Development Committee.

Signed ..... (candidate) Date 18/12/2007

Dedicated to my wife Jessica and my son Zachary

SUMMARY

This thesis uses industry 3D seismic to investigate the nature and distribution of strain in a deep water fold and thrust belt and describes the complex fault plane and stratal geometries that result from fold and thrust linkage. The principal aim is to gain a better understanding of the structural architecture and evolution of toe-of-slope compressional settings. To this end, the project represents a logical series of arguments involving the study of individual structures and fold and fault pairs, to considering a fold belt as a whole.

The outer thrust belt of the Niger Delta is observed to comprise of synthetic and antithetic faults that interact and link along strike. A preliminary geometric classification is proposed for antithetic thrust fault linkage zones based on observations of fault surface and stratal geometries. The relationship between fault interaction and fold characteristics is also investigated. The connectivity of stratigraphic horizons across fault surfaces and through transfer zones is shown to vary with the type of linkage and with depth. Conclusions drawn on the along strike variability of fault network density, orientation and vertical extent are shown to have significant application to modelling of fluid flow.

The concept of numerous and geometrically distinct thrust fault linkages forming through-going folds is developed through the investigation of a single isolated fold that comprises a number of linking forethrusts and backthrusts. This case study, involving the quantification of the development of this relatively simple structure, allows conclusions to be drawn on fold growth that are later applied to a more complex and closely spaced fold belt. The internal structural geometry of faults and stratigraphic horizons within the single fold are described though detailed three-dimensional mapping. The analysis of the distribution of fault and fold strain, both on individual thrusts within the fold and for the structure as a whole, suggest efficient displacement transfer between numerous linking faults that accommodated shortening as a coherent unit. In addition to this, variations in the magnitude of fault heave are compensated by complementary trends in fold strain. A study of syn-kinematic units demonstrates that the single structural culmination present today was initially made up of a number of folds with local structural highs. Major thrust surfaces within the fold are also interpreted to be the product of the along strike linkage and amalgamation of initially distinct faults.

These observations made on the isolated fold are applied to a complex, closely spaced fold belt. The relative timing of individual faults and folds agree with established models of a progressive foreland propagating sequence of thrust faults but also display out-of-sequence events. Findings demonstrate a significant period of synchronous development between all structures in the fold belt. Aggregation of fault and fold shortening profiles indicate that displacement transfer occurs along strike and also in a dip-parallel direction between within the fold belt. Bulk shortening is thus conserved along strike within the syn-kinematic units and low lateral heave gradients suggest efficient displacement transfer between all constituent structures. The evidence presented here shows that all elements of a fold belt can be kinematically linked during growth. Irregularities in the distribution of deformation in pre-kinematic units corroborate findings that the folds are the product of along strike linkage of discrete segments, in a similar manner to that documented in extensional systems.

AUTHOR'S NOTE

The principal research Chapters of this thesis (3, 4 and 5) have been prepared as scientific papers for publication in international journals. The status of these publications, at the time of the submission of the thesis, is as follows:

- **Chapter 3** has been published as:

  Higgins, S., Davies, R.J., Clarke, B., 2007. Antithetic fault linkages in a deep water fold and thrust belt. Journal of Structural Geology 29, 1900-1914. (doi:10.1016/j.jsg.2007.09.004)

- **Chapter 4** is in review as:

  Higgins, S., Clarke, B., Davies, R.J., Cartwright, J., Internal architecture and growth history of a thrust-related anticline in a deep water fold belt. Journal of Structural Geology.

- **Chapter 5** will be submitted to Basin Research.

Although the papers are jointly authored with the project supervisors they are the work of the lead author, Simon Higgins. Project supervisors provided editorial support in accordance with a normal thesis chapter.

ACKNOWLEDGEMENTS

Many people and organisations deserve my heartfelt gratitude and appreciation for the support they have offered over the last three years. I must start by thanking my project supervisors Richard Davies and Benjamin Clarke who gave me the opportunity to carry out this research and have provided continual guidance and support throughout. I must also thank Joe Cartwright for his invaluable input and encouragement, and for creating such an enjoyable place of work in the 3DLab.

This project has been solely funded by StatoilHydro and so without their backing, none of this would have been possible. I am also indebted to those in StatoilHydro who gave their assistance during the numerous visits to Norway, including Andy Robinson, Bruce Tocher and Paul Brockbank. The seismic data used within this thesis was kindly provided by CGGVeritas, interpretation software was supplied by Schlumberger and structural restoration programs came from Midland Valley Exploration. I am most thankful to all. The papers within this project were greatly improved by a number of reviewers including Rob Butler, Richard Lisle, Paivi Heinio, Catherine Baudon, David Peacock, Simon Stewart and Jonathan Imber.

I am also grateful to all those people who made living in Cardiff so enjoyable. All those in the 3DLab are thanked for their technical advice and for their friendship including Rob, Mostyn, Dorthe, Mads, Thomas, Mairi, Aggie, William, Tom, Ian, Jenny, Tiago, Sepribo and everyone else. In particular Cat and Paivi for being such wonderful office mates and fellow caffeine-anonymous attendees - and also Suze and Gordon for putting up with my final hours of madness.

Finally I save my biggest thank you for my inspirational and ever-loving family. Over the last three years I have married my beautiful wife Jessica and welcomed my little son Zachary into the world. They make life so sweet, that no amount of PhD-tribulation could ever diminish it. They are my endless source of happiness and made the years I spent in Cardiff the best of my life so far. Thankyou.

TABLE OF CONTENTS

Appendices

LIST OF FIGURES

Chapter 1. Introduction

Chapter 2. Niger Delta: Geological Setting, database and structural review

Chapter 3. Antithetic fault linkages in a deep water fold and thrust belt

Chapter 4. Internal architecture and growth history of a thrust-related anticline in a deep water fold belt

Chapter 5. Displacement transfer during the synchronous growth of a deep water fold and fault array

Chapter 6. Summary and discussion

Chapter 1

CHAPTER 1

1 INTRODUCTION

1.1 Rationale

Deep water fold and thrust belts have become the focus of ever-increasing geological investigation following the progressive move of hydrocarbon exploration into deeper water on continental margins during the 1990s. Prior to this, early studies of thrust systems were based almost exclusively on outcropping geology in onshore mountain belts, whose orogenic mechanism were driven ultimately by plate convergence. Deep water fold and thrust belts can also be related to plate convergence, as in the case of accretionary prisms such as the Sinu-San Jacinto fold belt of northern Colombia (e.g. Toto and Kellogg, 1992), or can occur by gravitational collapse on passive-margins, such as the fold belts offshore Angola (e.g. Morley and Guerin, 1996) or the Gulf of Mexico (e.g. Wu and Bally, 2000). Compressional structures can also form from a combination of gravity and orogenic driving mechanisms, such as in the north and east Borneo margins (e.g. Ingram et al., 2004). The development and proliferation of three-dimensional (3D) seismic surveys acquired in deep water settings has therefore resulted in high resolution imaging of a wide range of previously unknown, or at least poorly understood, thrust systems. Three-dimensional seismic data provide fresh insights into fault and fold growth in compressional settings and impacts our understanding of toe-thrust systems and of thrust systems in general.

Shortening of the post rift sediments in passive margins may be accommodated by thrust faults and folds, the formation of a deep water fold belt, and by the movement, extrusion or deformation of mobile substrate such as shale or salt (Rowan et al., 2004). Numerous studies have shown fold belts to be the product of the propagation and linkage of a number of initially discrete structures (e.g. Liu and Dixon, 1991; Rowan, 1997), however the mechanisms by which thrusts and folds initiate, propagate and link remain poorly defined (e.g. Davis et al., 2005). The relationship between thrust faults and associated folds has been extensively researched in the past two decades and distinct classes of structure have been described. These are widely based on orogenic belts exposed on land and more recently from fold and thrust belts

associated with gravity tectonic deformation of continental margins. The description of fault propagation folds (Williams and Chapman, 1983; Suppe, 1985; Suppe and Medwedeff, 1990), break-thrust folds (Jamison, 1987; Mitchell and Woodward, 1988; Butler, 1992; Woodward, 1992), fault-bend-folds (Rich, 1934; Boyer and Elliot, 1982; Suppe, 1983) and detachment folds at the lateral terminations of faults (e.g. Jamison, 1987) have mainly been based on cross-sectional geometry, either derived from exposed sections or from 2D seismic profiles. Three-dimensional models of thrust fault development are fewer, although some authors have built upon plane-strain models of fault-bend and fault propagation folds by modelling displacement variations alongstrike (e.g. Wilkerson et al., 1991; Rowan, 1997). Comparatively more research has been carried out into the development of extensional systems. Numerous studies on normal faults have provided insights into fault growth (e.g. Watterson, 1986; Barnett et al., 1987; Cartwright et al., 1995), along strike and down-dip displacement variations (e.g. Peacock and Sanderson, 1991), fault scaling laws (e.g. Dawers and Anders, 1995), and classifications of fault linkage geometries (e.g. Gawthorpe and Hurst, 1993). This level of insight is lacking for compressional settings, partly due to the lack of 3D data in the past.

This PhD thesis uses large commercial 3D seismic surveys to describe the geometries of fault surfaces, thrust linkages and associated fold forms in part of the outer thrust belt of the west Niger Delta. Quantification of deformation, through the study of fault displacement and bulk shortening variations and distributions, provides evidence for the kinematic relationship between constituent elements of the fold belt. The deep-water Niger Delta is ideal for such an analysis as the structures are extremely well imaged at deep levels in seismic reflection profiles and include syn-kinematic growth strata that record fold kinematics (Corredor et al., 2005). Growth strata preserved on fold limbs can be used to distinguish between various kinematic models (e.g. Rowan, 1997) and in this thesis are analysed using innovative techniques to determine the growth history of faults and folds. The application here of methodologies developed in the study of normal faults helps to address the imbalance in understanding of fault growth between extensional and compressional regimes.

This first chapter of the thesis commences by introducing the principal aims of the PhD research project. A brief introduction to 3D seismic data and interpretation follows, and a summary of the current understanding of the mechanics and kinematics of fault and fold growth is also included.

1.2 Aims of study

The research presented in this thesis focuses on the geometry and development of faults and folds in the toe-of-slope compressional domain of a passive margin. This includes a high resolution analysis of the distribution of strain in a deep water fold belt. The aims of the study are outlined below:

- Describe the various three-dimensional geometries of the lateral tip regions of thrust fault surfaces, including within the fault linkage and transfer zones, and outline the along strike structural variability of a deep water fold and thrust belt.
- Assess the along strike response of folding to variations in underlying fault plane geometry.
- Investigate the degree of down-dip stratal connectivity through a fold and thrust belt.
- Quantify the spatial variability and distribution of fault heave and bulk shortening for i) a singly faulted fold; ii) a fold comprising numerous, linking faults; and iii) a fold belt as a whole.
- Ascertain if the magnitude of continuous strain (such as folding) responds to variations in the amount of discontinuous strain (i.e. faulting) along strike.
- Analyse the geometry and spatial extent of syn-kinematic strata around a complex fold to provide a case study of the growth history of a propagating fold in a deep water fold belt.
- Determine the sequence of fault and fold initiation and propagation within a fold belt and assess the degree of overlap in the duration of growth of individual structures.
- Describe the along strike geometric complexities surrounding the hard-linkage of thrust faults of opposing dip in a closely spaced fault array.
- Document the nature and extent of displacement transfer between i) laterally linking faults and folds and ii) constituent structures of a fold belt.
- Investigate the differences in the distribution of displacement and shortening within pre- and syn-kinematic units.

1.3 Methodology

The analysis of the geometry and development of the fold belt featured in this study relies on the utilisation and interpretation of three-dimensional seismic reflection data. This section provides a basic introduction to seismic data, interpretation techniques, visualisation tools and the limitations and pitfalls of such methods.

1.3.1 *3D seismic data and interpretation*

The introduction and proliferation of three-dimensional (3D) seismic acquisition in the 1980s and 1990s dramatically improved upon the limited spatial resolution of previous 2D seismic surveys (Cartwright and Huuse, 2005). Line spacing in a 2D seismic survey is commonly around 1 to 10 km whereas a typical 3D seismic survey is acquired with a line spacing of 25 m or less, resulting in greater subsurface sampling density and enhanced lateral resolution (Hart, 1999; Cartwright and Huuse, 2005). The ability to image features in detail in all directions allows complex geological structures to be accurately mapped in three dimensions and has thus impacted the petroleum industry by significantly enhancing drilling success. In this study the enhanced imaging potential of seismic data has been utilised to describe, classify and quantify thrust faults and folds in an inherently inaccessible region of a deep water fold and thrust belt. The opportunity to view and record the characteristics of thrust faults in such detail with 3D seismic data provides new insights into the nature and development of these settings.

Seismic waves are produced by generating an acoustic pulse from a controlled source, commonly an airgun in marine acquisition, and propagate through the subsurface (e.g. Kearey et al., 2002). Waves are refracted and reflected at geological boundaries that represent a change in acoustic impedance within the subsurface. Hydrophones (marine) and geophones (terrestrial) detect the energy of returning waves and hence measure the arrival times of the waves at various distances and positions relative to the source (Kearey et al., 2002). Processing and migration of this data spatially distribute all reflections points correctly, can eliminate unwanted and erroneous events and increases the quality and resolution of the data. The location and geometry of a geological feature is thus calculated from the travel times of seismic

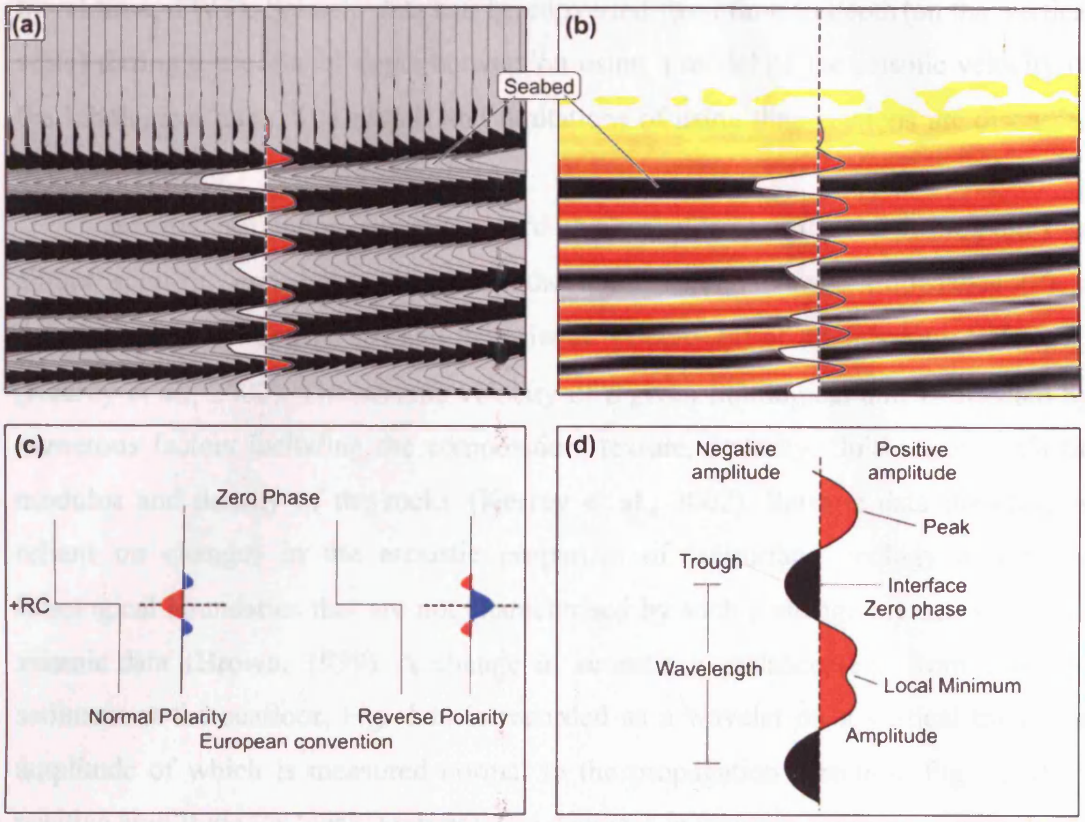

Figure 1.1: Seismic data polarity and phase. **(a)** Seismic time section from a Niger Delta survey to show the characteristics of the seabed reflection (displayed as 'variable area'). Note that the seabed produces a negative wavelet (trough). **(b)** Same section as a 'variable intensity' display. **(c)** Explanation of European polarity convention using a zero phase wavelet. Taken from *Simm and White (2002)*. +RC indicates an increase in acoustic impedance downwards. **(d)** Nomenclature of the seismic waveform. Positive amplitudes are displayed in red, negative amplitudes in black, as in the seismic section in (b). Taken from *Heinio (2007)*.

wavelets and hence the vertical scaling of the data is presented in time (or two-way-travel time, TWT). Seismic data can be converted from time to depth (on the vertical scale) during a process of depth conversion using a model of the seismic velocity of the lithological units. The pitfalls and limitations of using time sections are discussed in a later section.

Seismic reflection surveys record the waveforms reflected from points of abrupt acoustic impedance change in the subsurface. Acoustic impedance (Z) is determined by the density (ρ) and the seismic velocity (v) of the lithology ($Z = \rho v$) (Kearey et al., 2002). The seismic velocity of a given lithological unit is affected by numerous factors including the composition, texture, porosity, fluid content, elastic modulus and density of the rocks (Kearey et al., 2002). Seismic data therefore is reliant on changes in the acoustic properties of subsurface geology and hence lithological boundaries that are not characterised by such a change are not visible on seismic data (Brown, 1999). A change in acoustic impedance (e.g. from water to sediment at the seafloor, Fig. 1.1) is recorded as a wavelet on a vertical trace, the amplitude of which is measured normal to the propagation direction (Fig. 1.1d). A positive amplitude (or 'peak') represents a decrease in acoustic impedance with depth, whereas a negative amplitude (or 'trough') represents an increase in impedance with depth. This is known as 'normal polarity' by European convention (e.g. Simm and White, 2002). Data used in this thesis have normal polarity and hence the seabed reflection (i.e. an increase in acoustic impedance) is displayed as a trough (Fig. 1.1c). Finally, another characteristic of a wavelet is referred to as the 'phase' of a wavelet and involves the shape of the waveform. A seismic survey can be of maximum, minimum or zero-phase. Most interpreters in recent times prefer the latter as this means a wavelet is symmetrical with the maximum amplitude on the central lobe and also because the maximum energy is aligned with the geological interface that caused the reflection event (Brown, 1999). Data features in this thesis are all zero phase (Figure. 1.1).

A 3D seismic survey comprises a volume of data that can be manipulated in a number of ways. Only the methods relevant to this study are described here. The most common and simplest method is by studying one of three orthogonal slices through the 'data-cube'; 'inlines' and 'crosslines' are vertical sections aligned with the direction of acquisition, whereas 'time-slices' are horizontal planes at various depths within the

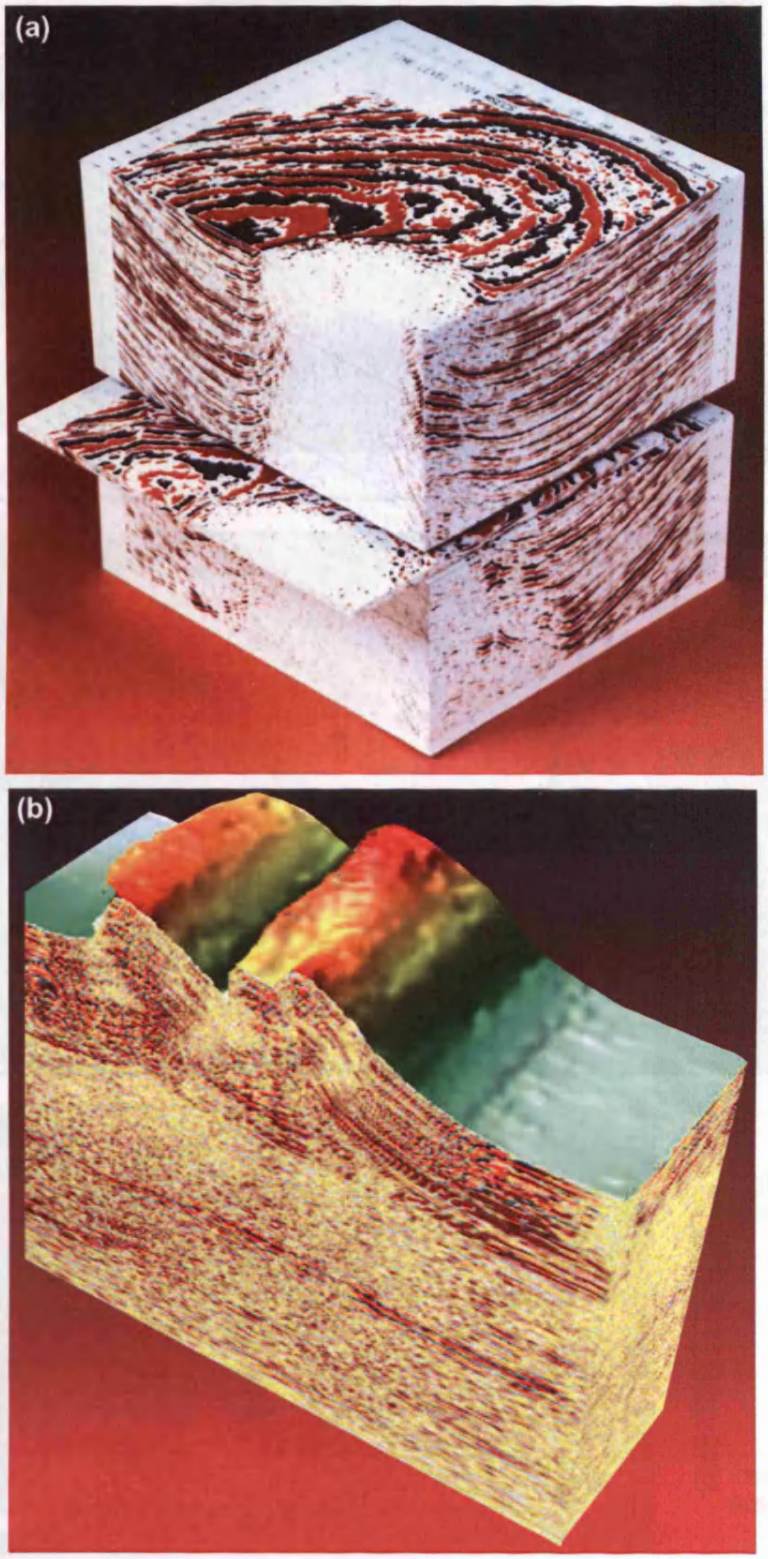

Figure 1.2: Three-dimensional seismic reflection data volumes. **(a)** a Gulf of Mexico salt dome with associated rim syncline showing three primary orthogonal slices; vertical inline and crossline, and horizontal timeslice. Taken from *Brown (1999)*. **(b)** part of the Niger Delta outer fold and thrust belt. Top surface represents an interpreted horizon.

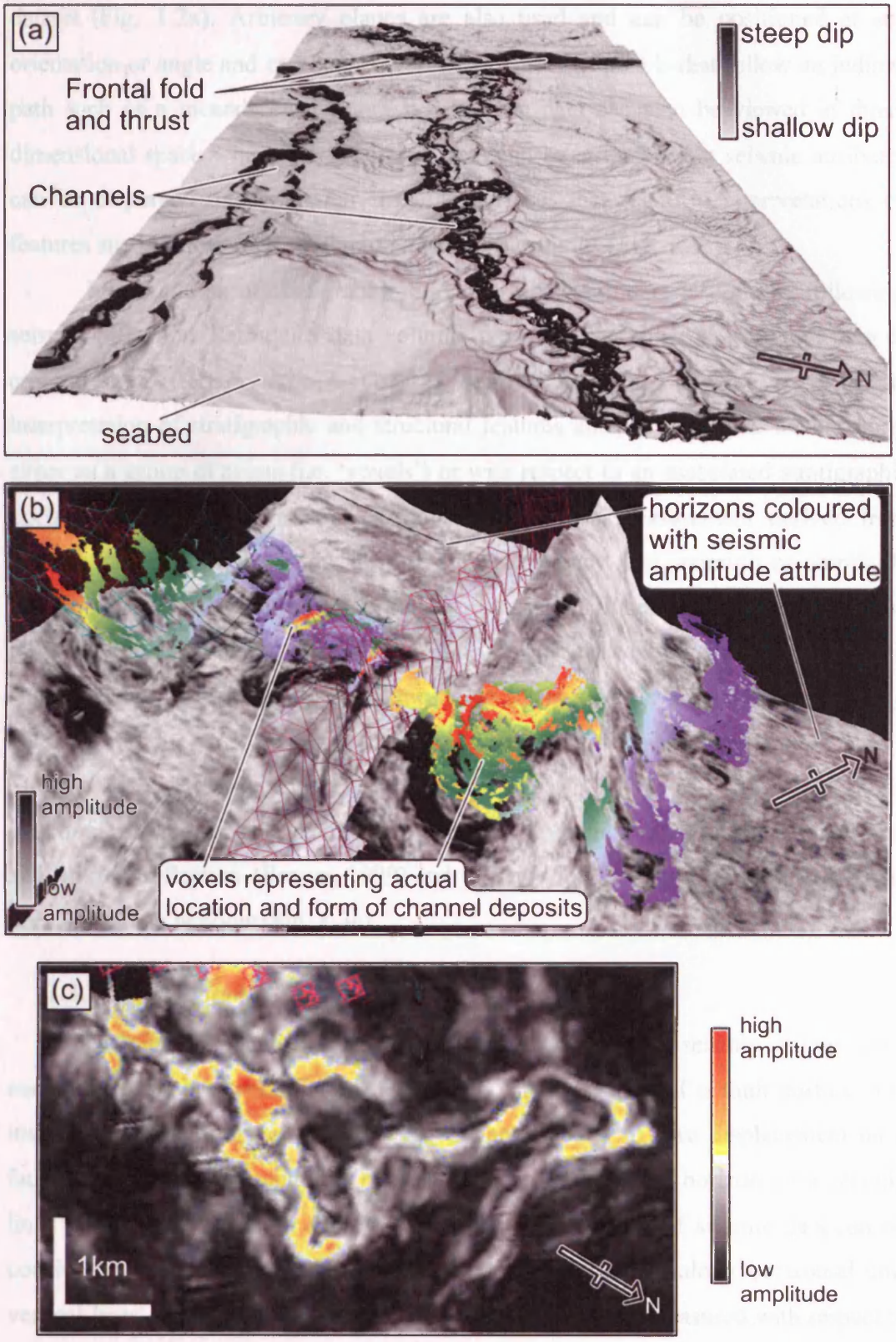

Figure 1.3: A demonstration of the use of seismic attributes in seismic interpretation. **(a)** Dip map of the seabed in the Niger Delta. Shades of grey correspond to the magnitude of dip of the seabed and highlight the morphology of present day channels. Field of view approximately 30 km. **(b)** Three-dimensional view of a channel crossing a faulted fold. Seismic amplitudes extracted from a time window (relative to stratigraphy) are used to colour the horizon (grey). The true location of high amplitude channel deposits are given by 'voxels' that comprises areas of similar amplitude. Field of view approximately 15 km. **(c)** Map of a seismic amplitude extraction showing sinuous channel form.

dataset (Fig. 1.2a). Arbitrary planes are also used and can be positioned at any orientation or angle and can be made up of a number of panels that follow an indirect path such as a meandering channel system. The data can also be viewed in three-dimensional space where the volume of data can be cut such that seismic attributes can be displayed on non-planar, irregular surfaces that relate to interpretations of features such as deformed stratigraphic horizons or faults (Fig. 1.2b).

Interpretation of stratigraphic horizons in seismic data is done by following seismic reflections through a data volume, typically to produce a structural map or cross-section. Certain attributes of the seismic data can also be used to aid interpretation of stratigraphic and structural features and are displayed in this study either as a group of points (i.e. 'voxels') or with respect to an associated stratigraphic horizon (Fig. 1.3b). A 'seismic attribute' is simply a measurement derived from seismic data and can be in the form of time, frequency, dip, azimuth or amplitude values, to name a few. In this study two attributes are utilised; magnitude of dip, and amplitude (Fig. 1.3c). The magnitude of dip is a time-derived horizon attribute and is calculated by comparing values of time on an interpreted surface with neighbouring values to produce a local plane that is assigned a true value of dip (Brown, 1999). These values are plotted and coloured on a map (Fig. 1.3a) and can reveal subtle structural and topographic features. Reflection amplitude is measured at the crest of an identified reflection (Brown, 1999) and is commonly displayed relative to a plane, horizon or time window (Fig. 1.3c).

1.3.2 *Resolution*

It is important to understand the limits of resolution of a seismic survey when constructing an interpretation. In defining the spatial extent of a fault surface, for instance, it must be understood that an interpreted point of zero displacement on a fault surface only represents the limit of detectable offset of a horizon on a seismic line, which may vary from survey to survey. The resolution of seismic data can be considered with respect to the minimum resolvable distance along horizontal and vertical lines. The resolving power of seismic data is always measured with respect to the seismic wavelength (λ), which is given by ($\lambda = v / f$) the quotient of velocity (v) and frequency (f) (Brown, 1999). As rocks commonly get older and more compacted with depth, so the velocity of seismic waves increases. The dominant frequency of

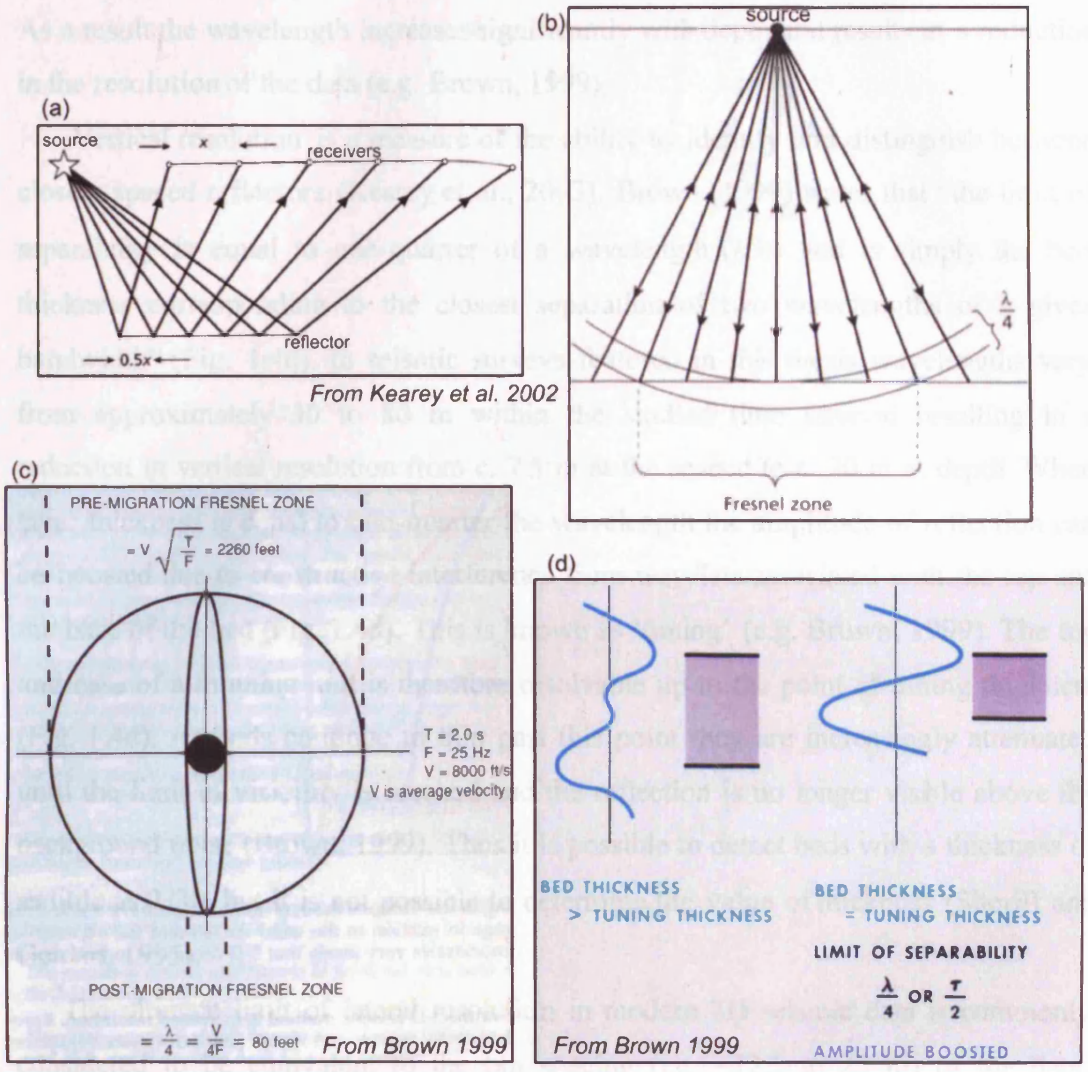

Figure 1.4: Limits of vertical and horizontal resolution of seismic reflection data. **(a)** The horizontal sampling of a seismic reflection survey is half the receiver spacing. **(b)** Energy is returned from all points of a reflector. The part of the reflector from which energy is returned within half a wavelength of the initial reflected arrival is known as the Fresnel zone. (a) and (b) taken from *Kearey et al. (2002)*. The width of the Fresnel zone represents the absolute limit of horizontal resolution **(c)** The effect of migration on the size and shape of the Fresnel zone. The focussing of energy during migration improves horizontal resolution dramatically. **(d)** Defining the vertical limit of separability of seismic reflections. Resolution from the top and bottom of a bed is dependent on the interaction of closely spaced wavelets. (c) and (d) are taken from *Brown (1999)*.

seismic data decreases with depth as higher frequencies are more quickly attenuated. As a result the wavelength increases significantly with depth and results in a reduction in the resolution of the data (e.g. Brown, 1999).

Vertical resolution is a measure of the ability to identify and distinguish between closely spaced reflectors (Kearey et al., 2002). Brown (1999) states that "the limit of separability is equal to one-quarter of a wavelength ($\lambda/4$) and is simply the bed thickness corresponding to the closest separation of two wavelengths of a given bandwidth" (Fig. 1.4d). In seismic surveys featured in this thesis wavelengths vary from approximately 30 to 80 m within the studied time interval resulting in a reduction in vertical resolution from c. 7.5 m at the seabed to c. 20 m at depth. When layer thickness is equal to one-quarter the wavelength the amplitude of reflection can be boosted due to constructive interference from wavelets associated with the top and the base of the bed (Fig. 1.4d). This is known as 'tuning' (e.g. Brown, 1999). The top and base of a thinning unit is therefore resolvable up to the point of tuning thickness (Fig. 1.4d). As beds continue to thin past this point they are increasingly attenuated until the limit of visibility is reached and the reflection is no longer visible above the background noise (Brown, 1999). Thus it is possible to detect beds with a thickness of as little as $\lambda/30$, but it is not possible to determine the value of thickness (Sheriff and Geldart, 1995).

The ultimate limit of lateral resolution in modern 3D seismic data is commonly considered to be equivalent to the bin spacing (i.e. ~12.5 to 25 m) of the data, although accurate calculations incorporate the dominant wavelength and hence resolution can still vary with depth (Cartwright and Huuse, 2005). There are two main controls on the horizontal resolution of a seismic reflection survey; the first is determined by the spacing of the receivers, and the second is intrinsic to the process of reflection of seismic energy (Kearey et al., 2002). It can be seen that for the simple case of a flat lying reflector (Fig. 1.4a) the horizontal sampling is equal to half the receiver spacing. The closer the spacing of receivers the more reliably reflections from a single interface can be correlated from trace to trace in areas of complex geology (Kearey et al., 2002). The latter control on horizontal resolution involves the way in which seismic energy is reflected back from the subsurface. The path of a seismic wave from source to receiver is commonly visualised as a single line ray path, however a more accurate description of a reflecting surface is an infinite number of

point scatters that each contribute to the received signal. Kealey et al (2002) state that "energy that is returned to a detector within half a wavelength of the initial reflected arrival interferes constructively to build up the reflected signal, and the part of the interface from which this energy is returned is called the first *Fresnel Zone*" (Fig. 1.4b and c). The Fresnel Zone is a function of the velocity and frequency of a wave and the two-way-time to the reflector (Sheriff and Geldart, 1995; Brown, 1999). Migration is the principal technique for improving horizontal resolution as it repositions out-of-place reflectors due to dip and reduces the size of the Fresnel Zone (Fig. 1.4c) by focussing energy (Brown, 1999). In theory the radius of the Fresnel Zone can be reduced to $\lambda/4$, but in practice it is commonly $\lambda/2$ (Brown, 1999).

1.3.3 *Fault diagnostics and measurements*

One of the most striking improvements in seismic interpretation to come from the move from 2D to the use of 3D seismic data is increased detail in fault mapping (Brown, 1999). In seismic data faults are commonly detected by the alignment of terminations of reflectors on both vertical (Fig. 1.5a) and horizontal planes (Fig. 1.5c); however it is also possible for fault ramps to be defined by prominent fault plane reflections (Fig. 1.5b). Other diagnostic features include horizon offsets, bed thickness variations (growth packages), dip changes and in some cases, seismic diffraction curves.

Measurements of the movement along a fault plane, or the amount of displacement on a fault, are made with reference to markers in the wallrocks. For faults where the hangingwall moves only vertically (that is directly up or down the fault plane) the term 'dip-slip fault' is applied. A fault with pure horizontal motion is termed a 'strike-slip fault'. Most faults have a component of both however (e.g. Burbank and Anderson, 2001). Displacement associated with a fault can be regarded as consisting of the heterogeneous or variable strain that occurs within the rock volume closely surrounding a fault (Barnett et al., 1987). Barnett et al (1987) states that "displacement on the discontinuity represented by a fault surface ranges from a maximum at some point on the fault surface to zero at the edge, or tip line" (Fig. 1.6a). Additional displacement can be distributed within the rock volume surrounding the fault in the form of ductile or continuous strain (Fig. 1.6b) (as opposed to the discontinuous deformation on the fault) or on other fault splays (Barnett et al., 1987).

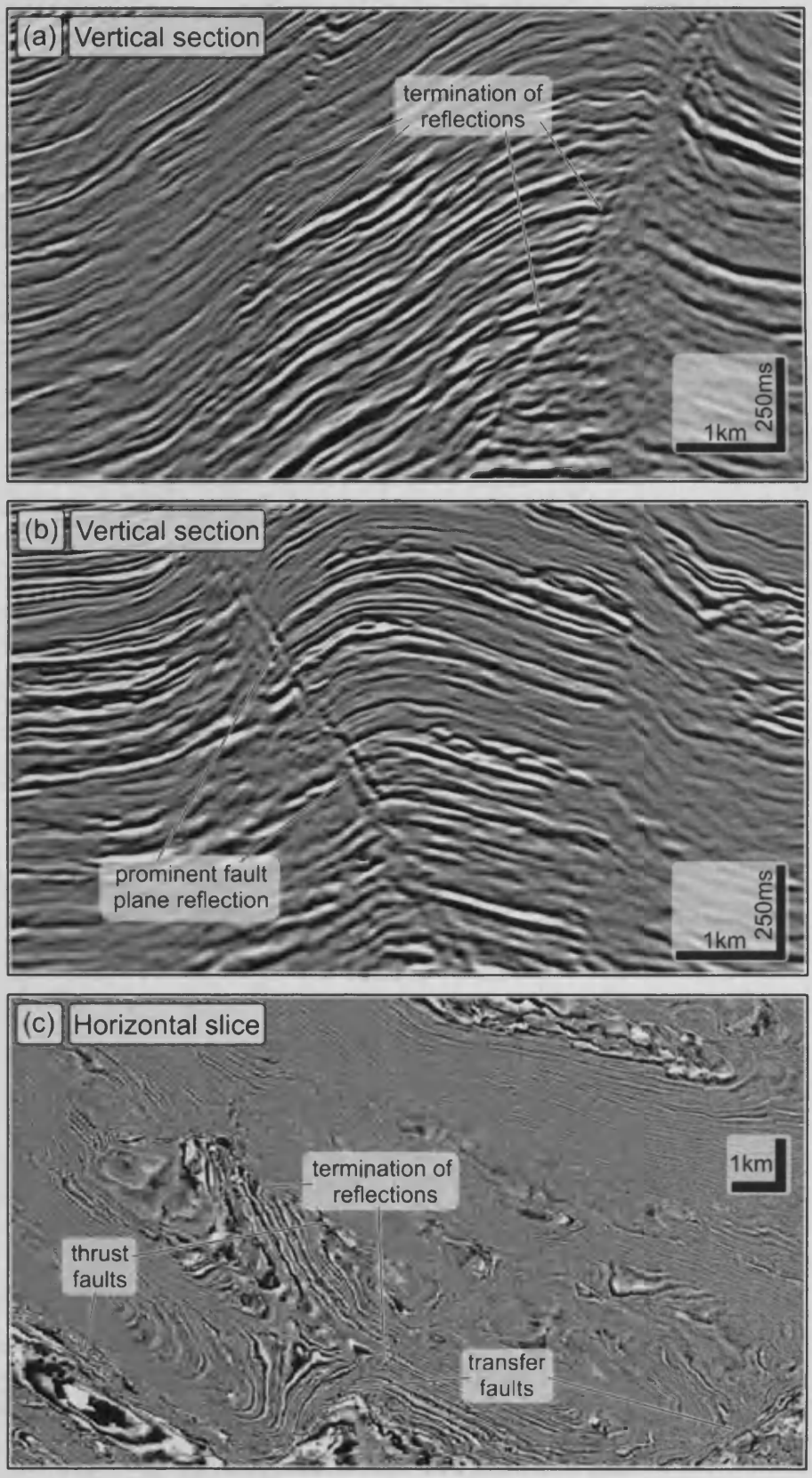

Figure 1.5: Fault characteristics on seismic reflection data in the deep water Niger Delta. **(a)** Vertical seismic section (dip-parallel) through a faulted sequence. The terminations of reflectors are aligned systematically. **(b)** Another section showing a prominent fault plane reflection. **(c)** Horizontal timeslice through a faulted sequence. Terminations of reflectors are once again aligned systematically revealing the position and extent of thrust faults.

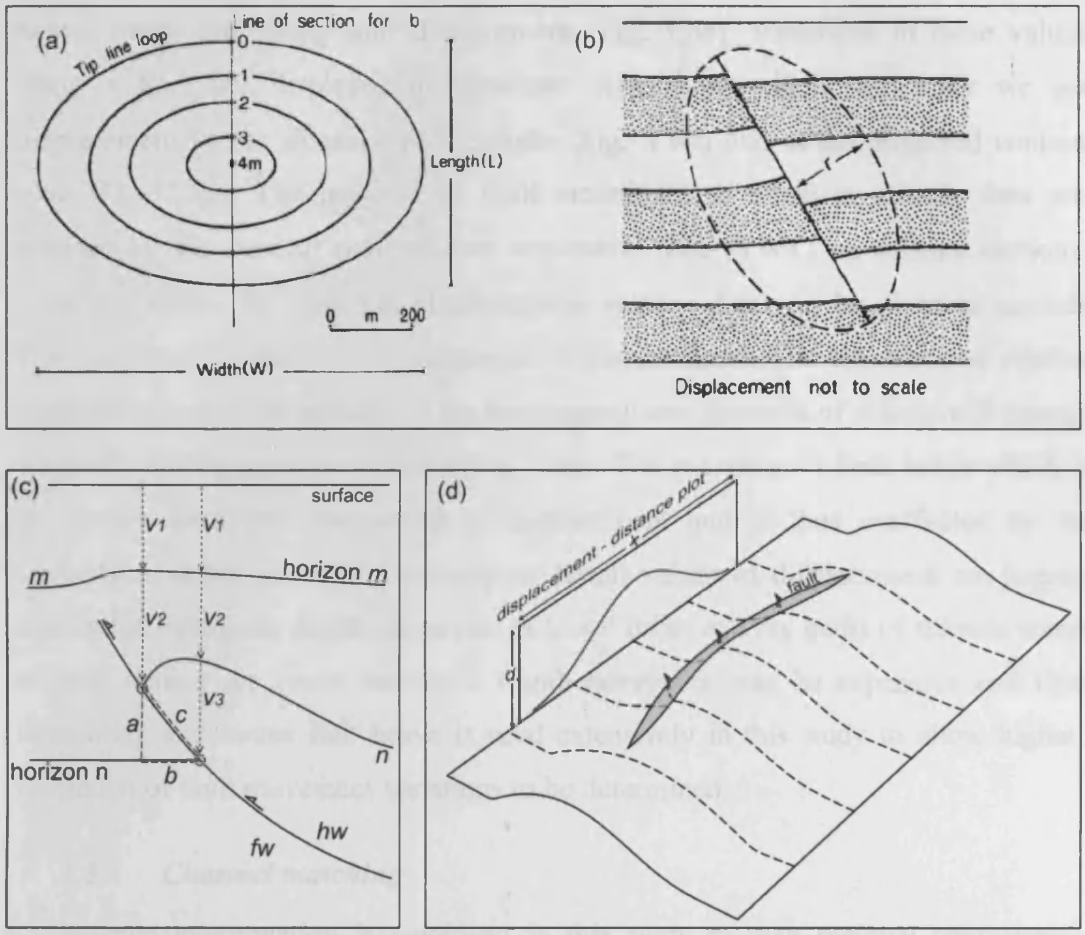

Figure 1.6: Fault measurements and display. **(a)** Schematic displacement contour diagram for a simple normal fault oriented normal to the fault surface. Contours represent constant values of fault displacement on a fault plane. **(b)** Cross-section through the simple fault. (a) and (b) are taken from *Barnett et al. (1987)*. **(c)** Schematic section of a thrust fault to show the principal displacement measurements. *a*: fault throw. *b*: fault heave. *c*: along-fault displacement. *fw*: footwall. *hw*: hangingwall. *v1,v2,v3*: varying interval velocities of stratigraphic units. Values of *a* and *c* will change during depth conversion due to differing velocity profiles above the hangingwall and footwall cutoffs. Imaging of the *fw* cutoff is affected by *v3*, whereas the position of the *hw* cutoff is not. **(d)** Schematic three-dimension diagram of a fold cut by a thrust fault along some of its length. Shows how displacement variations are plotted on vertical displacement-distance plots oriented parallel with fault strike.

The principal measurements of the discontinuous displacement on a fault plane are heave, throw and along-fault displacement (Fig. 1.6c). Variations in these values along a fault are displayed in numerous ways however in this study we use displacement versus distance (d-x) graphs (Fig. 1.6d) and strike projected contour plots (Fig. 1.6a). The majority of fault measurements made in seismic data are affected by the vertical scale of two-way-travel time (TWT) on seismic sections. Values of throw, for instance, obtained from seismic data will be given in seconds TWT as throw is the vertical component of displacement. The absolute and relative positions of a pair of markers in the hangingwall and footwall of a fault will change vertically during depth conversion (Fig. 1.6c). The exception is fault heave which is the purely horizontal component of displacement and is thus unaffected by the majority of depth converting techniques. Small values of displacement are largely unaffected by time to depth conversion as travel times and ray paths of seismic waves to each marker are much the same. Depth conversion can be expensive and time consuming and hence fault heave is used extensively in this study to allow higher resolution of fault movement variations to be determined.

1.3.4 *Channel matching*

Seismic interpretation is employed in this study to map regional stratigraphic horizons throughout the study area. All structural observation and measurements of deformation relating to faulting and folding are made and presented with respect to these interpreted horizons. The development of a rigorous stratigraphic framework is therefore imperative in achieving the aims of this thesis. The most reliable way of correlating horizons across faults with large displacements is to interpret a horizon along a continuous path around the tip of a fault. This relies on fault and fold tips being located within a survey area. Areas such as a deep water fold and thrust belt commonly comprise structures of greater lateral extent than data survey width. The following is a brief outline of an innovative method of 'channel matching' for interpreting seismic horizons across large displacement faults and in other geologically complex areas.

This method is designed to complement other seismic interpretation techniques and to validate existing stratigraphic interpretations. In many settings, such as deep water fold and thrust belts, sub-marine channel systems are important

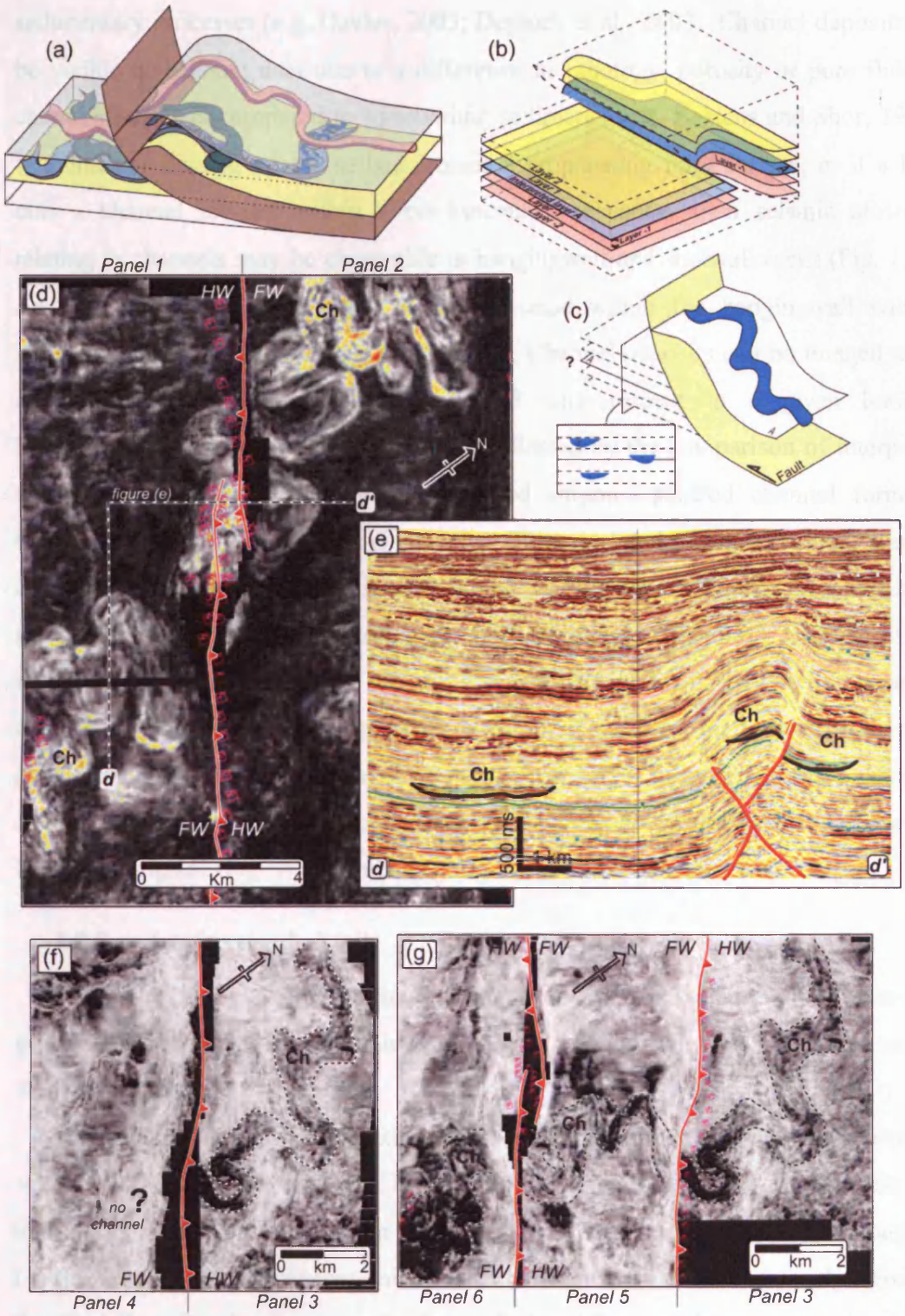

Figure 1.7: Simple method of channel matching across faults. **(a)** Assumption: Sinuous channel deposits in hangingwall strata that intersect a fault should also be present in footwall sequence. **(b)** A stratigraphic framework can be tested and validated across a through-going fault surface. **(c)** Channels in the hangingwall can be compared to channel forms located relative to arbitrary stratigraphic horizons in the footwall. **(d)** A successful channel match across two faults imaged using seismic amplitude attribute extractions. Warm colours = high amplitudes. Dark greys = low amplitudes. **(e)** Seismic corner-section through the matched channel deposits. **(f)** Unsuccessful channel match based on initial stratigraphic frame work. Panels are seismic amplitude attribute maps. **(g)** Successful channel matches by searching for corresponding channel deposits above and below initial stratigraphic interpretation. The interpretation must then by altered accordingly. Dark greys = high A mp. Light greys = Low Amp.

sedimentary processes (e.g. Davies, 2003; Deptuck et al., 2003). Channel deposits can be visible on seismic data due to a difference in lithology, porosity or pore fluid in channelised sands compared to surrounding sediments (e.g. Kastens and Shor, 1985). If a channel flowing on the seabed crosses a propagating fault surface, or if a fault cuts a channel located within a pre-kinematic sequence, then seismic attributes relating to channels may be observable in hangingwall and footwall rocks (Fig. 1.7a). As that fault develops, channel deposits located within the hangingwall will be increasingly offset from those in the footwall. Channel deposits can be imaged using amplitude extractions which are generated with respect to a given horizon. Stratigraphic frameworks therefore can be validated by the comparison of interpreted seismic horizons (Fig. 1.7b) with correlated sinuous, stacked channel forms in hangingwall and footwall strata (Fig. 1.7c). Figure 1.7d shows a correlated sinuous channel (imaged using amplitude extractions) crossing two antithetic thrust faults in the subsurface of the Niger Delta. The high amplitude reflections (HARs) of the channel deposits are visible on the seismic data (Fig. 1.7e). If HARs that relate to channel deposits are imaged on a hangingwall horizon, but not the footwall equivalent (Fig. 1.7f), this may suggest the stratigraphic correlation is incorrect. Such mistakes can be corrected by searching for correlating channel deposits on horizons above and below the original (Fig. 1.7g), and adjusting stratigraphic horizons accordingly.

1.3.5 *Artefacts and pitfalls*

When working with seismic data, it is imperative to understand the limitations and pitfalls that are inherent with this type of data. Below is a brief description of those most pertinent to this study.

As discussed in a previous section, 3D seismic volumes commonly have a vertical scale in two-way-travel time (TWT). The 'apparent' thickness of a stratigraphic unit in TWT is therefore dependent on the time it took seismic energy to pass through it, i.e. the seismic velocity of that unit. The form of structural features can therefore be distorted from 'true' geometries due to vertical and horizontal heterogeneities in the velocity profile of the stratigraphy. It is therefore important to establish the significance of any change to structural geometries that may occur during time to depth conversion (see Brown, 1999). To illustrate this point a typical thrusted fold is depth converted and the resultant structural geometries analysed in Figure 1.8. Depth

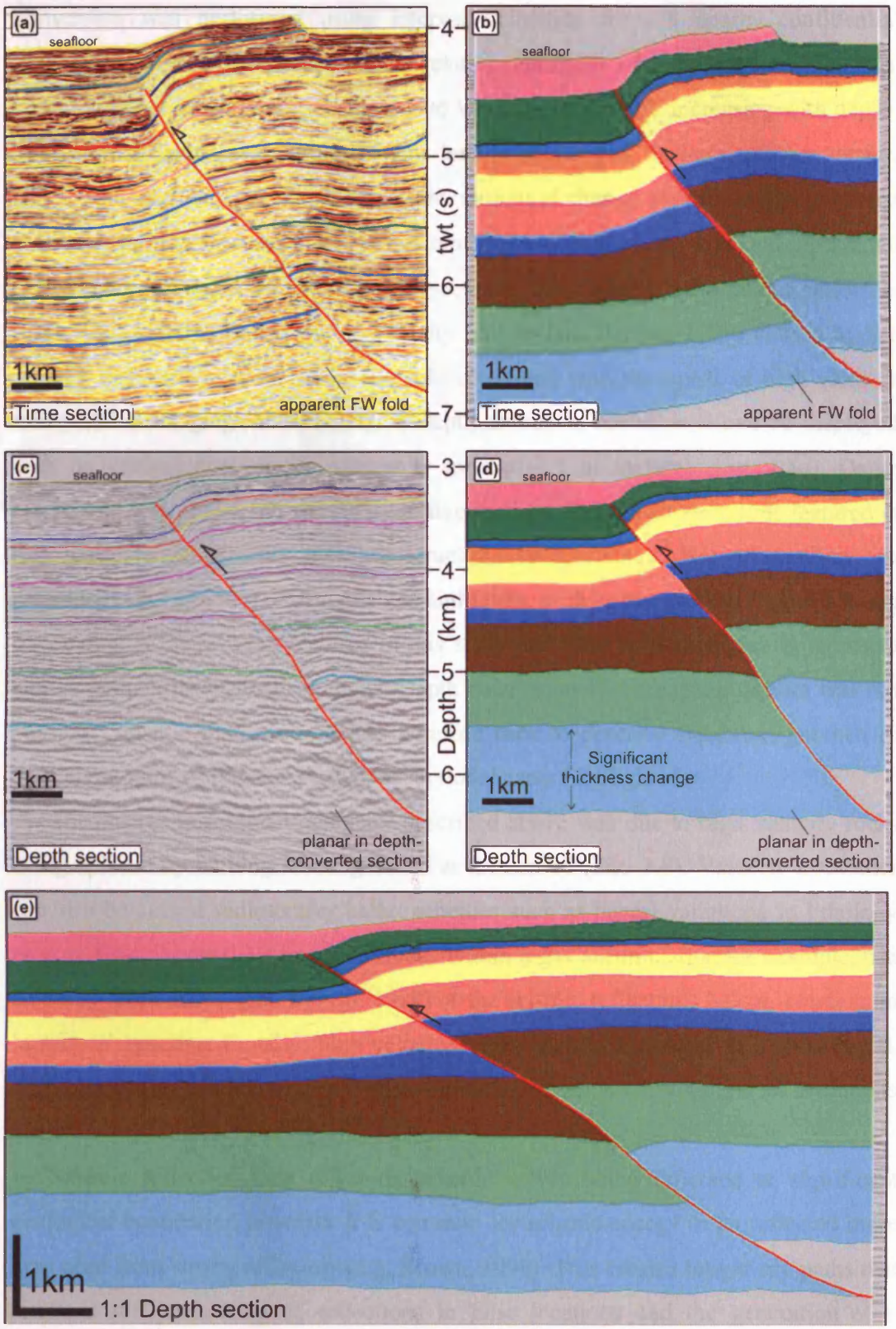

Figure 1.8: Depth conversion of a seismic time section using 2DMove™. **(a)** Seismic section through a thrust fault and hangingwall anticline with stratigraphic interpretation. **(b)** Corresponding polygon cross-section. Coloured polygons are assigned defining values such as seismic velocity. Note an apparent footwall (fw) fold towards the base of the section. **(c)** Depth converted seismic depth section. **(d)** Cross-section in depth showing the conversion of the apparent footwall fold into planar horizons. Note deeper units are significantly thickened during the conversion. **(e)** Cross-section at 1:1 scale.

conversion was performed using interval velocities from a nearby confidential exploration well. An increase in the relative thickness of stratigraphic units is a common effect of depth conversion due to velocity, in general, increasing with depth. The form of hangingwall strata remains largely unchanged during depth conversion (Figs. 1.8b and d). The most significant structural change to the depth converted section is the transformation of an apparent footwall fold (Figs. 1.8a and b), located between 6 and 7 seconds TWT on time sections, into planar sub-horizontal reflectors (Figs. 1.8c and d). This is due to velocity pull-up (see Brown, 1999) caused by the seafloor expression of the overlying fold combined with the uplift of high velocity rocks within hangingwall anticline. A depth section is useful as it can be displayed with no vertical exaggeration (i.e. at a scale of 1:1 in section) (Fig. 1.8e). Depth conversion was performed on representative sections through all structures featured in this thesis to validate and improve structural interpretations. Not all sections are presented. Changes to the form of folds and faults, such as that seen in Figure 1.8, are uncommon in the surveys featured in this study and time sections typically represent similar geometries to depth sections. Depth conversion of a complete dataset was not possible. Seismic time sections are therefore used to describe structural geometries throughout most of this thesis, with exceptional cases highlighted.

The change in footwall geometry described above was due to high velocity rocks being uplifted by faulting creating a fold at the seabed (Fig. 1.8). Velocity anomalies can also be caused sedimentary heterogeneities such as lateral variations in lithology or pore fluid. Anomalous low amplitudes within a gas accumulation for example, can result in 'push-down' (see Brown, 1999) of the seismic reflections below, creating an 'apparent' syncline. Equally, high velocity rocks, such as in a sand-rich channel fill, may produce a velocity 'pull-up' effect creating an apparent anticline in sediments below.

Seismic reflection data relies on seismic waves being reflected at significant geological boundaries, however it is common for seismic energy to be reflected more than once from strong reflectors (e.g. Brown, 1999). This creates longer ray paths that result in the positioning of reflections in false locations and the generation of a multiple (e.g. Kearey et al., 2002). In modern 3D seismic data multiples are commonly removed during processing.

1.4 Mechanics and kinematics of fault and fold growth

Over the last three decades numerous studies have focussed on the growth of faults in order to understand the processes governing the initiation, propagation and linkage of fault surfaces. Methods have included field based studies, numerical and analogue modelling and, more recently, three-dimensional seismic datasets. The majority of detailed quantified models into fault growth are derived from the study of normal faults and extensional systems. The behaviour and displacement distributions on contractional thrust fault remain poorly resolved and hence this study is pertinent in the investigation of fault and fold growth and development. The relationship between faults and folds has also been the subject of much discussion in recent times and has impacted our understanding of the evolution of fold and thrust belts. This section provides a brief summary of published literature on fault analysis, thrust fault propagation relating to fold growth and sediment dispersal around growing folds.

1.4.1 *Displacement analysis*

The lateral extent of faults varies dramatically from those found at ocean ridges that stretch many tens of kilometres (e.g. Pollard and Aydin, 1984) to microstructures found in granite (e.g. Granier, 1985). Displacement analysis along faults can give an indication of fault-growth history and the effects of fault interaction (Peacock and Sanderson, 1991; Dawers and Anders, 1995; Manighetti et al., 2001). Global datasets of fault length (L) and maximum displacement (D_{max}), measured primarily on normal faults, suggest that characteristics such as fault zone width, length and displacement may obey simple scaling relationships in the majority of fault systems (Scholz and Cowie, 1990; Gillespie et al., 1992; Schlische et al., 1996; Davis et al., 2005). The relationship between L and D_{max} is commonly written as a power-law: $D_{max} = kL^n$, where k and n are constants. Davis et al (2005) note that studies into fault dimensions have led to fault growth models where faults begin as isolated cracks and grow in a self-similar manner until they interact with neighbouring structures in zones of overlap at which point lateral growth is retarded (Fig. 1.9) until linkage removes the slip deficit (e.g. Cartwright et al., 1995; Gupta and Scholz, 2000). Alternatively, models have been put forward involving the early establishment of fault length, a suggestion that deviates away from the trend defined by the slip distribution of earthquakes (Walsh et al., 2002). Along strike displacement profiles of theoretical

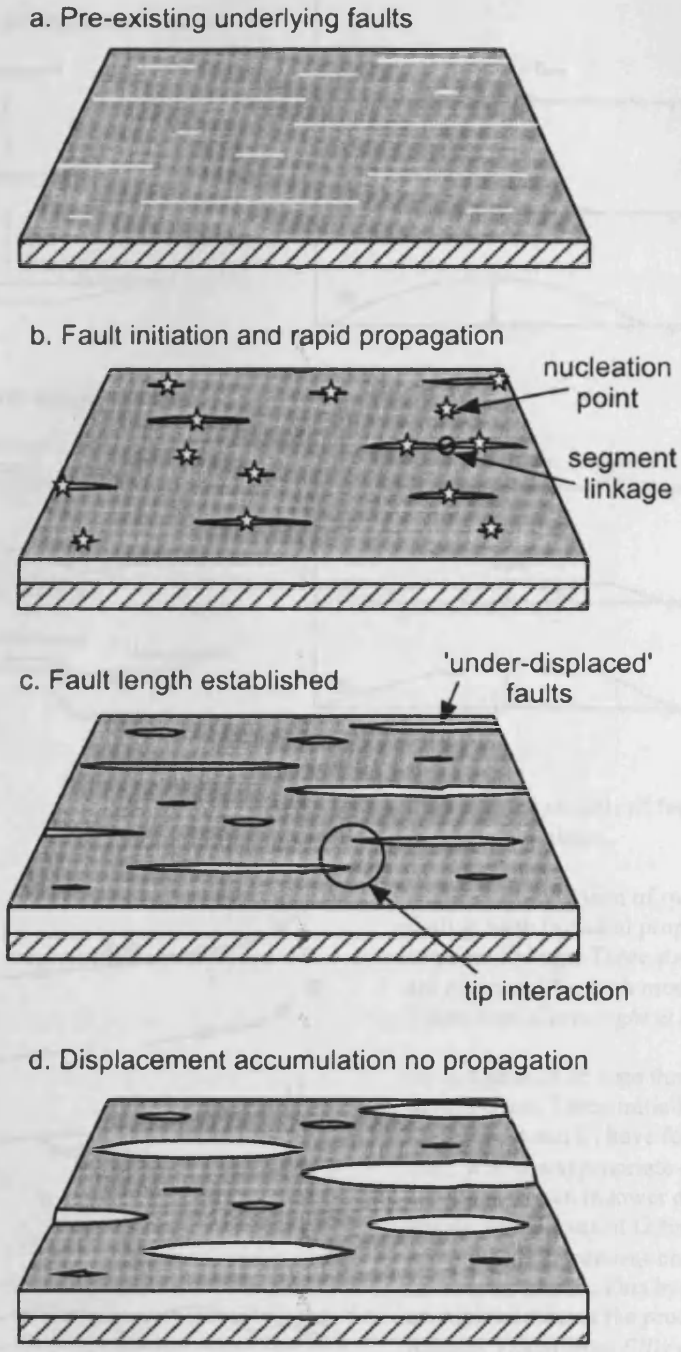

Figure 1.9: Schematic block diagram showing one model of fault growth from *Walsh et al. (2002).*

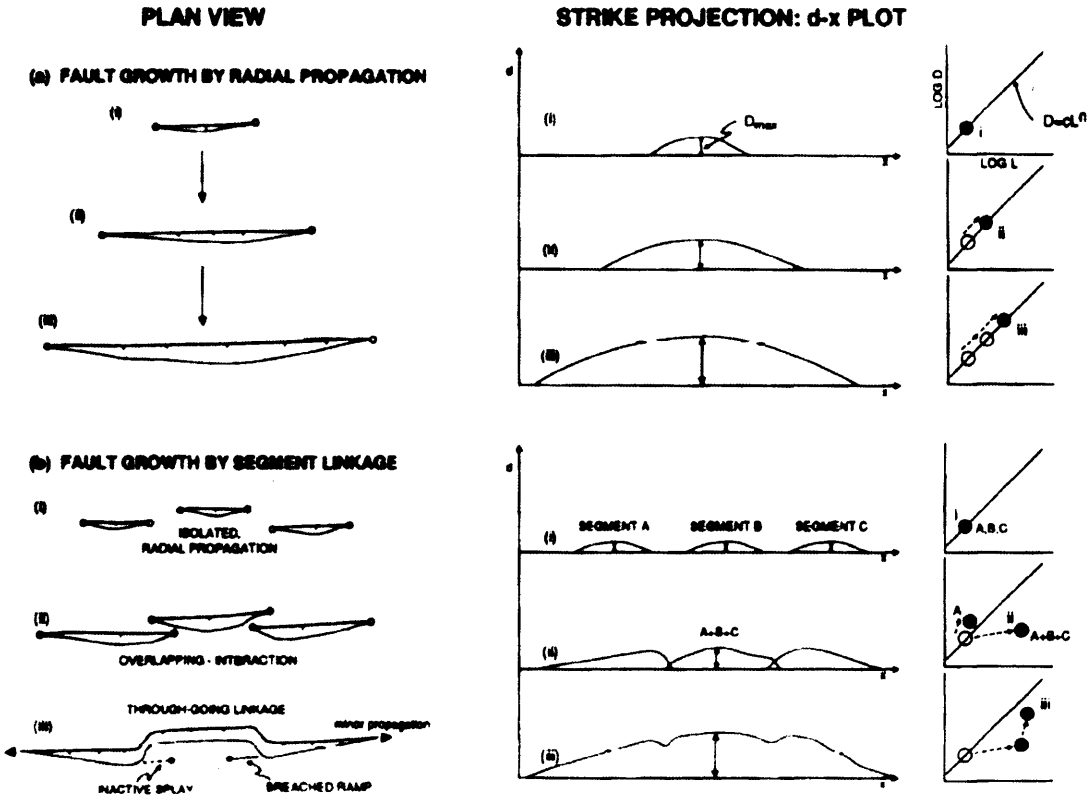

Figure 1.10: Models of fault development by segment linkage.

(a) (b) A comparison of two models of fault growth (a)radial propagation, and (b) segment linkage. Three stages of growth are compared for both models in plan view. Taken from *Cartwright et al. (1995).*

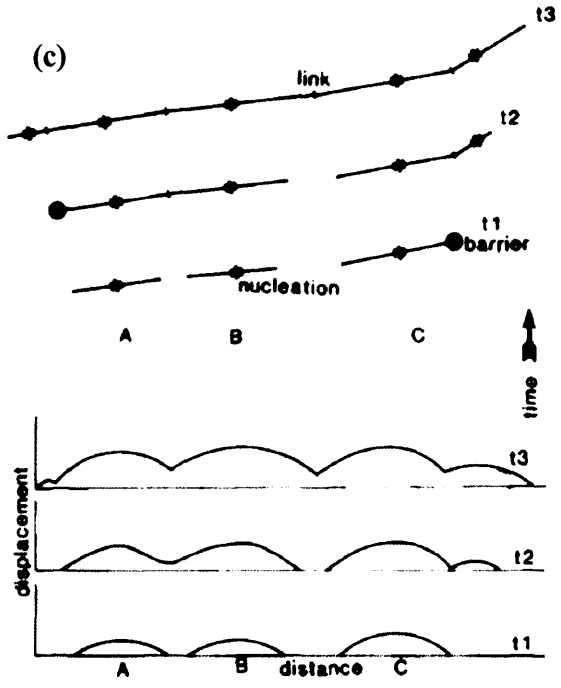

(c) Schematics of large thrust fault development. Three initially independent faults, A, B and C, have formed after tl time, with the appropriate displacement functions shown in lower diagram. Further seismic slip occurs at t2 time, such that A and B link. The process continues in like manner to time t3. This hypothetical example combines the processes of fault linkage. Taken from *Ellis and Dunlap (1989).*

models describe elliptical (Pollard and Segall, 1987) or bell shaped (Cowie and Scholz, 1992) patterns with zero displacement at the tips and a maximum measured near the centre of the crack (Davis et al., 2005). Data from real faults display significant variability away from these theoretical models in both profile shape and the location of maximum displacement (Dawers and Anders, 1995; Manighetti et al., 2001; Davis et al., 2005). Cartwright et al (1995) suggest that much of this variability in the accumulation of fault displacement may be due to mechanical interaction and linkage of fault segments (Fig. 1.10). As fault displacement profiles are partially controlled by the mechanism of fault-segment interaction it has been suggested that they also record the history of fault growth and delineate areas of initial nucleation and linkage.

1.4.2 *Fault growth by segment linkage*

Simple models of fault growth suggest two ways in which elongate faults may develop; by radial propagation and by segment linkage (Fig. 1.10). The conceptual framework of fault analysis is based on the characteristics of an individual blind normal fault (Fig. 1.6a) that grows by radial propagation with no migration of the point of maximum displacement (Brown, 1999). During radial propagation, an individual fault lengthens and accumulates displacement through time and is typified by an elliptical fault tip line. Fault growth by segment linkage deviates from this pattern and involves periods of sudden fault length increase as faults link to produce a larger through-going fault. Numerous authors have investigated this latter mechanism where faults in the brittle upper crust form by the interaction and linkage of previously individual segments (Segall and Pollard, 1980; Granier, 1985; Ellis and Dunlap, 1988; Martel et al., 1988; Peacock and Sanderson, 1991; Anders and Schlische, 1994; Peacock and Sanderson, 1994; Trudgill and Cartwright, 1994; Cartwright et al., 1995) (Fig. 1.9). Such fault segments can be initially geometrically and kinematically isolated structures (e.g. Peacock and Sanderson, 1991; 1994; Cartwright et al., 1995), or they can be interrelated from inception (Fig. 1.11), as in the example of the bifurcation of a single fault at depth (e.g. Childs et al., 1995; Huggins et al., 1995; Walsh et al., 2003). In the isolated fault model, developing segments will propagate towards each other until mechanical interaction is possible, causing interference in the stress fields of the faults. Retardation and arrest of

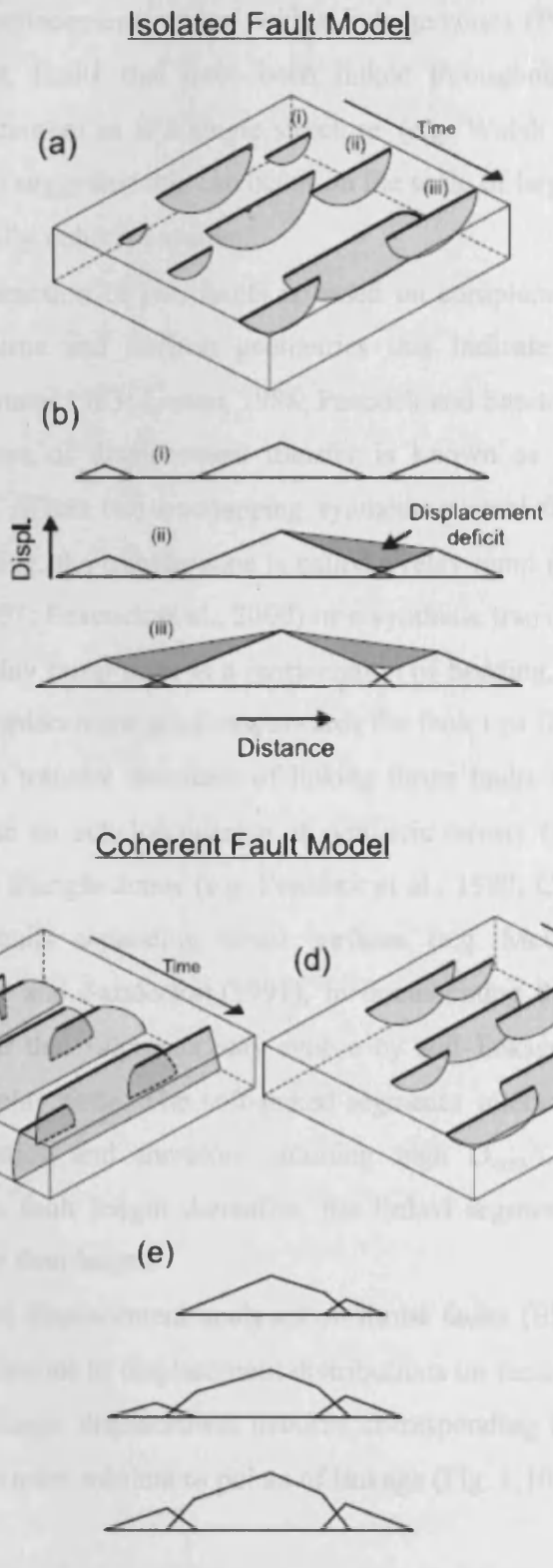

Figure 1.11: Schematic illustrations of the two end-member models of formation of segmented fault arrays. Displacement-distance plots for the isolated fault model (b) show displacement deficits on aggregate profiles within the linkage zones. Displacement-distance plots of the coherent model (e) show that fault displacements sum to produce smooth aggregate profiles within the relay zones. Taken from *Walsh et al. (2003)*.

propagating tips produces steeper displacement gradients on linking faults and results in a cumulative displacement minima within linkage zones (Peacock and Sanderson, 1991). In contrast, faults that have been linked throughout development should accumulate displacement as if a single structure (e.g. Walsh and Watterson, 1991). Walsh et al. (2003) suggested this can occur on the scale of large fault arrays that may act as a kinematically coherent system.

Kinematic interaction of two faults is based on complementary modification to displacement patterns and horizon geometries that indicate displacement transfer (Muraoka and Kamata, 1983; Larsen, 1988; Peacock and Sanderson, 1994; Huggins et al., 1995). The area of displacement transfer is known as a 'transfer zone' (e.g. Dahlstrom, 1970). When two overlapping synthetic normal faults are linked by an area of tilted bedding, the transfer zone is called a relay ramp (Larsen, 1988; Peacock and Sanderson, 1991; Peacock et al., 2000) or a synthetic transfer zone (Morley et al., 1990). Within a relay ramp there is a reorientation of bedding, due to the progressive increase of fault displacement gradients towards the fault tips (Peacock and Sanderson, 1994). Studies into transfer structures of linking thrust faults are fewer and, prior to this study, only the en echelon overlap of synthetic thrusts (e.g. Dahlstrom, 1970), interactions within triangle zones (e.g. Pennock et al., 1989; Couzens and Wiltschko, 1996) and tear faults separating thrust surfaces (e.g. McClay, 1992) had been described. Peacock and Sanderson (1991), in documenting the stages of growth of linked faults, noted that segments may evolve by soft-linkage or may hard-link by breaching of the relay zone. The soft-linked segments interact with adjacent faults, inhibiting propagation and therefore attaining high D_{max}/L ratios. Hard linkage suddenly increases fault length thereafter, the linked segments rapidly accumulate displacement rather than length.

One of the first displacement analyses on thrust faults (Ellis and Dunlap, 1988) concluded that variations in displacement distributions on faults of varying sizes were related to fault linkage; displacement maxima corresponding to areas of initial fault nucleation, displacement minima to points of linkage (Fig. 1.10b).

1.4.3 *Fault-related folding in compressional belts*

Fault-related fold systems can be found in a wide range of contractional terranes including foreland fold and thrust belts, inverted basins, accretionary prisms and deltaic toe-of-slope fold belts. Such areas are commonly structurally complex and can have limited sub-surface data. Despite this it is widely accepted that three principal types of fault-fold interactions can be used to explain the majority of individual structures found in all these settings. These can be conveniently classified in terms of the timing of fold growth relative to fault propagation (Thorbjornsen and Dunne, 1997) and are termed detachment folds (e.g. Jamison, 1987; Dahlstrom, 1990; Groshong and Epard, 1994; Hardy and Poblet, 1994), fault propagation folds (e.g. Williams and Chapman, 1983; Mitra, 1990; Suppe and Medwedeff, 1990; Erslev, 1991; Suppe et al., 1992) and fault bend folds (Rich, 1934; Suppe, 1983; Wiltschko et al., 1985; Medwedeff, 1992) (Fig. 1.12). These mechanisms are not mutually exclusive however, either temporally, spatially, in individual structures or within a fold and thrust belt (Hardy et al., 1996). A fault-propagation fold, for instance, may propagate upwards until it reaches a second detachment level, whereupon the fault may refract to become layer-parallel forming a fault-bend fold. Other hybrid folds can form that developed by a number of these processes such as break-thrust folds (e.g. Mitchell and Woodward, 1988; Butler, 1992; Morley, 1994) and fault-arrest folds (e.g. Williams and Chapman, 1983; Hedlund et al., 1994; Wickham, 1995). It has been suggested that the mechanical stratigraphy of the units involved in the thrusting may determine the fold-thrust relationships. The relationships between fault slip, fault-shape and fold-shape for many of these end member structures have been quantified in a number of geometric models (Suppe, 1983; Suppe and Medwedeff, 1984; Mitra, 1990; 1990).

Two basic groups of models have been proposed to explain the geometry and kinematics of upper crustal folds; namely kink-band migration models (e.g. Suppe, 1983; 1985; Suppe and Medwedeff, 1990) and limb-rotation models (e.g. Hardy and Poblet, 1994; Poblet and McClay, 1996). The former specify that folds grow in a self-similar manner by the widening of fold limbs during amplification (Fig. 1.13). Bedding surfaces undergo an instantaneous change in dip at axial surfaces and limbs maintain constant inclinations during fold growth (Suppe, 1983; Suppe and Medwedeff, 1990). In contrast, limb-rotation models involve progressive rotation of

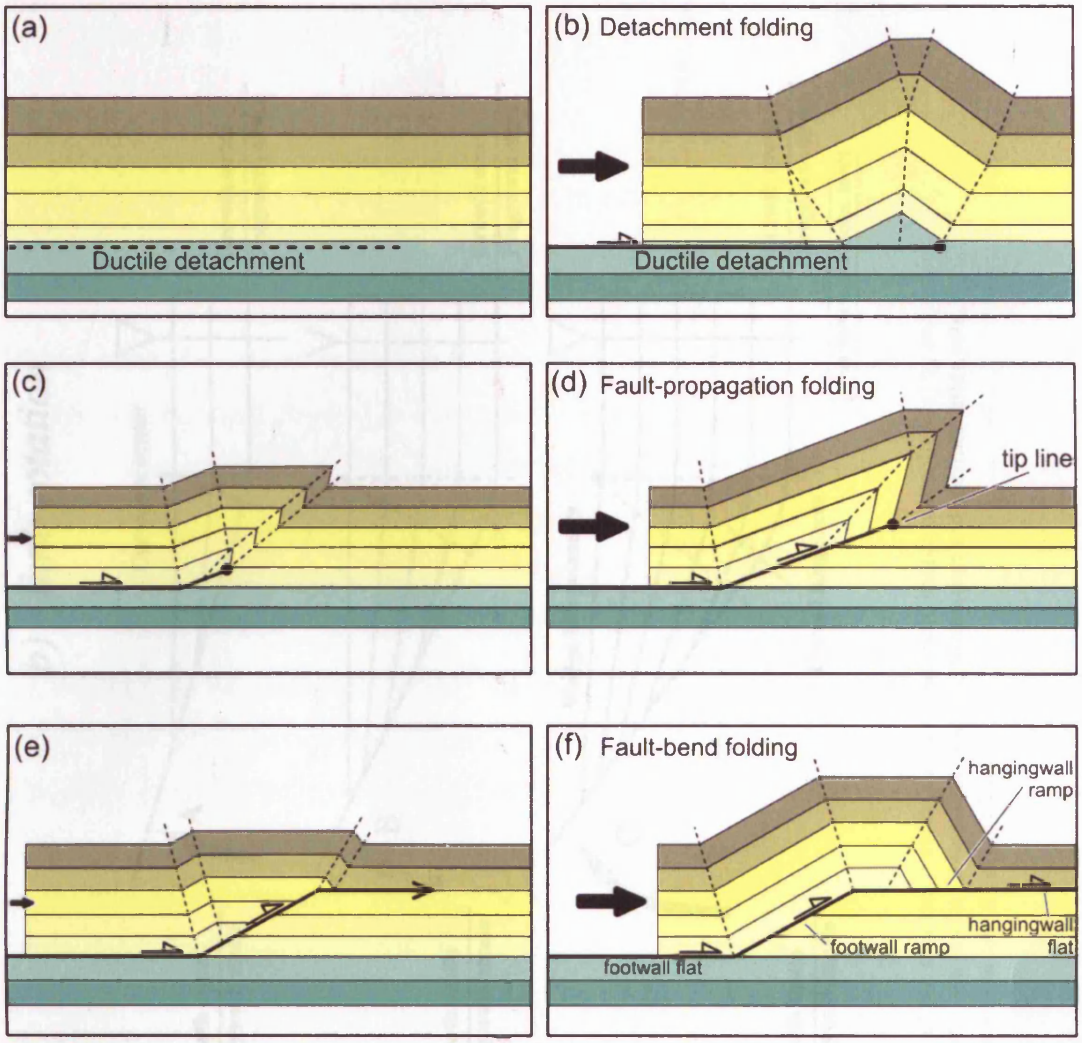

Figure 1.12: Three principal types of thrust-related folding. **(a, b)** Detachment fold. **(c, d)** Fault-propagation fold. **(e, f)** Fault-bend fold. After *McClay (1992)*.

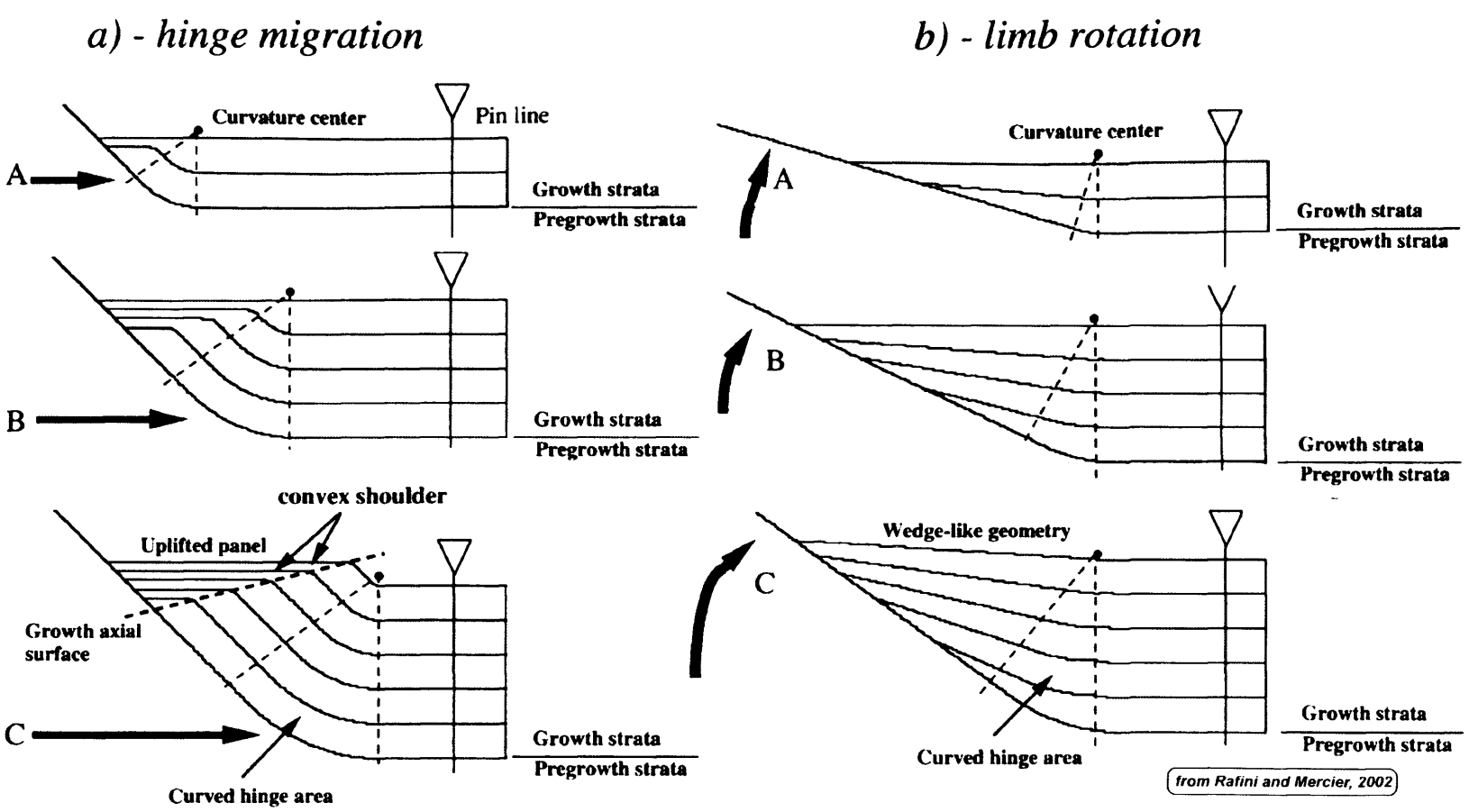

Figure 1.13: Schematic descriptions of the kinematic evolution of syntectonic basins controlled **(a)** by hinge migration, **(b)** by limb rotation. The models assume a constant ratio of deformation and sedimentation rate, and no erosional activity. Taken from *Rafini and Mercier (2002)*.

fold limbs such that they gradually steepen during fold evolution (Hardy and Poblet, 1994) (Fig. 1.13).

Detachment folds

Detachment folds develop either as the result of displacement accruement near a thrust tip or from buckling above a detachment such as shale or an evaporite (Thorbjornsen and Dunne, 1997). Such folds are not related to the development of a thrust ramp, but are associated with the termination of a layer parallel thrust fault within a detachment layer (Jamison, 1987; Dahlstrom, 1990; Homza and Wallace, 1995; Poblet and McClay, 1996) as displacement is transferred into folding above the leading edge (Fig. 1.12b). Detachment folds can also develop within a thrust sheet with a laterally decreasing displacement gradient.

Sedimentary units within detachment folds are commonly characterised by significant thickness and competency contrasts. Folds may display parallel geometries in the outer arcs and non-parallel, disharmonic geometries in the cores. Migration of ductile layers into the core of a fold during the early stages of fold growth can be followed by the expulsion of core material as shortening continues. Resultant anticlines can be flattened forming lift-off folds (Mitra and Namson, 1989). The evolution of a detachment fold can involve an increase in both fold amplitude and wavelength by hinge migration and/or limb rotation (e.g. Suppe, 1983; Mitra, 2002). Flexural slip between sedimentary layering is the primary mechanism that accommodates limb rotation, however continued amplification can cause fold hinges to lock resulting in internal deformation (Mitra, 2002).

A break thrust fold, also termed 'faulted detachment fold' (e.g. Mitra, 2002), requires the formation of a fold prior to the propagation of a thrust fault (Willis, 1893) and hence fold shape is less dependent on fault geometries (Thorbjornsen and Dunne, 1997). Mitra (2002) states that the rotation of limb segments between locked hinges results in the nucleation of thrust faults, which propagate through deformation zones on fold limbs. Eventually, a through-going fault connects one of the major faults with the basal detachment. Proceeding deformation may then be accommodated by fault-propagation folding producing folds that may superficially resemble fault propagation folds (Mitra, 2002).

Fault-propagation folds

Fault propagation folding occurs *during* the propagation of imbricate faults as a thrust ramps up from a detachment (Fig. 1.12d). This mechanism was originally included within the description of tipline folds (Williams and Chapman, 1983) however this terminology is rarely used (Thorbjornsen and Dunne, 1997). Suppe (1985) defined fault-propagation folds as folds that "represent deformation that takes place just in front of the propagating fault surface" (Erslev, 1991) and hence fault geometries strongly influence fold shape. Geometric models of fault propagation folding (e.g. Suppe and Medwedeff, 1984) have adapted kink-band migration kinematics described on fault-bend folds. These models predicted backlimb development by hinge migration and forelimb by either hinge migration or limb rotation. Erslev (1991) argued however that "kink-band kinematics cannot replicate the curved fold surfaces and complex strain patterns in natural and experimental fault-propagation folds" and proposed a trishear model for the deformation in front of a propagating fault tip. In this model, triangular zones of penetrative deformation are identified at the fault tip.

The above models all relate to synchronous fold growth and fault propagation. Fault-arrest folds however postdate fault propagation (Thorbjornsen and Dunne, 1997) and are characterised by continued deformation on an imbricate thrust with an arrested and stationary fault tip (Armstrong and Bartley, 1993; Wickham, 1995). Fold amplification in the hangingwall sequence accommodates accumulating displacement.

Fault-bend folds

Fault-bend folds postdate fault propagation and are the result of the change in fault trajectory (Suppe, 1983) such as when a fault steps up from one detachment layer to another (Rich, 1934). Folds are induced in hangingwall strata as it is forced over the non-planar fault surface (Fig. 1.12f). Suppe (1983) proposed a geometric and kinematic model in which he described a strong relationship between fault shape and fold shape at positions of sharp bends in faults. Fold limbs are thought to grow in a self-similar manner by hinge migration such that the angle of dip of the limbs remains constant throughout fold development (Suppe, 1983).

1.4.4 *Growth folds*

Fold growth in marine settings is typically accompanied by syntectonic sedimentation which can produce growth fold systems comprising syn-kinematic strata that typically thin towards and onto the crest of the growth anticline (Suppe et al., 1992). Many authors have recognised the importance of such kinematic indicators as preserving a record of the geometric and temporal evolution of fault-related fold systems (e.g. Suppe et al., 1992; Hardy et al., 1996; Poblet et al., 1997). A number of models have been developed to simulate syntectonic stratal patterns associated with detachment folds, fault propagation folds and fault bend folds (e.g. Medwedeff, 1989; Suppe and Medwedeff, 1990; Suppe et al., 1992; Hardy and Poblet, 1995; Hardy et al., 1995; Storti and Poblet, 1997). Storti and Poblet (1997) state that "different folding mechanisms give rise to different evolutionary paths in the shape of thrust-related anticlines and, consequently, different geometries in the associated syntectonic sediments". The shape of pre-kinematic folded units, and thus the architecture of the growth strata, is largely controlled by axial surface activity (i.e. the length of the limbs), the nature of fold amplification (i.e. by limb rotation of self-similar folding) and the ratio of the rate of uplift to the rate of sedimentation (Storti and Poblet, 1997).

Figure 1.14 shows a fault propagation fold and a fault-bend fold and the related growth stratal geometries. The latter is characterised by rotated strata of uniform thickness on the backlimb (Fig. 1.14a) and thinning or onlapping strata on the forelimb (e.g. Suppe et al., 1992). In the case of fault propagation folds (Fig. 1.14b), thinned and rotated growth sequences develop on both limbs (e.g. Suppe et al., 1992; Storti and Poblet, 1997) and are governed, in part, by the ramp angle. The role of limb-rotation and hinge migration in the amplification of folds was discussed in a previous section. Growth strata geometries generated by each model mechanism vary significantly (Fig. 1.15). Hinge migration generates limb-parallel and flat-lying panels in the growth strata (Suppe et al., 1992), whereas limb rotation causes continuous variation in the angle of dip of depositional surfaces on growing fold limbs (Fig. 1.15b and d) leading to wedge like geometries in the growth strata (Riba, 1976; Hardy and Poblet, 1994; Storti and Poblet, 1997). The competition between tectonic uplift rate (U) and the rate of syn-tectonic sedimentation (S) is also described. Storti and Poblet (1997) state that when the U/S ratio is greater than 1, tectonic uplift exceeds sedimentation and a positive bathymetric relief is generated during folding. A ratio

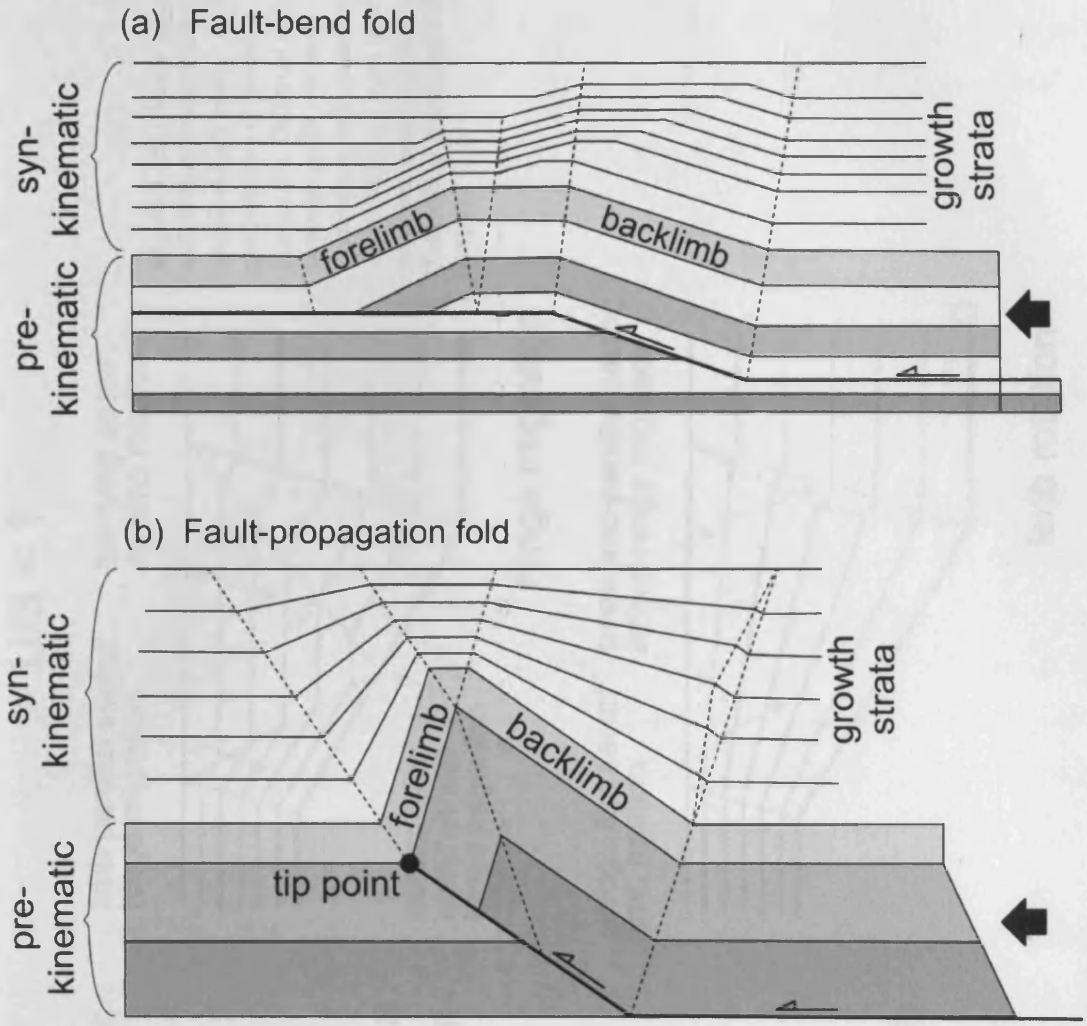

Figure 1.14: Growth stratal geometries relating to **(a)** fault-bend folds, and **(b)** fault-propagation folds. Adapted from *Suppe et al. (1992).*

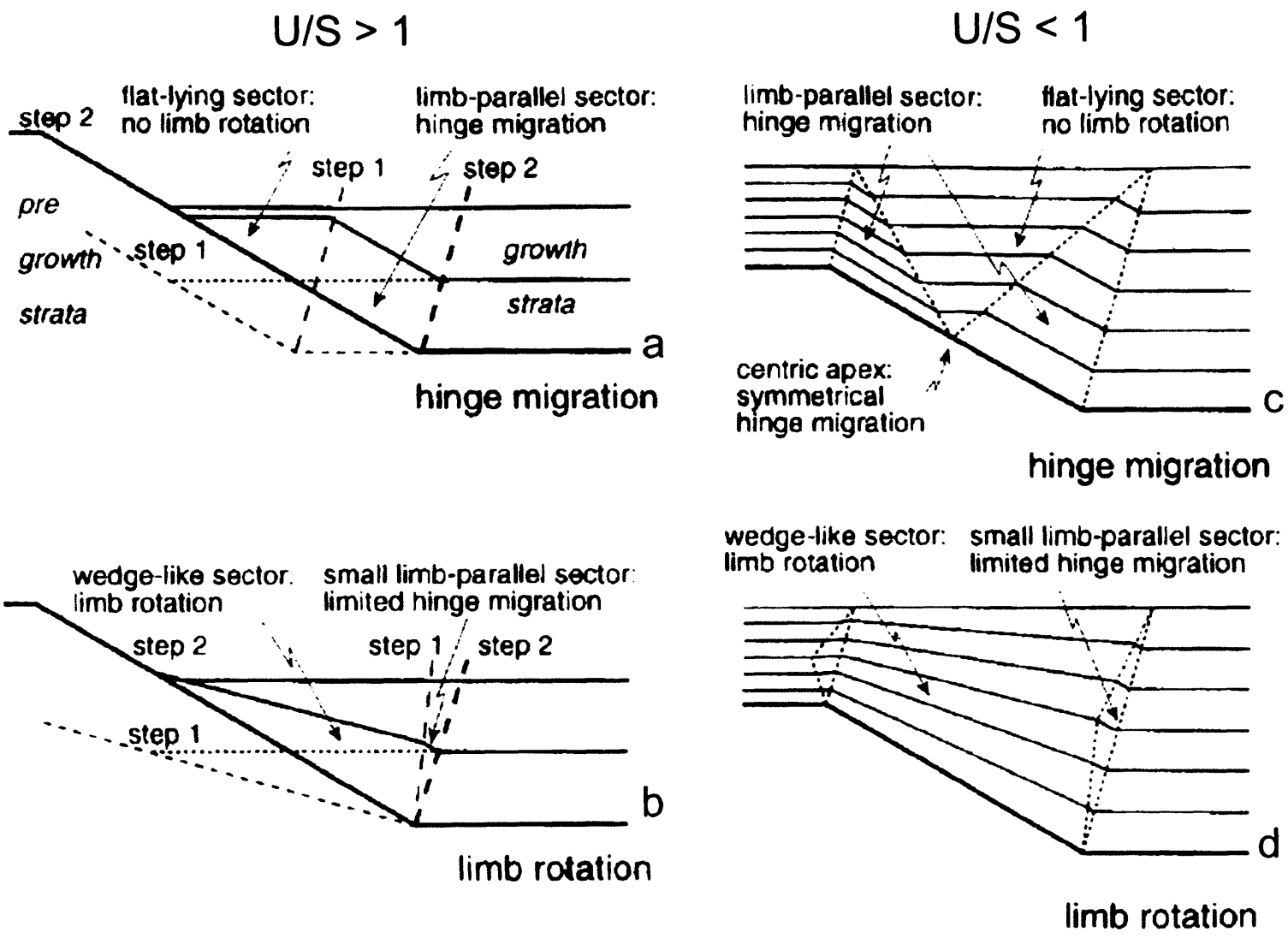

Figure 1.15: Growth stratal architectures associated with identical kink bands generated by different kinematics. Different ratios between uplift rate and syntectonic sedimentation rate (U/S) have been used to generate these models. Taken from *Storti and Poblet (1997).*

less than 1 results in syntectonic sediments being continuous across a fold. Different amounts of uplift and sedimentation rates, therefore, cause different onlap, offlap and overlap relationships in syn-kinematic strata in each mechanism of fold amplification (Storti and Poblet, 1997) (Fig. 1.15).

1.4.5 *Sediment dispersal and channel diversion in deep water settings*

Accommodation space on shelf settings is primarily controlled by sea level change and subsidence (e.g. Hooper et al., 2002). However in slope and basin floor settings fluctuations in sea level have less of an impact and the graded profile of the slope plays a more important role. Hooper et al (2002) state that "this profile represents a long-term morphodynamic equilibrium between depositional and erosional processes on the slope, establishing a stable angle of progradation". In deep water fold and thrust belts, like that of the Niger Delta, slope profiles are disrupted by gravitational deformation tectonic processes (i.e. faults and folds) and by the erosional and depositional action of gravity-flow systems. Thus, accommodation space in such areas may be largely impacted by structural and sedimentary controls (Hooper et al., 2002).

In the deep water Niger Delta the grade of the slope is initially altered by the development of toe-of-slope fold and thrust belt. Low relief structures create structural highs and lows which become influential in focussing submarine flows (Hooper et al., 2002). Channel systems can therefore be diverted by structural relief on the seabed (Fig. 1.16). Ductile movement of overpressured shale units can also contribute to changes in the delta slope angle. Accommodation space created by growing structures, such as on the back-limb of the frontal fold and thrust, is progressive infilled as sediments are 'intercepted'.

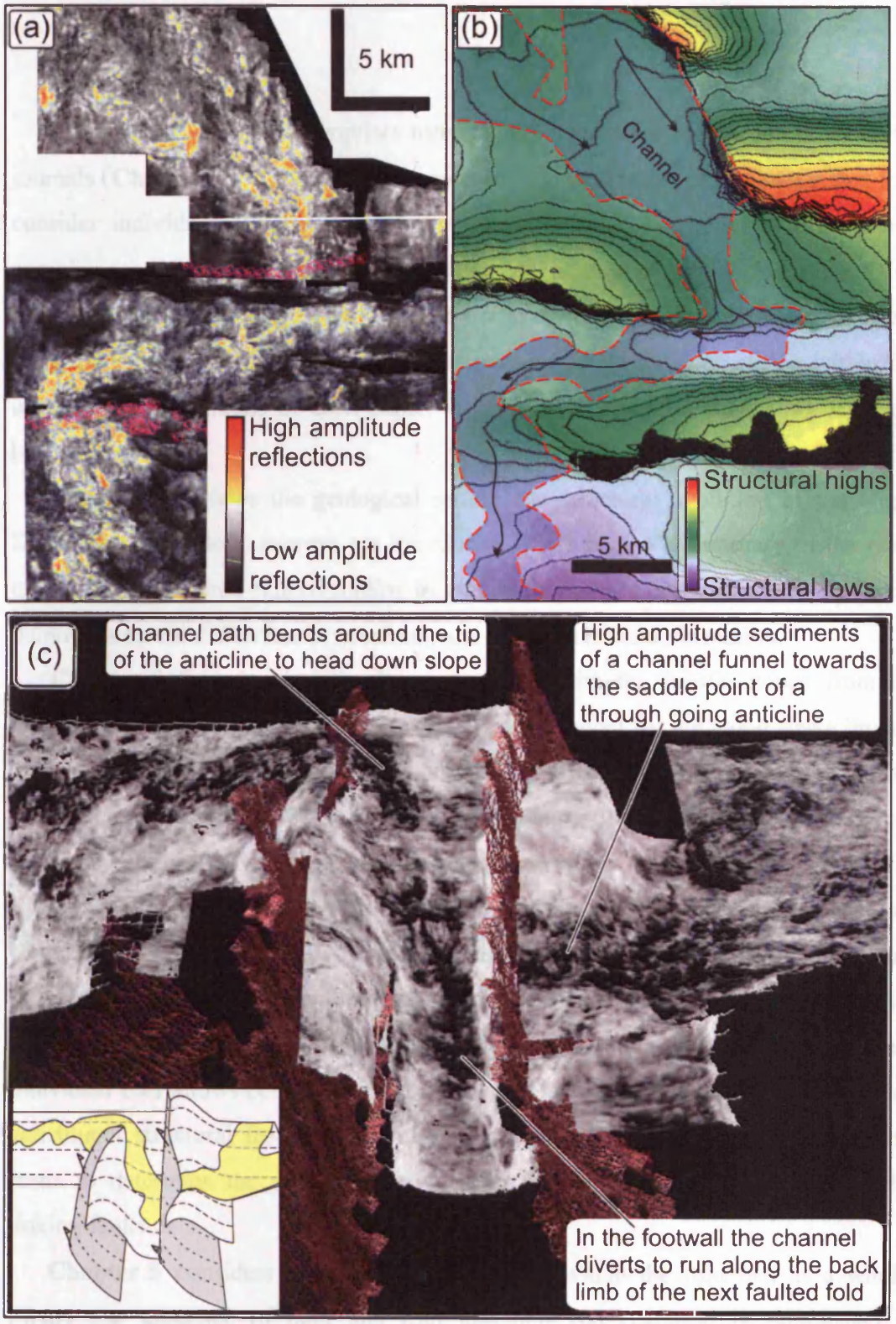

Figure 1.16: Channel diversion in response to changes in the slope profile due to gravitational deformation processes. **(a)** Seismic amplitude extraction map showing high amplitude reflections in a sinuous channel. **(b)** Topographic map of the stratigraphic horizon closest to the channel. The outline of the zone of high amplitude reflections is overlain. Note that the channel follows the structurally low regions. **(c)** Three-dimensional imaging of (a). Channel can be seen to, firstly, pass through the saddle point of a fold, and secondly deviate around the tip of the next downdip structure. Field of view approximately 30 km.

1.5 Thesis Layout

The core of this thesis comprises three papers written for publication in scientific journals (**Chapters 3, 4** and **5**). These represent a logical series of arguments that first consider individual structures and linking fault pairs, before moving to the more complex scenario of a closely spaced fold belt. At the time of submission of the thesis Chapter 3 has been published and Chapter 4 is in review. The writing of these sections for publication has affected their style and may introduce some repetition within the introductory paragraphs of each paper. A brief summary of each chapter is given below.

Chapter 2 reviews the geological setting and structural evolution of the Niger Delta. The 3D seismic surveys are introduced. There is also a summary of the main characteristics of fault-related folding in gravity-driven fold and thrust belts and some comments on the difference between salt and shale detached deformation.

Chapter 3 introduces static descriptions of antithetic transfer zones from 3D seismic data. A preliminary geometric classification model for the along strike linkage of thrust faults of opposing dip is proposed. The effects of fault interaction on fold geometries is described with reference to the along strike changes in fold vergence and stratal connectivity through various transfer zones.

Chapter 4 applies the geometries of fault linkage and the observations of stratal connectivity from Chapter 3 to an individual, isolated fold comprising numerous interacting faults. Measurements of fault heave and bulk shortening are presented for individual faults and the fold as a whole. The quantification of strain throughout an individual fold allows conclusions to be drawn on the kinematic relationship between constituent structural features. The chapter concludes with the analysis of growth strata to determine the growth history of the fold and structural evolution of the linking faults.

Chapter 5 considers the distribution of strain within the fold belt as a whole. Firstly the sequence of fault and fold initiation and cessation is established to determine the degree of synchronous growth in the system. Displacement transfer is investigated between structures both along strike and in a dip-parallel direction. A discussion of the degree of kinematic interaction and displacement transfer between constituent features of the fold belt concludes the chapter.

Chapter 6 draws together the conclusions of Chapters 3, 4 and 5. A model for fold and thrust belt development is proposed and the controls on the geometries of antithetic fault linkages are discussed. The implications of this study on other types of settings are considered. Finally, a brief overview of the limitations, uncertainties of this study and proposals for future work conclude the chapter.

Chapter 7 lists the main conclusions of the thesis.

Chapter 2

CHAPTER 2

2 NIGER DELTA: GEOLOGICAL SETTING, DATABASE AND STRUCTURAL REVIEW

2.1 Geological and stratigraphic framework

The Niger Delta extends into the eastern Gulf of Guinea on the western margin of Africa (Fig. 2.1) and is one of the largest regressive deltas in the world (Doust and Omatsola, 1990). Neogene clastic sediments reach an estimated maximum thickness of 12 km (Whiteman, 1982; Damuth, 1994) over extended oceanic and continental crust. The delta is located at the southern end of the Benue Trough which represents a failed arm of a triple junction that formed during the opening of the Atlantic in the late Cretaceous (Lehner and Ruiter, 1977; Whiteman, 1982; Damuth, 1994). Following this event the Benue trough progressively filled with Albian and younger post-rift deposits and the delta became established over the continental margin by the Late Eocene (Damuth, 1994).

A three-fold subdivision of stratigraphy into the Akata, Agbada and Benin Formations, representing prograding depositional environments, has been adopted by numerous authors (Knox and Omatsola, 1989; Doust and Omatsola, 1990; Damuth, 1994; Cohen and McClay, 1996; Morgan, 2004). The Late Cretaceous - Palaeocene Akata Formation at the base of the delta is of marine origin and is composed of thick shale sequences that are thought to be over-pressured (e.g. Morley and Guerin, 1996; Wu and Bally, 2000). On seismic sections this formation is characterised by a lack of internal reflections (Fig. 2.2) with the exception of a strong, high-amplitude reflection, which has been shown to act as a regional detachment level for deep water thrust faults (Corredor et al., 2005; Briggs et al., 2006). Anomalously low P-wave seismic velocities within the Akata Fm imply under-compaction (Morgan, 2003) and may point to regional fluid overpressures (Bilotti and Shaw, 2005).

The boundary between the Akata and Agbada megasequences is readily identified on seismic profiles (Fig. 2.2) in the lower slope region (the area of study in this thesis) as a regionally consistent seismic reflection event that separates two regions of distinct seismic character (Morgan, 2004). The base of the overlying Eocene-recent Agbada Formation is marked by a distinct change in depositional style

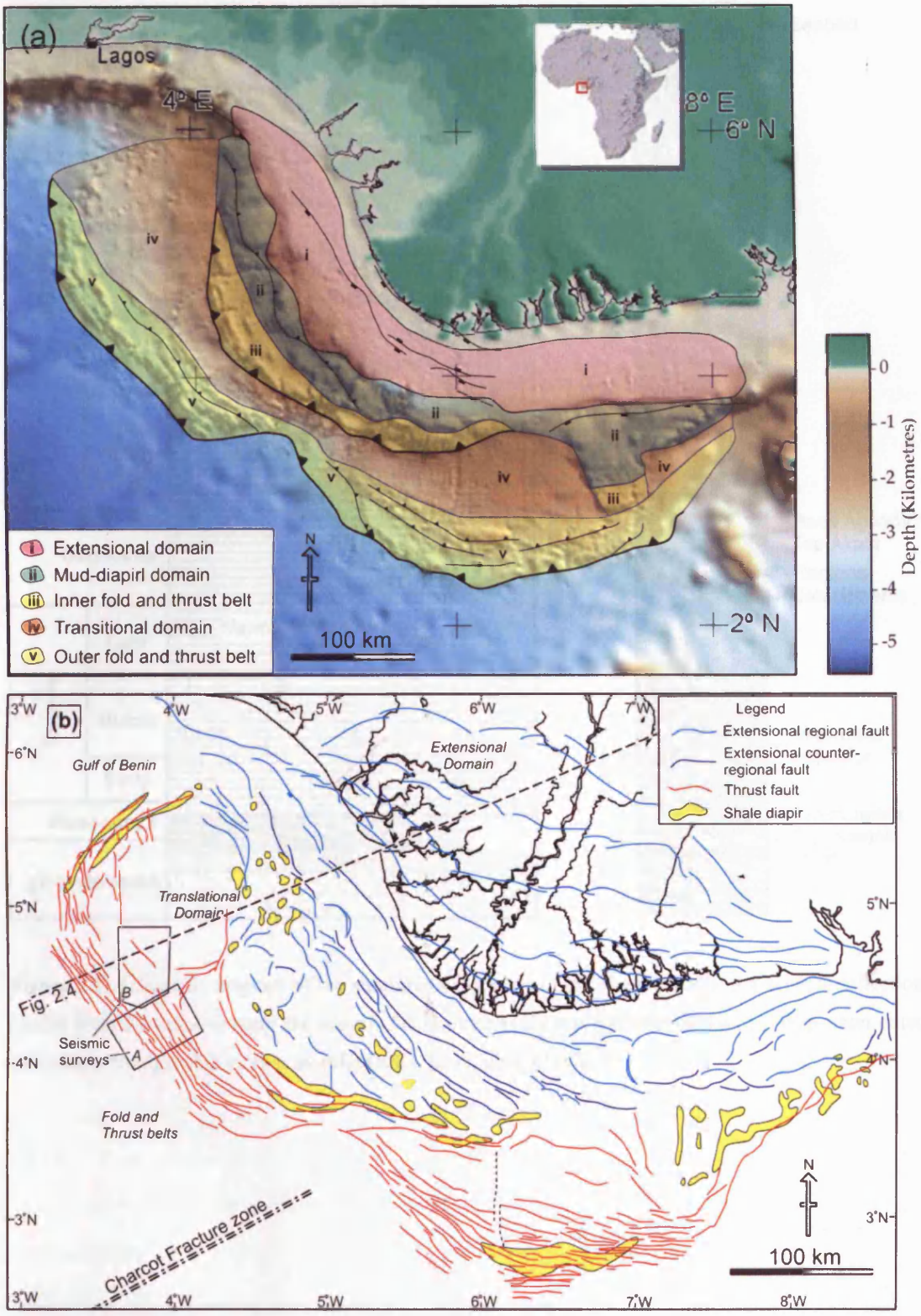

Figure 2.1: Regional maps of the Niger Delta. Showing **(a)** the main structural domains of i) an extensional province beneath the continental shelf, ii) a mud-diapir belt located beneath the upper continental slope, iii) the inner fold and thrust belt, iv) a transition zone beneath the lower continental slope, and v) the outer fold and thrust belt. Zones overlay a high resolution bathymetry image from *Corredor et al. (2005)*. **(b)** a structural map of extensional, diapiric and contractional features and the location of Surveys A and B. Locations of shale diapirs taken from *Saugy and Eyer (2003)*.

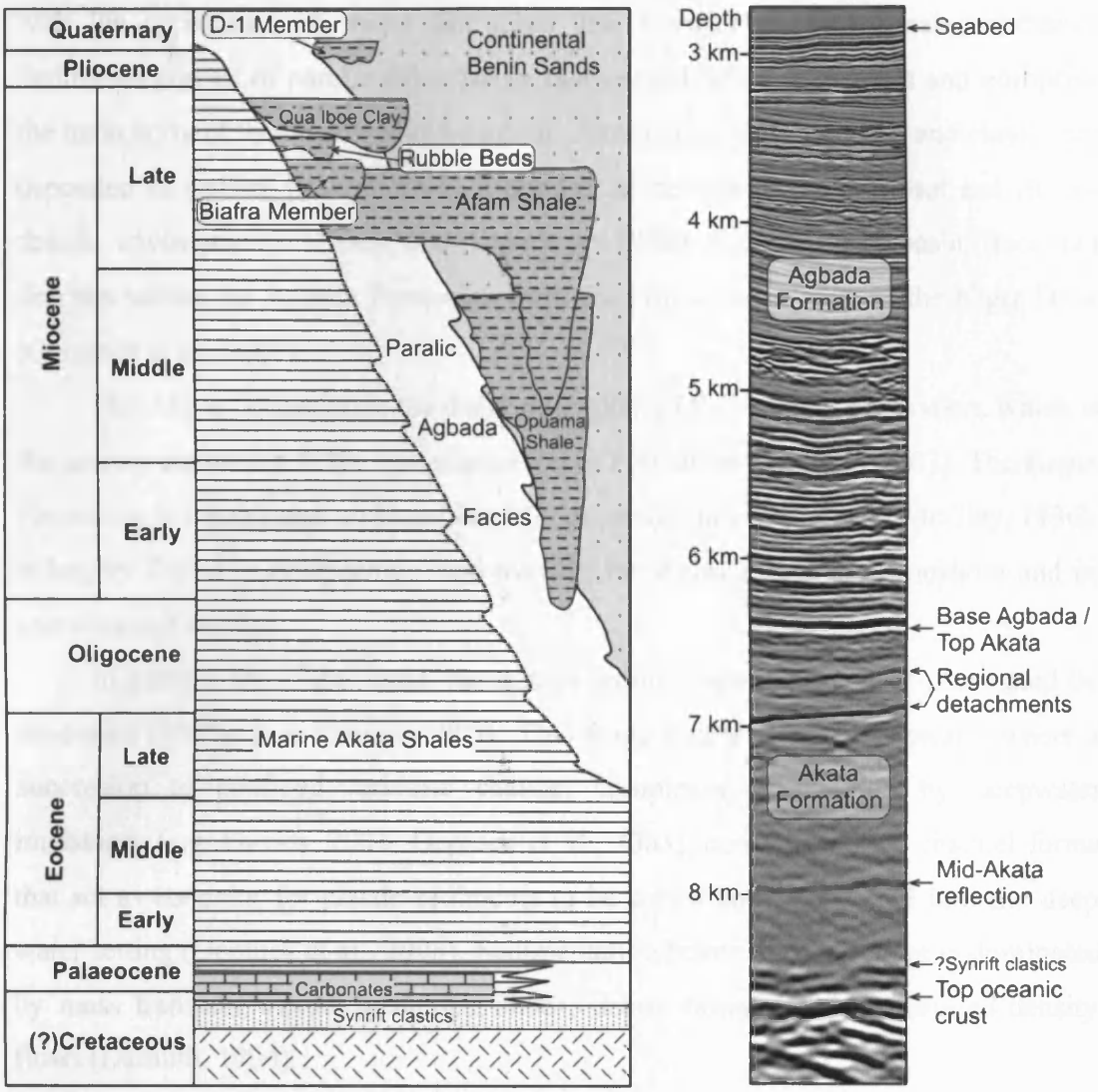

Figure 2.2: Schematic diagram of the stratigraphic column of the Niger Delta and a seismic reflection profile from Survey A to show the seismic facies of the main stratigraphic units in the deep water outer thrust belt. Stratigraphic section modified after *Jubril et al. (1998)*.

with the appearance of major fan lobes and a major progradational succession. Sediments consist of paralic siliciclastics that exceed 3.5 km thickness and comprise the main body of the Niger sediment apron. Alternations of sands, silts and clays were deposited in various proportions in a number of delta-front, delta-topset and fluvio-deltaic environments (Doust and Omatsola, 1990). Channel and basin floor fan deposits within the Agbada Formation form the primary reservoirs in the Niger Delta (Corredor et al., 2005).

The Akata Formation is the distal equivalent of the Agbada Formation, which is the marine equivalent to the non-marine Benin Formation (Morgan, 2003). The Benin Formation is the thinnest and least laterally extensive unit (Cohen and McClay, 1996), is largely fluvial in composition and overlies the Agbada Formation onshore and in some coastal settings.

In general, the Niger Delta has a high sedimentation rate and is dominated by mudstone (>80%) (e.g. Davies, 2003). This study focuses on the deepwater where a succession of confined turbidite channel complexes, surrounded by deepwater mudstones (e.g. Davies, 2003; Deptuck et al., 2003), contain sinuous channel forms that act as conduits for clastic sediments to be sorted and transported into the deep water setting (Deptuck et al., 2003). Sedimentation below the shelf edge is dominated by mass transport including slumps, slides, debris flows gravity-controlled density flows (Damuth, 1994).

2.2 Database

Two 3D seismic surveys (termed surveys A and B), acquired by CGGVeritas in 1999 and 2002, comprise the 3D seismic data used in this study (Fig. 2.3). The total coverage of these two datasets amounts to over 5000 km^2 of the deep water toe-of-slope region on the Niger Delta. Both surveys were acquired with line spacing, in both the inline and crossline direction, of 12.5 m and a sampling interval of 4 ms. All data were processed using ray-traced Kirchoff pre-stack time migration and are zero-phase with SEG reverse polarity.

The dominant frequency of the data changes with depth as velocities vary vertically due to lithology, compaction and diagenesis (e.g. Brown, 1999). The main stratigraphic interval of interest herein is the Agbada Formation, which comprises the majority of thrust faults in the deep water fold and thrust belts. The dominant

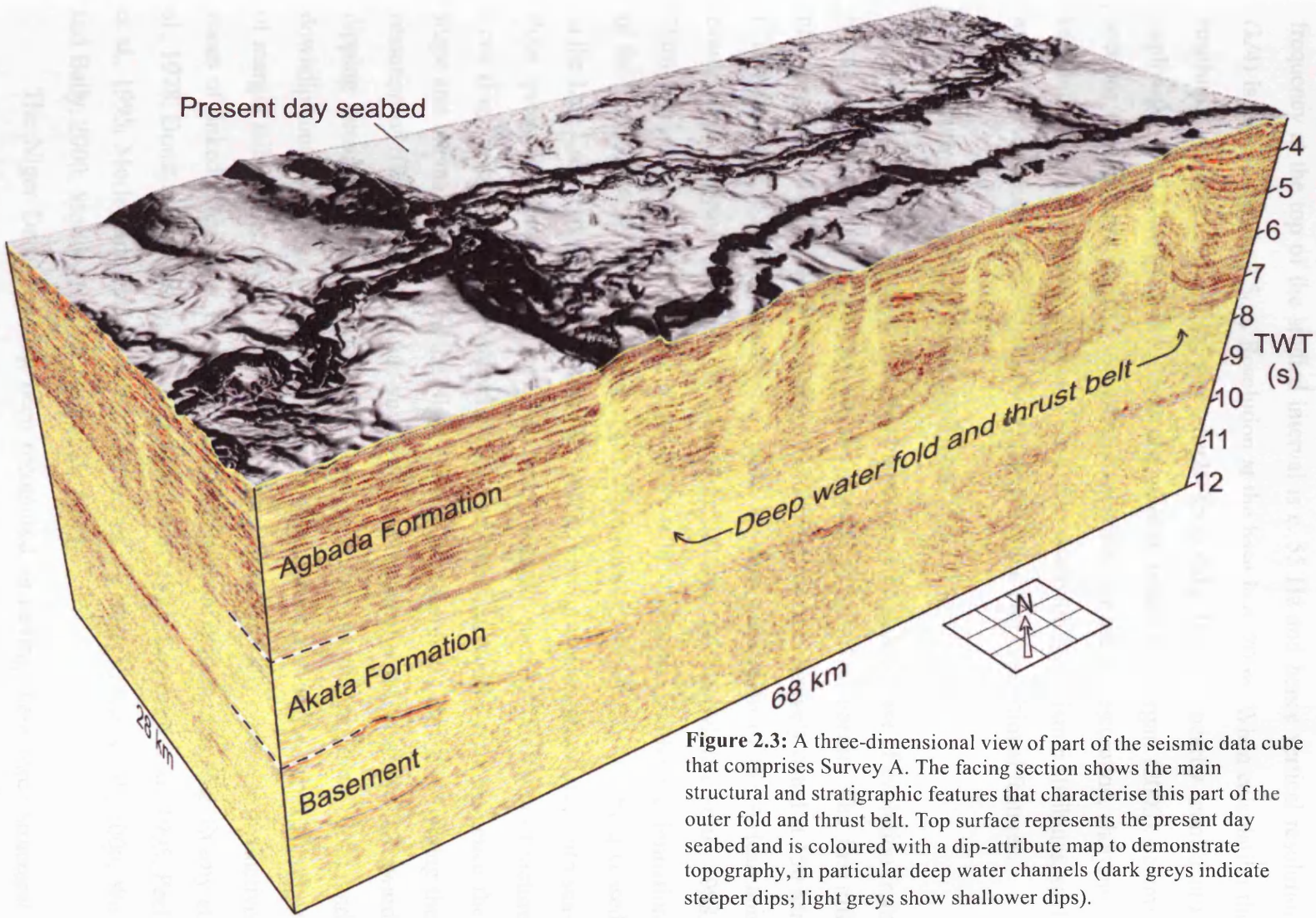

Figure 2.3: A three-dimensional view of part of the seismic data cube that comprises Survey A. The facing section shows the main structural and stratigraphic features that characterise this part of the outer fold and thrust belt. Top surface represents the present day seabed and is coloured with a dip-attribute map to demonstrate topography, in particular deep water channels (dark greys indicate steeper dips; light greys show shallower dips).

frequency at the top of the studied interval is c. 55 Hz and hence vertical resolution ($\lambda/4$) is approximately 7.5 m. Resolution at the base is c. 20 m. When calculating the resolution, interval velocities and check shot data from a nearby confidential exploration well were used along with the velocity model of Morgan (2003). Seismic sections were depth converted using these velocities for use in restoration, shortening calculations and to validate geometric structural observations. Seismic attributes, such as dip and amplitude, were utilized to reveal structural and depositional features.

2.3 Structural history of the Niger Delta

The Niger Delta continental margin has undergone a complex phase of evolution from initial extension in the Cretaceous to the present day passive margin. The first rift phase associated with the opening of the South Atlantic is tentatively dated at 150 Ma (Tithonian) to c. 130 Ma (Hauterivian) with the final separation of the African and South American continents occurring between 100 and 105 Ma (Mascle et al., 1988; Nürnberg and Müller, 1991). The Niger Delta is located at the southern culmination of the Benue Trough, a failed arm of a rift triple junction, in which the rifting ceased in the Late Cretaceous (Lehner and Ruiter, 1977). Fracture zones associated with sea-floor spreading during the opening of the South Atlantic, such as the Charcot Fracture Zone (Fig. 2.1b) with its associated ridges and trenches, continue to influence the shape and internal structure of the Niger Delta (Corredor et al., 2005). Following the cessation of rifting the margin has undergone gravitational collapse above basinward dipping detachments producing large scale extension in the proximal delta and downdip contraction in a toe-thrust system on the outboard part of the slope. This type of margin failure is common on passive margins which typically comprise distinctive zones of linked extensional, transitional and contractional deformation (e.g. Evamy et al., 1978; Doust and Omatsola, 1990; Cobbold et al., 1995; Letouzey et al., 1995; Peel et al., 1995; Morley and Guerin, 1996; McClay et al., 1998; Rowan et al., 2000; Wu and Bally, 2000; Morley, 2003; Rowan et al., 2004).

The Niger Delta has long been recognised as having these three structural domains of extension, translation and contraction (Damuth, 1994) (Figs. 2.4 and 2.5). More recently authors have further subdivided the delta into five zones (Corredor et al., 2005) including (i) an extensional domain comprising regional and counter-regional normal growth faults located below the continental shelf; (ii) a mud

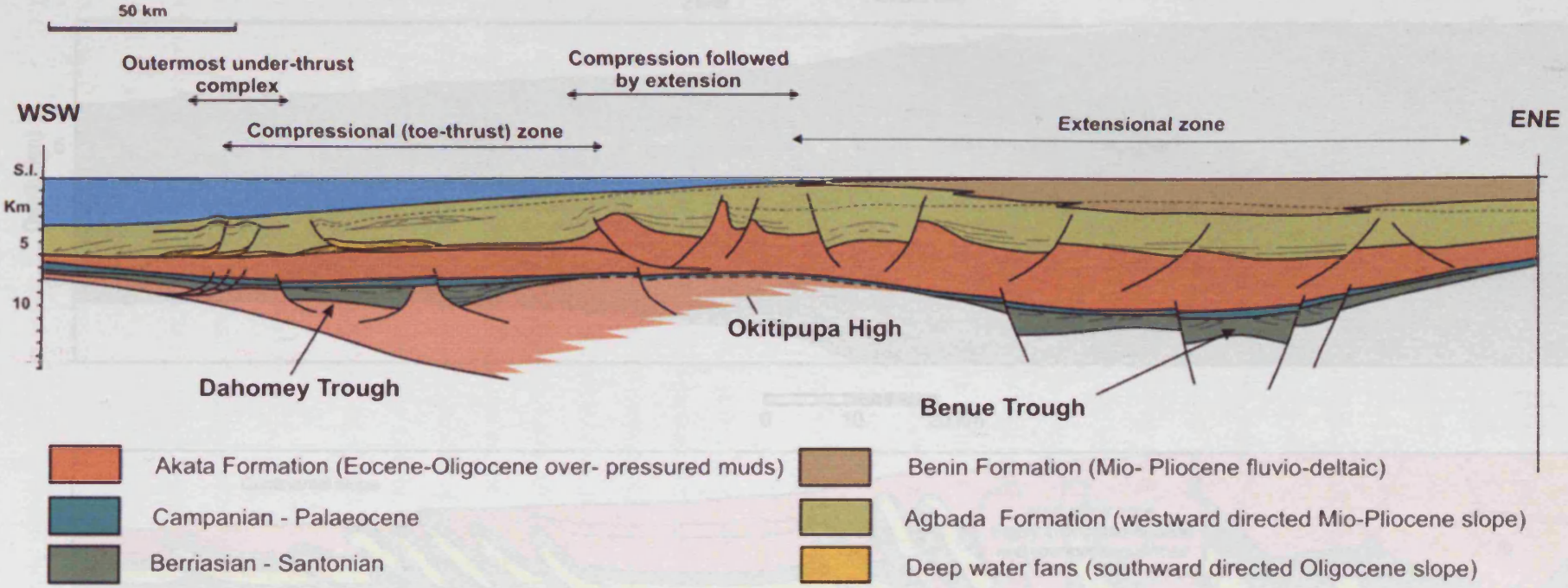

Figure 2.4: A regional scale cross section showing the main structural and stratigraphic elements of the Niger Delta. For location see Figure 2.1b. Note the change in structural styles from extension in proximal delta regions (ENE) to compressional in the distal region (WSW). The three main stratigraphic units are represented and it shows how the uppermost Benin Formation is not present downslope. Taken from *Morgan (2004).*

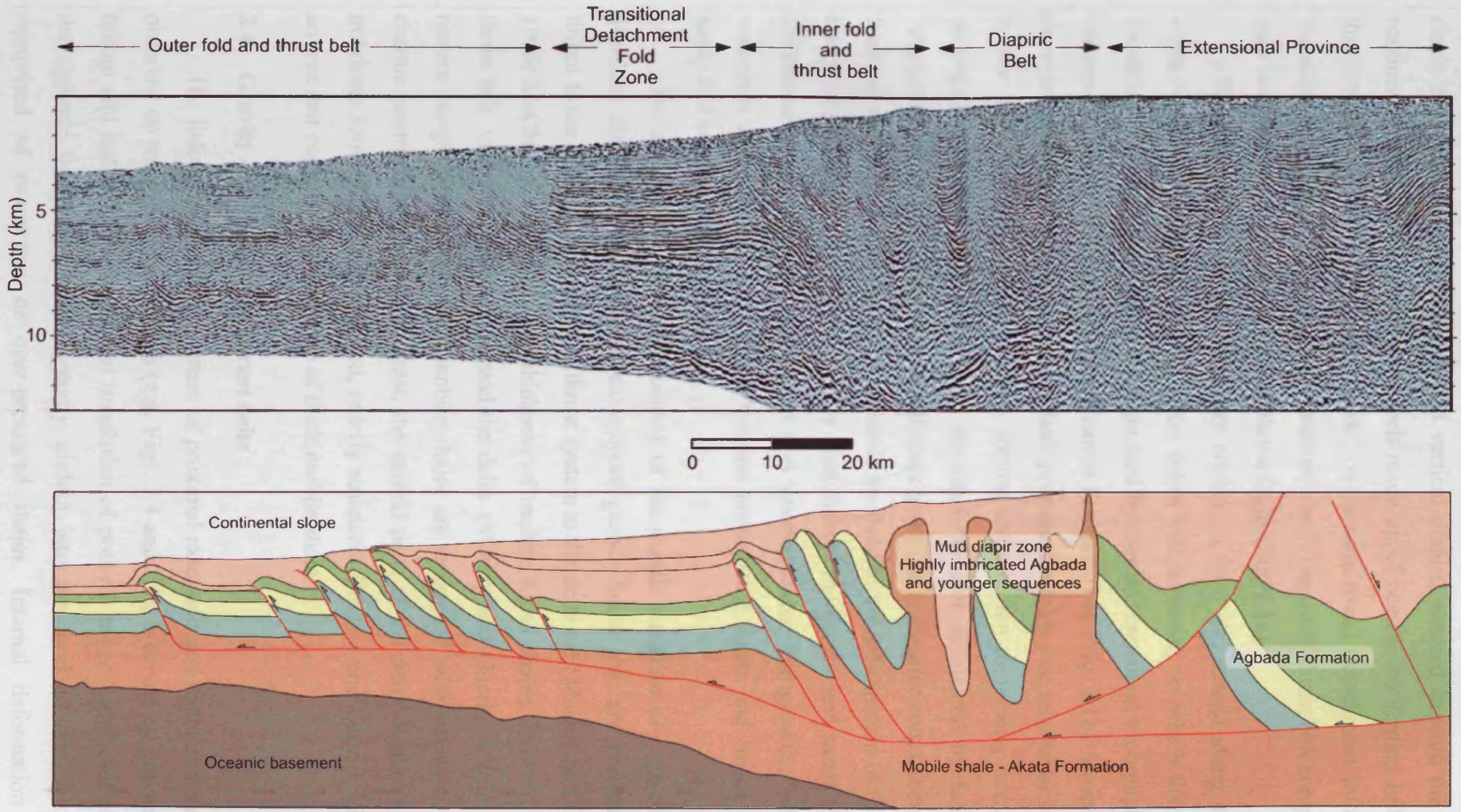

Figure 2.5: Regional seismic profile and interpreted section to show the progression through five main structural domains down slope. Adapted from *Corredor et al. (2005)*

diapir zone, including shale ridges and vertical diapirs, situated beneath the upper continental slope; (iii) an inner thrust belt made up of oceanward verging imbricate thrust faults and some detachment folds; (iv) a transitional detachment fold zone characterised by areas little or no deformation; and (v) an outer thrust belt comprising both landward- and oceanward-verging thrust faults (Fig. 2.1a).

The majority of these domains are arcuate in form and extend along the full width of the delta (Fig. 2.1a). The outer thrust belt however, on which this study focuses, forms two lobes (Fig. 2.1a), separated by elevated basement topography that corresponds to the northern end of the Charcot Fracture Zone (Fig. 2.1b). Structures in the outer thrust belt are predominantly fault propagation folds that may have initiated in low relief buckles. A typical cross section contains ten to twenty, oceanward propagating forethrusts however there are local domains dominated by landward verging backthrusts. In such areas fault linkage gives rise to transfer zones comprising faults of similar and opposing dip. Sediments involved in the deformation of the outer toe thrust belt are predominantly weakly consolidated muds, silts and sands limiting the amount of structural topography that may develop during fold growth. Failure of sediments at fold crests can rapidly truncate propagating faults and hence thrusts rarely roll over onto the seafloor.

Differential progradational loading of the ductile substrate of overpressured pro-delta shales has given rise to extensional growth faults that are mechanically linked to the contractional fold and thrust system at the delta toe (Morley and Guerin, 1996; McClay et al., 1998). The thickness of mobile Akata shales involved in the thrust belt varies considerably around the delta (Morley and Guerin, 1996). In the eastern margin of the delta thick mobile shales are associated with a narrow, rather chaotic contractional belt. In contrast, the central parts of the delta display a broad imbricate zone of regularly repeated, orderly structures (Morley and Guerin, 1996) in an area that contains little evidence of thick mobile shales.

2.4 Gravity-driven fold and thrust belts

The linked deformational system of proximal extension and distal compression, observed on many passive margins (e.g. Figs. 2.4 and 2.5), is driven by gravitational failure and results in the horizontal translation of post-rift cover. Landward dipping detachments that accommodate gravity gliding into the foreland are commonly comprised of evaporates or over-pressured shales. Internal deformation of a

sedimentary wedge by gravity spreading can take place where a rock mass distorts under its own weight by vertical collapse (e.g. Rowan et al., 2004). Distal shortening can be accommodated in a number of ways, including the formation of faults and folds in deep water fold and thrust belts, deformation relating to the movement and extrusion of salt nappes and the structural alteration of pre-existing diapirs. Layer parallel shortening, by lateral compaction, pressure solution and small scale folds, can also accommodate shortening however such features are rarely within the resolution of seismic data and are predicted as having minor contributions to bulk shortening (Rowan et al., 2004).

Deep water fold belts and collisional or accretionary fold belts share many structural characteristics but are distinguished by a fundamental difference in their driving force. The former is driven by the internal gravitational collapse of passive margins, the latter by external collision or subduction of tectonic plates. The amount of contraction and the rate of deformation in deep water fold belts is also less due to weaker driving forces that may only be marginally higher than the strength of the rocks they deform (Rowan et al., 2004). As a result distal shortening is largely controlled by, and sensitive to, sedimentation patterns in proximal regions as well as increases in margin tilting. Deformation by gravitational collapse is naturally self-limiting as margin failure seeks to reduce the bathymetric slope and gravity potential of sediments deposited on the shelf and upper slope.

Deep water fold and thrust belts are commonly characterised by arrays of regularly spaced, imbricate forethrusts that sole out onto a detachment (Morley, 2003) (Fig. 2.6). In general, fold and thrust belts display a hinterland to foreland sequence of deformation superposed with occurrences of out-of-sequence and hinterland verging thrusting events (e.g. Wiltschko and Dorr, 1983; DeCelles and Mitra, 1995; Mitra and Sussman, 1997; Chester, 2003). Fault related folds tend to form asymmetric, oceanward-verging hangingwall anticlines in the overburden (Fig. 2.7). Fault propagation folds are widespread in areas with a single detachment layer, whereas fault bend folds are common in regions with multiple detachments as thrusts climb stratigraphy from one detachment level to the next. Pre-kinematic sequences generally display a uniform thickness and comprise the lower parts of structures, whereas syn-kinematic packages thin over the crests of growing folds (Fig. 2.7). Faults and folds can dramatically influence sediment dispersal within the deep water settings as

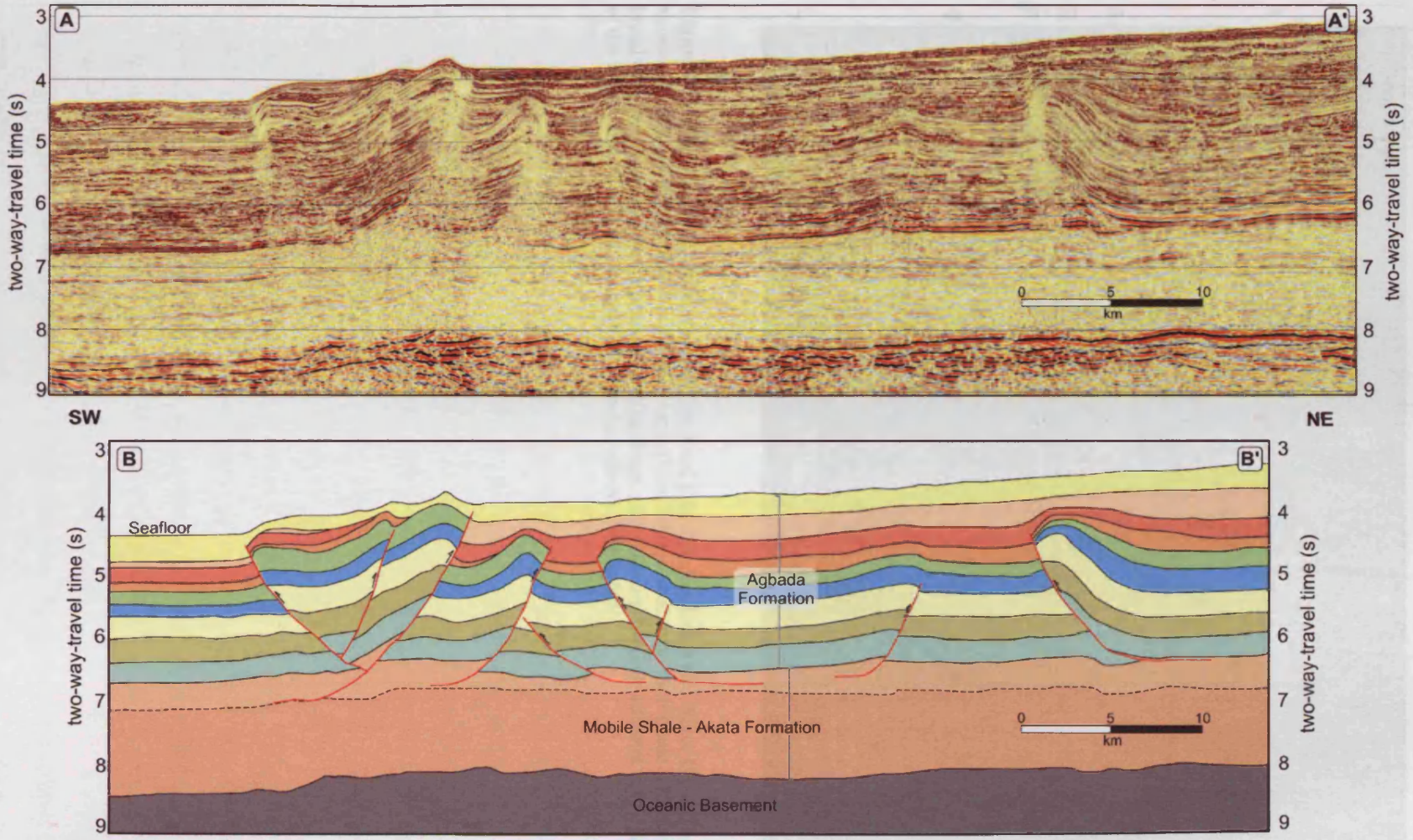

Figure: 2.6: A typical dip-line from Survey A to show the nature and distribution of thrust faults and to show the seismic facies of the main stratigraphic units. Note that the Akata Formation is nearly devoid of any internal reflections and comprises the detachment layers for the thrusts.

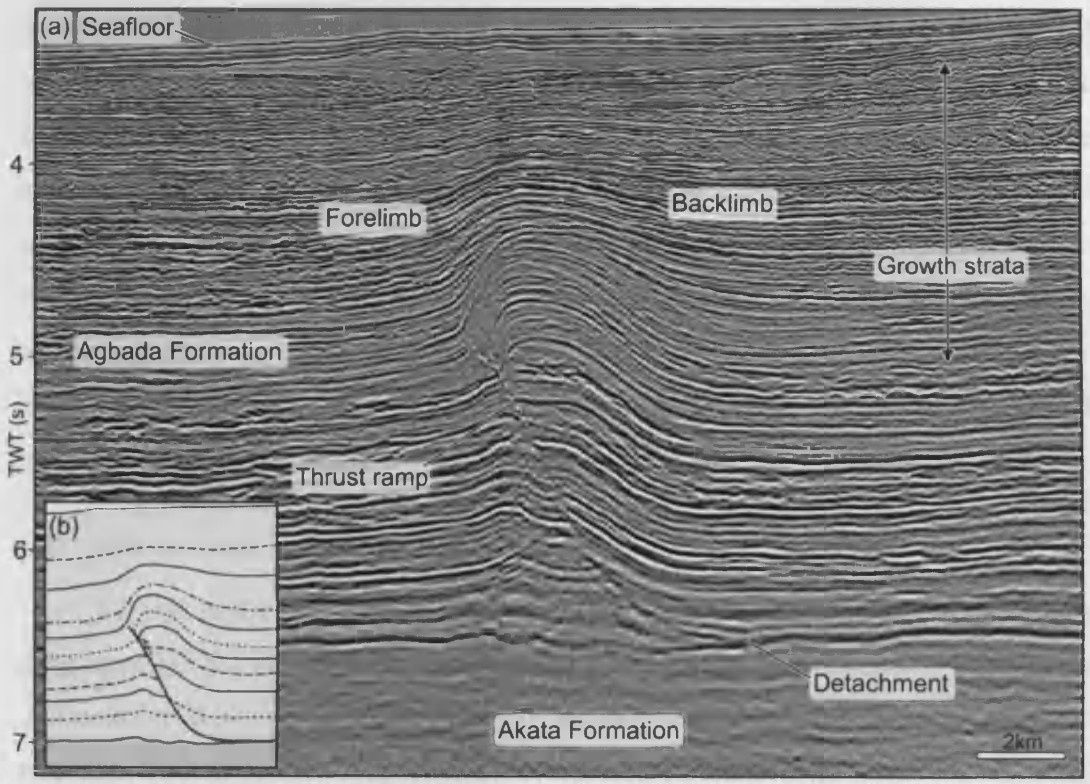

Figure 2.7: Seismic section across a typical thrust and fold from the deep water Niger Delta. Some structural characteristics include a relatively planar thrust ramp, a prominent fault plane reflection, a broad backlimb that dips less than the underlying thrust, and a narrow forelimb situated above the top of the thrust ramp. The fault detaches onto the Agbada-Akata interface

ponded basins form on the flanks of growing structures and act as possible traps for turbidite sands. Imbricate zones are limited in lateral extent and can often pass into regions of low shortening where only a few faults, detachment folds and triangle zones develop (Morley and Guerin, 1996; Hooper et al., 2002). Considerable changes in fold and thrust belt geometry and bulk shortening along strike may be linked to variations in thickness of the detachment unit (Morley, 2003). Although it is possible, as attempted above, to describe the general form and features of deep water gravity-driven fold and thrust belts this does not do justice to the significant lateral and temporal changes in structural styles that can occur in these settings (Morley, 2003).

2.5 Salt vs. shale tectonics

Various structural styles in deep water fold belts on passive margins are largely dependent on the nature of the detachment layer rather than the driving forces of deformation (Rowan et al., 2004). Deep water fold belts commonly detach onto one of two decollement layers: evaporites or overpressured shale (Fig. 2.8). Contractional salt tectonics occurs in the deepwater regions of passive margins such as offshore Brazil, Angola (e.g Marton et al., 2000; Hudec and Jackson, 2002; Cobbold et al., 2004; Fort and Brun, 2004) or the Gulf of Mexico (e.g. Rowan et al., 2004). Fold belts detached on overpressured shale include parts of the Gulf of Mexico (e.g. Weimar and Buffler, 1992; Peel et al., 1995), the Sergipe-Alagos and Para-Maranhao Basins in Brazil (e.g. Rowan et al., 2004) and the Niger Delta (e.g. Evamy et al., 1978; Doust and Omatsola, 1990). Morley and Guerin (1996) noted that the overpressured nature of mobile shales resulted in significant differences in structural style compared with salt tectonics. This is partly due to the rheological nature of each medium. Salt deforms as a viscous material having little or no ultimate strength. It can therefore flow when subjected to minimal shear stress (Urai et al., 1989; Weijermars et al., 1993) and the overall rheological properties of salt are constant through time. In contrast, shale is a plastic material and deforms only when the deviatoric stress overcomes the strength of the shale (Rowan et al., 2004). The rheological properties of shale are independent of the strain rate (Hubbert and Rubey, 1959; Weijermars et al., 1993). The shear strength of shale is partially dependent on the effective vertical stress which can be described as the lithostatic pressure at the base of the overburden minus the overpressure. Therefore as overpressure within a shale unit increases and

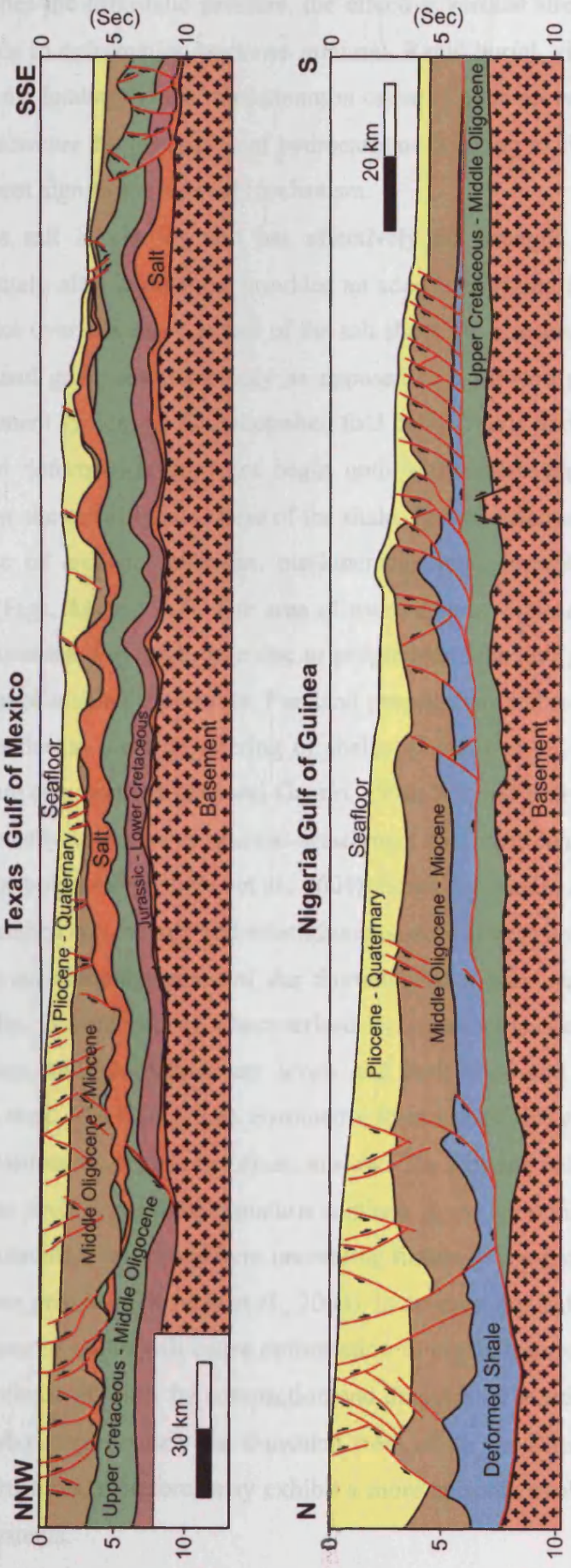

Figure 2.8: Regional seismic line drawings of offshore Texas slope and the Gulf of Guinea slope to compare and contrast salt and shale tectonics. Redrawn from *Wu and Bally (2000).*

approaches the lithostatic pressure, the effective vertical stress tends to zero and the resistance to deformation becomes minimal. Rapid burial, either by sedimentation or by tectonic loading, is the most common cause of over-pressure (Morley and Guerin, 1996), however the generation of hydrocarbons resulting in significant volume change is the most significant internal mechanism.

As salt is viscous and has effectively no strength, deformation can begin immediately after deposition, provided an adequate driving force is applied, and can take place over the entire extent of the salt sheet. As a result, salt-cored folds tend to initiate and grow simultaneously as opposed to a forward-propagating sequence of development typical of shale-detached fold belts (Davis and Engelder, 1985). Shale detached deformation does not begin until sufficient overpressure accumulates to overcome the critical yield stress of the shale. This is reflected in the Niger Delta by a sequence of uniform thickness, pre-kinematic units immediately above the Akata Shales (Figs. 2.6 and 2.7). The area of overpressure within a mobile shale unit may move oceanward through time due to prograding deltas on passive margins moving locations of major depocentres. Foreland propagating deformation follows this trend although due to local dewatering of shales (Rowan et al., 2004) out of sequence thrusts are common (Morley and Guerin, 1996; Wu and Bally, 2000). Salt-cored fold belts typically comprise symmetric detachment folds that can be cut by reverse faults on one or both limbs (Rowan et al., 2004). Squeezed diapirs and salt walls, thickened and shortened salt massifs and allochthonous salt canopies are also common (Fig. 2.8) and can accommodate some of the shortening in a deep water setting. Shale-cored fold belts, in contrast, are characterised by asymmetric, oceanward verging thrust imbricates, multiple detachment levels and fault bend and fault propagation folds (Rowan et al., 2004) (Fig. 2.8). Symmetric features can also exist within this setting if over-pressures are high or deformation slow. The extreme mobility of salt is such that structures involving salt deformation continue to evolve until the salt source layer is either exhausted, salt welds form preventing further movement, or the salt is dissolved by surface processes (Rowan et al., 2004). In contrast the leaking off of pore fluids in overpressured shales will cause deformation to cease. Repressurisation can occur by further release of water by compaction and dehydration reactions or the generation of hydrocarbons, particularly the transition from oil to gas (Morley and Guerin, 1996). Shale structures, therefore, may exhibit a more episodic evolutionary path compared to salt systems.

2.6 Fault-related folding in the deep water Niger Delta

Thrust faults in the deep water Niger Delta are commonly characterised by discrete, planar surfaces and extend for several tens of kilometres along strike. Fault surfaces sole out on multiple detachment levels within the Akata Formation and are readily identified on seismic section by truncated stratigraphy and fault-plane reflections (Fig. 2.7). Associated hangingwall anticlines are generally characterised by long planar backlimbs that dip to a lesser degree than the underlying fault ramp. Evidence for a component of limb rotation during fold growth exists as upward reduction in dip of growth strata on backlimbs (e.g. Hardy and Poblet, 1994; Shaw et al., 2004) (Fig. 1.13). Folds verge in the direction of dip-parallel fault propagation producing shorter and typically steeper forelimbs. Strong fold asymmetry is often associated with an underlying thrust tip similar to fault-propagation folds. Growth structures on the forelimbs display more consistent dips than those on the backlimbs possibly suggesting a dominant mechanism of folding by kink-band migration rather than limb rotation (Corredor et al., 2005). The relationship between growth sedimentation rates and fold and fault uplift rates varies from structure to structure. Patterns of fold onlap above fold limbs are apparent on some folds indicating relatively low sedimentation rates compared to uplift, whereas others demonstrate continuous reflections across fold crests at all stratigraphic levels suggesting similar rates of growth and deposition.

In parts of the deep water of the Niger Delta, in particular the western lobe of the outer fold and thrust belt, backthrusts (i.e. landward-vergent faults) and tectonic wedges are common. In such areas the bathymetric slope and basal detachment show less disparity in their angle of dip and are sub-parallel with the maximum horizontal stress. In such a scenario there is no mechanical advantage between the formation of a forethrust or a backthrust (Bilotti and Shaw, 2005) and hence fault arrays comprise thrusts of opposing dip. The close spacing and along strike propagation of such faults leads to antithetic thrust fault linkages and the merger of the overlying associated asymmetric folds (Fig. 2.9). Along strike vergence reversals of folds characterises much of the area of interest in this study.

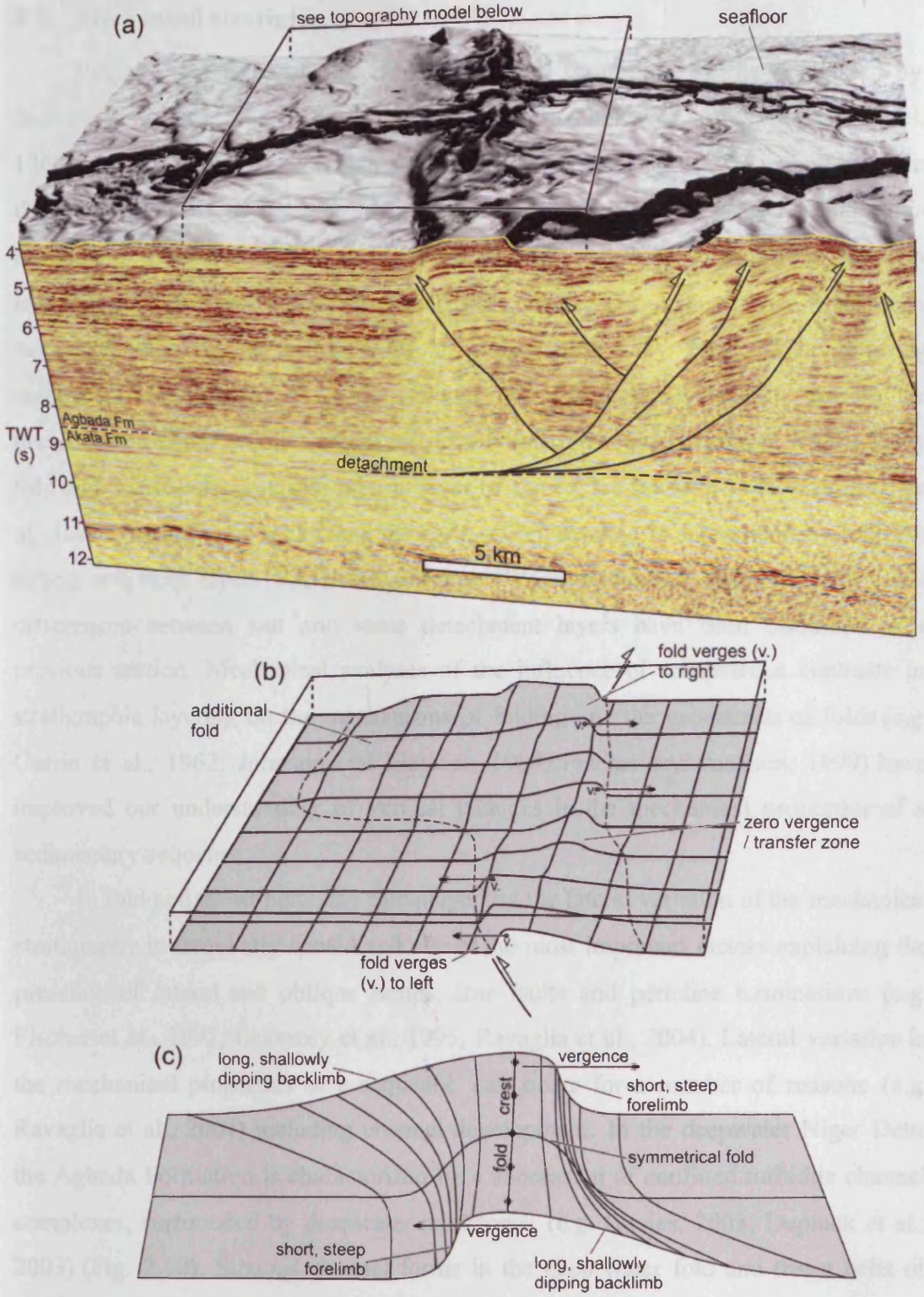

Figure 2.9: An example and illustration of an along strike vergence reversal in folding of the present day seabed. **(a)** is part of the 3D seismic survey A. Front panel shows interpreted hard-linked thrust faults and associated hangingwall anticlines. **(b)** Gridded surface representing seabed topography to illustrate the change in vergence of the fold. **(c)** Diagrammatical description of an along strike vergence reversal in a fold.

2.7 Mechanical stratigraphy

Regions that have undergone layer parallel shortening can be dominated by faulting or folding. The Idaho-Wyoming-Utah thrust belt (e.g. Armstrong and Oriel, 1965) and southern Appalachian thrust belt (e.g. Rich, 1934) for example, have deformed primarily by faulting, whereas other regions such as the central Appalachian Plateau (e.g Gwinn, 1964), Jura (e.g. Pierce, 1966) and Parry Islands (e.g. Harrison and Bally, 1988) have deformed primarily by folding (Erickson, 1996). It has been suggested that the differing styles of deformation may result from differing mechanical stratigraphy (i.e. the strength and thickness of layers), namely the presence and characteristics of a weak decollement layer (e.g. Erickson, 1996). Many fold and thrust belts comprise a basal layer of salt or overpressured shale and a cover of clastic or carbonate rocks, and the style of deformation is determined by both the strong and weak layers within the sequence (Woodward and Rutherford, 1989). The differences between salt and shale detachment layers have been discussed in a previous section. Mechanical analyses of the influence of competence contrasts in stratigraphic layering on the mechanisms of folding and the geometries of folds (e.g. Currie et al., 1962; Johnson and Fletcher, 1994; Fischer and Jackson, 1999) have improved our understanding of vertical changes in the mechanical properties of a sedimentary sequence.

In fold and thrust belts, the role played by the lateral variation of the mechanical stratigraphy is frequently considered one of the most important factors explaining the presence of lateral and oblique ramps, tear faults and pericline terminations (e.g. Fischer et al., 1992; Letouzey et al., 1995; Ravaglia et al., 2004). Lateral variation in the mechanical properties of a sequence can occur for a number of reasons (e.g. Ravaglia et al., 2004) including channel development. In the deepwater Niger Delta the Agbada Formation is characterized by a succession of confined turbidite channel complexes, surrounded by deepwater mudstones (e.g. Davies, 2003; Deptuck et al., 2003) (Fig. 2.10). Sinuous channel forms in the deep water fold and thrust belts of offshore West Africa and the Gulf of Mexico have been proven to be viable exploration targets (e.g. Kolla et al., 2001) as they act as conduits for clastic sediments to be sorted and transported into the deep water setting (Deptuck et al., 2003). High amplitude reflections (Fig. 2.10) within a background of lower amplitude

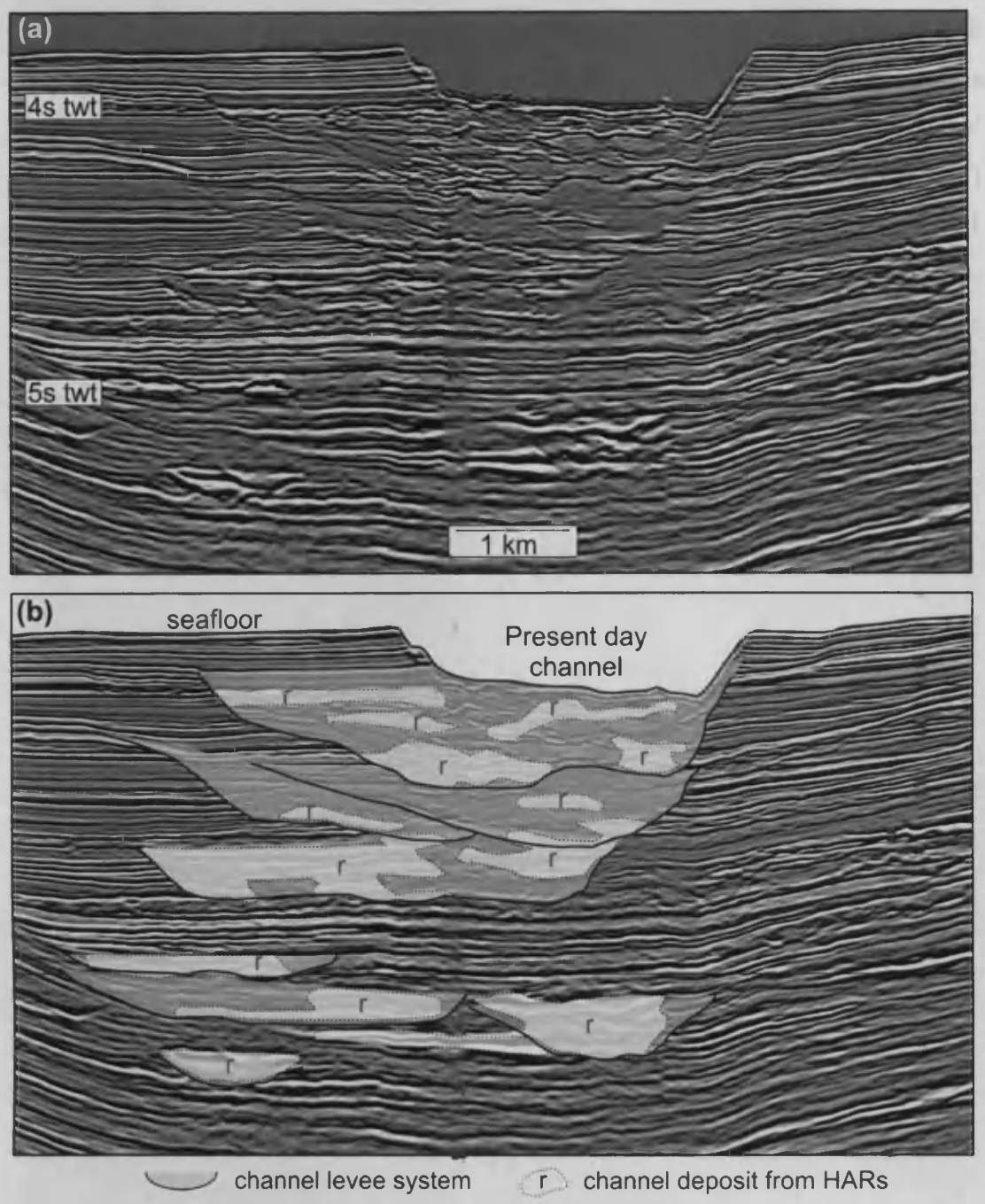

Figure 2.10: A seismic section orientated perpendicular to delta slope to demonstrate lateral variability is seismic facies within the Agbada Formation. **(a)** 3D seismic crossline imaging a stacked channel levee complex. **(b)** Interpreted section highlighting high amplitude reflections (HARS).

seismic facies are thought to indicate coarser-grained turbidites associated with aggrading or migrating channel axes (e.g. Kastens and Shor, 1985). Structural features, such as seafloor relief above a toe-thrust, can cause the deflection of channel complexes resulting in ponding of coarser-grained sediments. Morgan (2004) documented channel complexes following transfer faults such that repeated channel development lead to the clustering of channel complexes around these structures. This compartmentalization of lithologies leads to heterogeneity in the Agbada Formation and variation in its mechanical properties along strike.

Chapter 3

Published as:

Higgins, S., Davies, R.J., Clarke, B., 2007. Antithetic fault linkages in a deep water fold and thrust belt. Journal of Structural Geology 29, 1900-1914. (doi:10.1016/j.jsg.2007.09.004)

Although the papers are jointly authored with the project supervisors they are the work of the lead author, Simon Higgins. Project supervisors provided editorial support in accordance with a normal thesis chapter.

CHAPTER 3

3 ANTITHETIC FAULT LINKAGES IN A DEEP WATER FOLD AND THRUST BELT

3.1 Abstract

Deep water fold and thrust belts consist of both forethrusts and backthrusts that can link along strike to form continuous folds in the overburden. The interaction of faults of opposing dip are termed 'antithetic thrust fault linkages' and share the common feature of a switch in vergence of overlying hangingwall anticlines. Using three-dimensional seismic data, on the toe-of-slope of the Niger Delta, linkages are classified into three distinct structural styles. This preliminary classification is based on the vertical extent of faulting within a transfer zones relative to the branch line of the antithetic faults. The stratigraphic level of the lateral tip of the fault, the shape of lateral tip region of a fault plane and the stratal deformation within the transfer zones is also distinctive in each type of fault linkage. A Type 1 linkage comprises faults that overlap exclusively above the level of the branch line. A 'pop-up' structure forms within the transfer zone with sediments below remaining planar. The lower tip lines of faults climb stratigraphy towards the linkage zone creating asymmetric, upward-tapering lateral tip regions. In Type 2 linkages fault overlap occurs lower than the level of the branch line such that lateral fault tips are located within the footwall of the counterpart fault. Faulting is thus limited to the deeper section within the transfer zone and creates unfaulted, symmetric, bell-shaped folds in the overburden. Upper tip lines of faults lose elevation within the transfer zone creating asymmetric, downwards-tapering lateral tip regions. In Type 3 linkages both faults continue above and below the branch line within the transfer zone resulting in cross-cutting fault relationships. Horizon continuity across the folds, through the transfer zones, varies significantly with depth and with the type of fault intersection.

3.2 Introduction

Research into the growth, propagation and linkage of faults has predominantly focused upon extensional rather than reverse displacement. Numerous studies on extensional faults have provided insights into along strike and down-dip displacement variations (e.g. Peacock and Sanderson, 1991), fault growth (e.g. Watterson, 1986; Barnett et al., 1987; Cartwright et al., 1995), fault scaling laws (e.g. Dawers and Anders, 1995), and classifications of fault linkage geometries (e.g. Gawthorpe and Hurst, 1993). Thrust faults are fundamental as a mechanism for accommodating shortening in convergent tectonic settings and in gravitational detachment systems. Despite this, the mechanisms by which thrusts initiate, propagate and link are not well defined. Most studies have focused on fault geometries, displacement variations and growth using dip-parallel outcrop exposures (e.g. Williams and Chapman, 1983; Eisenstadt and De Paor, 1987; Ellis and Dunlap, 1988). Analyses of along strike variations and linkage are fewer (e.g. Dahlstrom, 1970; Aydin, 1988; Harrison and Bally, 1988; Nicol et al., 2002; Davis et al., 2005), possibly due to partial exposure and the preferential erosion of hangingwalls within ancient thrust systems (Davis et al., 2005). Analogue modeling of thrust systems provide useful indications as to how thrusts may initiate and grow by segment linkage (e.g. Liu and Dixon, 1991) but remain largely untested in the field. This paper will describe and classify along strike linkages of thrust faults of opposing dip and demonstrate an associated change in fold geometry. This is intended as a preliminary classification to form a basis for further research.

The acquisition of high resolution three-dimensional seismic data over deep water fold and thrust belts offers an opportunity to better resolve fault plane geometries and linkages in three-dimensions. We have selected the compressional domain of the deep water Niger Delta fold and thrust belt, as it provides first class examples of along-strike linkage of thrusts.

3.2.1 Along strike thrust fault linkage

Thrust faults can link in the direction of strike such that displacement reduces to zero on one fault, whilst increasing in the same direction on the next (e.g. Davis et al., 2005) in a similar manner to extensional fault systems (Larsen, 1988). This can take

place on faults that have similar or opposing direction of dip, termed synthetic and antithetic respectively (Peacock et al., 2000). The regions where fault displacement is transferred from one fault to the next are termed 'transfer zones' (Dahlstrom, 1970). Connectivity of thrusts through transfer zones is not a new concept (e.g. Douglas, 1958; Dahlstrom, 1970; Boyer and Elliott, 1982). Pfiffner (1985), for instance, described a decrease in master fault displacement by the "consumption" of slip by minor splays, whilst Dahlstrom (1970) illustrated the transfer of displacement between paired faults (and folds) along a through-going sole thrust. This led to a simple three-dimensional model of a synthetic transfer zone of en echelon thrust faults (Dahlstrom, 1970 their Figure 26).

Descriptions of antithetic interactions are less common and are largely contained within studies of triangle zones and descriptions of back thrust splays on larger synthetic 'master' faults (e.g. Mandl and Crans, 1981). McClay (1992) and Couzens and Wiltschko (1996) classify two types of triangle zone from existing literature; the first involving two thrusts detaching on a single decollement (Fig. 3.1a) and the second, also described as an intercutaneous wedge (McClay, 1992), containing multiple decollements (Fig. 3.1b). The first type can be described as a structure composed of two dipping reflections underlain by horizontal reflections (Couzens and Wiltschko, 1996) (Fig. 3.1a). Some interactions between faults in this study fulfill this criteria but, importantly, overlap both laterally and downdip within the transfer zone. Back thrust splays have less relevance to this study as they are not thought to be due to the interaction and linkage of two distinct, independent faults and may exist to accommodate strain induced in the hangingwall during ramp climb of the master fault (Butler, 1982).

The initiation and propagation of thrusts can lead to the development of an asymmetric hangingwall anticline ahead of the fault (e.g. Suppe, 1985 their Figure 9.47). Figure 3.2 describes how this asymmetry can be given as a direction of fold vergence, defined here as being towards the shorter, commonly steeper limb from the axial surface. The most evident indication that thrust faults of opposing dip are linking along strike, within the subsurface, can be a switch in the direction of vergence of associated folds in the overburden (Fig. 3.2). These changes in vergence of hangingwall anticlines are common in the deep water Niger Delta and represent the interaction of detaching forethrusts and backthrusts in the underlying sediments. The

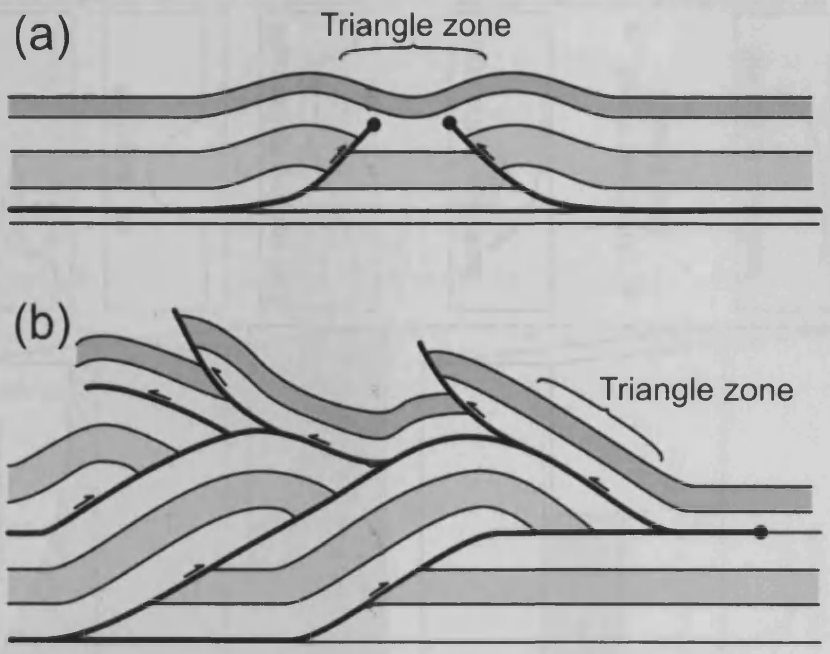

Figure 3.1: Illustration of triangle zone geometries (from Couzens and Wiltschko, 1996). **(a)**: "Type I triangle zone" (Couzens & Wiltschko 1996). **(b)** Intercutaneous wedge (McClay 1992) or "Type II triangle zone" (Couzens & Wiltschko 1996).

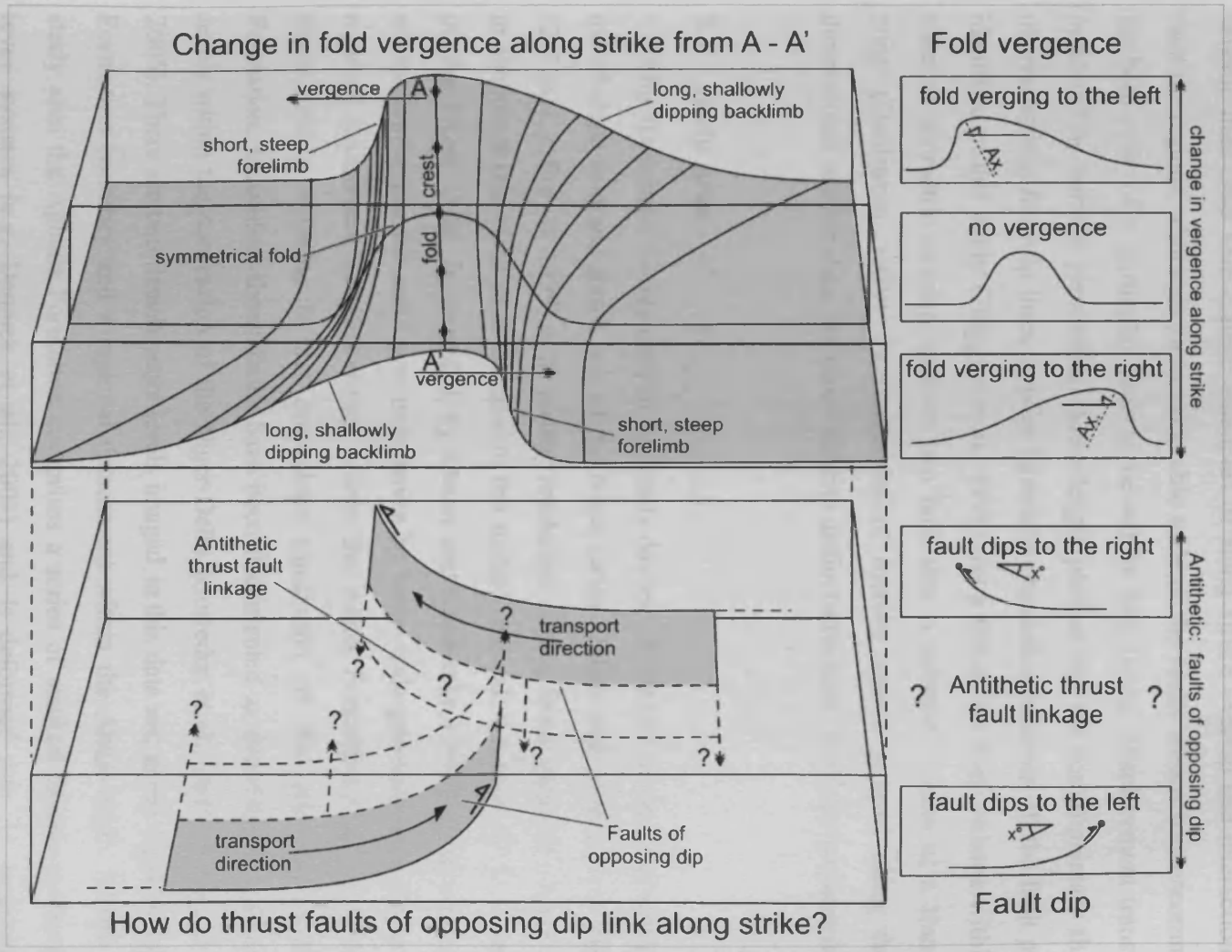

Figure 3.2: Diagrammatical description of fold vergence reversal and antithetic thrust fault linkage. Thrust faults in the subsurface underlie asymmetric, verging anticlines. Vergence is defined as toward the shorter, steeper limb from the core of the fold. The upper block diagram shows a switch in the vergence of the fold along strike coinciding with an antithetic thrust fault linkage below. Antithetic linkage is defined as the interaction of faults with opposing dip. The geometry of the transfer zone between the two thrusts varies and is classified into three types in the text. Ax.: Axial plane

seismic data used here contain examples of along strike overlap and interaction of fault tip regions, although the considerable scale of the faults means it is uncommon for both ends of a particular fault to lie within data limits. Displacement transfer, indicated by horizon geometries, heave-length profiles and the complimentary shape of overlapping fault tip lines, implies kinematic interaction between all the fault pairs identified in this study (Huggins et al., 1995). As a result, the rock volume within a zone of geometric overlap between two fault tips is referred to here as a 'transfer zone' (Dahlstrom, 1970). The examples of transfer zones, imaged using three-dimensional seismic data, are classified into distinct structural styles and geometries.

3.3 Study Area

The 3D seismic survey used in this study covers ~ 3000 km^2 of the compressional toe-of-slope fold and thrust belt of the Niger Delta. Inline and crossline spacing is 12.5 m (e.g. Brown, 1999) with vertical resolution varying from approximately 7.5 m in shallow levels to 20 m at the base of the studied interval. A review of the geology of the Niger Delta is provided by Doust and Omatsola (1990). Extension and contraction within the delta system is driven by large-scale gravitational collapse on regional detachment levels existing within the Akata Formation (e.g. Bilotti and Shaw, 2005) resulting in the downslope translation of the overlying Agbada Formation. Individual thrust faults have been documented as detaching at numerous levels within the succession of the Niger Delta (Corredor et al., 2005; Briggs et al., 2006). There are two detachments levels imaged in this data set; at the Agbada-Akata Formation boundary and a regional detachment within the Akata itself. Within the study area the Agbada Formation comprises a series of stacked deepwater channel-levee systems (e.g. Deptuck et al., 2003) and is deformed into 21 large-scale, detaching oceanward-vergent forethrusts and landward-vergent backthrusts. The fold and thrust belt, if modelled as a critical taper wedge, has a relatively shallow bathymetric slope (Bilotti and Shaw, 2005) leading to the inference of a weak basal detachment. This causes the maximum principal compressive stress to be subhorizontal and close to the angle of the detachment. In such a scenario there is little mechanical advantage between the formation of a forethrust or a backthrust, which have similar dip angles and are equally efficient at accommodating shortening (Bilotti and Shaw, 2005). The focus of this paper surrounds the linkage of thrusts of

opposing dip. We do not expect the predominance of antithetic linkage to be generic or universal; it simply indicates a difficulty in clearly imaging synthetic interactions, due in part to overprinting of displacement variations by well-developed, closely-spaced, stacked forethrusts. Forethrust-forethrust interactions in this area are commonly characterised by a subtle bend in the fault trace and an along strike displacement minimum. It is conceivable that if linkage between similarly dipping and laterally aligned faults occurred early in their history then signs of this mechanism may be lost at the resolution of seismic data.

3.4 Depth Conversion

This paper will describe the geometries of fold and thrust structures using 3D seismic data and two-way-travel time (twt) seismic sections. It is therefore important to establish the significance of any change to structural geometries that may occur during time to depth conversion (see Brown, 1999). Depth conversion was performed on all seismic sections used in the study using interval velocities from a nearby well. Figure 3.3 shows two representative time sections (a & c) across two linkage zones and their depth converted equivalents (b & d). It is apparent that, in both cases, the shallow section (< ~ 5 seconds and ~ 4 km) is relatively unchanged in thickness and geometry during the calculation. The deeper section however displays some dramatic thickening of the section, below 6 seconds and 5 km, due to an increase of velocity with depth. If one ignores the thickness changes, the (d) depth section is largely unchanged geometrically and is typical of the majority of sections in this data set. Depth conversion of the (a) time section, however, results in apparent symmetric folds (between 6 and 7 seconds) being transformed into planar dipping reflectors in the (b) depth section (Fig. 3.3). This is less common in this study and is due to velocity pull-up (see Brown, 1999) caused by the seafloor expression of the overlying fold combined with the uplift of high velocity rocks within the pop-up structure.

Seismic time sections are therefore used to describe structural geometries herein as the large majority of time sections are not significantly altered during depth conversion (as in Fig. 3.3, (c) to (d)). Exceptional velocity effects are referred to in the text.

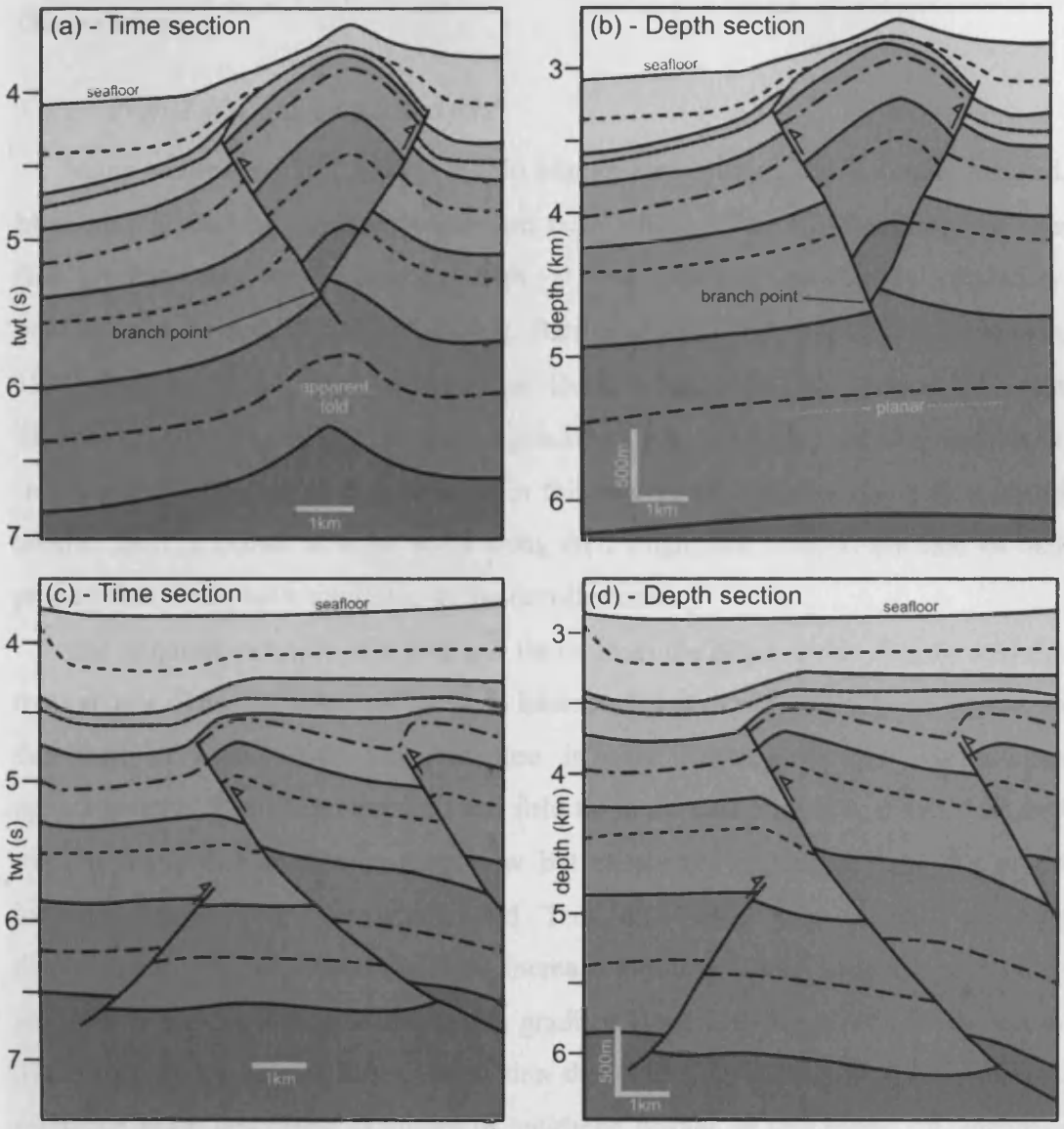

Figure 3.3: Cross sections to show depth conversion of representative time sections. **(a)**, **(b)**: A section containing a pop-up structure in a Type 1 linkage. **(c)**, **(d)**: A section towards the lateral edge of a Type 2 linkage. Above 4km (b & d) sections are relatively unchanged by depth conversion. Deeper than 4km, there is significant thickening. In (a), symmetrical folds beneath the pop-up are transformed into planar, dipping reflectors during depth conversion (b). Geometrically (ignoring thickness changes) (c) resembles (d), even at depth.

Observations

3.4.1 Profile of a single fault and fold

Many studies of fault linkage within extensional settings use a single, isolated, blind normal fault as a reference standard from which to identify modifications to a fault profile due to interaction with a free surface, mechanical boundary, unconformity or neighbouring fault (e.g. Barnett et al., 1987; Walsh and Watterson, 1991; Huggins et al., 1995). In the Niger Delta, where faults are commonly longer than the extent of 3D datasets, there is a paucity of fully imaged, compressional faults. In addition to this, all faults observed in this structural domain either interact with another fault or detach at some point along their length and may, in the case of fault propagation folds, have nucleated in the decollement.

The simplest example of a fold and thrust from the Niger Delta dataset, and one that shows little evidence of having interacted with neighbouring structures, is described in Figure 3.4. This structure is only partially imaged and extends approximately 25 km from the fault and fold tip to the data edge (Fig 3.4a). The fault trace is somewhat arcuate in map view but shows no significant jogs that could indicate linkage (e.g. Cartwright and Trudgill, 1994). The profiles of fault displacement and fold crest elevation increase similarly away from the tip of the structure and show no major changes in gradient along their length (Fig 3.4b and c). The shape of the single fault plane within the fold (Fig. 3.4d and e) is used as a reference when describing examples of antithetic linkage in this study. Of particular importance here is the shape of the lateral tip region of the fault expressed by the upper tipline, the upper edge of the gridded surface (Fig. 3.4d and e). Ideal isolated normal faults (Barnett et al., 1987) are described as elliptical with a symmetric lateral taper, such that upper and lower tiplines converge equally towards a central lateral fault tip. In the case of this detaching thrust (Fig. 3.4) a large part of the fault plane is hidden in a zone of bed parallel shear within the detachment, whilst a lateral portion is not imaged due to the location of the data limits. As a result it may be argued that as little as a quarter of the fault is observable. It is evident from the gridded surface of the single thrust (Fig. 3.4e) that the tipline decreases in elevation along strike towards the tip, whilst increasing in gradient, such that the shape of the fault plane resembles a

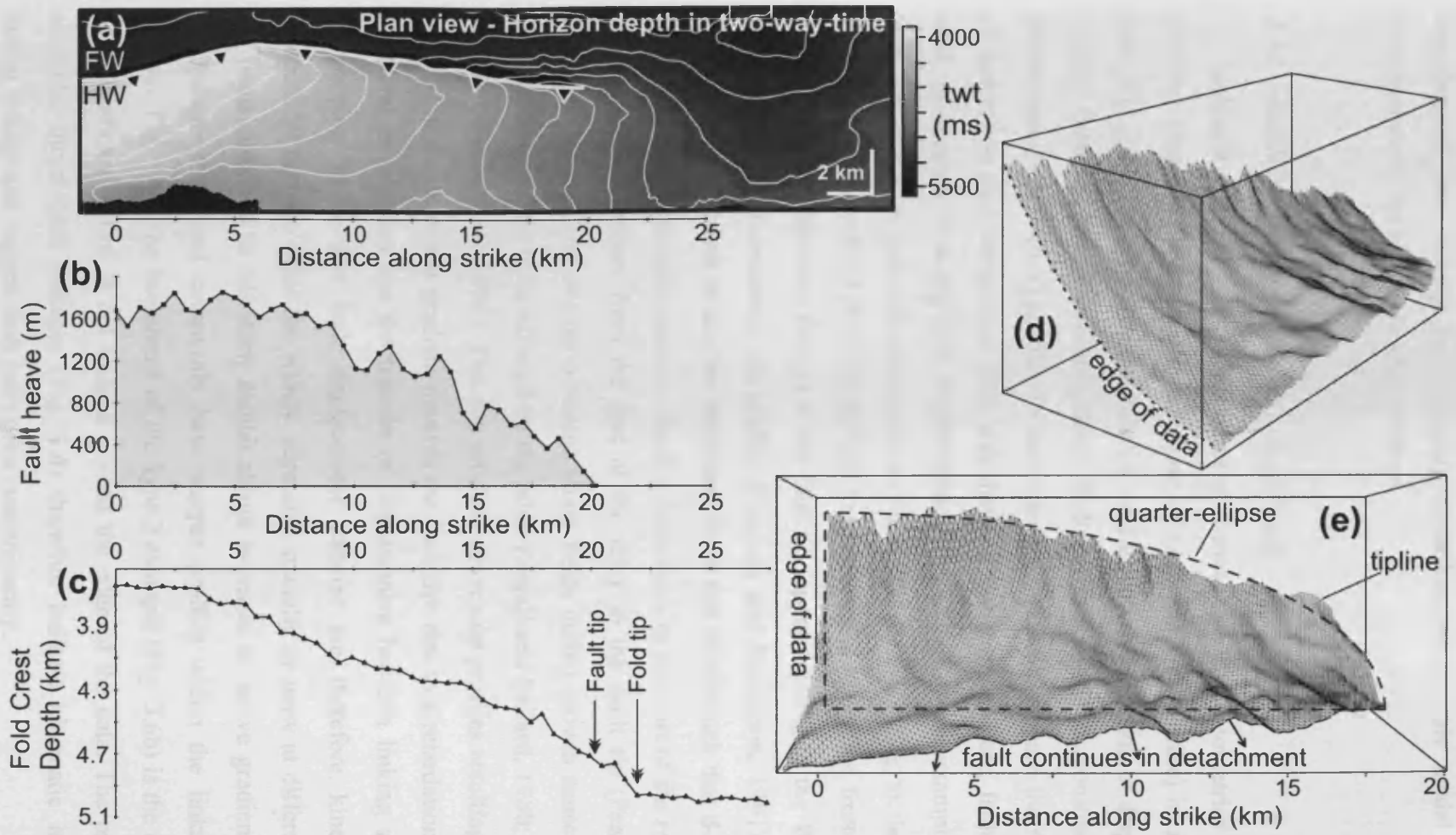

Figure 3.4: Profile of a single fault and fold. **(a)** Map of a folded horizon given in two-way-time (ms). Dark greys represent structural lows, lighter greys are structural highs. FW: footwall; HW: hangingwall. **(b)** Heave-length plot for the selected horizon. **(c)** Fold elevation chart plotting depth to fold crest vs. distance along strike. **(d)** 3D visualisation of a gridded thrust fault surface. **(e)** 3D visualisation of a thrust surface looking down-dip to show the shape of the fault tipline.

quarter-ellipse (Fig. 3.4e). It is predicted that a complete, isolated fault would form a semi-ellipse, the chord of which would be located on the detachment. It is hypothesised that linking faults display modifications to this model that are characteristic of the type of linkage involved.

3.4.2 Antithetic linkage (forethrust to backthrust)

Antithetic transfer zones have a range of distinct structural geometries whilst all showing vergence reversals (the switching of vergence along strike) in associated folds (Fig. 3.5). The term 'transfer zone' is used to describe a region of displacement transfer between two interacting thrust faults. This can be demonstrated using displacement-length (d-x) profiles for each transfer zone that compare the magnitude of faulting on each constituent fault with distance along strike. Here, fault heave is used, as opposed to along-fault displacement (Fig. 3.6). Note the example profiles (Fig. 3.6) comprise measurements made on the faults corresponding to the folds of Figure 3.5. Ideal, isolated faults are thought to have linear d-x profiles, from the point of maximum displacement (d_{MAX}) to the fault tip, approximating to the Walsh and Watterson (1987) cumulative slip profile (Peacock and Sanderson, 1991). Linking faults have been shown to display modifications to this model such that d-x profiles can consist of two straight portions, the first from d_{MAX} to the start of the relay and a second, steeper section, from the start of the relay to the fault tip (Peacock and Sanderson, 1991). The overlap of elastic strain fields during growth causes the slip distribution of a fault to be affected by the other (Segall and Pollard, 1980; Childs et al., 1995; Nicol et al., 1996). This can produce convex-up profiles resulting from an increase in displacement gradient towards the fault tips due to a retardation or arrest of lateral propagation and the transfer of displacement between linking structures. Overlapping faults that lack displacement transfer are therefore kinematically independent and are either too widely separated spatially or grew at different times. All faults described in this study exhibit abrupt increases in heave gradient towards the linkage zones and commonly have steeper profiles within the linkages than without (Fig. 3.6). The backthrust of the Type 2 example (Fig. 3.6b) is the exception as a significant part of it not imaged beyond the edge of the data. The profiles of antithetic thrust fault linkages (Fig. 3.6) therefore indicate kinematic interaction during linkage and suggest fault pairs grew concomitantly.

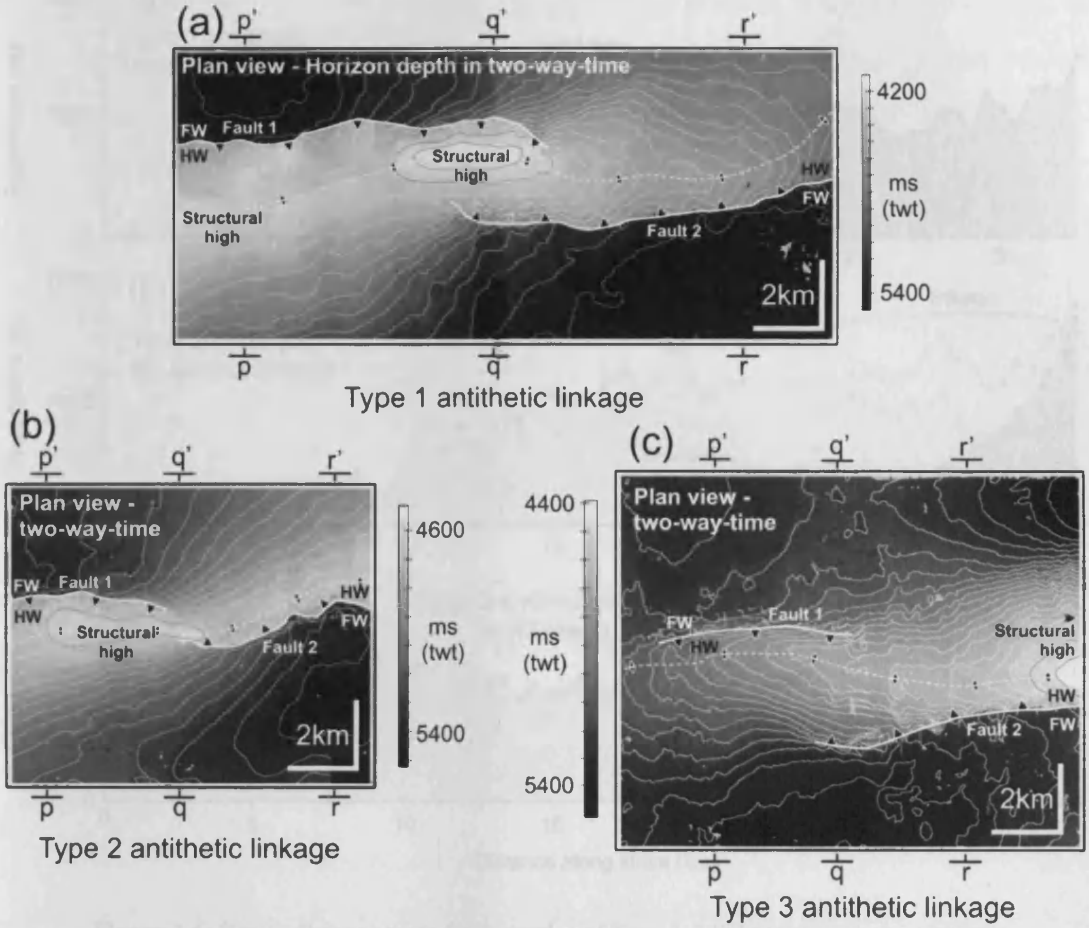

Figure 3.5: Maps of a folded horizon for antithetic Types 1, 2 & 3 linkages given in two-way-time (ms) to demonstrate vergence reversals along strike. Dark greys represent structural lows, lighter greys are structural highs. FW: footwall; HW: hangingwall. Hinge lines are represented by a stippled white line and black diamonds. The hangingwall intersection with the fault is given by black triangles. (p-p', q-q', r-r') give the locations of seismic sections in Figures 3.7, 3.9 & 3.10. The vergence of the fold can be determined to be towards the steeper limb from the fold crest as shown by the contours and shading. Note that structural highs occur close to the zone of overlap of the faults in Type 1 & 2 linkages. Also, the amount of overlap of the faults seen here only corresponds to this given horizon. For maximum fault overlap see later Figures.

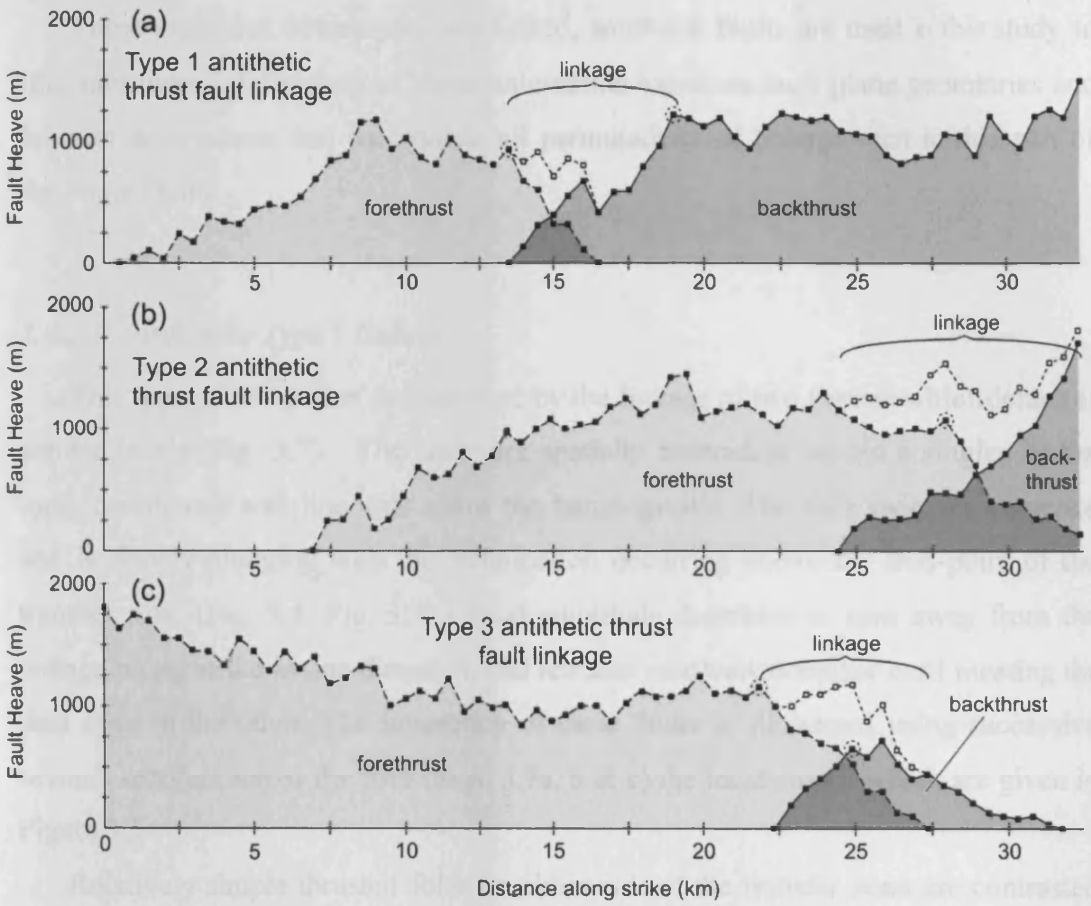

Figure 3.6: Heave-distance plots for examples of Type 1-3 linkage. **(a)** Type 1 antithetic thrust fault linkage. Stippled circles indicate points of abrupt change in displacement gradient towards the linkages. **(b)** Type 2 antithetic thrust fault linkage. **(c)** Type 3 antithetic thrust fault linkage.

These examples of kinematically linked, antithetic faults are used in this study to illustrate three subdivisions of thrust interaction based on fault plane geometries and horizon deformation that incorporate all permutations of linkage seen in this part of the Niger Delta.

3.4.2.1 Antithetic Type 1 linkage

This type of interaction is illustrated by the linkage of two thrusts which detach at similar levels (Fig. 3.7). The faults are spatially coincident within a single, 30 km long, continuous anticline that spans the hangingwalls. The fold switches vergence and is doubly-plunging with the culmination occurring above the mid-point of the transfer zone (Fig. 3.5, Fig. 3.7b). Fold amplitude decreases to zero away from the linkage along strike in one direction, and remains relatively constant until meeting the data limit in the other. The interaction of these faults is illustrated using successive seismic sections across the fold (Figs. 3.7a, b & c) the locations of which are given in Figure 3.5.

Relatively simple thrusted folds on either side of the transfer zone are contrasted with the structures within. Along strike of the zone of overlap a single backthrust (Fig. 3.7a) ramps upward from the detachment and has an approximate maximum along-fault displacement of 1.5 km (Fig. 3.7 p-p') measured on horizons immediately above the Agbada-Akata Fm boundary. The hangingwall anticline verges in the transport direction (to the right) with the shorter forelimb facing upslope and the longer, shallowly dipping backlimb facing downslope. The Agbada - Akata Fm boundary is offset and displays 'apparent' footwall folding caused by a velocity effect due in part to the seafloor expression of the fold (see below & Fig. 3.3).

This geometry is mirrored along strike, in the opposite direction from the transfer zone (Fig. 3.7c). An oceanward propagating forethrust, with approximately 1.3 km displacement in this section, produces an asymmetric hangingwall anticline that verges downslope (to the left, Fig. 3.7 r-r'). The Akata marker surface is again offset in a reverse sense, with 'apparent' folding (see below & Fig. 3.3) close to the fault plane in the footwall.

The transition along strike from forethrust to backthrust occurs within a transfer zone, the centre of which is shown in Figure 3.7b (q-q'). Here the fold displays no

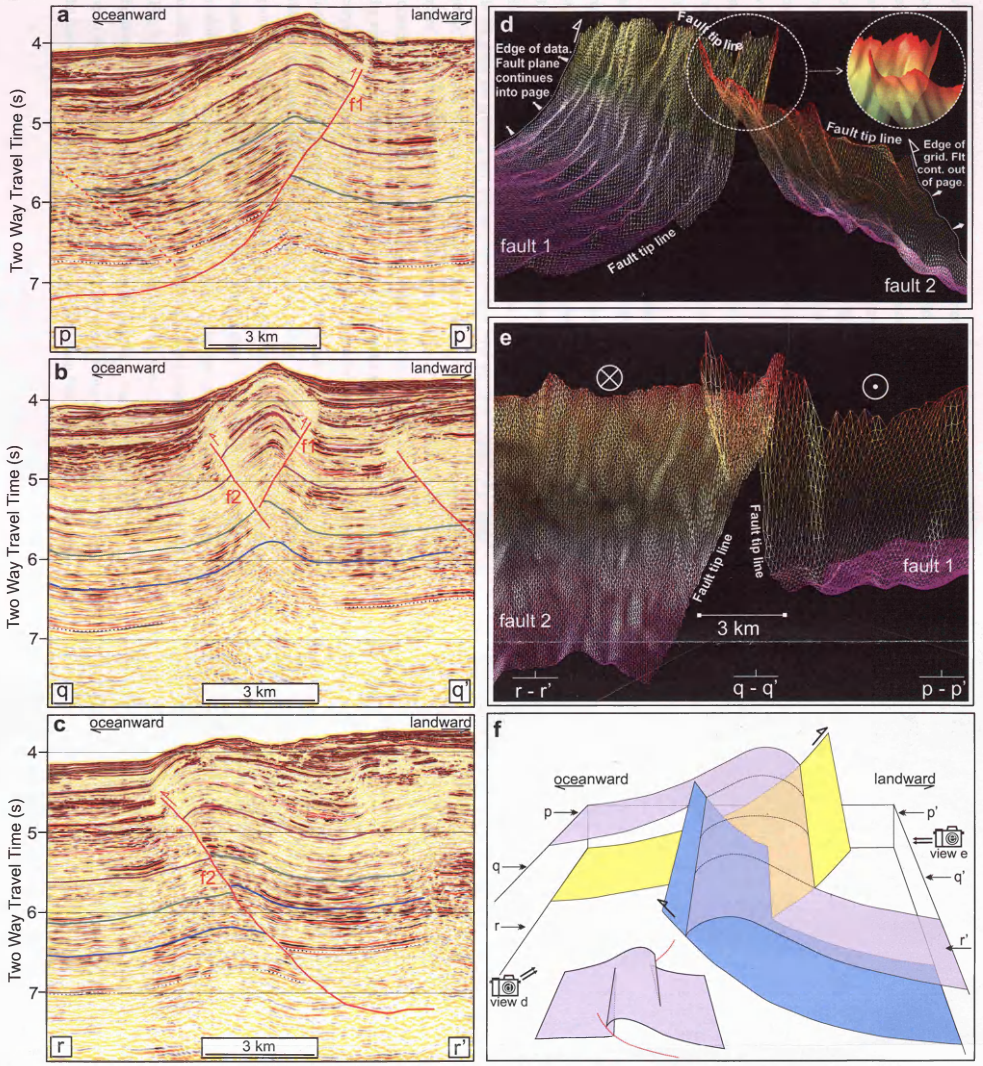

Figure 3.7: Antithetic Type 1 linkage. **(a, b, c)** Downdip, sequential seismic sections in two-way-time (s). Fault 1 (f1) is a backthrust. Fault 2 (f2) is a forethrust. Agbada-Akata boundary: stippled white line. **(d, e)** 3D visualisations of fault planes using IESX Geoviz™ software. Surfaces are gridded from interpreted seismic fault sticks. Surfaces represent faults planes near the transfer zones only. Edges of the grids either represent fault tip lines (point of zero displacement) or the edge of the data set as labelled. In **(e)** a crossed circle indicates propagation into page; a dotted circle, propagation out of page. **(f)** Simplified block diagram of a Type 1 linkage. Yellow fault: backthrust. Blue fault: forethrust. Transparent surface represents the hangingwall-hangingwall section of a typical shallow horizon. Inset surface shows increasing displacement along strike of typical shallow horizon away from the zone of fault overlap.

vergence and two faults converge on a predicted point of intersection, or 'branch point' (e.g. McClay, 1992). A symmetrical fold in the shallower stratigraphy has equally dipping limbs and is bounded on both sides by faults in a 'pop-up' structure above the branch point. At deeper levels, below the intersection, the faults no longer offset horizons and deformation appears to be by folding alone. Depth conversion however reveals that apparent folding of the sub-thrust stratigraphy is due to velocity pull-up (see Brown, 1999) caused by the seafloor expression of the fold and the higher velocity rocks within the uplifted pop-up structure (Fig. 3.3a). Following conversion, stratigraphy below the branch point is planar (Fig. 3.3b) with a dip similar to the regional delta slope. Accurate description of the true deformation of this lower section is problematic due to poor imaging.

Cross sections are essential in clearly presenting the changing geometries, but 3D seismic data allow the along strike transition from forethrust to backthrust to be resolved in greater detail. Fault sticks interpreted on successive diplines through this structure have been gridded to produce a 3D representation of the fault planes (Fig. 3.7d & e). The edges of the grids either correspond to the tip lines of the fault where displacement is zero, or the edge of the data set as labelled on the images. The Figures do not show the entire grids, but only the portions near the fault linkage. The along strike, horizontal overlap of the faults is approximately 3 km in this example. The upper tip-lines of both faults, shown as the top edges of the gridded surfaces, are located no more than 0.5 seconds (twt) under the seafloor. Tracing the tip-lines into the transfer zone there is a change in strike of the faults such that, at the tips, they curve as if to intersect each other (Fig. 3.5). This is similar to results from studies of fault segment linkage in extensional settings (e.g. Peacock and Sanderson, 1994). The shape of the lateral tip region of a fault plane is used in this study to define the geometry of fault interaction. The profile of a single fault and fold (Fig. 3.4) predicts isolated faults to be characterised by semi-ellipses (Fig. 3.8). Linked faults display modifications to this ideal that can be diagnostic of the type of linkage involved. In an antithetic Type 1 linkage faults have asymmetric, upward-tapering lateral tip regions (Fig. 3.8). This requires the lower tip lines to leave the zone of bed parallel shear in the detachment and climb stratigraphy towards relatively shallow lateral fault tips, while the upper tip lines maintain elevation. The result is an overlap of faults above the line of fault intersection, or 'branch line' (Boyer and Elliott, 1982; Butler, 1982;

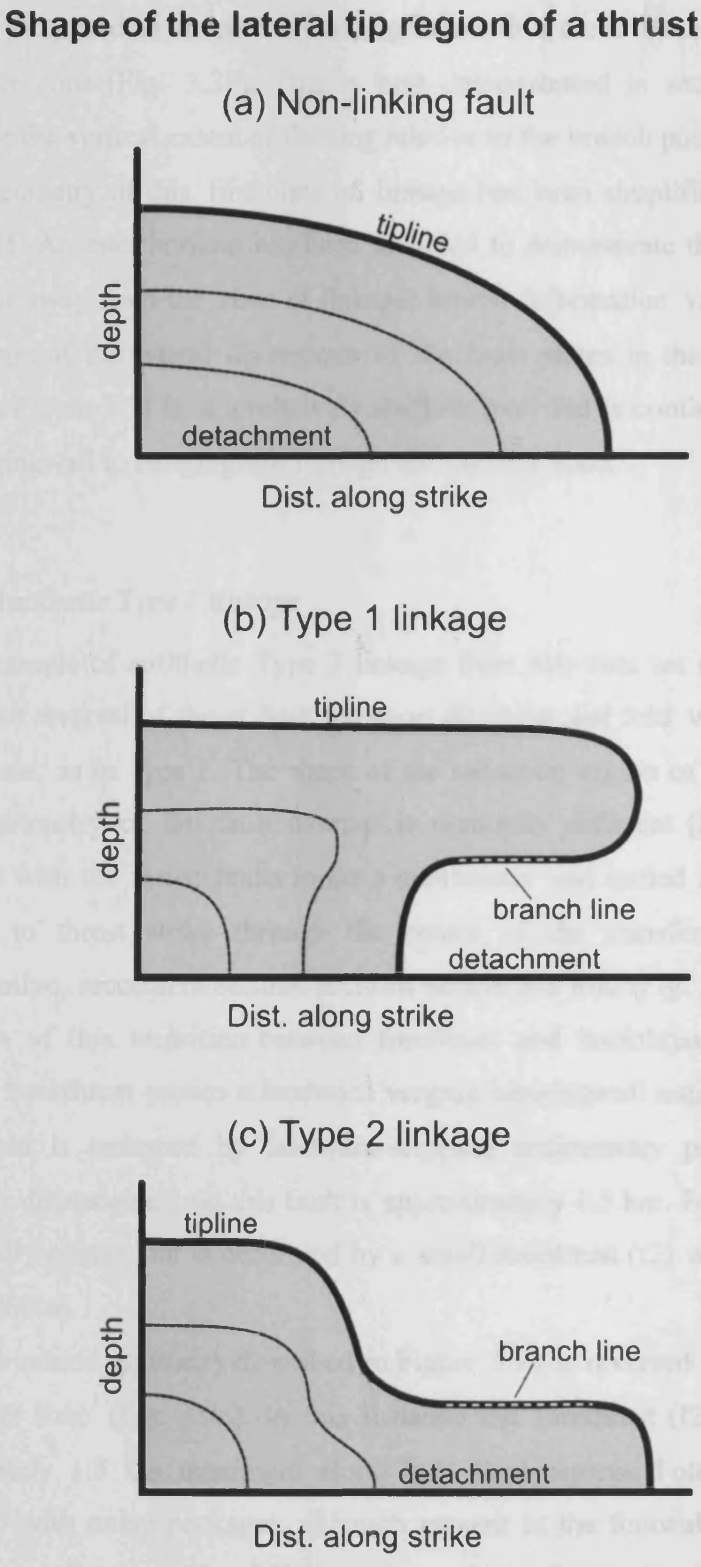

Figure 3.8: Diagrammatical strike projections of faults to describe the shape of a fault plane around the region of the lateral tip for non-linking and linked faults. **(a)** A non-linking fault describes a quarter-ellipse from dMAX to tip (as here) and a semi ellipse from tip to tip. **(b)** A Type 1 linkage has an elevated lower tip line and an upward-tapering lateral tip region. **(c)** A Type 2 linkage has a 'depressed' upper tip line and a downwards-tapering lateral tip region. Portions of tip lines that may form branch lines with counterpart faults (see Fig. 3.11) are indicated by white stippled lines. Type 3 is not shown as it does not have a diagnostic fault shape.

McClay, 1992), and an absence of faulting below this, close to the detachment, within the transfer zone (Fig. 3.3b). This is best demonstrated in section (Fig. 3.7b) by contrasting the vertical extent of faulting relative to the branch point (Fig. 3.3b).

The geometry of this first class of linkage has been simplified in block form in Figure 3.7f. An inset horizon has been included to demonstrate the increase in offset of horizons away from the zone of linkage. Stratal deformation varies with depth due to the shape of the lateral tip regions of the fault planes in the transfer zone. The horizon in Figure 3.7f is at a relatively shallow level and is continuous and unbroken from hangingwall to hangingwall through the transfer zone.

3.4.2.2 Antithetic Type 2 linkage

An example of antithetic Type 2 linkage from this data set (Fig. 3.9) shows an along strike reversal of thrust fault transport direction and fold vergence through the transfer zone, as in Type 1. The shape of the lateral tip region of the faults, however, and the geometry of the fault overlap is markedly different (Fig. 3.8). The fold associated with the thrust faults forms a continuous and buried anticline that trends obliquely to thrust strike through the centre of the transfer zone (Fig. 3.5b). Representative, successive seismic sections across this fold (Fig. 3.9a, b & c) give an illustration of this transition between forethrust and backthrust. In Figure 3.9a a detaching backthrust carries a landward verging hangingwall anticline. The backlimb of this fold is onlapped by landward-stepping sedimentary packages. Maximum along-fault displacement on this fault is approximately 1.5 km. Footwall stratigraphy is essentially planar, but is deformed by a small forethrust (f2) with displacement of less than 200 m.

The structural geometry described in Figure 3.9a is reversed on the other side of the transfer zone (Fig. 3.9c). In this instance the forethrust (f2) is dominant with approximately 1.3 km maximum along-fault displacement. Fold vergence is now oceanward with onlap packages, although present in the footwall, predominating in the hangingwall where they abut the long shallowly-dipping backlimb. Footwall deformation is characterised by a small backthrust with a maximum displacement of less than 200 m in this section.

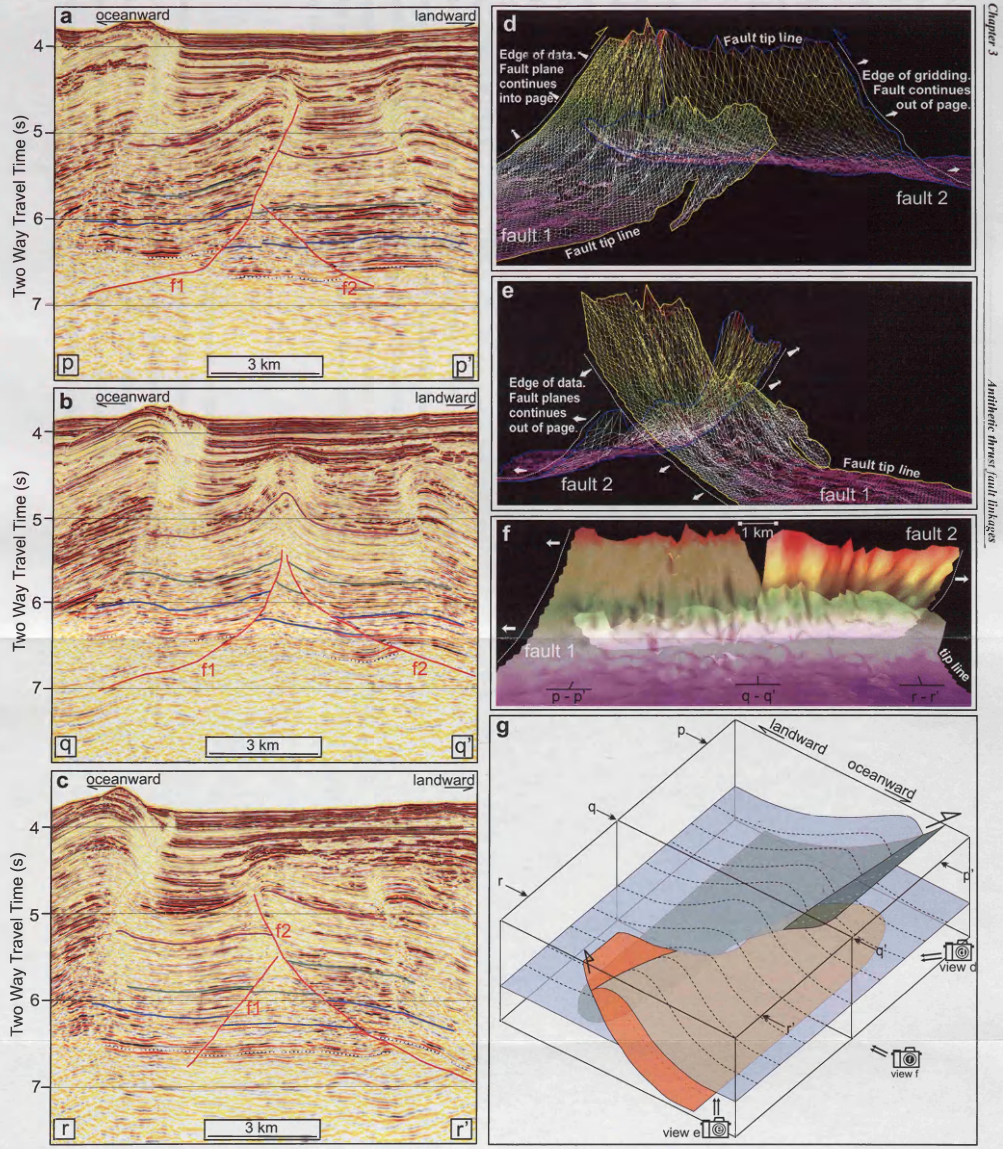

Figure 3.9: Antithetic Type 2 linkage. **(a, b, c)** Downdip, sequential seismic cross-sections in two-way-time (s). Fault 1 (f1) is a backthrust. Fault 2 (f2) is a forethrust. Agbada-Akata horizon: stippled white line. **(d, e, f)** 3D visualisations of fault planes using IESX Geoviz™ software. Surfaces are gridded from interpreted seismic fault sticks. Surfaces represent fault planes near the transfer zones only. Edges of the grids either represent fault tip lines (point of zero displacement) or the edge of the data set as labelled. **(g)** Simplified block diagram of a Type 2 linkage. Green fault: forethrust. Orange fault: backthrust. Transparent surface represents a typical shallow horizon.

A transfer zone lies between these two selected lines where neither forethrust nor backthrust is dominant (Fig. 3.9b). Maximum displacements are almost identical at 800 m and 900 m respectively. The two opposing thrusts are seen to abut, are over-steepened and underlie a 'bell-shaped' fold in the overburden. Changes to this structure during depth conversion were considered inconsequential. The symmetry of the fold and the vertical axial plane demonstrate a lack of vergence at this point and onlap packages occur on both limbs, stepping towards the anticlinal crest. This fold shape, with a lower interlimb angle, characterises Type 2 linkages within the dataset.

The wireframe and transparent fault planes (Fig. 3.9d, e and f) illustrate the forethrust and backthrust geometries in and around the transfer zone. The amount of along strike overlap of these faults is calculated, by extrapolating fault displacement gradients for fault 2 beyond the data boundaries, as approximately 9.5 km. The switch in dominance of the corresponding faults, indicated by the amount of displacement and the height of the upper fault tip-line, occurs over a distance of 2 km. Unlike the Type 1 example, the trends of the fault planes in map view do not change strike into the zone of overlap despite a decrease in the elevation of the upper tip-line. Downward-tapering lateral tip regions (Fig. 3.8) lead to relatively deep lateral fault tips as the lower tip lines remain within a zone of bed parallel shear within the detachment. This causes faults to overlap exclusively below the branch point, seen in cross section (Fig. 3.9b), close to the detachment and results in an absence of faulting in the hangingwall above. Shallower horizons, those stratigraphically higher than the branch line, remain unbroken across the midpoint of the linkage zone (Fig. 3.9g, q-q') due to displacement along a fault, and hence horizon offset, decreasing to zero at the tip lines and the shape of the lateral tip regions.

3.4.2.3 Antithetic Type 3 linkage

Linking faults need not be of similar displacement or lateral extent to form through-going folds. The antithetic Type 3 example (Figs. 3.6c and 3.10) comprises a backthrust measuring 9.5 km between lateral tips and a forethrust that extends 47 km from one lateral tip before being lost at the edge of the data set. Again, sequential seismic sections illustrate the changing fault geometries. In Figure 3.10a a landward propagating backthrust (f1), detaching on the Agbada-Akata Fm boundary, produces a

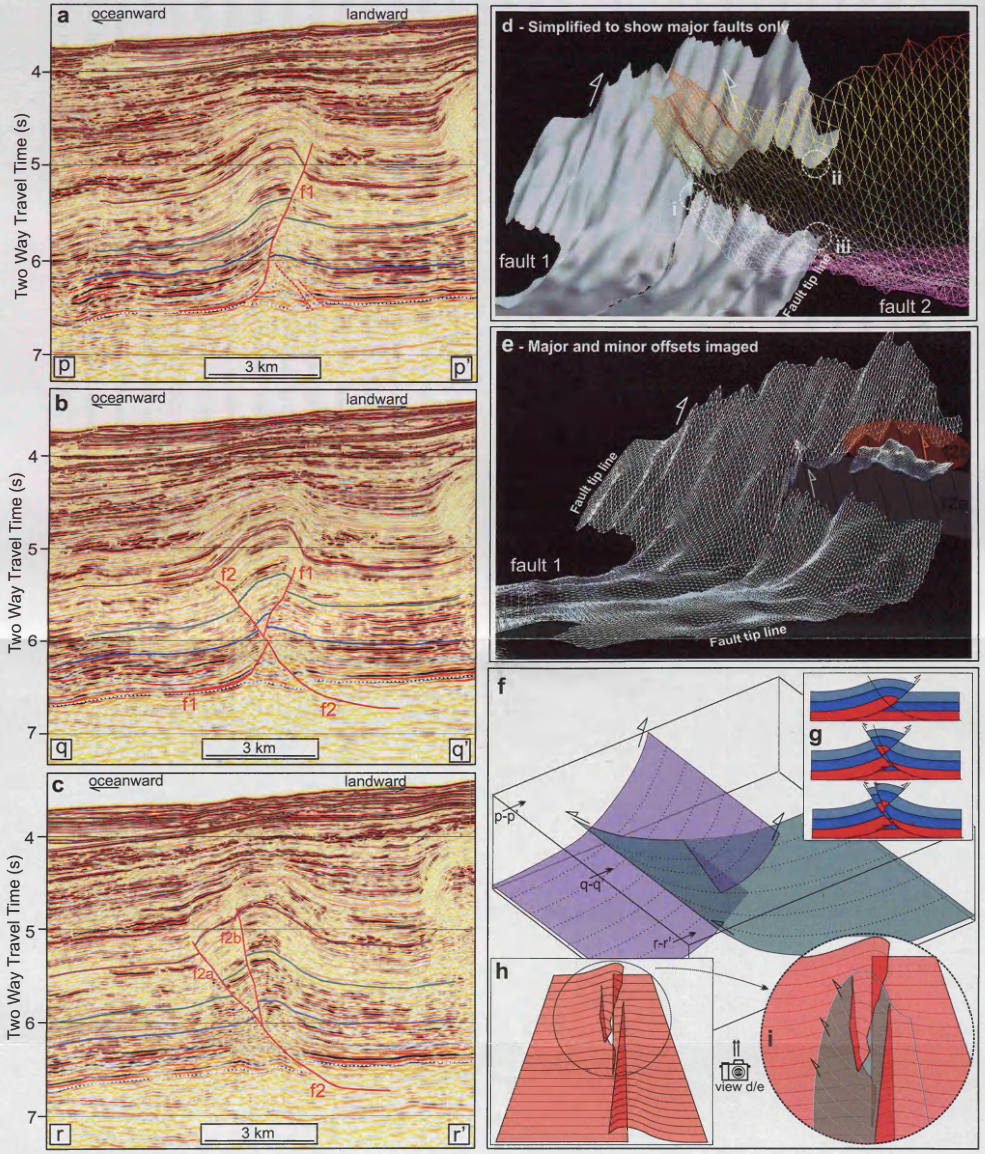

Figure 3.10: Antithetic Type 3 linkage. **(a, b, c)** Downdip, sequential seismic cross-sections in two-way-time (s). Fault 1 (f1) is a backthrust. Fault 2 (f2a&b) is a forethrust. Agbada-Akata horizon: stippled white line. **(d, e)** 3D visualisations of fault planes using IESX Geoviz™ software. Surfaces are gridded from interpreted seismic fault sticks. Surfaces represent fault planes near the transfer zones only. Edges of the grids either represent fault tip lines (point of zero displacement) or the edge of the data set as labelled. In **(d)** fault 2 cross-cuts fault 1 displacing point (ii) from point (iii). (i) lies on the tip line of fault 2 and represents zero displacement along f2. In **(e)** idealised fault ellipses (f2a, f2b) represent the planes which cross-cut fault 1. **(f)** Simplified block diagram of a Type 3 linkage. Green fault: forethrust. Blue fault: cross-cut backthrust. **(g)** suggests a simple evolutionary history of fault linkage. **(h)** Stylised deformation of a horizon. An idealised fault semi-ellipse of f2 creates a new hangingwall (hw) anticline (right) whilst offsetting an existing hw anticline (left) producing a tapering, triangular section of stratigraphy.

landward verging hangingwall anticline. An undisturbed seafloor suggests this fault is no longer active and depth conversion did not alter structural geometries to any significant degree. Small, very low displacement forethrusts are present in the footwall and align with a slight bend in the backthrust fault plane. Displacement on the dominant backthrust is about 600 m here. Along strike (Fig. 3.10c), an oceanward verging fold overlies a forethrust (f2) that detaches within the Akata section. The shape of the fold is complicated by branching of the fault plane at around 6 seconds twt, possibly due to the formation of a footwall imbricate. This geometry is not spatially extensive and is only present for 2.5 km of the fold length close to the transfer zone. The footwall is relatively undeformed indicating this is outside the area of overlap.

Within the transfer zone (Fig. 3.10b) the backthrust (f1) is cross-cut by the less developed forethrust (f2), and complicated stratal geometries result along strike (Fig. 3.10 g & h). The complexity ensues due to the complimentary displacement patterns of faults 1 and 2 along strike (i.e. both faults are losing displacement towards the transfer zone). In Figure 3.10d, 'i' represents a point of zero displacement on fault 2, whereas 'ii' and 'iii' locate two points of zero displacement on fault 1. Points 'ii' and 'iii' were once joined and have been separated by movement on fault 2. Fault 1 has therefore been cross-cut by fault 2. The crucial point to note therefore is that displacement *along* fault 1 decreases from the centre of its fault plane to the tipline, whilst the degree by which fault 1 is displaced when cross-cut increases in the same direction due to the interaction and nature of fault 2. This can lead to tapering, triangular sections of stratigraphy existing within the hangingwall-hangingwall section of the anticline (Fig. 3.10h). The fold retains a slight landward vergence within the transfer zone (Fig. 3.10b) due to the backthrust, at this point, having the larger displacement despite both faults acting upon the fold. The backthrust segment isolated within the forethrust hangingwall has convex-up curvature (Fig. 3.10b), suggesting deformation of the backthrust by folding prior to being cross-cut. The steady plunge of the fold across the transfer zone (Fig. 3.5c), the complimentary heave gradients and the cumulative heave curve similar to that of a single fold (Fig. 3.6) indicate these faults have been kinematically linked since conception (e.g. Nicol et al., 2002). The exclusive cross-cutting of fault 1 by fault 2, however, suggests fault 1 may have become inactive prior to the hard linkage of the faults.

The 3D model of the intersecting fault planes is more complicated than other types due to cross-cutting faults. The shape of lateral tip regions within the transfer zone (Fig. 3.10d) resemble that of non-linking faults (Fig. 3.8) with lower tiplines remaining in the detachment. The shape of the fault plane is therefore not distinctive for a Type 3 linkage and classification is based on both faults extending above and below branch lines in 3D, or the continuation of both faults past branch points in section, producing cross-cutting fault planes.

3.4.3 Comparing the structural geometry of transfer zones

The three types of antithetic fault linkage display very distinct fault plane geometries and fold styles within the transfer zones. The location and extent of faults relative to branch lines, and the offset and shape of selected horizons at various levels within the stratigraphy, are compared in Figure 3.11.

The shape of the upward-tapering lateral tip regions of the faults in the Type 1 example leads to a 'pop-up' structure forming in the shallower section, such that neither fault reaches detachment within the zone of linkage. Hence, along the entire length of the related anticline there can be a maximum of one fault detaching into the shaly Akata Fm. In contrast to this, the anticlines associated with antithetic Types 2 & 3 linkages display double detachments within the transfer zones.

Horizon continuity across the folds, through the transfer zones, varies between the three types of linkage depending on the vertical extent of faulting relative to the branch lines (Fig. 3.11). Here, strata above this line are considered shallow and those beneath described as deep. In Type 1 the deeper horizons are continuous, planar and unbroken in a down-dip direction across the transfer zone, although a loss of seismic resolution in this area means smaller scale deformation may not be recorded here. Shallower horizons are also continuous along a convoluted surface through a hangingwall-hangingwall (hw-hw) transfer fold (Fig. 3.11). In contrast the deeper horizons in both the Type 2 and Type 3 geometries are connected through an indirect, undeformed footwall-footwall (fw-fw) 'corridor'. They differ within the shallow section however with the Type 2 horizons being continuous in a down-dip direction through the tight 'bellfold' whilst Type 3 horizons are connected by a tortuous hw-hw transfer fold (Fig. 3.11). Type 3 is more complex and horizons in the mid section, close to and above the convergence of the detaching thrusts, frequently show recurring repetition of stratigraphy.

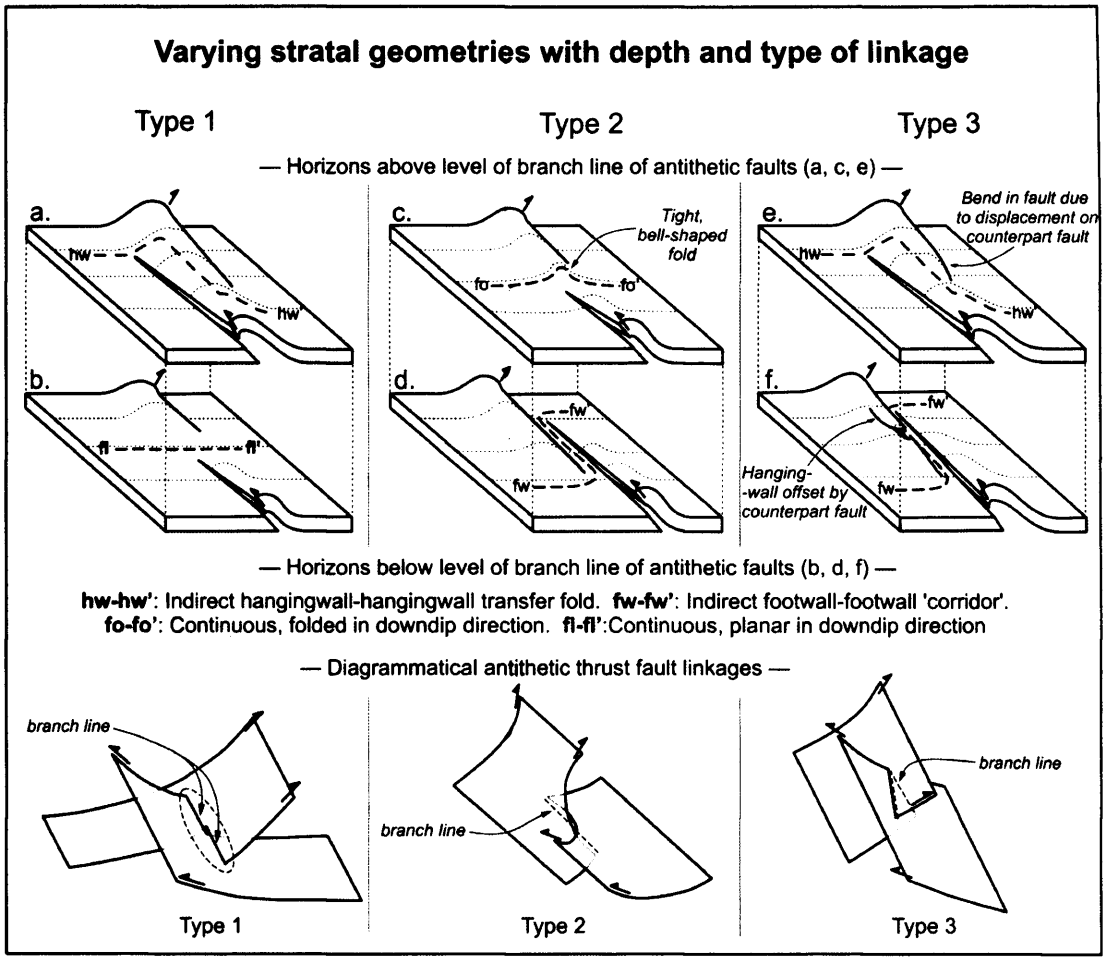

Figure 3.11: Diagrammatical representation of the main stratal geometries of antithetic thrust fault relay zones. Two horizons are depicted for each linkage type, demonstrating the deformation above a branch line **(a, c & e)** and below **(b, d & f).** Simplified fault geometries are given to demonstrate the position of the branch lines.

3.5 Discussion

This is the first classification of antithetic thrust fault linkages and contributes to the understanding of fold and thrust belts. The three classes of forethrust-backthrust interaction are presented as static geometric observations. One of the major questions concerning how these geometries formed is whether folding predates fault growth and interaction, or whether fault interaction drives fold formation. Until this is determined, we cannot conclude the root causes of the different geometries, and therefore this contribution is descriptive. Several possible models could account for the structures seen in this study, for example:

1. Two kinematically separate faults with associated fault-propagation folds propagate laterally, converging and linking, creating a continuous fold (Fig. 3.12a).

2. Folding precedes faulting. In this case a laterally extensive fold forms first, then nucleating numerous faults along its length that grow by segment linkage; synthetic faults joining to form larger through-going faults, faults with opposing dip forming antithetic transfer zones (Fig. 3.12b).

Analogue models exist that support the second hypothesis, that folding precedes faulting (Dixon and Liu, 1991; Liu and Dixon, 1991). These authors suggest that numerous thrusts could nucleate at different points along a single fold and propagate along strike, to link and produce larger structures. The models also show that the encompassing fold may be the product of along strike propagation and linkage of several smaller, doubly plunging folds.

Few published examples of along strike antithetic thrust linkage can be found within literature: three are discussed here. Harrison and Bally (1988) describe the Parry Island Fold Belt, in the Canadian Arctic, as having a near equal development of forward- and backward-verging fold and thrusts. Numerous surface folds demonstrate along strike vergence reversals (Harrison and Bally, 1988 their Figure 6) associated with apparent antithetic thrust fault linkage in the underlying succession (Harrison and Bally, 1988 their Figure 7). The authors describe "pop-up" structures within the transfer zones and relate them to displacement transfer between the overlapping thrusts. They create a model for "pop-up" formation that is similar in general to our Type 3 linkage (Harrison and Bally, 1988 their Figure 13).

Aamir and Siddiqui (2006) document an apparent Type 2 Linkage between the

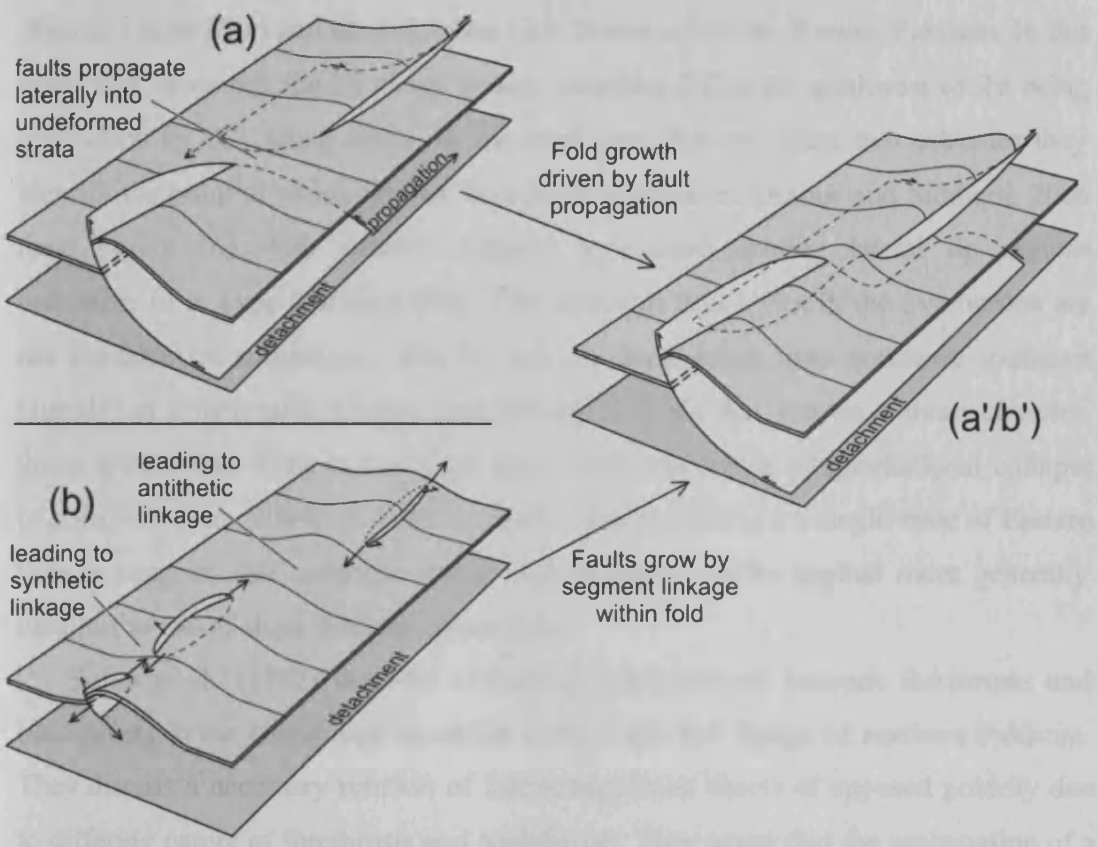

Figure 3.12: Hypothetical models of the evolution of antithetic thrust fault linkage (based on a Type 2 linkage geometry). Two possible mechanisms of fold and fault linkage. **(a)** Two kinematically separate faults with associated fault-propagation folds propagate laterally, converging and linking, creating a continuous fold. **(b)** Folding precedes faulting. In this case a laterally extensive fold forms first, then nucleating numerous faults along its length that grow by segment linkage; synthetic faults joining to form larger through-going faults, faults with opposing dip forming antithetic transfer zones. **(a'/b')** A schematic diagram of a Type 2 linkage observed in the data.

Domeli Thrust (DT) and the Dil Jabba (DJ) Thrust in Eastern Potwar, Pakistan. In this study they show that the DJ thrust system overrides DT in the southwest whilst being overridden by DT, along strike, in the northeast. Between these two extremes they identify the point at which neither fault holds dominance (Aamir and Siddiqui, 2006 their Figure 16). This pattern suggests downward-tapering lateral tip regions indicative of a Type 2 linkage (Fig. 3.8), although fold styles in the overburden are not available for comparison. The DJ and DT faults result from northwest-southeast Himalayan compression (Aamir and Siddiqui, 2006) that creates a more complex thrust system than those in the Niger delta which are driven by gravitational collapse (e.g. Rowan et al., 2004). A Type 2 transfer zone present in a triangle zone of Eastern Potwar suggests that antithetic thrust fault linkages can be applied more generally than just to toe-of-slope fold and thrust belts.

Butler et al. (1987) describe alternating displacement between forethrusts and backthrusts in the Himalayan mountain front in the Salt Range of northern Pakistan. They discuss a necessary rotation of interacting thrust sheets of opposed polarity due to differing nature of forethrusts and backthrusts. They argue that the propagation of a backthrust may lead to the movement of the footwall ramp into the foreland due to footwall rocks being forced under the hangingwall. Forethrusts, on the other hand, have static footwall ramps as hangingwall rocks are simply transported up and over the footwall (Butler et al., 1987). This was not observed in the fold and thrust belt of the Niger Delta, possibly due to lower fault displacements.

3.5.1 Implications

This research raises important questions about fault growth and linkage in compressional settings. Future work involving detailed displacement analyses and examination of fold and thrust timing may give clues to the controls on the type of linkage created at a point of fault interaction and the relationship between fault displacement and shortening within the transfer zones.

The geometry of three-dimensional thrust fault linkages described here could also impact modeling of fluid migration and transmissibility of deep water deltaic sequences. Understanding of (a) the connectivity of sand bodies in a stacked channel-levee system (b) the 3D geometry of the faults that intersect potential reservoir and

seal lithologies and (c) how faults link the reservoirs to the underlying source rocks are all critical questions for successful hydrocarbon exploration and production.

3.6 Conclusions

We define three types of linkages of thrust faults of opposing dip within a fold and thrust belt.

Type 1. Faults overlap laterally within the shallow section only, above the level of the branch line of the antithetic thrusts. This creates a 'pop-up' structure within the transfer zone and a convoluted hangingwall-hangingwall (hw-hw) transfer fold.

Type 2. Faults overlap laterally within the deep section only, below the level of the branch line of the antithetic thrusts. This creates distinctive, tight folds in the overburden and an indirect, undeformed footwall-footwall (fw-fw) 'corridor'.

Type 3. Faults cross-cut one another so that both are present above and below the branch line. Strata above this line form a convoluted hw-hw transfer fold, those below form an indirect, undeformed fw-fw 'corridor' with an increase in horizon repetition in the mid section.

All share the common feature of an along strike switch in vergence in the respective hangingwall anticline, however deformation of sediments within the transfer zones varies with depth due to the shape of the lateral tip regions of fault planes as they overlap.

Such intersections represent a fundamental aspect of compressional fold and thrust belts and hence this simple scheme for defining how the component faults and folds link should have global applicability.

Chapter 4

In review as:

Higgins, S., Clarke, B., Davies, R.J., Cartwright, J., Internal architecture and growth history of a thrust-related anticline in a deep water fold belt. Journal of Structural Geology.

Although the papers are jointly authored with the project supervisors they are the work of the lead author, Simon Higgins. In this chapter, Upward dip reduction data and isopach data acquired by Benjamin Clarke at StatoilHydro were re-measured, analysed and interpreted by Simon Higgins. Project supervisors provided editorial support in accordance with a normal thesis chapter.

CHAPTER 4

4 INTERNAL ARCHITECTURE AND GROWTH HISTORY OF A THRUST-RELATED ANTICLINE IN A DEEP WATER FOLD BELT

4.1 Abstract

The structural evolution of a fold-and-thrust belt is investigated through the analysis of a single, isolated fold imaged using 3D seismic data over part of the deep water Niger Delta. Numerous thrust faults, of similar and opposing dip, link and transfer displacement through transfer zones within the structure creating a central structural culmination and causing the vergence to vary along strike. These linkages vary in spatial extent and have distinctly different styles. Fault heave and shortening measurements are presented for each instance as displacement-length profiles and strike projections with reference to a simple fold comprising a single fault plane. Syn-kinematic growth packages are used to chart fold and fault growth through time and allow for an understanding of the early structural growth history. This evidence forms the basis for a model of fold-and-thrust fault growth for toe-of-slope compressional settings. Several detachment folds initiate with individual structural culminations and grow towards each other by lateral propagation along strike. Numerous faults nucleate at various stratigraphic levels along the length of the structure on both flanks producing an asymmetric fold shape. Analysis of lateral fold tip structures suggests the faults propagate some distance above the detachment. Continuing fault development results in the migration of the point of maximum displacement, observed in a given 2D section, downwards towards the detachment. Folds coalesce and faults link along strike, resulting in structural culmination migration to a single central apex and the formation of synthetic and antithetic thrust fault linkages. The bulk shortening profile resembles that of an individual fault and fold indicating component structures have acted as a coherent unit since inception. Final fault and fold geometries display fluctuating fault heave values and a smoother shortening profile that suggests deformation by folding compensates for deficits in fault heave along strike.

4.2 Introduction

The relationship between thrust faults and associated folds has been extensively researched in the past two decades (Thorbjornsen et al., 1997). Distinct classes of structure are now clearly defined and widely described from orogenic belts exposed on land and more recently from fold and thrust belts associated with gravity-driven deformation of continental margins. The description of fault-bend-folds (Rich, 1934; Boyer and Elliott, 1982; Suppe, 1983), fault propagation folds (Williams and Chapman, 1983; Suppe, 1985; Suppe and Medwedeff, 1990), break-thrust folds (Jamison, 1987; Mitchell and Woodward, 1988; Butler, 1992; Woodward, 1992) and detachment folds at the lateral terminations of faults (e.g. Jamison, 1987) have mainly been based on cross-sectional geometry, either derived from exposed sections or from 2D seismic profiles. However, our current understanding of the initiation, propagation and along strike linkage of such structures remains limited, although analogue and numerical models have led to significant recent advances (e.g. Liu and Dixon, 1991). The advent of 3D seismic data as a research tool has been a major factor in the revolution in our understanding of normal fault propagation and linkage (Childs et al., 1995; Nicol et al., 1995; 1996; Meyer et al., 2002) and thus far, this imaging potential has not been employed to analyse the three-dimensional evolution of thrust related folds to the same degree.

A primary aim of this paper is to demonstrate the potential for the use of 3D seismic data in the structural analysis of fold and thrust belts. Advancements in seismic imaging resulting from modern 3D migration algorithms enable thrusts to be accurately mapped and reveal subtleties of geometrical form that are vital for the correct reconstruction of their growth history. We use the example of a superficially simple fold structure from a deepwater fold and thrust belt of the Niger Delta (Corredor et al. 2005; Briggs et al. 2006) to analyse thrust and fold growth histories through detailed strain analysis. We describe several novel techniques to define the strain history, and fom this we show that a single, kinematically coherent structure has evolved by a process of segment propagation and linkage directly analogous to that known for normal faults (e.g. Segall and Pollard, 1980; Ellis and Dunlap, 1988; Peacock and Sanderson, 1991; Cartwright et al., 1995). Linkage of propagating segments to form thrust faults with relay structures or transfer zones is not a new

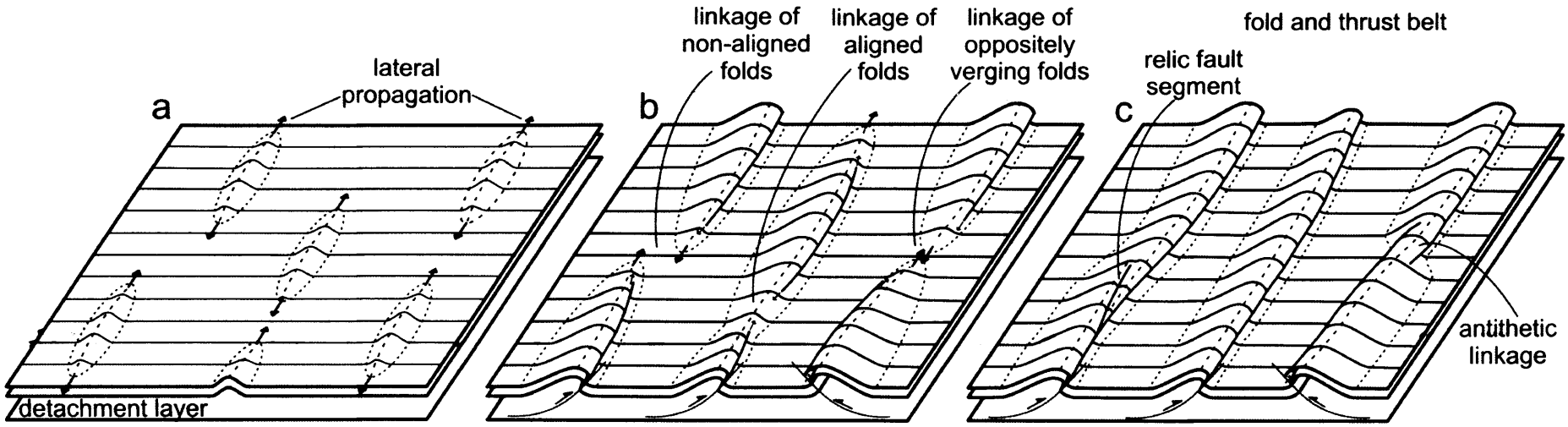

Figure 4.1: A model of the structural evolution of a fold and thrust belt. Based partly upon and expanded from the modelling results of *Liu and Dixon (1991).* **(a)** Numerous low amplitude detachment folds initiate and grow by lateral propagation. **(b)** Faults nucleate within competent units and propagate along strike within the folds. Forethrusts form in the forelimbs, backthrusts in the backlimb. Each fold may nucleate a number of faults along its length. **(c)** Fault linkage follows fold linkage creating through-going thrust surfaces.

concept (Dahlstrom, 1970; Elliott, 1976; Ellis and Dunlap, 1988; Nicol et al., 2002), but the use of 3D seismic data to constrain this process has not previously been attempted for fold and thrust settings.

The paper concludes with a discussion of the growth history of a fold in the context of current uncertainties in how thrust faults evolve. This uncertainty is reflected in the various competing models of thrust development in vogue at present (e.g. Thorbjornsen and Dunne, 1997). Some authors propose that the role of the fault is over-emphasised in fold-and-thrust belt literature and conclude that fault ramps nucleate at points localised by earlier folding of competent units. Dixon and Liu (1991) argued that fault linkage may be preceded by the along strike propagation and merger of colinear, periclinal detachment folds (Fig. 4.1). Upward propagation of faults into the competent units produce fault propagation folds. Subsequent fault refraction into the weaker units above may eventually lead to the development of fault bend folds. A final aim of this paper, therefore, is to evaluate these models against a single, but well constrained case study example. The quantitative description of thrust fault linkages that exist within a single fold, along with detailed analysis of the spatial extent and form of syn-kinematic packages, provides the basis for a discussion of: i) the internal architecture of a complex faulted fold, ii) the geometry and kinematics of thrust fault linkage, iii) the relationship between folding and faulting in accommodating shortening and iv) the timing and location of fold and fault growth.

4.3 Database

This paper is based on two 3D seismic surveys (A and B) acquired over the compressional fold and thrust belt located in the toe-of-slope region of the Niger Delta. Survey A covers 3000 km^2, and was acquired with a 6 km offset length, a 12 seconds (s) record interval and a sampling interval of 4 milliseconds. Inline and crossline spacing is 12.5 m with vertical resolution varying from approximately 7.5 m in shallow levels to 20 m at the base of the thrusted interval. Survey B (Fig. 4.2) is located upslope of the main fold and thrust belt, covers an area of c. 2000 km^2 and has lines spaced at 12.5 m The resolution of survey B is comparable to that of survey A. Eleven key seismic horizons were mapped in both survey areas using Schlumberger's IESX interpretation software and dated biostratigraphically by correlation to a nearby

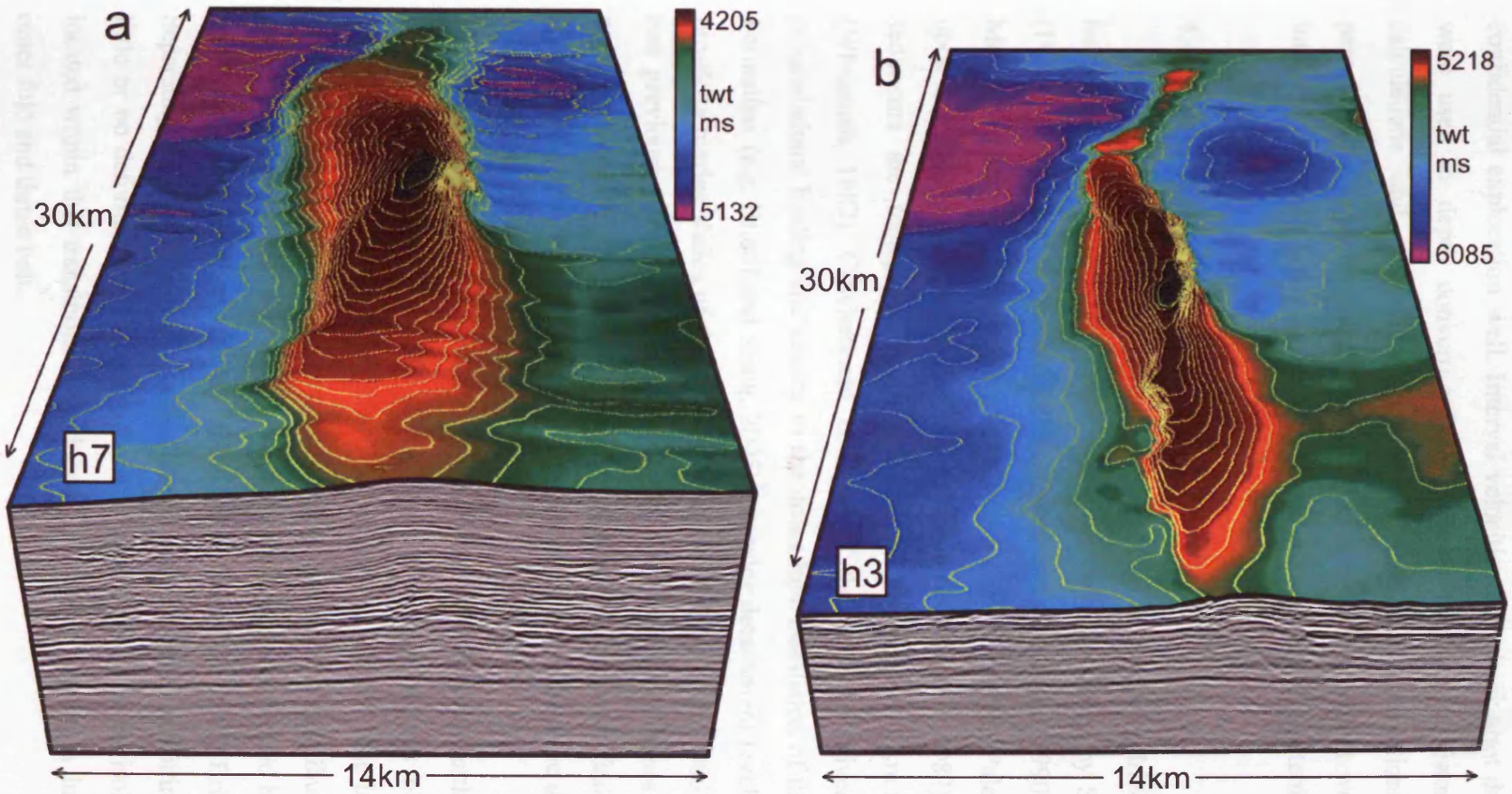

Figure 4.2: Seismic survey B. Two selected stratigraphic horizons (h7 and h3) showing a single, isolated thrusted-fold. Horizon h7 is stratigraphically above horizon h3. Elevation of the horizon is presented in two-way-time (ms). Note the change in fold vergence along strike indicated by closely spaced contours (yellow lines). Red/orange colours : structural highs. Purple/blue colours : structural lows. Contour interval: 40 ms.

confidential exploration well. Interval velocities and check shot data from the well were used to depth convert seismic sections for use in restoration, shortening calculations and to validate geometric structural observations. Seismic lines perpendicular to the regional strike of fold and fault structures were used for fault interpretation, fault heave measurements and calculations of shortening.

4.4 Structural setting

Surveys A and B are located in the outer part of a gravity-driven fold and thrust belt in the deepwater Niger Delta which has been described by Short and Stauble (1967), Onuoha and Ofoegbu (1988), Doust and Omatsola (1990) and Cohen and McClay (1996). Deltaic sedimentation began during the late Paleocene to Eocene upon the underlying Albian marine succession (Whiteman, 1982). Neogene clastic sediments are thought to reach a maximum thickness of 12 km in the Niger Delta (Whiteman, 1982). Gravitational collapse of the delta is driven by differential progradational loading and results in the downslope translation of the paralic Agbada Formation (e.g. Bilotti and Shaw, 2005) on major detachment levels that exist within pro-delta marine shales of the Akata Formation (Briggs et al., 2006). The Niger Delta has previously been described as having three structural zones: an extensional province beneath the outer shelf comprising listric growth faults; a zone of mud diapirism located beneath the upper continental slope; and a more distal compressional zone (Damuth, 1994).

This deep water compressional zone has been subsequently further subdivided to differentiate two fold and thrust belts with differing degrees of forethrusts and backthrusts (e.g. Connors et al., 1998; Corredor et al., 2005). The inner thrust belt is predominantly made up of oceanward-verging imbricate thrust faults and folds and some detachment folds. The outer belt, in contrast, is characterized by both landward- and oceanward-verging thrusts and folds (Corredor et al., 2005; Briggs et al., 2006). Separating the two is a transitional detachment fold zone exhibiting large areas of little or no deformation. The main focus of this study is on an isolated faulted fold located within this transitional detachment fold zone. Survey A images part of the outer fold and thrust belt.

Gravitational deformation is active at present, having initiated in the early Tertiary on detachments thought to be a product of overpressure in the shaly Akata unit (Morley and Guerin, 1996; McClay et al., 1998). Thrust faults are documented as

detaching at numerous levels within the succession of the Niger Delta (e.g. Corredor et al., 2005; Briggs et al., 2006), although only two detachment levels are seen in this data; at the Agbada-Akata Formation boundary and a regional detachment within the Akata itself. In this study area, the Agbada Formation comprises a series of compensationally stacked deepwater channel-levee systems (e.g. Deptuck et al., 2003) and is deformed by both oceanward-vergent forethrusts and landward-vergent backthrusts. The relative age of thrust and fold initiation does not simply progress from the foreland into the hinterland. Thrust systems can locally show signs of both break-forward and break-backward thrusting (Corredor et al., 2005).

4.5 Methods

4.5.1 Strike projected contour plots

Shortening values and fault heave measurements are presented using plane-vertical strike-projections, following techniques developed for analysis of normal faults (e.g. Rippon, 1985). Shortening calculations incorporate folding as a major mechanism of deformation. Shortening values are based upon and refer to marker horizons as the datum for plotting purposes. Fault heave and bulk shortening are calculated for each of the eleven key seismic horizons and are plotted at a corresponding undeformed, 'regional' horizon depth downdip of the fold structure to avoid introducing spatial positioning errors resulting from variable fold amplitudes (Fig. 4.3). Fault heave is plotted using the same methodology as for shortening values, rather than at a cut-off position (e.g. Williams and Chapman, 1983) or at the midpoint between cut-offs (e.g. Ellis and Dunlap, 1988). Our plotting convention allows direct comparison between variations in faulting and bulk shortening. The major limitation of our method, however, is that upward displacement gradients along fault planes will be apparently reduced compared to previous studies. This effect is compounded if a fault has a listric character in sectional profile such that a fault decreases in dip with depth, as heave will be seen to increase for the same along-fault displacement. This may produce an apparent increase in the upward displacement gradient. This has limited impact however, as faults in this study are approximately planar for the majority of their height as ramps are restricted to within 300 – 400 milliseconds (ms) above the detachment. In addition, the main focus of this paper is on along strike changes in fault and fold geometries which are unaffected by these limitations.

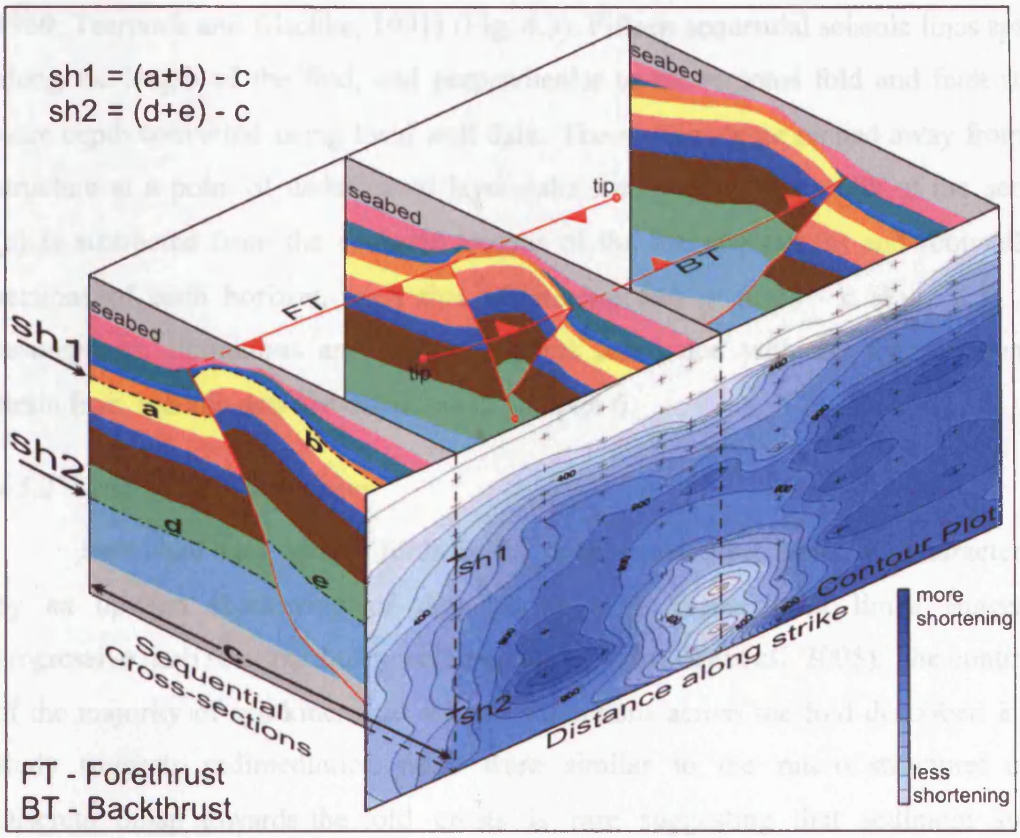

Figure 4.3: Methodology for the calculations of shortening and the display of strike projected contour plots. Three sequential depth converted cross-sections showing a change in structural geometry along strike through an antithetic thrust fault linkage. *FT*: forethrust. *BT*: backthrust. Values of shortening (e.g. sh1, sh2) are calculated by line length analysis. **a**, **b**: length of selected stratigraphic horizons in the footwall. **d**, **e**: length of selected horizons in the hangingwall. **c**: length of section. Values of shortening (e.g. sh1, sh2) are plotted on a vertical strike projection plane at depths corresponding to undeformed, 'regional' horizon depths downdip of the fold structures to allow correlation with fault heave measurements. Values are contoured.

Shortening values are calculated by simple line length balancing (e.g. Dahlstrom, 1969; Tearpock and Bischke, 1991) (Fig. 4.3). Fifteen sequential seismic lines spaced along the length of the fold, and perpendicular to the regional fold and fault strike were depth converted using local well data. The sections were pinned away from the structure at a point of undeformed layer-cake stratigraphy. The width of the section (c) is subtracted from the summed lengths of the hangingwall (a) and footwall (b) sections of each horizon, such that Shortening (sh) = (a+b) - c (Fig. 4.3). The assumptions, limitations and potential errors associated with the measurement of strain from seismic data are discussed in Chapter 6.

4.5.2 Timing of deformation

Individual fault-related folds in the deep water Niger Delta are characterized by an upward shallowing of dips above long, planar back limbs suggesting progressive limb rotation during sedimentation (Corredor et al., 2005). The continuity of the majority of syn-kinematic seismic reflections across the fold described in this study suggests sedimentation rates were similar to the rate of structural uplift. Discrete onlap towards the fold crests is rare suggesting that sediment supply generally exceeded fold amplification rate. The onset and duration of folding and faulting are quantified by the analysis of growth packages on the limbs of anticlines (e.g. Medwedeff, 1989; Suppe et al., 1992; Storti and Poblet, 1997). Two variables are defined and measured here; isopach ratios and upward dip reductions.

Isopach ratios compare the depth converted, orthogonal thickness of sediments on the limbs of a fold to those on the crest (Fig. 4.4) and are expressed as the flank thickness relative to crestal thickness. As folds begin to grow, synform sedimentary confinement causes the interval isopach ratio to increase. In layered siliciclastic sediments pre-kinematic sediments should have a constant thickness across a fold, whereas syn-kinematic sediments should thin towards and onto a fold.

Upward dip reductions quantify the change in dip of stratal reflections along vertical profiles positioned on the limb of folds (Fig. 4.4). Progressive limb rotation due to fold growth causes strata on the flanks to steepen (e.g. Storti and Poblet, 1997), while the depositional surface above them remains sub-horizontal. Hence, the dip measured upwards along a vertical profile should show an abrupt decrease as folding begins. Measurements are made on depth converted dip attribute maps that eliminate

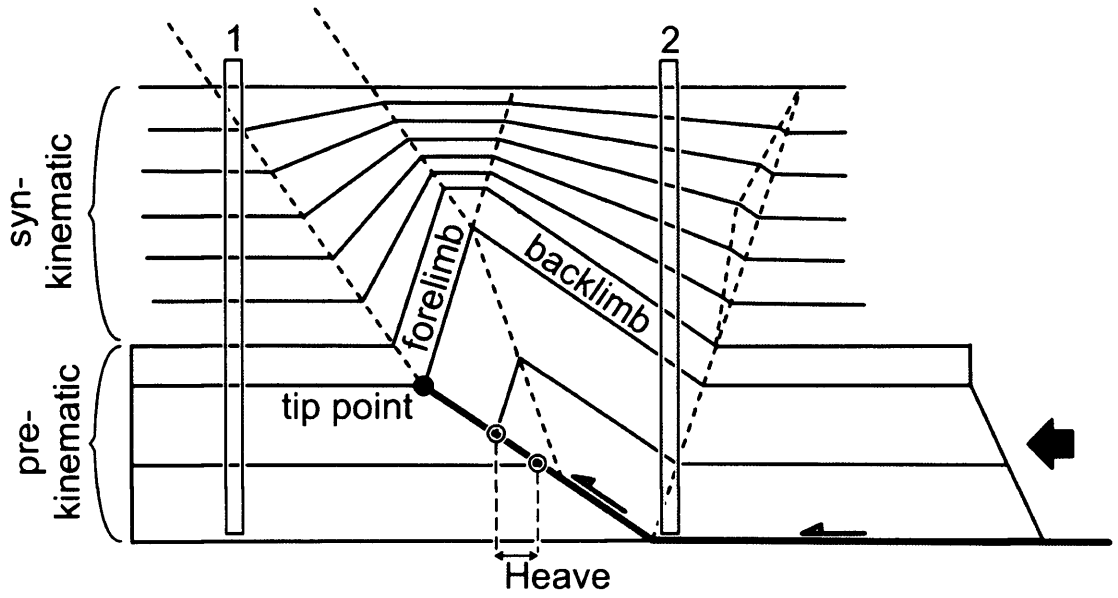

Figure 4.4: Diagrammatical description of locations of vertical profiles (used in calculating isopach ratios and upward dip reductions) relative to growth packages associated with Fold B. 1, 2: locations of vertical profiles in forelimb and backlimb respectively. Geometry of growth strata adapted from *Storti and Poblet (1997)* and represents stratal forms associated with fold development predominantly by limb rotation and similar rates of uplift and sedimentation.

errors produced by local dip variations such as within channel-levee complexes. Dips of successive horizons are subtracted (Fig. 4.4), and a negative value is interpreted as indicative of a syn-kinematic package. Pre-kinematic sediments, deposited as layer-cake stratigraphy, should have consistent dip along the vertical profile. Comparisons of values recorded by forelimb-backlimb paired profiles allow conclusions to be drawn on the degree of asymmetry of the fold through time (Fig. 4.4).

4.6 Results

Two case studies have been selected from the array of thrusts and associated folds in the two survey areas to demonstrate the techniques that can be employed in strain analysis using 3D seismic data, and to provide a basis for the later discussion of fold growth. We contrast two faulted folds: Fold A represents the simplest example of a faulted fold within the surveys, in terms of fault plane geometry, linkage, fold shape, fault displacement and shortening profile. Fold B, in contrast, is more complex, consisting of numerous faults of opposing dip, includes synthetic and antithetic fault linkages, along strike fold vergence reversals and irregular fault displacement profiles. The growth history of Fold B is the main focus of this paper and hence is the subject of more analysis than Fold A.

4.6.1 Fold A

Fold A is developed within the frontal zone of the fold belt, but exhibits little evidence of along strike interaction with neighbouring structures (Fig. 4.5). Full analysis, however, is unfortunately limited as this structure is only partially imaged for 23 km along strike from the fold tip to the edge of the survey (Fig. 4.5a). The structure consists of a single seismically resolved fault plane (Fig. 4.5d) with no significant jogs in the fault trace (Fig. 4.5a) that are commonly interpreted as zones where fault linkage has occurred (e.g. Peacock and Sanderson, 1991; Cartwright et al., 1995). Fold amplitude of a selected horizon, termed horizon 'x', exceeds 1200 m between 0 and 4 km along strike and decreases at a steady gradient towards the fold tip at the 22 km position (Fig. 4.5c). Fault heave displays a first-order tapering, convex-up profile (horizon x) along the length of the fold, superimposed on which are small amplitude irregularities (Fig. 4.5b). These irregularities correlate with undulations in fault heave contours (Fig. 4.5f). Fault heave increases with depth on all parts of the fault such that maximum displacement is predicted to be located within

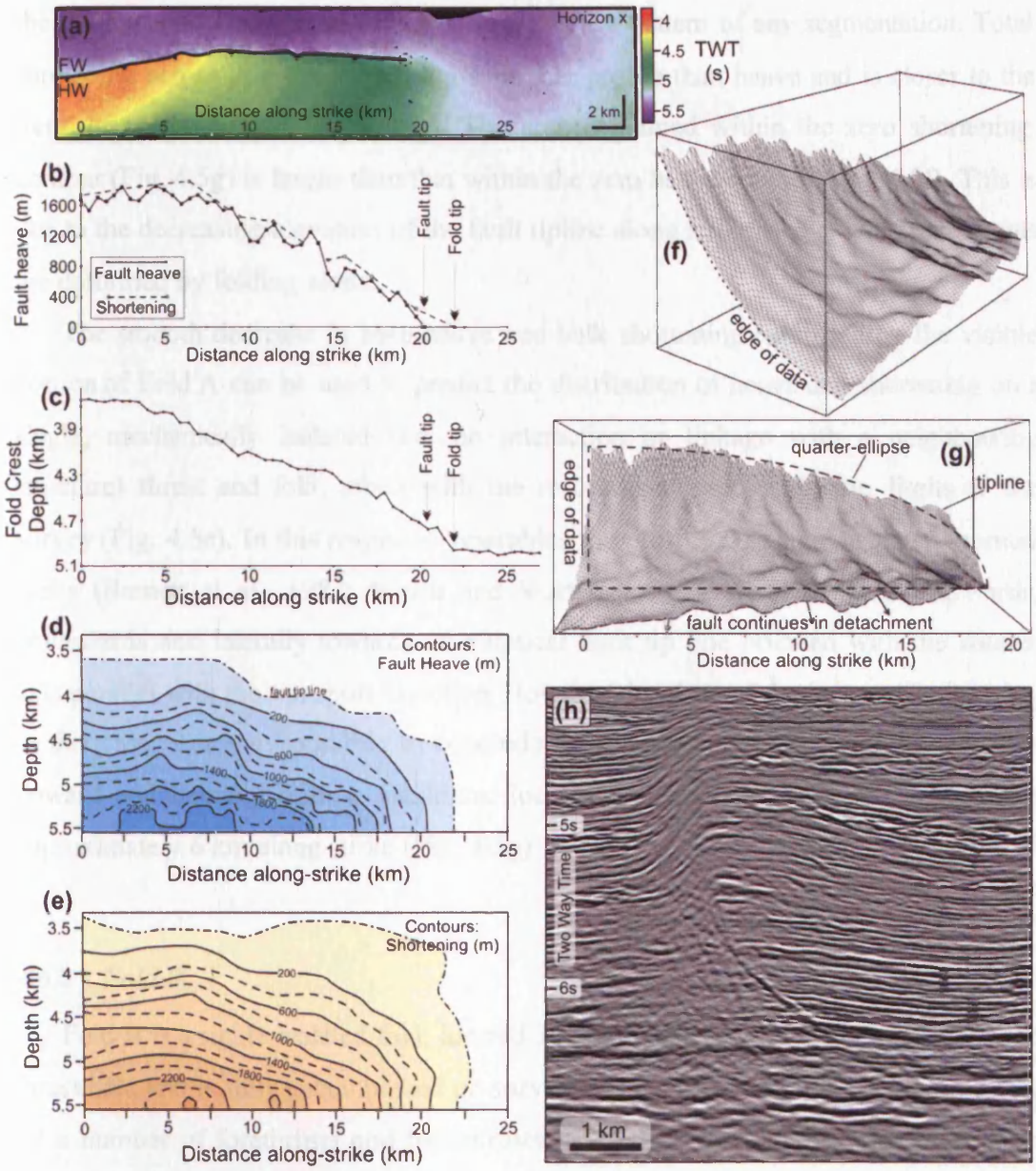

Figure 4.5: Heave and shortening profile of Fold A. Along strike distances measured from a point close to the edge of the survey area. **(a)** Elevation map of horizon 'x' in two-way-time showing fault trace and hangingwall anticline. Thrust fault trace denoted by black triangles in the hangingwall. FW: footwall. HW: hangingwall. **(b)** Heave- length and shortening profile of the thrust fault measured on horizon x. **(c)** Depth to fold crest for horizon x. **(d)** Fault heave strike projected contour plot. **(e)** Bulk shortening strike projected contour plot. **(f)** and **(g)** 3D images of fault plane. Note that the tipline of the thrust surface resembles a quarter-ellipse **(g)**. **(h)** Representative seismic section oriented perpendicular to fault strike.

the detachment. There is no evidence in the heave pattern of any segmentation. Total shortening across this structure has a smoother profile than heave and is closer to the trend of crestal height (Fig. 4.5b). The area contained within the zero shortening contour (Fig. 4.5g) is larger than that within the zero heave contour (Fig. 4.5f). This is due to the decreasing elevation of the fault tipline along strike, above which sediments are deformed by folding alone.

The smooth decrease in both heave and bulk shortening exhibited by the visible portion of Fold A can be used to predict the distribution of heave and shortening on a single, mechanically isolated (i.e. no interaction or linkage with a neighbouring structure) thrust and fold, albeit with the restrictions imposed by the limits of the survey (Fig. 4.5e). In this respect it resembles the profiles of single, isolated, normal faults (Barnett et al., 1987; Walsh and Watterson, 1991) which die out upwards, downwards and laterally towards an elliptical fault tip line oriented with the shorter axis parallel with the transport direction. However, because of the incomplete imaging in this case, it is only possible to conclude that shortening decreases systematically upward and laterally from a maximum located immediately above the detachment approximately 6 km along strike (Fig. 4.5g).

4.6.2 Fold B

Fold B is a single isolated fold, located 30 km upslope of the major outer fold and thrust belt, and is fully encompassed on survey B (Fig. 4.2). Stratal horizons are offset by a number of forethrusts and backthrusts that detach at Akata-Agbada Formation boundary and link along strike within the fold producing a maximum fold amplitude in excess of 1 km. Surrounding strata are undeformed for a minimum lateral distance of approximately 12 km away from Fold B.

4.6.2.1 Fold shape

Superficially Fold B appears to be a simple, single structure (Fig. 4.2a), however in detail fold and thrust geometries vary along strike and with depth. Changes in fold vergence are clearly related to faulting and are therefore indicative of the interaction of a number of thrusts of opposing dip within the fold.

Two key seismic horizons (h7 & h3) mapped in the survey area (Fig. 4.6) and six

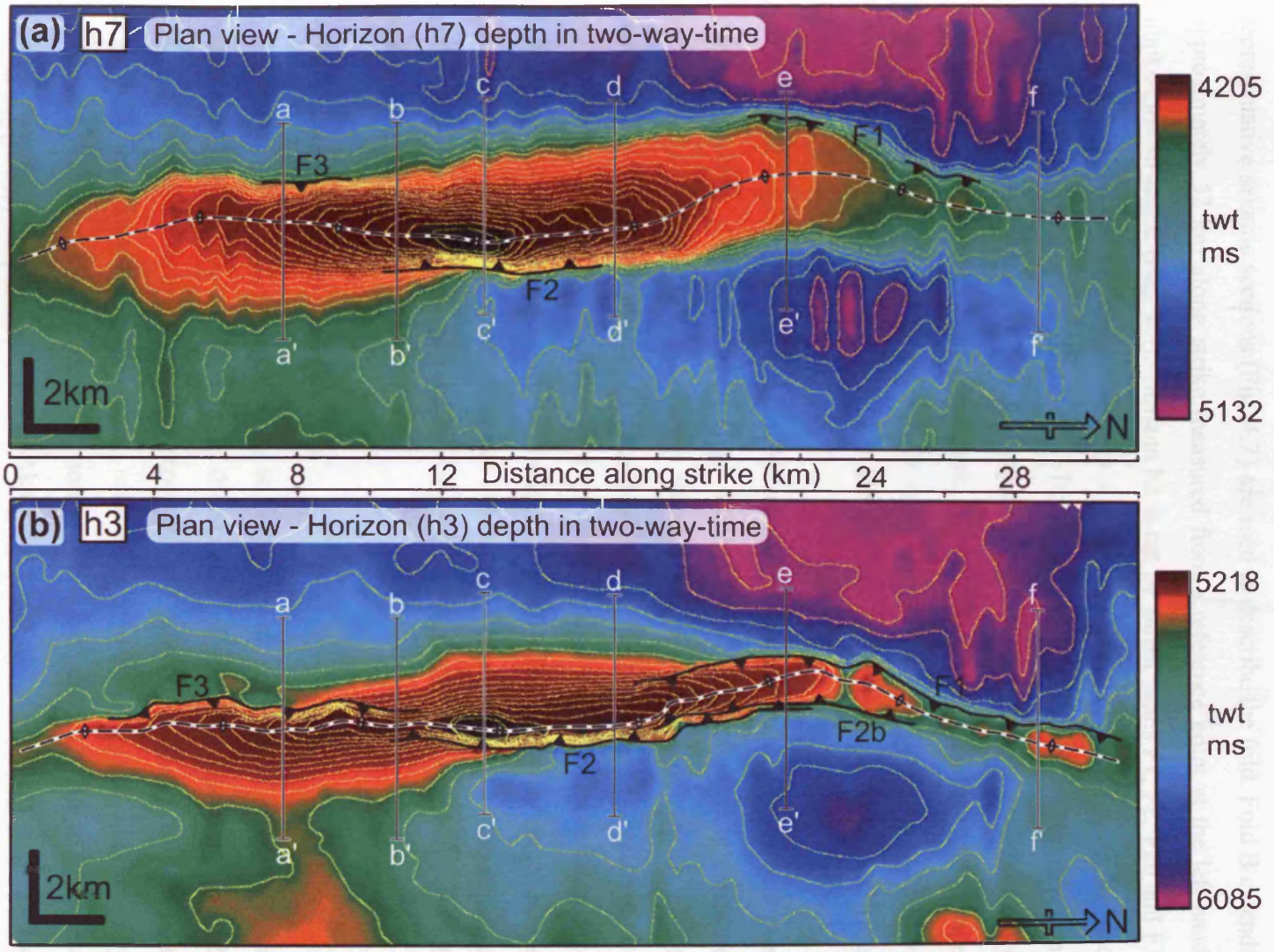

Figure 4.6: Fold B. Maps of horizon elevation in two-way-time (ms). **(a)** Horizon h7. **(b)** Horizon h3. Fault traces of the four major faults comprising Fold B are labeled F1, F2, F2b and F3. Fault traces denoted by black triangles in the hangingwalls. Note the changes in fold vergence along strike. Lines a-a' to f-f' show the locations of the six sections through Fold B presented in Figure 4.7. Red/orange colours: structural highs. Purple/blue: structural lows. Contour interval: 40 ms.

representative seismic sections (Fig. 4.7) are used to describe the fold. Fold B extends approximately 32 km along strike measured from a reference point at the left hand limit of the structure (Fig. 4.6). Horizon h3 is cut by thrust faults F1, F2, F2b and F3 along the majority of fold length (from 3 – 31 km along strike) whereas only isolated sections of h7 are offset (Fig. 4.6). Both horizons exhibit a single structural culmination at approximately 13 km along strike with the fold plunging symmetrically away from this point in both directions. Beyond 26 km along strike the plunge decreases and the fold changes strike by approximately 20°. A low amplitude, local structural culmination at around 29 km along strike is apparent on horizon h3 (Fig. 4.6b).

The fold vergence varies along strike resulting in an irregular fold shape in plan view, particularly at the level of h3 (Fig. 4.6b). This horizon has a strong westward vergence at the 8 km mark, but verges eastwards at the culmination at the 13 km position (Fig. 4.6). The transition of vergence corresponds to a zone of overlap of two major faults, the traces of which can be mapped along the base of the steep limbs. The fold is symmetrical at the centre of these zones. These changes in vergence are expressed in deflections of the hinge on horizon h7 (Fig. 4.6). This detailed fold geometry differs considerably from Fold A and is suggestive of more than one fault acting upon the fold.

4.6.2.2 Internal architecture of the fold

The changes in fold vergence along strike, observed on horizons h7 and h3, are related to the interaction and linkage of thrust faults of opposing dip (Higgins et al. 2007), and are illustrated further using representative seismic sections across the fold (Fig. 4.7). Evidently the distribution, orientation and intensity of faulting vary significantly along strike. Towards the southern end of the fold a single forethrust (F3), detaching close to the Agbada-Akata interface (h1), produces a westward verging hangingwall anticline in the overburden (Fig. 4.7a). Approximately 5.5 km to the north, the dominant fault is a backthrust (F2) that detaches within the Akata and carries a fold that verges to the east (Fig. 4.7c). Two smaller faults, F1 and F3, are imaged in the hangingwall and footwall respectively. Towards the northern end of the fold there is a low displacement, single forethrust (F1) with a low amplitude, westward verging fold in the overburden (Fig. 4.7f). These three faults (F1, F2 and

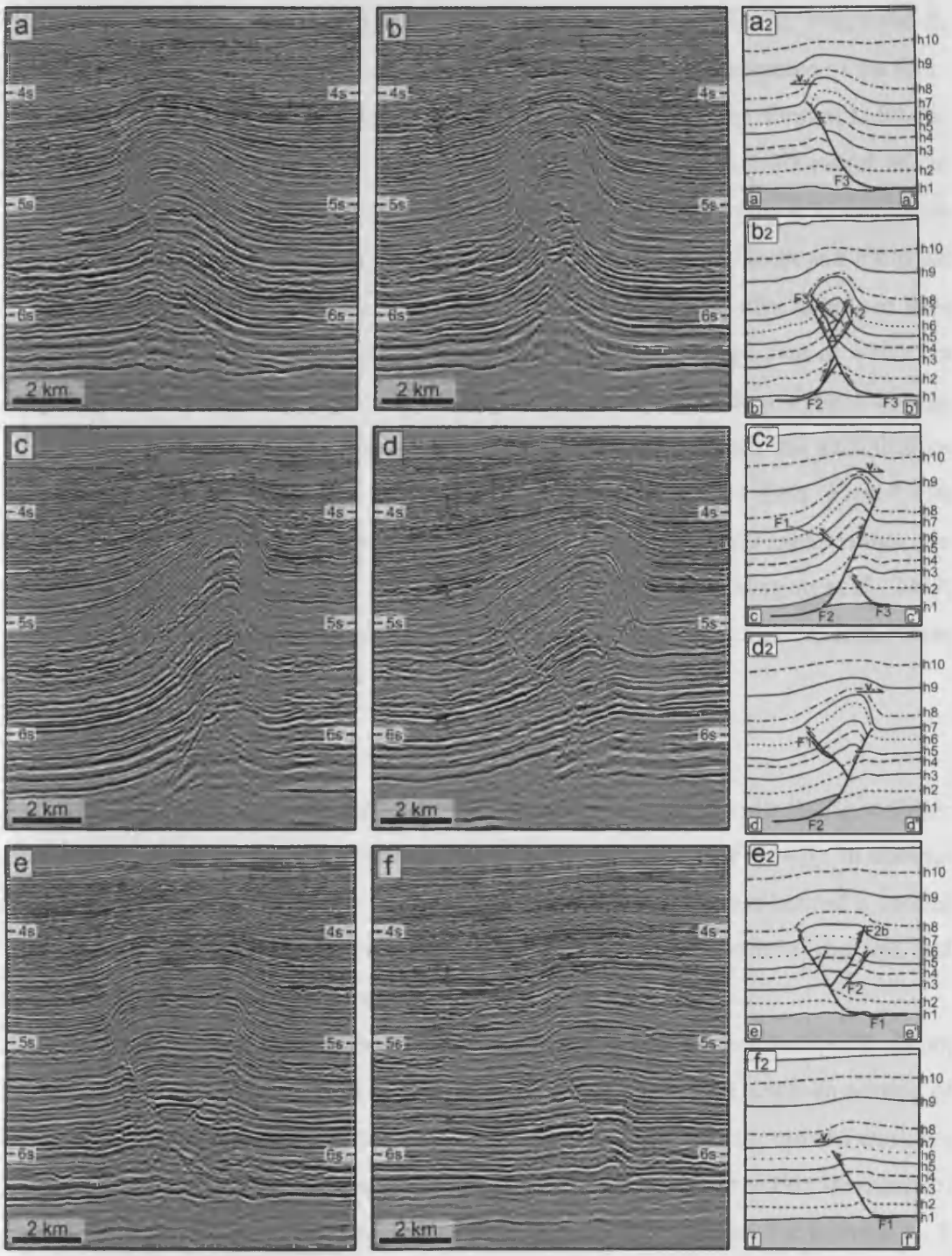

Figure 4.7: Fold B. Selected seismic sections perpendicular to fold strike illustrating change in fold vergence, fault geometry and dominance along strike. Locations of seismic lines is given in Figure 4.7. Each seismic section **(a-f)** is displayed along side a seismic interpretation (a2, b2, etc). F1, F2, F2b and F3 are major faults. h1 – h10 are regional stratigraphic horizons. v. indicates the direction of vergence of a fold.

F3) are the dominant structural features along the length of Fold B (Fig. 4.7a, c and f), accommodating the majority of displacement and controlling the vergence of the fold.

The transitions from one fault to another along strike are in the form of antithetic thrust fault linkages (Fig. 4.7b, d and e) (Higgins et al., 2007). A 3D model of the geometry of the fault planes is presented in Fig. 4.8. The backthrust (F2) dominates the central portion of the fold and links with forethrusts F1 to the north and F3 to the south. Higgins et al. (2007) used the vertical extent of faulting relative to branch lines of antithetic faults to describe three types of antithetic fault linkage, two of which are apparent within fold B (Figure 4.8). Faults F1 and F2 interact in a Type 1 linkage (Higgins et al., 2007) as they overlap exclusively above their branch line such that the lateral tip regions are located in the hangingwall of the counterpart fault (Figs. 4.7d/e and 4.8). Faults F2 and F3 form a complex cross-cutting relationship within the transfer zone indicative of Type 3 antithetic thrust fault linkages (Higgins et al., 2007) where fault planes continue above and below branch lines (Fig. 4.8), or branch points if viewed in section (Fig. 4.7b).

4.6.2.3 Individual fault heave profiles

Strike projection plots of the four main faults that comprise Fold B (Fig. 4.9) are much more complex than the simple profile of fault and fold A (Fig. 4.5). In contrast to smooth fault heave contours forming approximate semi-ellipses around a central maximum, profiles commonly have an irregular shape, exhibit several maxima and have lateral tips located some distance above the detachment.

For the most part, strike projections of the detaching thrusts within Fold B do not resemble an ideal semi-elliptical profile, with the exception of the southern portion of fault F3 (c. 0 - 5 km along strike) which displays smooth, evenly spaced contours (Fig. 4.9). The most dramatic disruptions to contour patterns occur within the zones of antithetic fault linkage. Lateral tip regions within the F2/F3 linkage, for instance (c. 8 – 14 km along strike), are downwards-tapering and faults display depressed tip lines that can be concave-up in shape (F3).

Fault F3 is the only fault within Fold B to reach a detachment along its entire length. Faults F1 and F2 interact in a Type 1 antithetic thrust fault linkage (Higgins et al., 2007) such that within the transfer zone, lower tiplines are not located in the zone of bed parallel shear within the detachment, but form a branch line with the

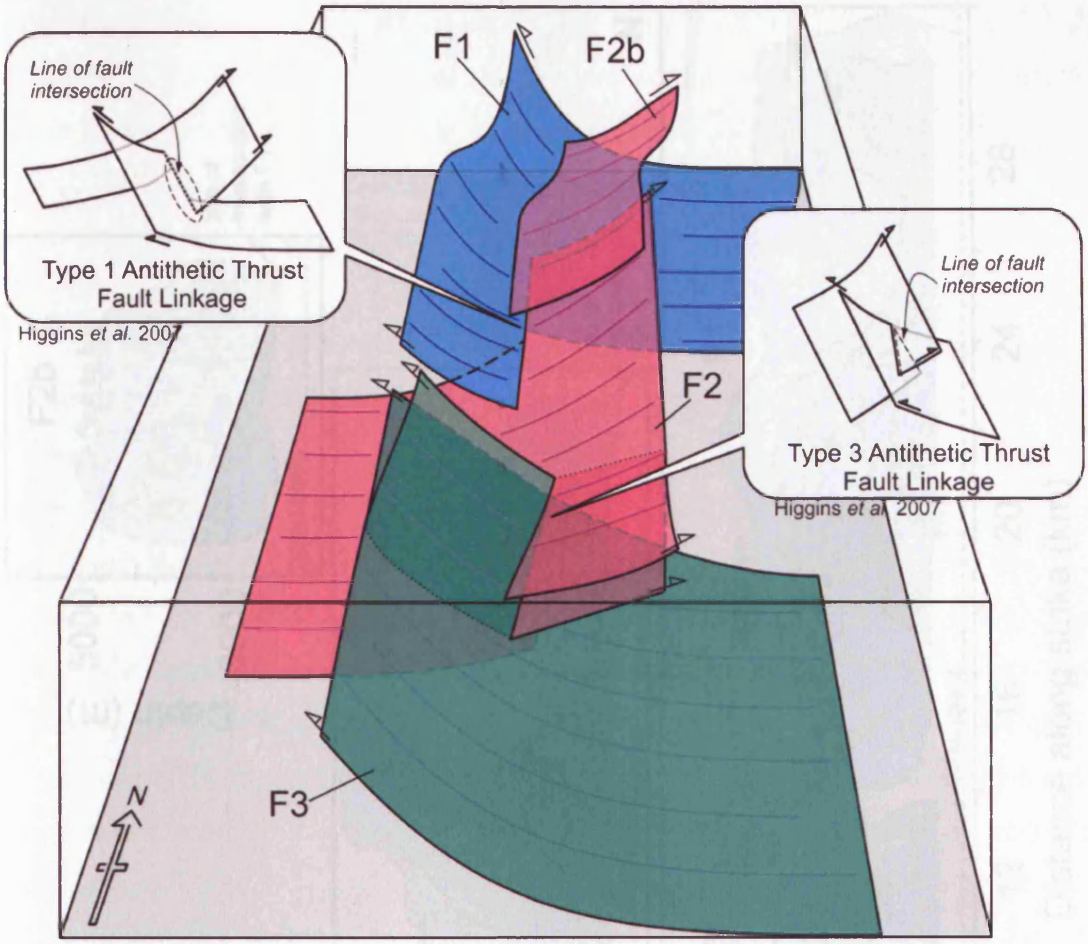

Figure 4.8: Three-dimensional conceptual diagram of antithetic fault geometries and linkages in Fold B. Faults F1 (blue), F2, F2b (pink) and F3 (green) detach on the grey surface. The Types of antithetic fault linkages taken from *Higgins et al. (2007)*. Faults F1 and F2 interact in a Type 1 linkage as fault surfaces overlap exclusively above the line of intersection or branch line. Faults F2 and F3 interact in a Type 3 linkage as both fault surfaces continue above and below the branch line resulting in cross-cutting relationships. Both these faults have cross-cut the other a number of times creating the inter-leaved geometry of a number of thrust surfaces.

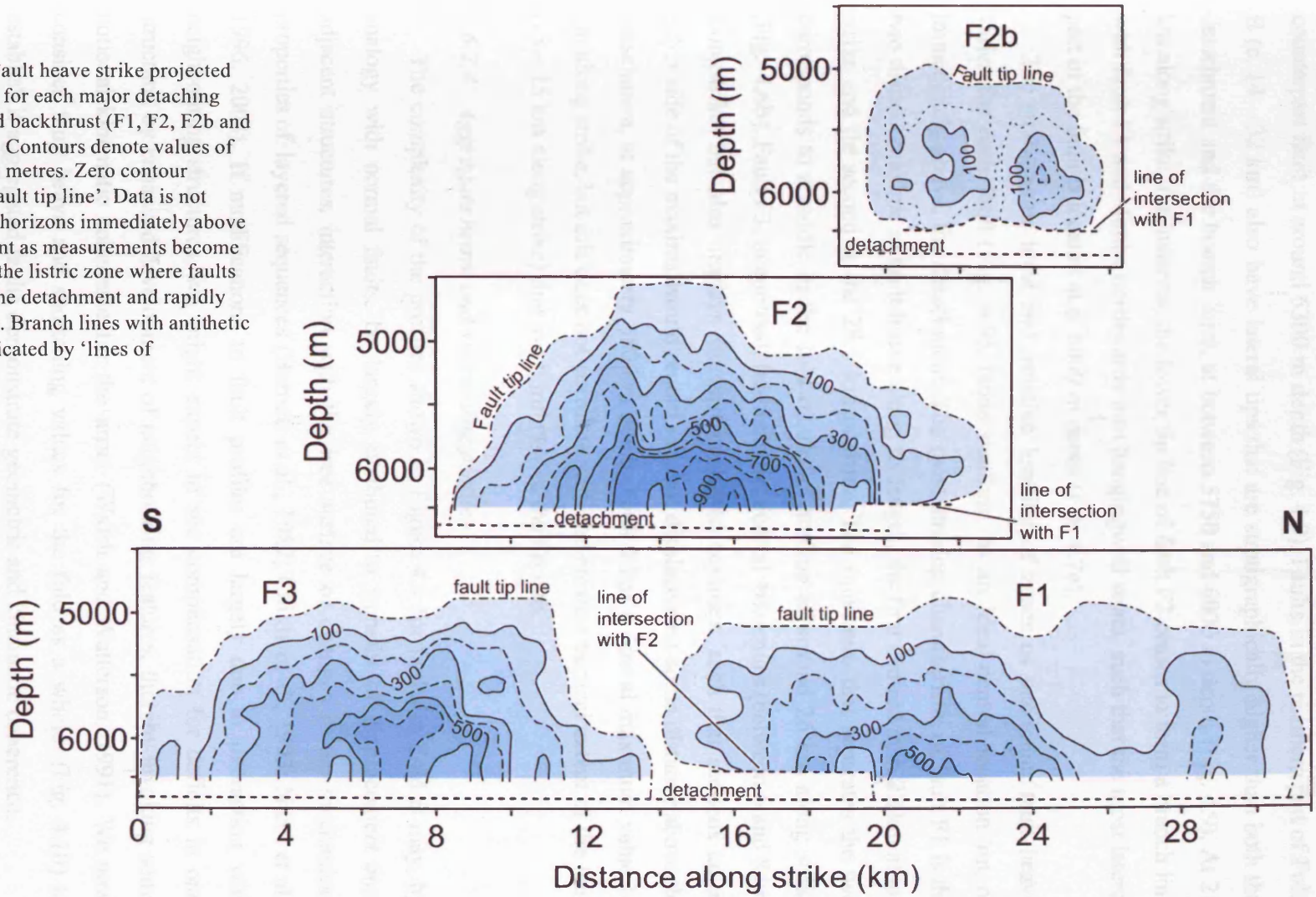

Figure 4.9: Fault heave strike projected contour plots for each major detaching forethrust and backthrust (F1, F2, F2b and F3) in fold B. Contours denote values of fault heave in metres. Zero contour labelled as 'fault tip line'. Data is not projected for horizons immediately above the detachment as measurements become unreliable in the listric zone where faults ramp out of the detachment and rapidly change in dip. Branch lines with antithetic faults are indicated by 'lines of intersection'.

counterpart fault at around 6300 m depth (Fig. 4.9). Faults in the northern part of Fold B (c. 14 – 32 km) also have lateral tips that are stratigraphically higher than both the detachment and the branch lines, at between 5750 and 6000 m depth (Fig. 4.9). At 21 km along strike, for instance, the lower tip line of fault F2 ceases to form a branch line with fault F1 and climbs northwards into hangingwall strata, such that the most lateral part of the fault is located at c. 6000 m depth (Fig. 4.7e).

The stratigraphic level and relative location of zones of maximum fault heave varies for each fault (Fig. 4.9). None conform to an ideal central location on, or immediately above, the detachment. The most striking characteristic of fault F1 is the two distinct maxima in fault heave along its length, the first centred at c. 22 km along strike and the second at the 28.5 km position. The minimum that separates the two corresponds to a saddle in the fold of the h3 horizon at around 26 km along strike (Fig. 4.6b). Fault F3, in contrast, has a single, central maximum (between 6 and 8 km alongstrike) but also displays mushroom-shaped contours, such that sections taken either side of the maxima would record greatest displacement some distance above the detachment, at approximately 5800 m depth. Fault 2 has a central maximum value 16 km along strike, but this does not correlate with the greatest vertical extent of the fault (13 – 15 km along strike) due to asymmetry of the tip line.

4.6.2.4 Aggregate heave and shortening profiles

The complexity of the profiles shown in Figure 4.9 for faults in Fold B may, by analogy with normal faults, be largely attributed to transfer of displacement onto adjacent structures, interaction with the free surface or changes in the mechanical properties of layered sequences (Barnett et al., 1987; Childs et al., 1993; Nicol et al., 1996; 2003). If modifications to fault profiles are largely due to interaction with neighbouring structures, we might expect to see compensation for deficits in one structure, by enhanced development of neighbouring features, thereby invoking some notional kinematic coherence for the array (Walsh and Watterson, 1991). We now consider fault heave and shortening values for the fold as a whole (Fig. 4.10) to establish if aggregated faults demonstrate geometric and kinematic coherence.

The northern end of the fold (13 – 32 km along strike), involving the aggregation of faults F1, F2 and F2b (Fig. 4.10d), is characterised by a smooth summed d/L profile and aggregate strike projection. The smooth form of the summed d/L profile

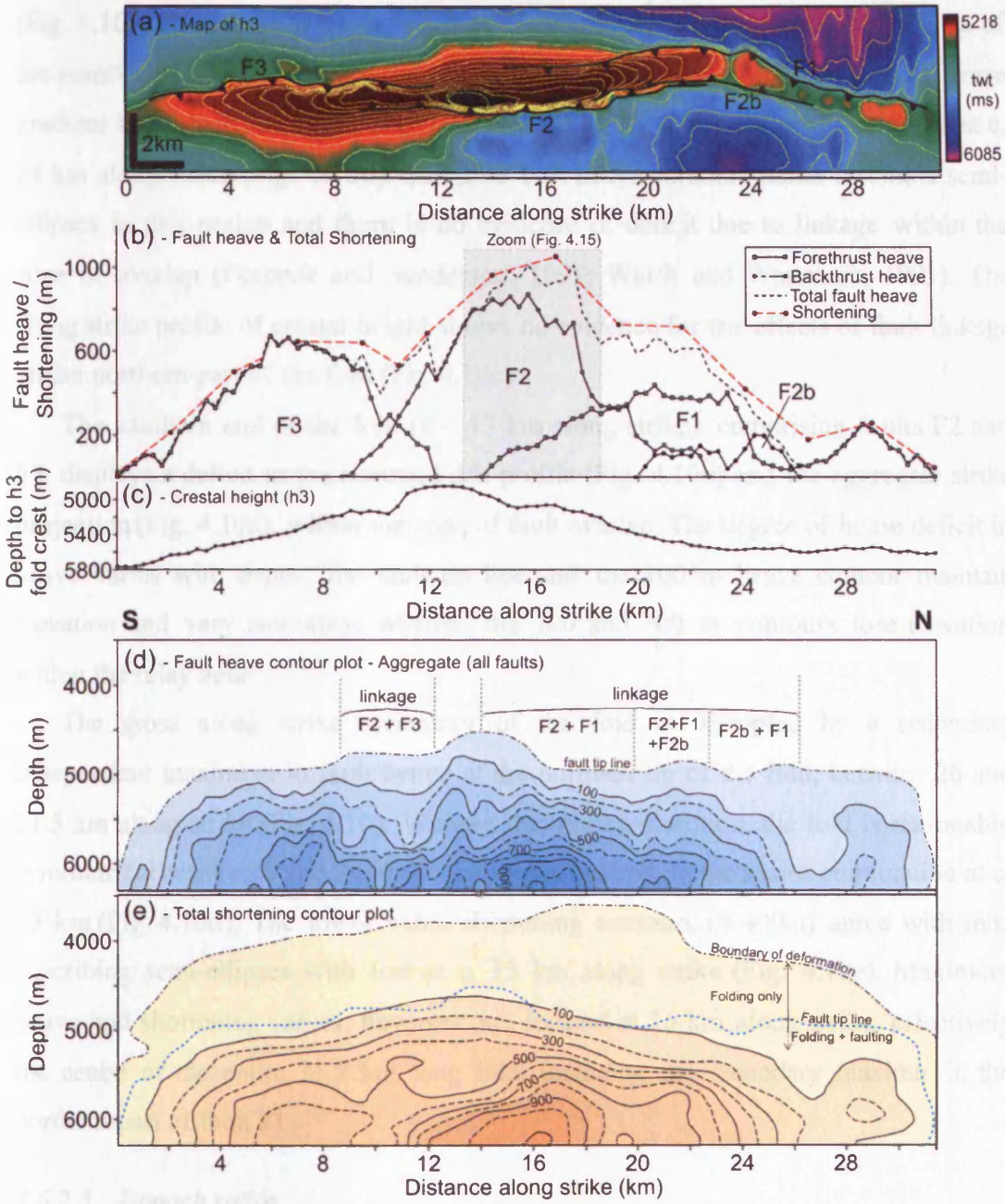

Figure 4.10: Fold B. Aggregate values of fault heave and shortening. **(a)** Map of h3 horizon in two-way-time with fault traces. Fold is aligned with the graphs and contour plots below. Contour interval: 40 ms **(b)** Heave-distance profiles for each individual fault measured on h3. Dashed line: Aggregate heave-distance profile summed on h3. Dashed red line: Bulk shortening of horizon h3. **(c)** Depth to fold crest for horizon h3 in metres. **(d)** Aggregate fault heave strike projected contour plot of Fold B. Lateral overlap of faults F1, F2, F2b and F3 indicated in linkage bracket. **(e)** Total shortening strike projected contour plot. Blue dashed line indicates the location of the aggregate heave fault tip line from **(d)**. Note semi-elliptical contours.

(Fig. 4.10b) is inferred to be the product of complimentary displacement gradients of the constituent faults. This is exemplified by corresponding, abrupt changes in heave gradient between F2 and F2b at c. 20 km along strike, and between F1 and F2b at c. 24 km along strike (Fig. 4.10b). Summed fault heave contours better resemble semi-ellipses in this region and there is no evidence of deficit due to linkage within the zone of overlap (Peacock and Sanderson, 1991; Walsh and Watterson, 1991). The along strike profile of crestal height shows no evidence for the effects of fault linkage on the northern part of the fold (Fig. 4.10c).

The southern end of the fold (0 – 13 km along strike), comprising faults F2 and F3, displays a deficit in the summed d/L profile (Fig. 4.10b) and the aggregate strike projection (Fig. 4.10d), within the zone of fault overlap. The degree of heave deficit in heave varies with depth. The fault tip line and the 100 m heave contour maintain elevation and vary smoothly, whereas the 200 and 300 m contours lose elevation within the relay zone.

The gross along strike symmetry of the fold is disrupted by a secondary independent maximum in fault heave at the northern tip of the fold, between 26 and 31.5 km along strike (Fig. 4.10). Without this northern section, the fold is reasonably symmetrical between 0 and 26 km along strike, centred on the major culmination at c. 13 km (Fig 4.10d). The lower value shortening contours (0-400m) agree with this, describing semi-ellipses with foci at c. 13 km along strike (Fig. 4.10e). Maximum heave and shortening values, however, are located at 16 km along strike, effectively the centre of the entire 31.5 km long fold, including the secondary maxima in the northern part of fault F1.

4.6.2.5 Isopach ratios

Analysis of isopach ratios of the biostratigraphically defined units h1-11 suggests the sedimentary sequence of fold B can be separated into syn-kinematic and pre-kinematic packages delineated approximately by the h4 horizon. Pre-kinematic sediments within the Agbada Formation, h1 – h4, display uniform orthogonal thickness across all parts of the fault and fold. The syn-kinematic package, separated into four units using key seismic horizons, demonstrates systematic variations in the isopach ratios along strike (Fig. 4.11a).

It is intuitive to expect the along strike trend of the amount of fold growth to

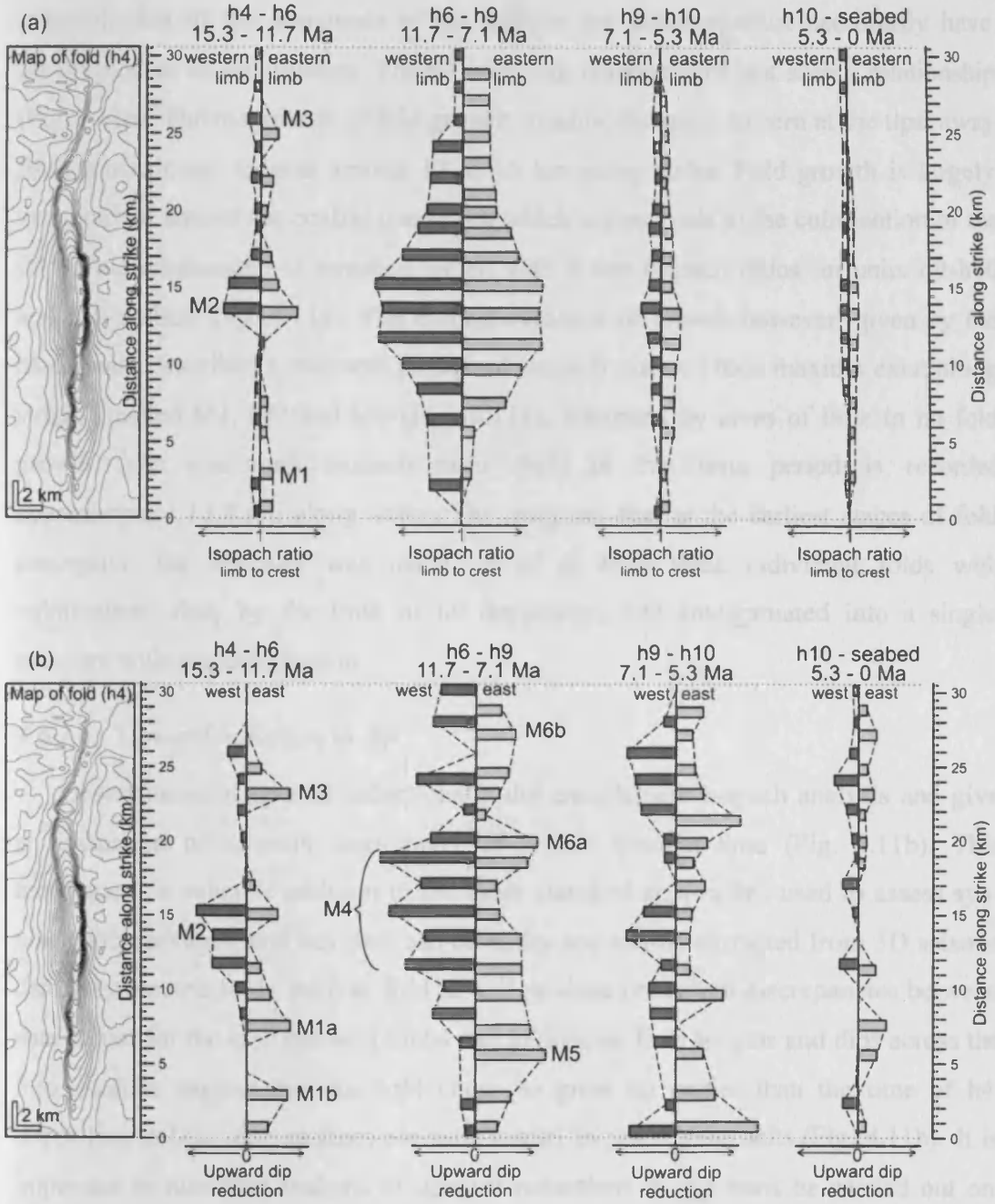

Figure 4.11: Fold B. Analysis of distribution and spatial extent syn-sedimentary units within the stratigraphic column. **(a)** Isopach ratios (comparing orthogonal thickness of sediments on the limbs of a fold to those on the crest). Calculated for 17 vertical profiles along length of the fold and displayed as bar charts. Ratio of 1 = no growth. Large bar = significant fold growth. Small bar = minor fold growth. Presented with reference to four time periods, delineated by horizons h4-h6, h6-h9, h9-h10 and h10-seabed. M1, M2 and M3 indicate three areas of high isopach ratio separated by low ratios in the h4-h6 unit. **(b)** Values for Upward Reductions in Dip. Presentation of results is as in (a). Note asymmetry of the plot due to differing value of upward reductions in dip on each limb. M1a, M1b, M2 and M3 indicate similar areas of early fold growth in the h4-h6 unit as in (a). M4, M5, M6a and M6b indicate similar local areas of growth in the h6-h9 unit.

resemble that of the amplitude of the fold, as the structure must necessarily have grown most at its culmination. The h6 – h9 unit demonstrates just such a relationship (Fig. 4.11a). The magnitude of fold growth steadily decreases to zero at the tips, away from a maximum located around 12 to 15 km along strike. Fold growth is largely symmetrical around the central maximum which corresponds to the culmination of the fold. This relationship is repeated, albeit with lower isopach ratios, in units h9-h10 and h10-seabed (Fig. 4.11a). The earliest evidence of growth however, given by the h4-h6 unit, describes a different pattern of isopach ratios. Three maxima exist along strike, labelled M1, M2 and M3 (Fig. 4.11a), separated by areas of little to no fold growth. The maximum isopach ratio (M2) in this time period is recorded approximately 13.5 km along strike. This suggests that at the earliest stages of fold conception the structure was made up of at least three individual folds with culminations that, by the time of h6 deposition, had amalgamated into a single structure with one culmination.

4.6.2.6 Upward reduction in dip

Observations of upward reductions in dip complement isopach analysis and give an indication of downdip asymmetry of a fold through time (Fig. 4.11b). This technique is a valuable addition to the more standard approaches used to assess syn-kinematic packages, and key data can be easily and swiftly extracted from 3D seismic data. Asymmetric folds, such as fold B, will produce consistent discrepancies between data values for the east and west limbs due to unequal limb lengths and dips across the fold. Results suggest that the fold began to grow no earlier than the time of h4 deposition as bounding surfaces are sub-parallel in underlying units (Fig. 4.11b). It is important to note that analysis of upward reductions in dip must be carried out on depth converted surfaces and horizons. Thickness changes on seismic time sections, such as in Figure 4.7, may not reflect true growth stratal geometries.

Important variations can be discerned along strike for each interval. The three most recent time periods (h6-h9, h9-h10 and h10-seabed) all show the fold to be active along its entire length, however the along strike trends in magnitude of the values do not match those of the isopach analysis (Fig. 4.11b). Several maxima occur in all time periods, as opposed to one central high, and are interpreted as reflecting local growth of numerous faults of opposing dip, within a single coherent fold producing structural asymmetry. In unit h6-h9, for example, the western limb is

characterised by a broad zone of relatively high upward dip reduction values (labelled M4, Fig. 4.11b) at the centre of the fold, between 12 and 18 km along strike. This corresponds to the portion of the present day fold that has a dominant eastward vergence and incorporates the area of maximum heave of backthrust F2 (Fig. 4.9). The eastern limb, on the other hand, displays three distinct regions of increased dip reduction values centred at approximately 6, 20 and 28 km along strike, labelled M5, M6a and M6b respectively (Fig. 4.11b). M5 corresponds closely with the zone of maximum heave of forethrust F3 at 6 to 8 km along strike (Fig. 4.9). M6a and M6b are coincident with the two displacement maxima of forethrust F1; the first located between 20 and 22 km and the second at just over 28 km along strike (Fig. 4.9).

4.7 Discussion

An isolated fold comprising numerous thrust faults is an excellent example to consider how faults and folds coalesce and link along strike to form larger, through-going structures. The range of geometric relationships within the linkage zones of both synthetic and antithetic faults of Fold B (Fig. 4.8) point to a complex and fascinating growth history. One of the most interesting aspects of this study surrounds the kinematic relationship between constituent features and the response of fold strain to variations in the magnitude of faulting along the length of the fold. Questions we need to consider include; were thrusts faults active in the earliest phases of deformation and at what point did hard linkage occur? On the evidence presented here, we put forward a model of growth of a single fold where at least eight spatially distinct thrust faults nucleated along the length of three early folds.

4.7.1 Fold growth by segment linkage

Examination of the earliest periods of fold development (Fig. 4.11) indicates that Fold B was initially made up of at least three structural culminations separated along strike by saddles or areas of limited fold growth (Fig. 4.11). The locations of early saddle points are consistent with the sites of present day transfer zones between the major faults. The positions of early folds correspond to regions of strong fold vergence, where one of the three major faults (F1, F2, F3) now dominate the accommodation of shortening. Upward dip reduction values also suggest that these early folds quickly developed down-dip asymmetry. It is not possible to determine

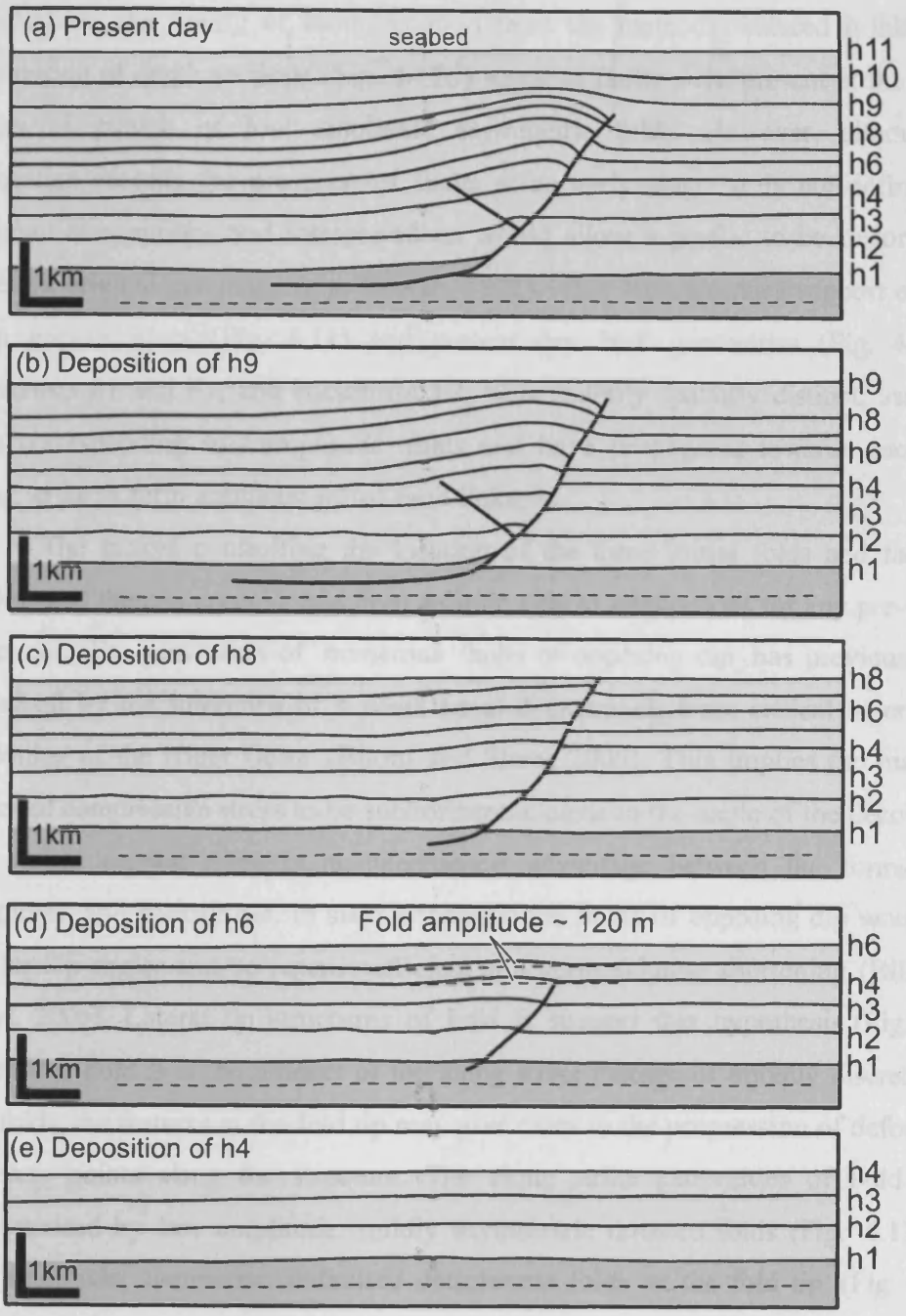

Figure 4.12: Sequential restoration of depth-converted seismic profile through Fold B showing different stages of structural evolution. Depth conversion used vertical ray paths and interval velocities obtained from a nearby confidential exploration well. Restoration was carried out in 2DMove™ software from Midland Valley Exploration. Restoration was performed using *flexural slip unfold* and *Trishear* algorithms. Limitations, assumptions and errors induced by these methods are discussed in Chapter 6. No vertical exaggeration.

conclusively the timing of fault initiation from the methods featured in this paper. Restoration of depth sections (Fig. 4.12d) suggests faults were present at the earliest stages of growth of low amplitude asymmetric folds. However, although the restoration records the presence of faults at an early stage, it is not definitive as different assumptions and interpretations would allow a profile to be restored to a different original geometry (e.g. Rowan, 1997). This scenario does support evidence from growth strata (Fig. 4.11) and present day fault geometries (Fig. 4.8) that forethrusts F1 and F3, and backthrust F2, were initially spatially distinct, associated with corresponding low amplitude folds and have propagated towards each other along strike to form antithetic thrust fault linkages.

The factors controlling the location of the three initial folds and faults are unclear and there is no evidence from seismic data or restorations for any pre-existing structures. The generation of numerous faults of opposing dip has previously been explained by the inference of a weak basal detachment, from critical taper wedge modelling of the Niger Delta (Bilotti and Shaw, 2005). This implies the maximum principal compressive stress to be subhorizontal, close to the angle of the decollement, and would suggest there is no mechanical advantage between the formation of forethrusts and backthrusts. In such a scenario the faults of opposing dip would have similar dip angles and be equally efficient at accommodating shortening (Bilotti and Shaw, 2005). Lateral tip structures of Fold B support this hypothesis (Fig. 4.13). Given that Fold B is the product of the along strike linkage of initially discrete faults and folds, the features at the fold tip may give clues to the progression of deformation at many points along the structure. The along strike extremities of Fold B are characterised by low amplitude, mildly asymmetric thrusted folds (Fig. 4.13a) and low amplitude, symmetric, unfaulted detachment folds at the fold tip (Fig. 4.13b). This is of particular interest as both a forethrust and a backthrust, of approximately equal displacement (Fig. 4.13a), have nucleated in, or propagated into, a low amplitude fold (Fig. 4.13a and b). It is likely that subsequent growth would lead to one orientation of fault gaining dominance resulting in increased fold asymmetry.

Fault interactions in fold B are not exclusively antithetic however. Antithetic linkages are easily identified by the observation of a change in fold vergence, the overlap of fault traces in map view and of faults of opposing dip converging on a point in section. Synthetic linkages are less apparent as originally distinct fault planes

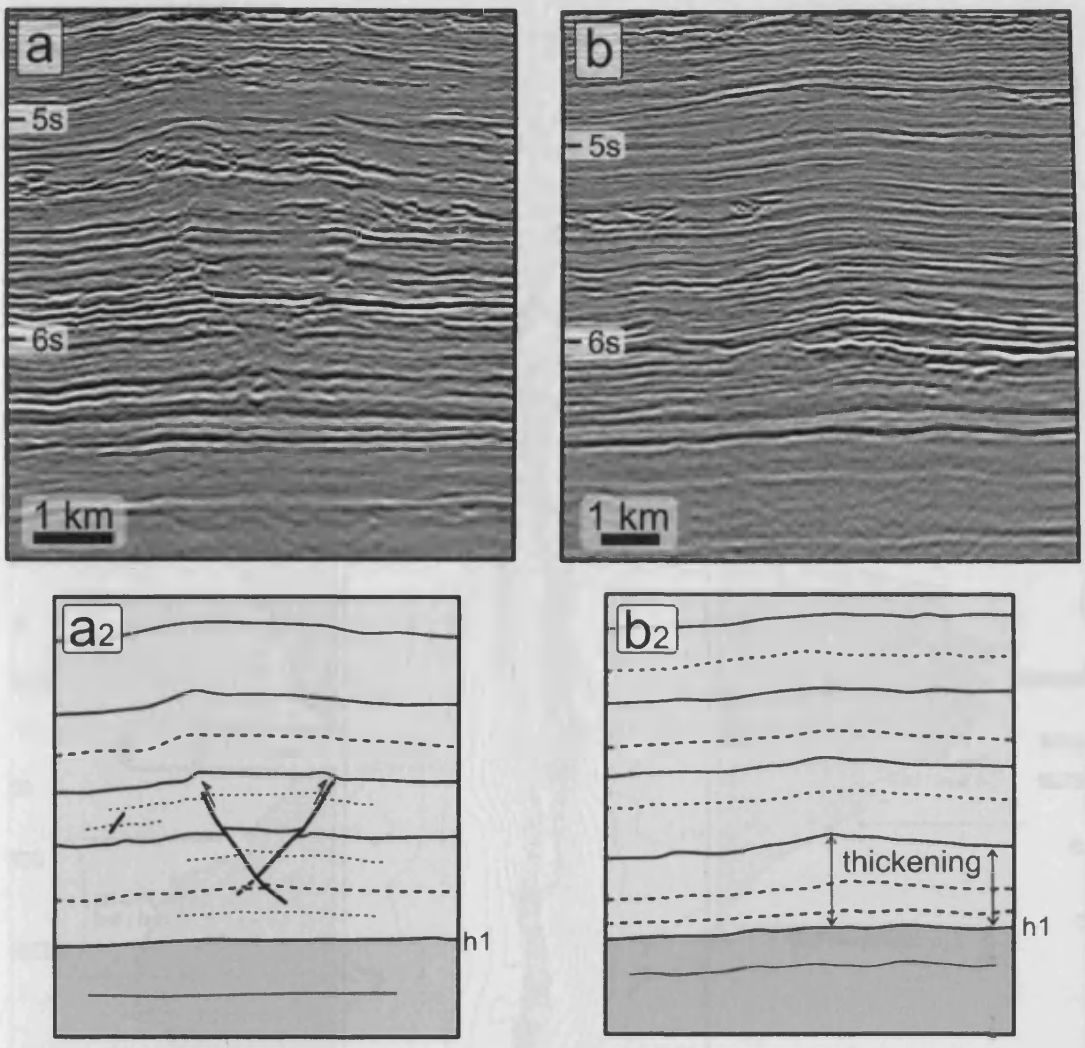

Figure 4.13: Two seismic sections showing examples of lateral tip structures in Fold B. **(a)** shows a low amplitude, mildly asymmetric thrusted fold. Two faults of opposing dip cut the section (a forethrust and a backthrust) and have approximately equal displacement. Neither fault reaches the detachment. Maximum displacement on both faults is around the level of the h3 horizon. **(b)** low amplitude symmetric, unfaulted detachment fold. Interpretations of each section is given in **(a2)** and **(b2)**. Seismic section (a) is closer to the lateral tip of the fold than section (b).

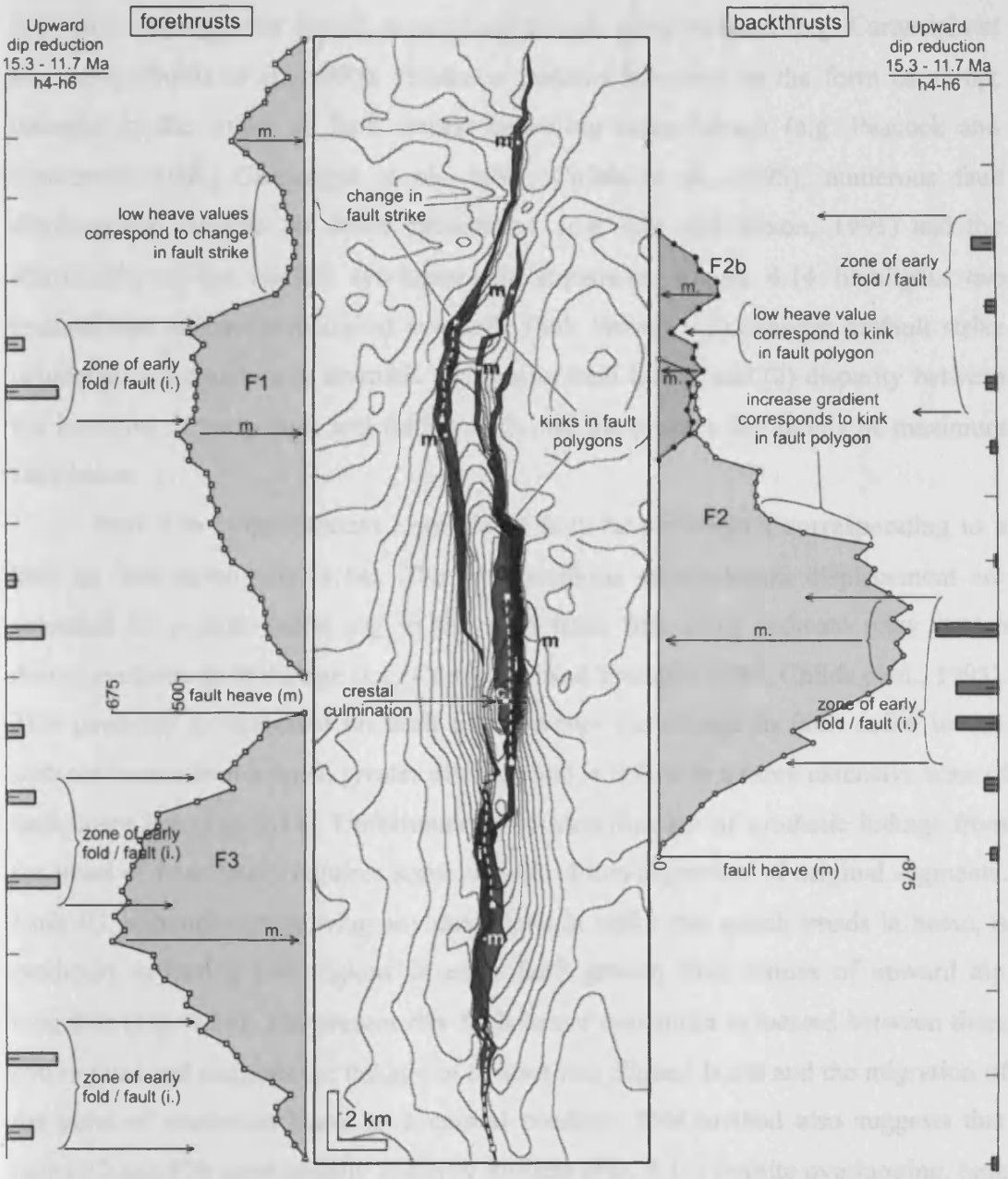

Figure 4.14: Fold B. Correlation of the location of early fold culminations (as indicated by Upward Dip Reductions) with present day locations of maximum fault heave. Figure also contrasts areas of abrupt gradient change on heave-distance plots (shaded graphs) with changes in strike of fault traces (given by shaded fault polygons on map). Upward dip reductions for h4-h6 time period given as bars. Fault heave-distance profiles (F1, F2, F2b and F3) given as shaded line graphs. m.: point of maximum fault heave along length of fault trace. i.: area of early fold growth (dashed white lines). c.: location of crestal culmination. Contours on map describe topography of horizon h3 (see Fig. 4.6).

may have subsequently joined to produce though going surfaces (e.g. Cartwright et al., 1995; Childs et al., 1995). Evidence remains however, in the form of abrupt changes in the strike of fault traces indicating relay breach (e.g. Peacock and Sanderson, 1991; Cartwright et al., 1995; Childs et al., 1995), numerous fault displacement maxima on strike projections (e.g. Liu and Dixon, 1991) and the distribution of the earliest syn-kinematic sequences. Figure 4.14 highlights two features that are symptomatic of synthetic fault linkage: (1) changes in fault strike coinciding with minima or dramatic changes in fault heave, and (2) disparity between the locations of early fault and fold growth and the present day points of maximum fault heave.

Fault F2b is the clearest example of fault heave minima corresponding to a kink in fault strike (Fig. 4.14). The two positions of maximum displacement are separated by a right-lateral jog in the fault trace that could indicate relay breach during synthetic fault linkage (e.g. Cartwright and Trudgill, 1994; Childs et al., 1995). This geometry is replicated on fault F1, however the change in fault strike in this instance occurs over a much greater distance and is linked to a more extensive zone of fault heave low (Fig. 4.14). Unfortunately the identification of synthetic linkage from the trend of fault traces requires some degree of non-alignment of original segments. Fault F3, although not showing any deviations in strike that match trends in heave, is predicted as having two regions of early fault growth from values of upward dip reduction (Fig. 4.14). The present day fault heave maximum is located between these two regions and suggests the linkage of at least two aligned faults and the migration of the point of maximum heave to a central position. This method also suggests that faults F2 and F2b were initially spatially discrete (Fig. 4.14) despite overlapping, both along strike and down dip, at present. In this case then, the lateral propagation of similarly dipping, collinear thrusts has not lead to hard linkage and has resulted in a relay structure similar to that of a relay ramp in extensional studies (e.g. Peacock and Sanderson, 1991; Cartwright and Trudgill, 1994; 1994).

4.7.2 Displacement transfer

Bulk shortening contours on strike projections of both fold A, comprising a single fault (Fig. 4.5g), and fold B, made up of numerous linking faults (Fig. 4.10e), have orderly patterns and regular spacing. Recent deformation along the length of fold B

has been accommodated in a manner similar to that of a single structure (fold A), and would therefore imply kinematic interaction and the efficient transfer of displacement between constituent faults, through 'transfer zones' (Dahlstrom, 1970). The criteria for kinematic interaction include complementary modifications to fault displacement patterns from a reference standard (Barnett et al., 1987; Walsh and Watterson, 1991) and the observation of relay structures that indicate displacement transfer (Muraoka and Kamata, 1983; Larsen, 1988; Huggins et al., 1995). Each of the three major faults (F1, F2, F3) within fold B show an increased irregularity of heave contours (Fig. 4.9) compared to the single fault plane of fold A (Fig. 4.5f). This is most apparent in the abrupt changes to d/L gradients (Fig. 4.10b) that can define the limits of a relay zone (e.g. Peacock and Sanderson, 1991) and in the trend of fault tip lines away from elliptical profiles in zones of linkage. Displacement appears to have been transferred smoothly between faults F1 and F2 in the northern half of fold B (Fig. 4.10a) leading to little evidence of linkage on the aggregate fault heave profile (Fig. 4.10d). The relay zone between faults F2 and F3, in contrast, produces an area of fault heave deficit when aggregated. It has been suggested that the nature of displacement distributions in relay zones may be informative of the original kinematic relationship of the linking faults (e.g. Nicol et al., 2002; Walsh et al., 2003). Faults that have been kinematically linked since inception have a summed displacement profile resembling that of a single, isolated fault, with no deficit in the relay zone (e.g. Nicol et al., 2002; Walsh et al., 2003). Initially isolated faults, which subsequently interact through accidental linkage (e.g. Peacock and Sanderson, 1991; Cartwright et al., 1995; Dawers and Anders, 1995), are thought to maintain distinct displacement maxima on the adjacent fault segments, separated by a deficit in the relay zone. This rationale would advocate different kinematic histories for the F1/F2 and F2/F3 fault linkages in fold B, a conclusion not support by our data. The comparison of bulk shortening with aggregate fault heave indicates that the deficit in discontinuous deformation (i.e. faulting) around the transfer zone of fault F2/F3 is compensated for by a rise in continuous displacements (Peacock and Sanderson, 1991; Dawers and Anders, 1995; Nicol et al., 2002; Davis et al., 2005), such as folding, as shown by the increased regularity of shortening contours (Fig. 4.10e). The shortening profile of fold B therefore resembles that of a single fault and fold (Fig. 4.5g) and suggests that its components have been spatially and mechanically related since inception (Walsh et al., 2003).

An alternative hypothesis is that the deficit observed within the F2/F3 linkage may be related to the mode of linkage rather than the kinematic history of the interaction. Davis et al. (2005) observed a positive relationship between the length of along strike fault overlap and the efficiency of displacement transfer. The lesser length of fault overlap in the F2/F3 example, the steeper gradients of heave profiles and the heave deficit within the transfer zone all suggest a retardation of lateral propagation rates during linkage (e.g. Peacock and Sanderson, 1991; Nicol et al., 1996) resulting in increased fold strain.

4.7.3 Fault related folding

The relative importance of faulting and folding in accommodating shortening was documented as varying through time during centrifuge modeling of a fold and thrust belt (Liu and Dixon, 1991). Displacement was transferred between folding and faulting along strike and between en-echelon fault pairs within transfer zones. Other studies have shown that, in contrast to some established models of fault-related folding in which fault slip accumulation directly relates to fold magnitude (e.g. Suppe and Medwedeff, 1990), displacement deficits within transfer zones are compensated for by an increase in fold strain (Nicol et al., 2002; Davis et al., 2005). A similar result is recorded in this study as bulk shortening strike-projections display more regular and smooth contour patterns than that of aggregated fault heave (Figs. 4.5 and 4.10). This would suggest that significant variation in the amount of folding along strike is needed to compensate for fluctuations in the magnitude of fault heave. This effect is due, in part, to a lower sample density in the generation of shortening values which may reduce the irregularity of contours. There is also, however, evidence from seismic data to suggest that the amount of folding is not consistent along strike. To demonstrate this, two seismic sections across fold B are compared (Fig. 4.15) with reference to measurements made on the h3 horizon.

Both seismic lines are taken from the southern end of the F1/F2 linkage zone. An enlarged portion of the d/L profile of faults in fold B (Fig. 4.10b) is included in Figure 4.15e to highlight the areas where perturbations in fault heave result in small deficits below idealised fault profiles. The aggregate value of fault heave is similar in each section although the amount of heave accommodated by each of the component

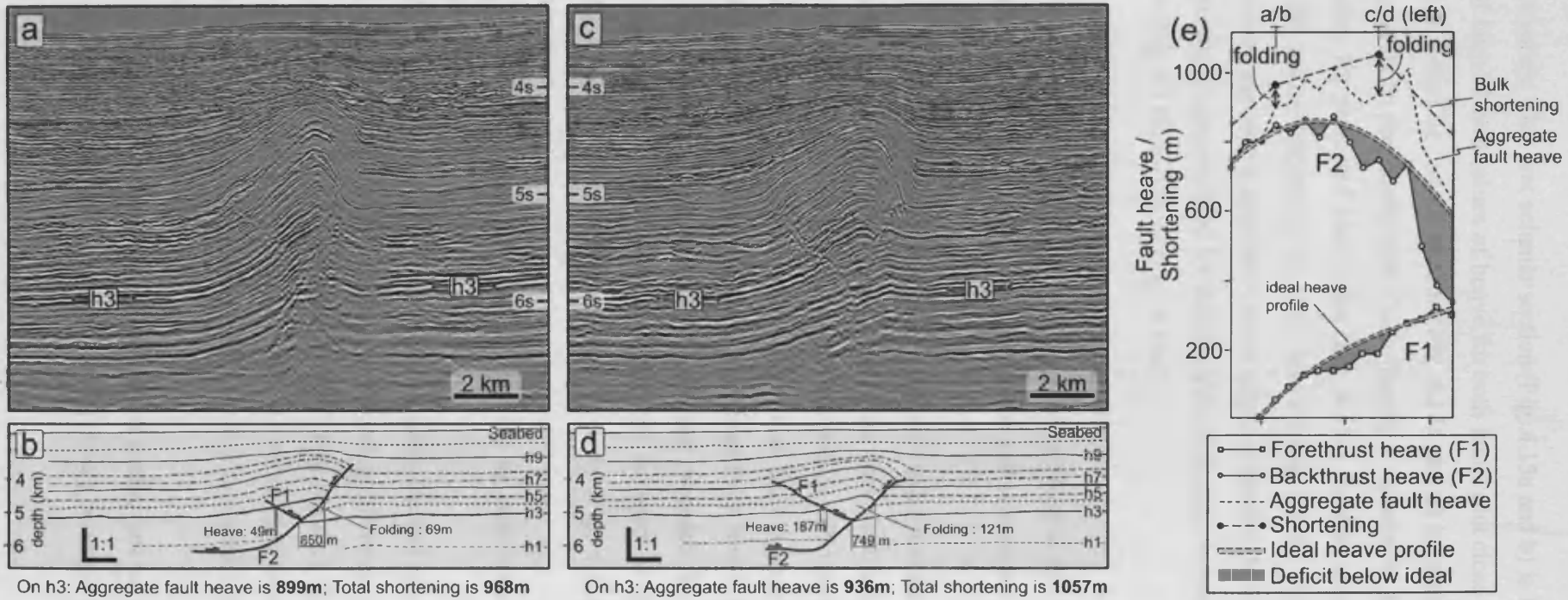

Figure 4.15: Fold B. Comparison of two seismic sections to demonstrate changes in the magnitude of folding along strike. Analysis of strain made with respect to horizon h3. **(a)** and **(c):** seismic sections in two-way travel time. h3 horizon labeled. **(b)** and **(d)** depth converted cross-sections of **(a)** and **(c)** displayed at 1:1. F1, F2 indicate main faults. Values of heave are indicated for the h3 horizon. **(e)** Enlarged portion of the distance-heave profile of Figure 4.10b. Shaded areas indicate deficit in fault heave of faults F1 and F2 below ideal profiles. Note the difference between aggregate fault heave and bulk shortening varies along strike. Locations of section **(a)** to **(d)** indicated on the graph.

faults varies. The first seismic section (Fig. 4.15a and b) is located close to the lateral tip of fault F1 and values of heave for both faults plot close to the ideal heave profiles (Fig. 4.15e). The second section (Fig. 4.15c and d) is located approximately 2.4 km along strike to the north. Here faults display a cumulative heave deficit of around 10 % below the predicted ideal value (Fig. 4.15e). Folding compensates, to some extent, for the minor variations in fault heave along strike such that measurements of shortening produce a smoother, more elliptical profile. In this example the amount of shortening accommodated by folding almost doubles between the two sections, from 69 m (Fig. 4.15b) to 121 m (Fig. 4.15d).

4.8 A structural evolution model of fold B

An evolutionary model of a single, isolated fold in the deep water Niger Delta is proposed based on the analysis of structural and sedimentary features associated with fold B (Fig. 4.16).

(1) Detachment folds initiate with individual structural culminations and grow towards each other along strike. Numerous faults nucleate as both forethrusts and backthrusts along the length of the low amplitude anticlines (Fig. 4.16a). The model proposed by Dixon & Liu (1991) states that fault linkage follows the along strike propagation and merger of collinear, periclinal folds however there is little conclusive data in this study to determine if folding preceded faulting or vice-versa. The distribution of syn-kinematic sediments can be used to show that the along strike length of fold B was established relatively early (Fig. 4.16a), albeit as three separate culminations.

(2) Folds coalesce along strike resulting in culmination migration to a central, single apex.

(3) Lateral fault propagation produces synthetic and antithetic thrust fault linkages (Fig. 4.16b and c). Initial offset by a propagating tip commonly occurs above the level of the detachment (Figs. 4.9 and 4.13a) This requires the point of maximum fault heave to subsequently move downwards, to either the level of the detachment or the point of intersection with another fault in order to produce the profiles seen along the majority of the faults' lengths.

(4) Fold B accommodates shortening as a coherent unit, producing displacement and shortening profiles similar to that comprising a single fault (fold A) suggesting

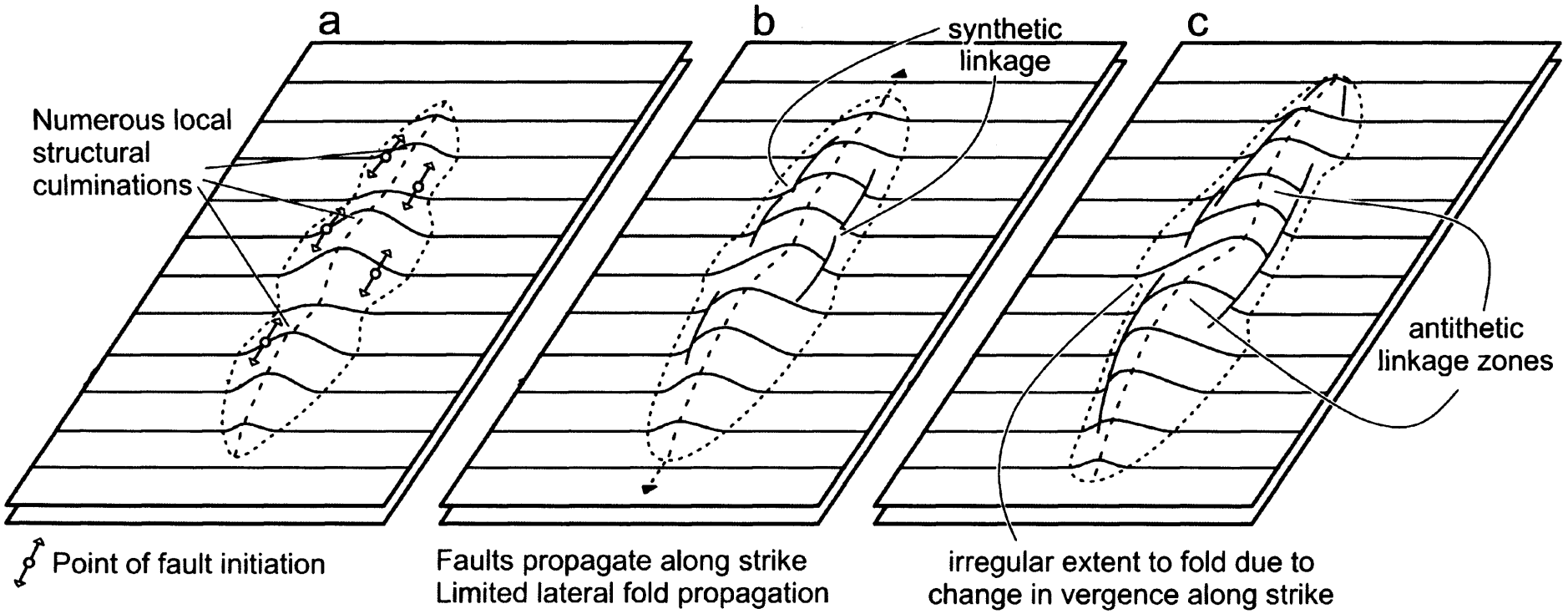

Figure 4.16: Fold B. Example evolutionary model of fold and fault growth. **(a)** Several low amplitude, symmetric detachment fold form, propagate and link laterally to form a single structure with a number of distinct structural culminations. Numerous forethrusts and backthrusts nucleate along the length of the structure and propagate along strike within the fold. Faults nucleate in competent units some distance above the detachment. **(b)** The length of the fold is established early and migration of structural culminations results in a single, central apex. Faults link along strike in synthetic and antithetic interactions. **(c)** Length of fold fixed. Fold continues to develop strong dip-parallel asymmetry as faults accumulate displacement. Antithetic fault linkages result in changes in fold vergence along strike, and an irregular extent of folding in map view.

component faults have been kinematically linked throughout development. Displacement is transferred between constituent faults through transfer zones. Deficits and perturbations in fault displacement are compensated by complementary variations in the amount of fold strain along strike.

4.9 Summary and conclusions

The fault heave and bulk shortening profiles along a single, isolated faulted fold of a deep water fold and thrust belt, Niger Delta, were presented in the first quantitative study of thrust faults to use strike-projected contour plots. Measurements of growth sequences and detailed fault plane geometries, produced from 3D seismic data, described numerous faults of similar and opposing dip linking along strike to create a through-going fold. The data and analyses support the following conclusions:

1. The distribution of bulk shortening along faulted folds that comprise either a single thrust fault or numerous linked thrusts can be simple, systematic and similar to that observed for extensional fault displacement.
2. Individual heave profiles of overlapping, linked faults show modification of contours away from systematic patterns. Displacement transfer occurs between overlapping faults leading to more regular profiles on aggregated plots.
3. Deficits in fault heave, both in the form of perturbations on non-linking or aggregated profiles and displacement minima within linkage zones, are compensated to some degree by an increase in the amount of fold strain. Fold amplitude or fold crest elevation is largely unaffected by minor variations in fault heave.
4. The geometry and distribution of syn-kinematic growth strata indicates that the evolution of fold B involved the nucleation and amalgamation of three smaller folds and culminations. There is evidence to suggest at least eight thrusts initiated with the early folds before lateral propagation and along strike synthetic linkage eventually created four major faults of opposing dip within fold B.

Chapter 5

Although the papers are jointly authored with the project supervisors they are the work of the lead author, Simon Higgins. Project supervisors provided editorial support in accordance with a normal thesis chapter.

CHAPTER 5

5. DISPLACEMENT TRANSFER DURING SYNCHRONOUS GROWTH OF A DEEP WATER FAULT AND FOLD ARRAY

5.1. Abstract

A three-dimensional seismic survey over the west Niger Delta comprises a complex interconnected network of forethrusts and backthrusts. Stratal connectivity across the fold and thrust belt is continuous through a series of transfer structures related to antithetic and synthetic thrust fault linkages. Syn-kinematic strata record the growth history of folds and suggest a general foreland-propagating sequence of thrust and fold development, however out-of-sequence events occur within this trend. Significant overlap in the duration of activity on all faults and folds in the survey indicates a sustained period of synchronous growth. Complementary heave and shortening profiles within a hard-linked fault array demonstrate both along strike and dip-parallel displacement transfer between faults and folds. Deficits in shortening associated with some of the fault and fold linkage zones correlate with increases in deformation on structures up- and down-dip. Fold amplitude is commonly unaffected by along strike decreases in heave and shortening within transfer zones and it appears fold shape is adapted to maintain fold height. Aggregate profiles of all faults and folds show a conservation of total heave and bulk shortening along strike within the syn-kinematic units. Extremely low lateral heave gradients suggest efficient displacement transfer between constituent structures. Irregularities in the distribution of deformation in pre-kinematic units are evident on profiles of single structures, linking faults and folds and the aggregation of the fold belt as a whole. Heave-length profiles measures within this stratigraphic section display numerous maxima and minima relating to the locations of linkage zones. Evidence of displacement transfer between all structures within a fold belt that developed by the synchronous growth of its constituent structures suggests this is a geometrically and kinematically coherent fold and fault array.

5.2. Introduction

Component faults of laterally extensive, thin-skinned fold-and-thrust belts are finite in map length and display along strike decreases in displacement towards their tips (e.g. Dahlstrom, 1970; Boyer and Elliott, 1982). Kinematic linkage between structures can allow shortening values to remain relatively constant along strike within a thrust sheet (e.g. Price and Mountjoy, 1970) and results in a range of transfer structures that affect stratal continuity and connectivity across a fold and fault array (e.g. Douglas, 1958; Dahlstrom, 1970; O'Keefe and Stearns, 1982; Higgins et al., 2007). These observations lead to the concept of displacement transfer through transfer zones (Dahlstrom, 1970), defined as a zone of overlap between two thrusts linked via a common basal detachment (Lebel and Mountjoy, 1995). The widespread development of backthrust zones within deep water fold and thrust belts (e.g. Bilotti and Shaw, 2005; Corredor et al., 2005; Briggs et al., 2006) can result in transfer zones comprising faults of similar or opposing dip in synthetic or antithetic thrust fault linkages respectively (Higgins et al., 2007) (Chapter 3). The majority of studies have focussed on synthetic interactions and almost exclusively on the along strike linkage of a set of laterally aligned thrusts (e.g. Rowan, 1997; Davis et al., 2005; Higgins et al., 2007) or dip-parallel overlap of faults seen in section (e.g. Ellis and Dunlap, 1988; Nicol et al., 2002). The kinematic coherency of all elements of a complex fault array, a topic that has been examined in extensional systems (e.g. Walsh and Watterson, 1991), has not been discussed in a contractional setting and hence the way in which thrust faults and folds interact, beyond those that are spatially coincident, is not well understood.

The principal aim of this chapter is therefore to document displacement transfer within an extensive, complex network of structures linked by common basal detachments in a deep water fold and thrust belt, offshore Nigeria. Displacement transfer can only occur between contemporaneous structures and hence kinematic coherence of an array is dependent on a degree of synchronous growth (Walsh and Watterson, 1991). In the past, various models of the sequence of fault propagation have been proposed advocating foreland progressing deformation (e.g. Dahlstrom, 1970), hinterland progressing deformation (e.g. Boyer and Elliott, 1982; Butler, 1982) and out-of-sequence propagation (e.g. Wiltschko and Dorr, 1983; DeCelles and Mitra, 1995; Mitra and Sussman, 1997; Corredor et al., 2005), the majority of which invoke

a cessation of movement on older structures soon after inception of the new (e.g. Boyer and Elliot, 1982). The deep water Niger Delta offers an excellent opportunity to investigate the timing and duration of fold and thrust growth within an intricate array, as syn-kinematic strata record the development of structural features and are extremely well imaged by 3D seismic reflection data. This study focuses on the controls of displacement distribution and will therefore include discussion on the relative timing of fault growth and the effects of pre- and syn-kinematic strata on the deformation.

Thrust fault growth is intrinsically associated with folding; a relationship that is seen to evolve through time and can vary considerably along strike (Liu and Dixon 1991; Davis et al 2005). Isolated thrusted folds, such as Fold B described in Chapter 4 (Fig. 4.6), have been shown to be the product of the along strike propagation and linkage of numerous, initially distinct culminations and fault surfaces that accommodate shortening in a manner similar to a single structure (Rowan 1997) (Chapter 4). The application of this work to the more interconnected geometries of fold and thrust belts will provide insight into the development of structures in deep water settings. This can have wide ranging implications from an understanding of the controls on sediment dispersal to the timing of hydrocarbon trap and seal formation.

5.3. Database

The 3D seismic survey used in this study images approximately 3000 km^2 of the toe-of-slope region of the Niger Delta. The improved resolution and imaging quality of such datasets mean this is an excellent tool for the study of stratal offset variations along fault surfaces and the spatial extent of growth strata. This area comprises a suite of large scale thrust faults in a gravity-driven compressional fold and thrust belt (Fig. 5.1). Seismic lines sub-perpendicular to the regional strike of fold and fault structures were used for fault interpretation, fault heave measurements and calculations of shortening. Fourteen key seismic horizons were mapped throughout the region on a dataset with inline and crossline spacing of 12.5 m (e.g. Brown, 1999). Vertical seismic resolution varies with depth, from approximately 10 – 20 m within the studied interval. This is the minimum vertical distance at which reflections from two horizons can be differentiated. The vertical resolution of fault measurements from

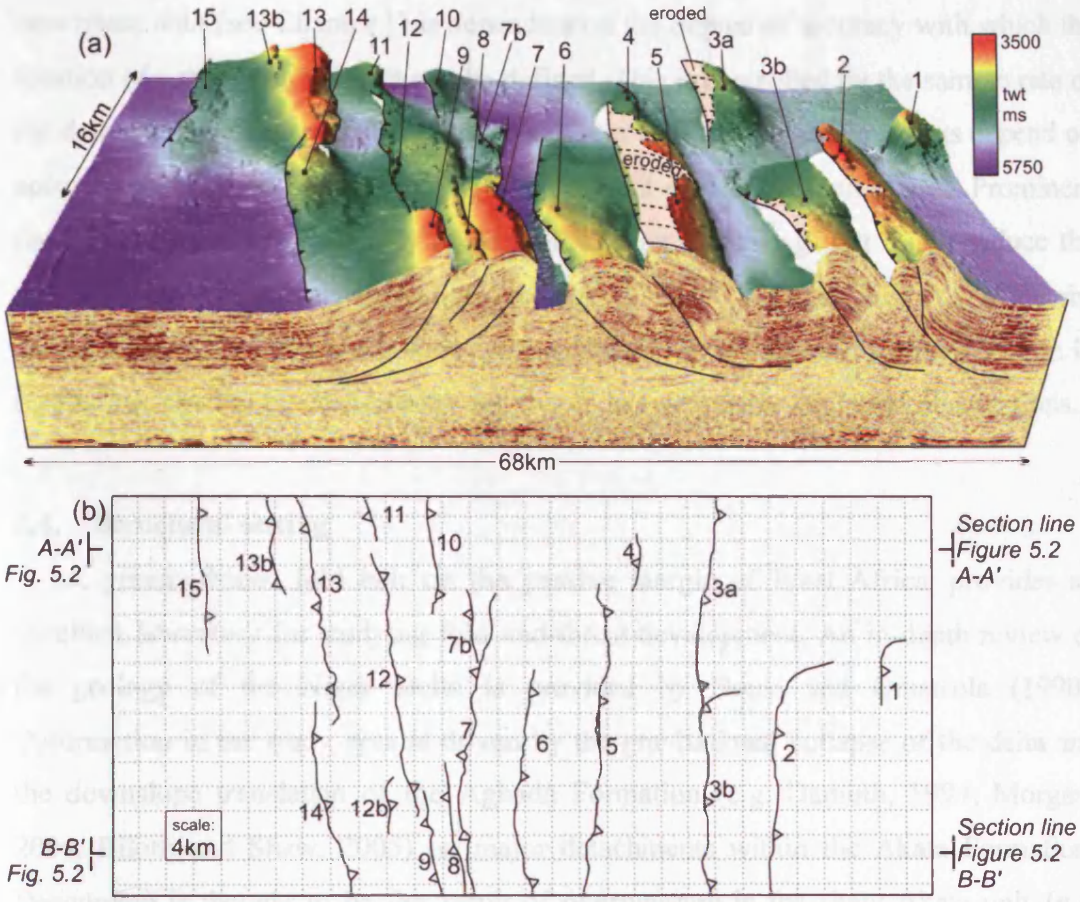

Figure 5.1: Compressional structures comprising part of the outer fold and thrust belt of the deep water Niger Delta. **(a)** Seismic survey A. 3D visualisation of horizon m4. Horizon m4 is a buried stratigraphic horizon located between approx. 1.8 and 2.5 km below the seabed in undeformed areas of the study area. Major thrust faults and fold are labelled 1 – 15 (referred to as *ff* 1-15 in the text). Vertical axis displayed in two-way-travel time (ms). Eroded areas of horizon m4 on crests of some anticlines are reconstructed and labelled. **(b)** Plan view of fault traces (w.r.t. to horizon m3 hangingwall cut-offs). Note that no fault spans the full width of the seismic survey and that through-going folds can be made up of two thrust faults (e.g. *ff* 13 and 14).

zero phase data (see Chapter 1) is dependent on the degree of accuracy with which the location of a crest of a wavelet can be defined. This is controlled by the sample rate of the data and is estimated to be $\pm$ 2 ms. Reliable fault heave measurements depend on accurate observation of hangingwall and footwall cutoffs on fault planes. Prominent fault plane reflections on many faults in the Niger Delta (e.g. Fig. 1.5b) reduce the potential error. Interval velocities, relating to key horizons tied to a nearby confidential exploration well, were used to depth convert seismic sections for use in restoration, shortening calculations and to validate geometric structural observations.

5.4. Structural setting

A gravity-driven fold belt on the passive margin of West Africa provides an excellent laboratory for studying fold and thrust development. An in-depth review of the geology of the Niger Delta is provided by Doust and Omatsola (1990). Deformation in the study area is driven by the gravitational collapse of the delta and the downslope translation of the Agbada Formation (e.g. Damuth, 1994; Morgan, 2004; Bilotti and Shaw, 2005) on major detachments within the Akata Formation. Decoupling is thought to be the result of overpressure in the shaly Akata unit (e.g. Morley, 2003; Rowan et al., 2004). Previous authors have described numerous detachment layers within the deltaic succession (e.g. Corredor et al., 2005; Briggs et al., 2006), two regional detachment levels are seen in this data set; at the Agbada-Akata Formation boundary and within the Akata itself. Critical taper wedge modeling has inferred a weak basal detachment in the Niger Delta (Bilotti and Shaw, 2005) and a sub-horizontal maximum principal compressive stress. Both of these factors have a major influence on the ratio of backthrust-to-forethrust formation (e.g. Davis and Engelder, 1985) and the mechanism of fold and fault growth (e.g. Mitra, 2002). Deformation, by oceanward-vergent forethrusts and landward-vergent backthrusts, is largely confined to the Agbada Formation which comprises a series of compensationally stacked deepwater channel-levee systems (e.g. Deptuck et al., 2003). The stratigraphy of the deformed interval consists of hemi-pelagic sediments, mass transport complexes and channel-confined sand bodies surrounded and sealed by finer grained mudstones (e.g. Davies, 2003; Deptuck et al., 2003). This is therefore a mechanically heterogeneous medium whose rheological complexity may have implications for fault and fold propagation. Existing models for propagation are

largely based upon homogeneous, layer-cake stratigraphic models, and one of the themes of this research investigates the effect of mechanical stratigraphy on fault growth.

5.5. Methods

5.5.1. Growth package analysis

Structural uplift of the seabed caused by growing thrusts and folds can lead to the formation of depositional packages that thin onto the crest of an antiform or onlap onto a fold limb. Assuming the depositional system is accommodation-limited and not sediment supply-limited sedimentary geometries can reveal the history of fold growth (e.g. Suppe et al., 1992; Hardy et al., 1996; Poblet et al., 1997). Analysis of seismic waveform attributes around the structures in this study area does not support the possibility that low energy deposition, such as hemi-pelagic drapes, are concealing deformation by implying apparent periods of quiescence during times of active deformation. Channel-levee deposits respond to changes in slope and are therefore sensitive indicators of deformation-controlled topography (e.g. Hooper et al., 2002). Analysis of sedimentary growth packages has long been used to estimate the timing and duration of structural growth (e.g. Suppe et al., 1992). Chapter 4 showed the detailed analysis of fold growth utilizing isopach ratios and measurements of upward reductions in dip on the limbs of an isolated fold. In this case such methods are hampered structurally by closely spaced thrusts and folds and stratigraphically by stacked channels levee complexes (e.g. Deptuck et al., 2003) that break up regional marker reflections and hinder identification and correlation of onlap packages along strike. As a consequence, the along strike propagation of a fold is not measured here. Timing of fold initiation and cessation is therefore derived from onlap geometries and sedimentary thickness variations and represent the earliest evidence of structural growth along structures as a whole. The duration of fold growth is determined from the observation of the upper and lower bounding surfaces of growth strata defined by a change from uniform thickness units to horizons that onlap or stratigraphically thin across the fold. Depth converted sections were utilised to confirm sediment thickness variations from limb to crest. The timing of fold development is dated using stratigraphic ages derived from biostratigraphic data from the exploration borehole

located within the data limits. This dating method can be prone to error (e.g. Miall, 1992) and hence is not used here to convey absolute ages of horizons, but instead provide a first-order estimate of the relative timing of structural features.

5.5.2. Fault heave and total shortening calculations

Quantification of fold and fault characteristics derived from measurements on fourteen key seismic horizons are presented using three variables; fault heave, bulk shortening and fold crest elevation.

Fault heave is defined as the horizontal offset between hangingwall and footwall cut-offs for a given horizon (Fig. 4.4). This value does not require time-consuming depth conversion and is therefore less affected by velocity variations in the dataset. This enables a more detailed and higher resolution study of fault offset variation to be carried out. Fault heave is also a closer approximation to the amount of shortening accommodated by faulting than displacement along a fault plane.

Shortening calculations are made by line length analysis (Dahlstrom, 1969; Hossack, 1979) (Fig. 4.3) and assumes the dominant mechanism of folding in this system is flexural slip. Measurements were made across the width of the seismic dataset on fifteen seismic lines perpendicular to the prevalent regional fold and fault strike. Depth conversion was performed using interval velocities between the fourteen key horizons tied to the nearby confidential exploration well. The sections were pinned away from the structure at points of undeformed layer-cake stratigraphy or at a regional level in the core of synclines (Dahlstrom, 1969). The close spacing of anticlines and faults limited the viable locations of structural pins and hence it was not possible to perform shortening calculations across all individual folds and thrusts. As a result some structures are presented with heave measurements only, however shortening values are included wherever possible.

We present shortening values and fault heave measurements as heave-length profiles and contour patterns on strike-projections. Contoured displays provide a visual demonstration of displacement variation over a fault plane (Walsh and Watterson, 1991) and were first utilised in extensional studies (Rippon, 1985). Plane-vertical surfaces present displacement values, recorded as the difference between hangingwall and footwall cut-offs and commonly plotted at the midpoint between

these two values. In the observation of a compressional domain the degree of significance of folding is expressed most effectively in the form of shortening calculations. However, in order to allow direct comparisons between variations in folding and faulting, shortening values are not plotted with respect to horizon cut-offs. Instead, both the shortening and heave measurements are plotted for each of the fourteen key seismic horizons at a corresponding undeformed, 'regional' depth downdip of the fold and fault structure(s) (Fig. 4.3). This assumes that the dominant mechanism for folding in this system is flexural slip, an assumption implicit in the calculation of shortening by line length analysis. Aggregate profiles are generated by the summation of all measurements for a given horizon along dip-parallel lines, and are displayed in the same manner as above.

The major limitation of this method of data plotting is that upward displacement gradients along fault planes will be apparently reduced compared to previous studies that used points relating to cut-offs. This unfortunately does not enable comparison with most published cross-section projections of thrust fault displacement. The majority of these display offset values against a distance measured along a fault plane from a reference point to either (1) the hangingwall cut-off (Muraoka and Kamata, 1983; Williams and Chapman, 1983) or (2) the midpoint between hangingwall and footwall cut-offs (e.g. Ellis and Dunlap, 1988) (Fig. 4.3b). Similar limitations occur if a fault has a listric character in sectional profile such that a fault decreases in dip with depth, as heave will be seen to increase for the same along-fault displacement. This may produce an apparent increase in the upward displacement gradient. These limitations are disregarded as it is noted that most ramping occurs in a limited zone above the detachment as a fault leaves the region of over-pressure (e.g. Corredor et al., 2005) (Fig. 5.2, e.g. faults 10 and 11). Also when assessing the relationship between faulting and folding, measurements of heave represent a closer approximation to the amount of shortening accommodated by faulting than displacement along a fault plane. Finally conclusions regarding the along strike changes in fault and fold geometries are unaffected by these limitations and comprise the main focus of this paper.

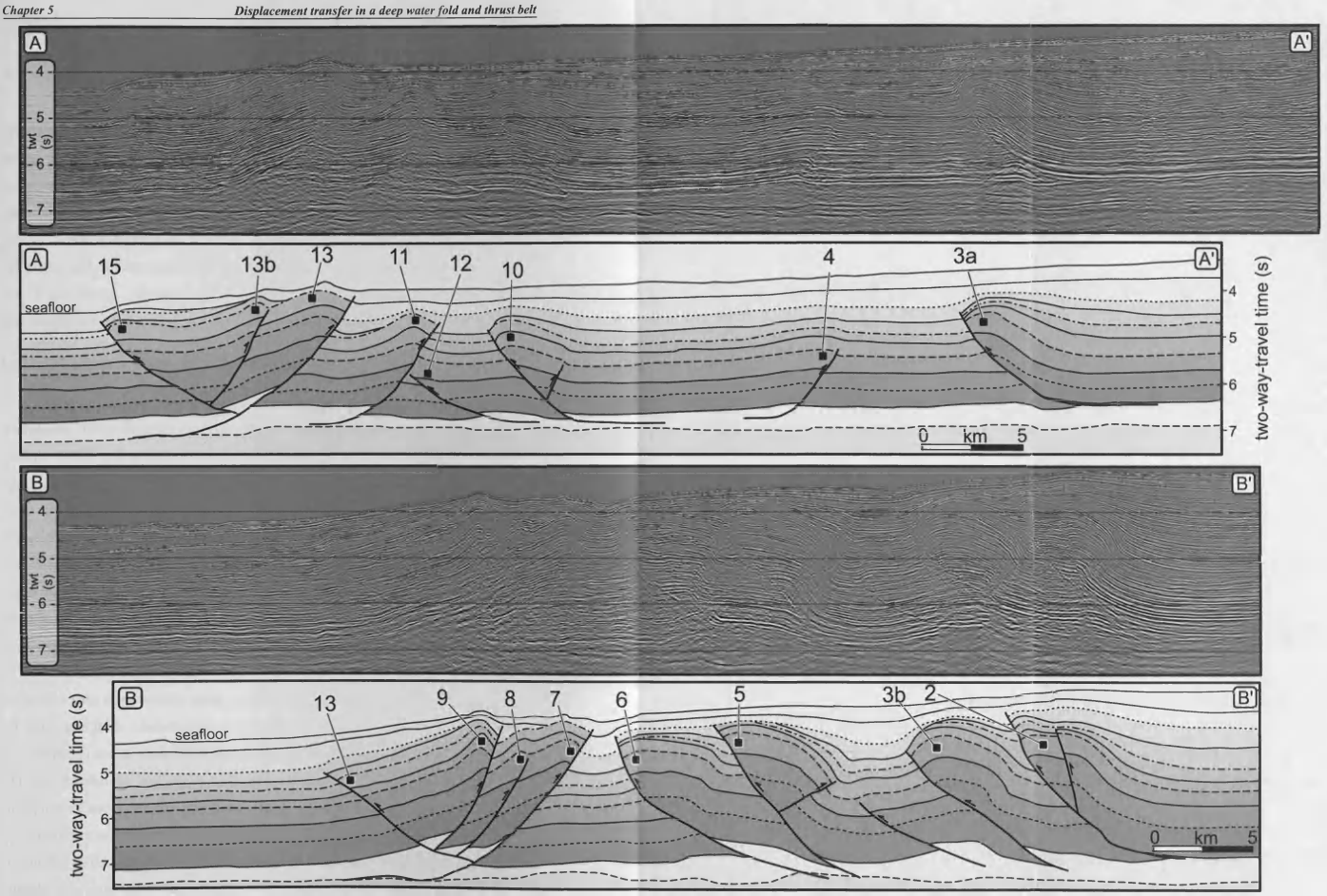

Figure 5.2: Two representative seismic sections oriented parallel to regional dip to show the change in structural geometry, orientation of fault planes and fault spacing along strike. Stratigraphic and structural interpretation is presented below of each seismic line. Locations of the lines are given in Figure 5.1b. Note the greater degree of hard-linkage of faults located towards the foreland of the fold belt (left) above the level of the detachment, compared to faults in the hinterland (right).

5.6. Results

The isolated fold described in Chapter 4 (Fold B) documented the growth of a single structure by segment linkage. Three initially distinct folds, and as many as eight thrust faults, nucleated and grew together along strike producing a single structural culmination and forming both synthetic and antithetic fault linkages (Fig. 4.14). The distribution of shortening along strike resembled the profile of an individual structure due to displacement transfer between constituent faults. The application of this model of single fold development to a fold and thrust belt, located towards the foreland of the Niger Delta, provides insight into the accommodation and distribution of shortening in a more complex, closely spaced fold and fault array (Fig. 5.1).

5.6.1. Fault intersections and stratal connectivity across a fault and fold array

The process of fault growth by segment linkage is widely documented (e.g. Dahlstrom, 1969; Peacock and Sanderson, 1991; Cartwright et al., 1995; Gupta and Scholz, 2000) and observed over a large range of scales (Aydin, 1988) and for all modes of faulting (Walsh et al., 1999). Stratigraphy can be continuous across faults, from hangingwall to footwall, through the development of relay structures (e.g. Peacock and Sanderson, 1991) or transfer structures (e.g. Dahlstrom, 1970; O'Keefe and Stearns, 1982; Higgins et al., 2007) (Chapter 3). In this first section we expand upon the descriptions of stratal connectivity and fault plane geometries of the linking fault pairs featured in Chapter 3 (Higgins et al., 2007) and consider the full width of a fold and thrust belt.

Geometric and spatial relationships between shortening accommodating structures vary considerably along strike resulting in a complex inter-linking network of faults and folds. Deformation is continuous along this section of fold belt and yet no individual thrust spans the 40 km width of the dataset (Fig. 5.1). Eleven landward-dipping forethrusts and eight oceanward-dipping backthrusts underlie asymmetric hangingwall anticlines that link along strike in folded transfer zones. The distribution of forethrusts and backthrusts is important in controlling the degree of hard linkage within the thrust belt above the detachment (Fig. 5.3). If synthetic thrust faults form a simple imbricate stack (e.g. Butler, 1982) their figure 4) they will be linked (in section) via a floor thrust or detachment. This is the case for faults and folds (*ff*) 1 to 6

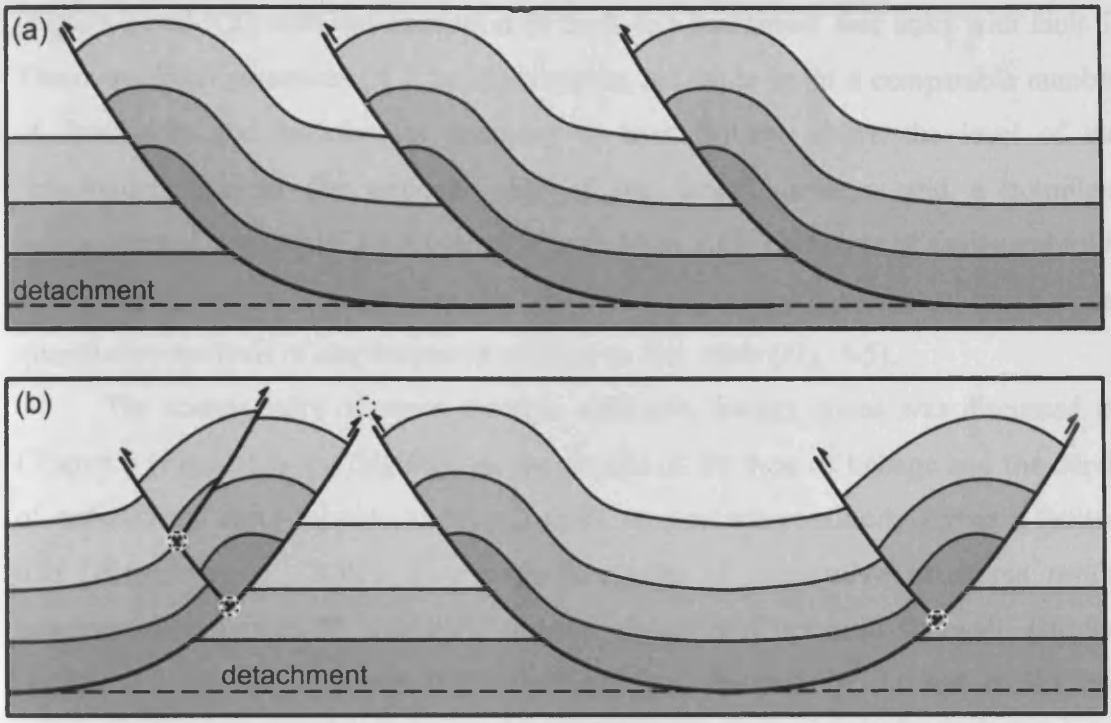

Figure 5.3: A schematic cross sections of a series of thrust faults to demonstrate differences in linkage of synthetic and antithetic faults. **(a)** All faults are of the same direction of dip (i.e. synthetic) forming an imbricate stack. Note that within this section faults are only hard-linked via a common detachment. **(b)** Section comprising faults of opposing dip (i.e. antithetic). Note that this can create numerous branch points (stippled circles) that represent hard-linkage of faults above the level of the detachment.

(Figs. 5.1 and 5.2) with the exception of fault 4; a backthrust that links with fault 5. The more distal structures (*ff* 7 to 15) however, are made up of a comparable number of forethrusts and backthrusts resulting in hard linkage above the level of the detachment, due to the opposite dip of the thrust surfaces, and a complex, interconnected network of fault planes (Fig. 5.2 and 5.4). This suite of faults and folds (*ff* 7 – 15) are referred to herein as the 'Frontal Array' and is the focus of much of the quantitative analysis of displacement transfer in this study (Fig. 5.5).

The connectivity of strata through antithetic linkage zones was discussed in Chapter 3 (Fig. 3.11) and highlighted the impact of the type of linkage and the depth of sedimentary units relative to branch lines, on horizon continuity across a faulted fold (Higgins et al., 2007). Two main categories of connective structures result; hangingwall-hangingwall (hw-hw) transfer folds and footwall-footwall (fw-fw) corridors. However, both synthetic linkages (e.g. between *ff* 3a and *ff* 3b) and antithetic linkages (e.g. between *ff* 4 and *ff* 5) exist within the survey area (Fig. 5.4 and 5.5). Transfer structures relating to synthetic faults are affected by the along strike alignment of faults, exemplified by the comparison of the *ff* 3a/3b linkage with that of *ff* 7/7b (Fig. 5.1). In the former example the faults are aligned along strike, there is no lateral deviation in the fold trend and the linkage is characterised by a saddle point in horizon m4 (Fig. 5.1). The fault planes have hard linked to form a through-going surface which causes most horizons to be discontinuous across *ff*3a and 3b. Faults in the latter example are non-aligned laterally and therefore overlap along strike producing a hangingwall-footwall (hw-fw) transfer fold (Fig. 5.5b) within the linkage zone (Fig. 5.5a).

Horizon m4 is therefore continuous in a down dip direction across the full width of the fold and thrust belt via a tortuous path through numerous transfer structures (Fig. 5.1). Within the Frontal Array it is clear that transfer zones do not necessarily correspond to structural lows or saddles (Fig. 5.5). In most cases the linkage zones correlate with structural culminations in the hangingwalls or have fold crests with consistent plunge. Given the evidence from Chapter 4 that suggests fault linkages in this region are the product of along strike propagation and interaction of initially distinct faults and folds, it is predicted that structural culminations have migrated along strike through time and that present day linkage zones were initially saddle points during the early stages of deformation (Fig. 4.16).

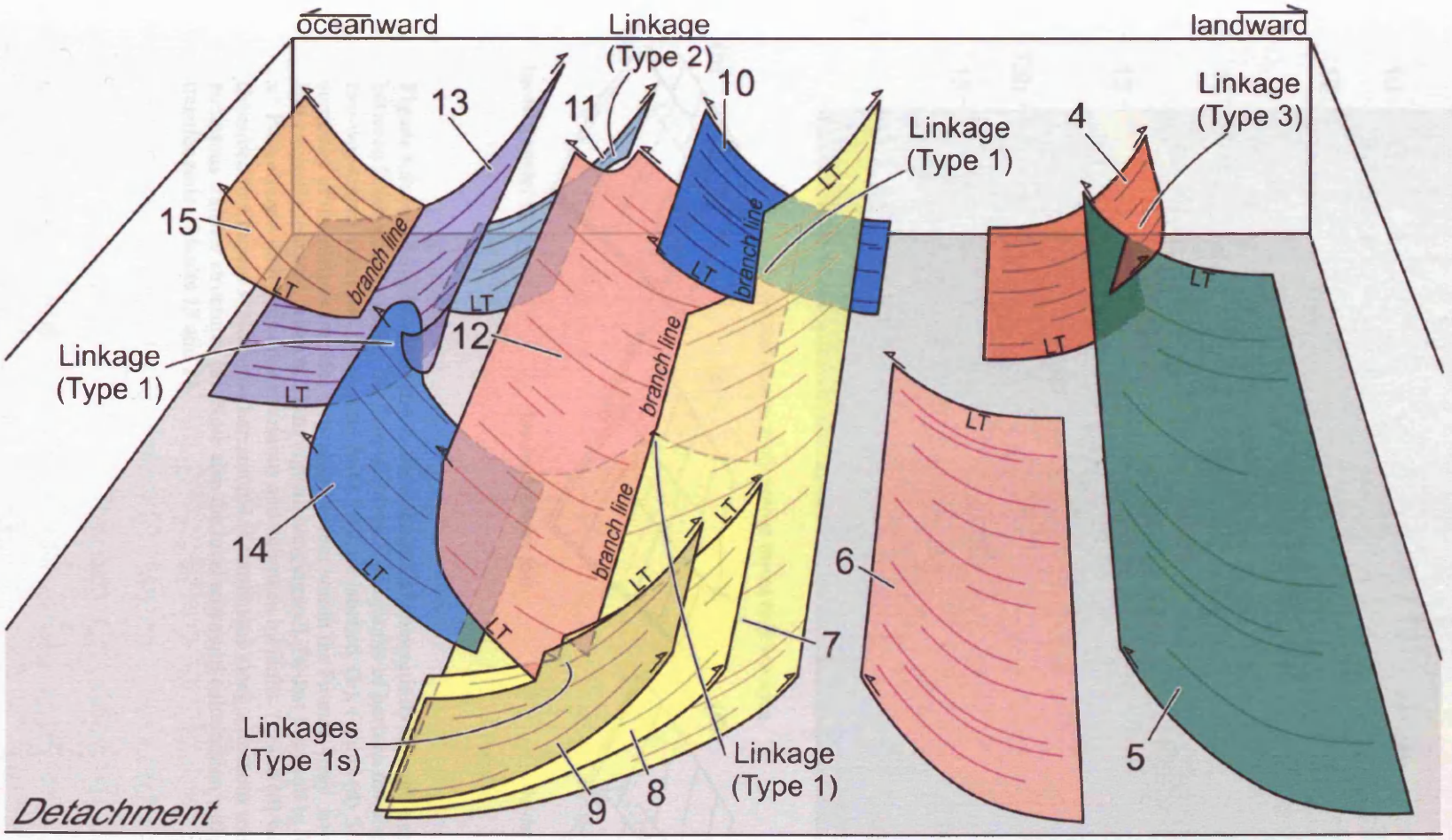

Figure 5.4: Conceptual 3D visualisation of some of the major thrust fault surfaces (*ff* 4-15) within seismic survey A to illustrate the structural complexity of a fold belt comprising thrust faults of opposing dip (antithetic). Grey surface represents a common detachment. Lines of intersection between antithetic faults are labelled as 'branch lines'. LT: lateral tip. Thrust fault surfaces interact along strike in a range of structural geometries. These are labelled with respect to the classification scheme proposed in Chapter 3 (Types 1 to 3). Note the high degree of linkage between faults towards to foreland (left). Faults 7 to 15 are all interconnected via hard linkages above the level of the detachment. These faults are referred to as the 'Frontal Array' in the text.

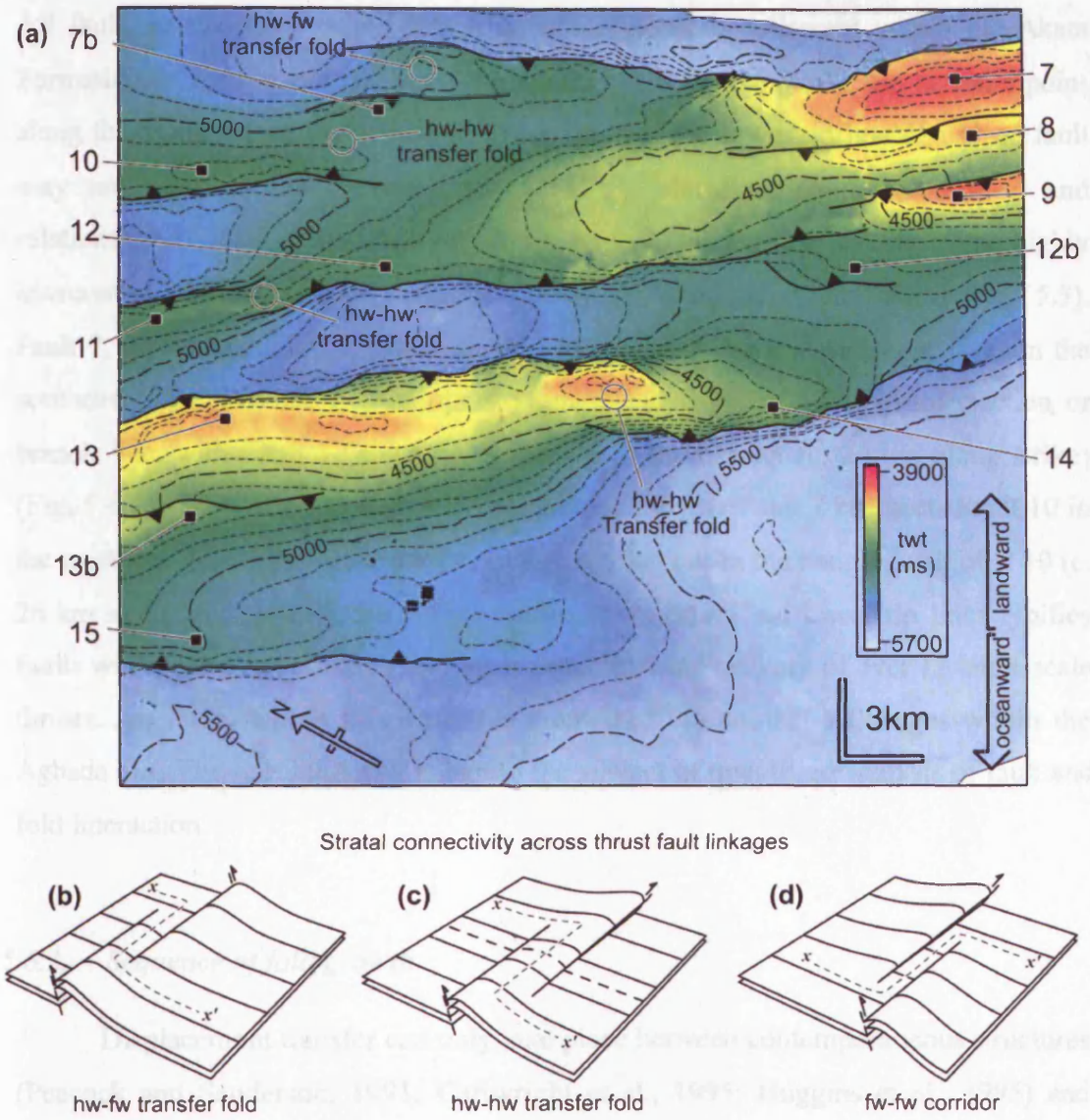

Figure 5.5: (a) Map of horizon m4 to show the stratal connectivity through transfer zones between linking faults within the Frontal Array. Topography of horizon m4 displayed in two-way-travel time (ms). Faults and folds 7-15 are labelled. **(b), (c)** and **(d)** Schematic summary of the various transfer structures present within the Frontal Array. **hw-fw**: Hangingwall-footwall. **hw-hw**: Hangingwall-hangingwall. **fw-fw**: Footwall to footwall. ***x-x'***: Path along which beds are continuous and unbroken by faults. **(c)** and **(d)** were described in Chapter 3. Note that horizon m4 is continuous along a tortuous route through numerous transfer structures (a). Note also the local structural culmination within the transfer zone of faults 13 and 14.

All faults in this area either detach onto a regional decollement within the Akata Formation or form a branch line with another fault at their lower tip at some point along their length (Fig. 5.4). The characteristics of the lower tip line of a given fault may not be consistent laterally such that its elevation, stratigraphic level and relationship to other faults may vary along strike. This is most striking in the highly interconnected suite of hard-linked faults (*ff* 7-15) of the Frontal Array (Fig. 5.5). Fault 7, for instance, has a lower tip line located within the detachment layer in the southeast (Fig. 5.4), but then climbs stratigraphically to form a line of intersection, or branch line, with Fault 12 towards the centre of the dataset (c. 20 km along strike) (Fig. 5.4 and 5.6). This geometry is repeated laterally as Fault 7 intersects Fault 10 in the northwest (c. 24 km along strike) before tipping out in the hangingwall of *ff* 10 (c. 26 km along strike) (Fig. 5.6). This 'staircase-trajectory' of lower tip lines typifies faults within the Frontal Array and leads to an intricate network of over 12 large-scale thrusts. All faults within this array are connected via antithetic linkages within the Agbada Fm. The Frontal Array is herein the subject of quantified analysis of fault and fold interaction.

5.6.2. Sequence of fold growth

Displacement transfer can only take place between contemporaneous structures (Peacock and Sanderson, 1991; Cartwright et al., 1995; Huggins et al., 1995) and hence an understanding of the relative timing of faults is essential to describe the distribution of shortening through time. Here we investigate the degree of overlap in the duration of activity of folds and faults in the study area.

The study of growth packages and onlap markers on the limbs of folds in this survey provide evidence for highly synchronous growth between all structures in the fold belt and a general trend of foreland progressing deformation. The onset and cessation of folding is presented for each hangingwall anticline in Figure 5.7. The dating of stratigraphic horizons is intended to provide relative timings of structural growth rather than the absolute age of deformation. The earliest structural growth (*ff* 3a) occurred at approximately 11.5 Ma with the youngest feature, the most distal fault (*ff* 15), initiating around six million years later at 5.5 Ma (Fig. 5.7). There is a broad pattern of foreland stepping deformation that supports the theory that younger faults

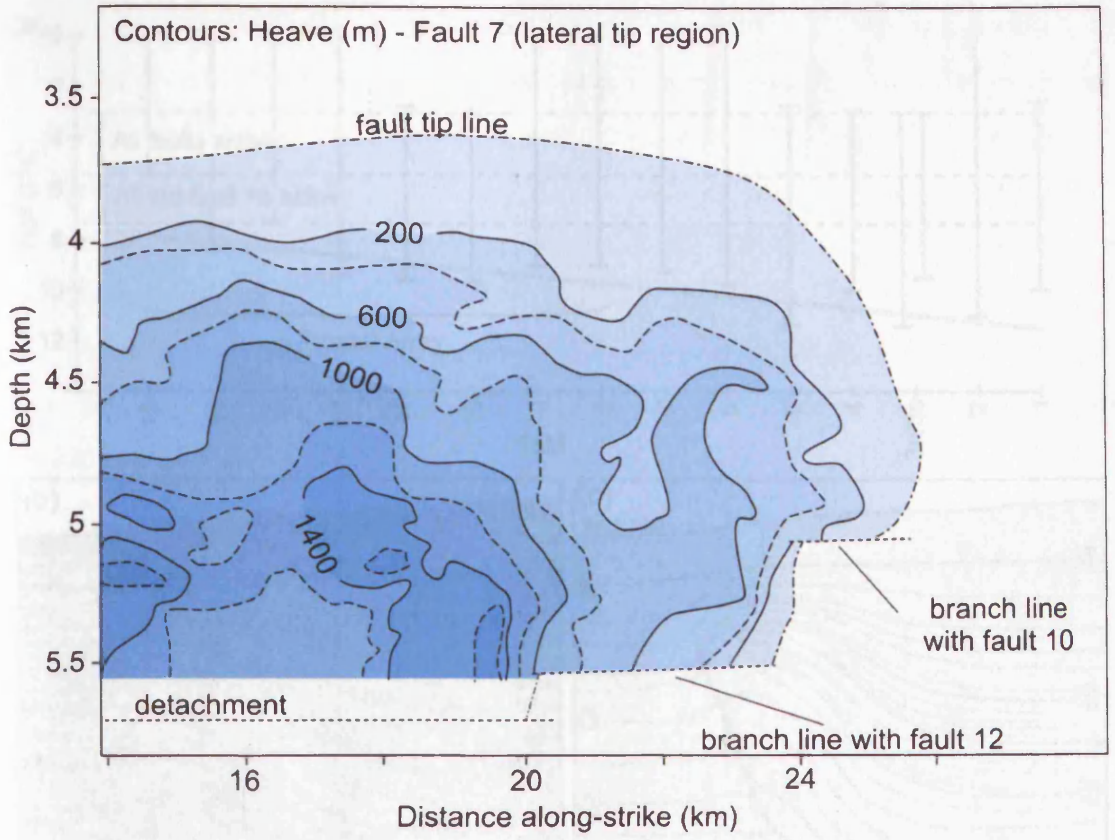

Figure 5.6: Strike projection of heave values from the lateral tip region of Fault 7 showing the shape of the fault plane at its lateral tip. Fault tip line joins the points of zero fault heave observable on seismic data. Note that towards the main body of the fault (left) the lower tip line is located within the detachment. Towards the lateral tip (right) the lower tip line forms a branch line with Faults 12 and 10 creating a 'staircase' trajectory. The lateral tip of the fault is located at approx. 4.75 km depth within the hangingwall of Fault 10 (i.e. above the level of the branch line).

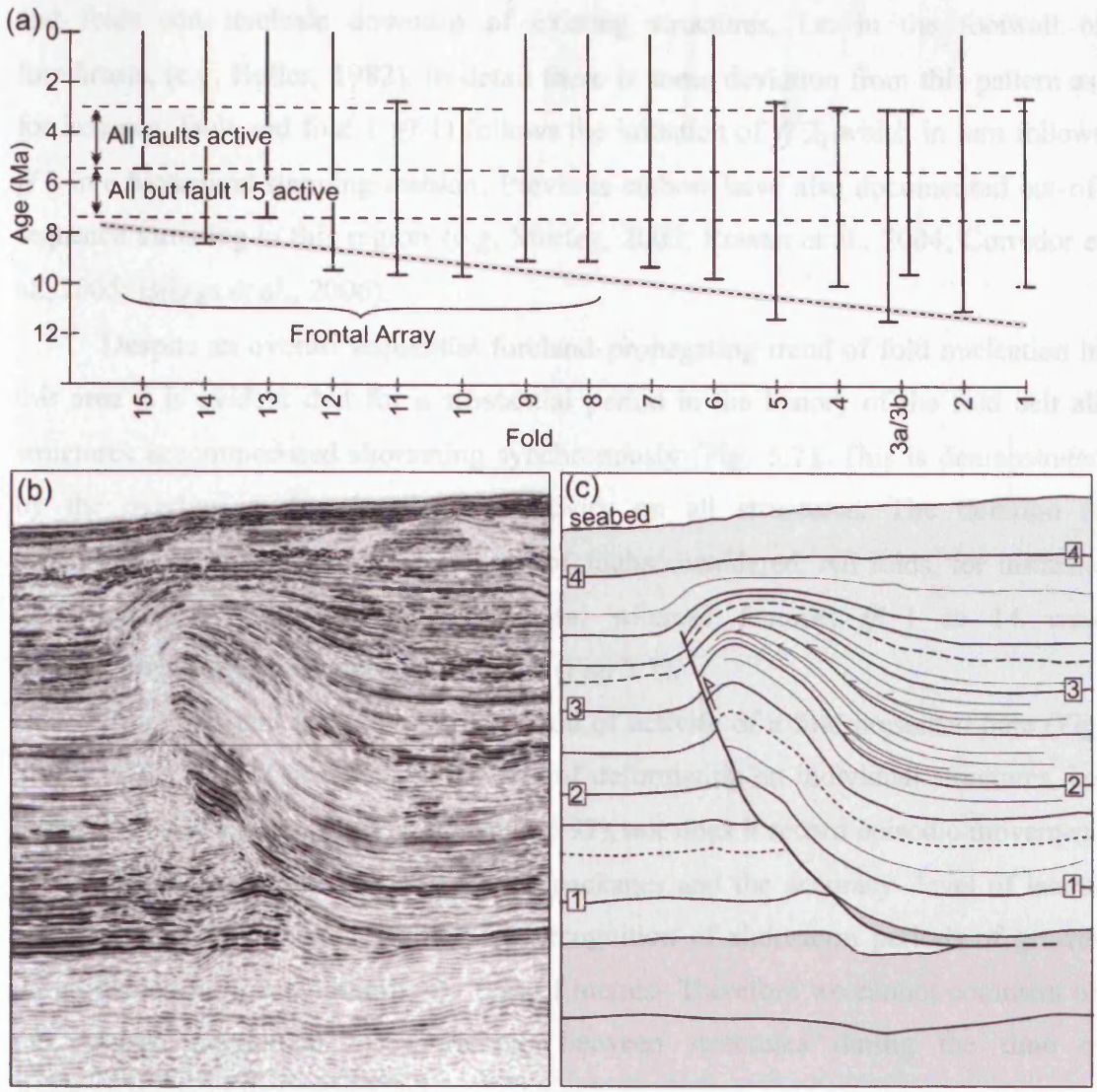

Figure 5.7: (a) Chart of the relative timing of fold growth within survey A. Initiation and cessation of fold activity was determined by analysis of syn-kinematic growth strata on the limbs of folds. The duration of deformational activity of each fold is represented by a vertical bracket. Note the general foreland-propagating trend to fold initiation (younger to the left). All faults were active between approx 5.5 and 3 Ma, whereas all folds bar Fault 15 were active between approx. 7.5 and 3 Ma. **(b)** An example seismic section through a thrust-related fold. **(c)** Interpretation of the seismic section (b) showing growth packages and onlapping surfaces. Sediments below horizon 2 are of uniform thickness across the fold and are interpreted to be pre-kinematic. Folding initiated at the time of horizon 2. Folding is interpreted to have ceased between the deposition of horizon 4 and the seabed.

and folds can nucleate downdip of existing structures, i.e. in the footwall of forethrusts, (e.g. Butler, 1982). In detail there is some deviation from this pattern as, for instance, fault and fold 1 (*ff* 1) follows the initiation of *ff* 2, which in turn follows *ff* 3 in a hinterland stepping fashion. Previous authors have also documented out-of-sequence thrusting in this region (e.g. Morley, 2003; Rowan et al., 2004; Corredor et al., 2005; Briggs et al., 2006).

Despite an overall sequential foreland-propagating trend of fold nucleation in this area it is evident that for a substantial period in the history of the fold belt all structures accommodated shortening synchronously (Fig. 5.7). This is demonstrated by the overlap in the duration of activity on all structures. The duration of synchronous growth varies given the set of faults considered. All folds, for instance, grew together for approximately 2 Ma, whereas features *ff* 1 to 14 were contemporaneous for approximately 4 Ma (Fig. 5.7).

It is important to note that the period of activity of a fold presented here (Fig. 5.7) does not record variations in the rate of deformation on individual structures, i.e. periods of rapid shortening (e.g. Rowan, 1997), nor does it record episodic movement. The resolution within the syn-kinematic packages and the accuracy level of lateral horizon correlation does not allow for recognition of short-term periods of growth during which folds may amplify by tens of metres. Therefore we cannot comment on the relative magnitude of shortening between structures during the time of synchronous growth.

5.6.3. Kinematic interaction between faulted folds

Displacement transfer as a conceptual process is often discussed with reference to a pair or group of thrust faults that interact either along strike (e.g. Davis et al., 2005) or in section (e.g. Ellis and Dunlap, 1988). Studies of complete normal fault arrays gave rise to concepts of geometric and kinematic coherency (Walsh and Watterson, 1991). This hypothesis has not yet been applied to compressional tectonics. In this section the distribution of fault heave and shortening on individual and linking structures are contrasted with aggregate profiles comprising the Frontal Array and all faults in the fold belt. Given the synchronous growth of structures in the fold belt (Fig. 5.7) it was considered valid to investigate the degree of along strike and dip-parallel

displacement transfer between component features, and this forms the central theme of this chapter.

5.6.3.1. Along strike displacement transfer

Antithetic faults that interact laterally to produce hw-hw transfer folds (Fig. 5.5c) transfer displacement such that aggregate profiles either plot close to the ideal of a single fault, or display a cumulative deficit in fault heave within the transfer zone (Fig. 5.8). Remarkably however, crestal height and values of fold plunge rarely distinguish between these two scenarios. This can be demonstrated by the comparison of two Type 1 linkages (i.e. antithetic faults that exclusively overlap above the level of the associated branch line) as defined by Higgins et al (2007) (Chapter 3, Fig. 3.7 and 3.11). The linkage zone between faults F1 and F2, located within Fold B described in Chapter 4 (Fig. 4.6), extends c. 7 km along strike (Fig. 5.8a) and has an aggregate profile similar to that predicted for a singly faulted fold (Fig. 4.5). This Type 1 linkage is situated in the northern half of the structure and the plunge of the fold (Fig. 5.8c) corresponds to the smooth gradient of cumulative fault heave that decreases steadily from the culmination to the tip (Fig. 5.8b). This can be compared with another Type 1 linkage involving fault and fold 13 (*ff* 13) and *ff* 14 which have an along strike fault overlap of just c. 3.5 km (Fig. 5.8d). The transfer zone, defined by abrupt changes in displacement profiles (e.g. Peacock and Sanderson, 1991), extends further than the zone of overlap and contains an area of significant fault heave deficit below the ideal aggregate profile (Fig. 5.8e). The fold amplitude, presented as the depth to the fold crest (Fig. 5.8f), is unaffected by the shortfall in fault heave and is, moreover, expressed as a local culmination within the zone of linkage. This observation that fold amplitude is largely unaffected by deviations in fault heave away from the ideal profile is made on all types of linkage described by Higgins et al. (2007) (Chapter 3) and characterises the majority of fault interactions in this study area.

In previous studies it has been shown that fold strain increases to compensate in areas of fault heave deficit (e.g. Davis et al., 2005) (Chapter 4; Fig. 4.15) and hence it should perhaps be expected for fold amplitude to be maintained through such areas. However, it is clear that consistent fold height profiles can coincide, not only with instances of fault heave minima, but also with minima in bulk shortening, which

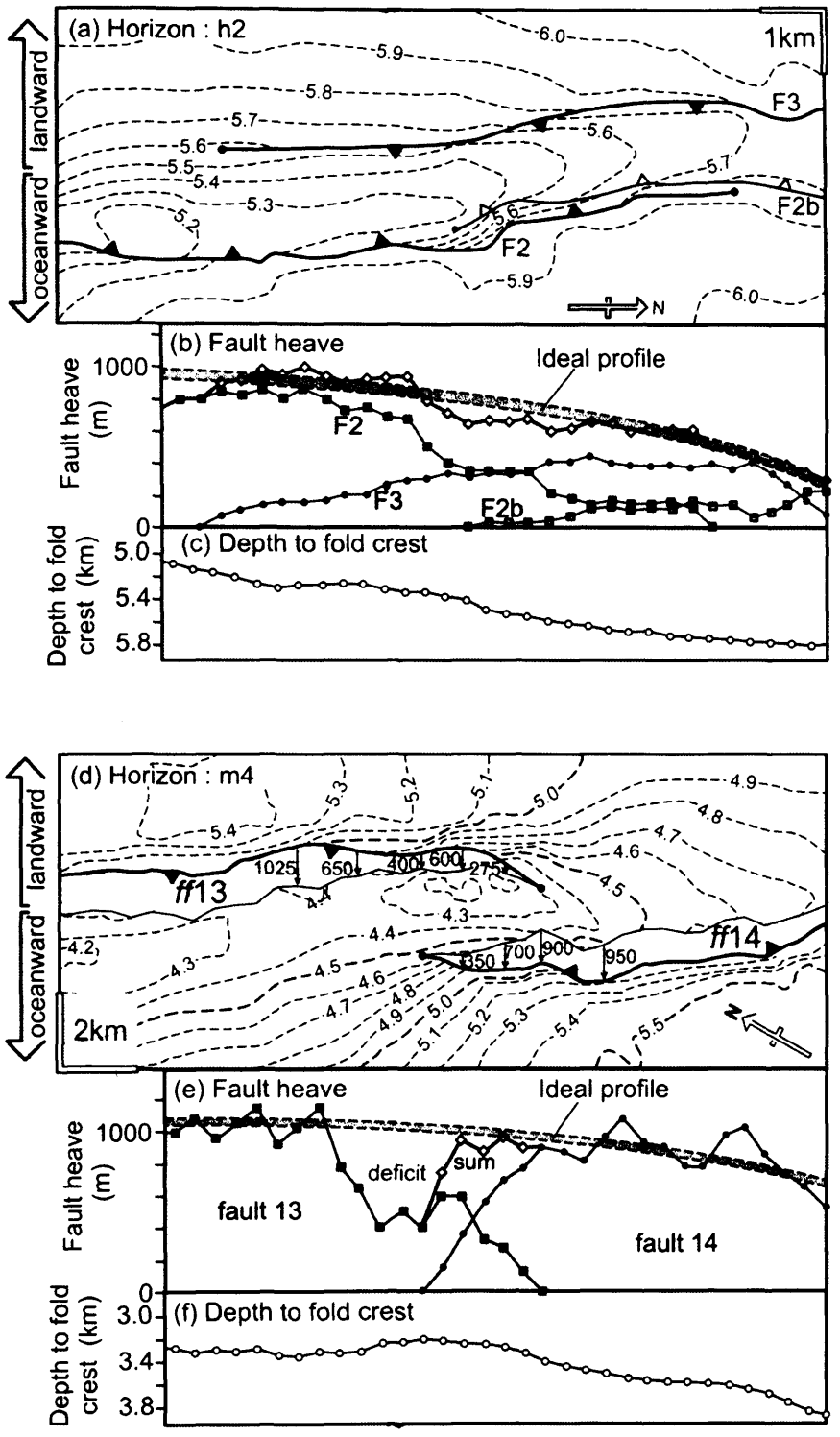

Figure 5.8: Comparing displacement and fold profiles through two Type 1 antithetic thrust fault linkage zones (as defined in Chapter 3). **(a)** and **(d)** Structure contour maps. (a) features horizon h2 in the fault F2/F3 linkage zone featured in Chapter 4. (d) shows horizon m4 in the linkage zone between fault and fold (*ff*) 13 and 14 from this chapter. Fault heave values are displayed in polygons in (d). Contour values represent depth to horizon in two-way-time (seconds). Lower contour values indicate structural highs. **(b)** and **(e)** Heave – distance profile of faults through the transfer zones. Summed profiles are given by white diamonds. The ideal fault profiles are displayed, predicted from the elliptical profile of an isolated, non-linking fault. **(c)** and **(f)** Charts of the along variability of the depth to the fold crests. Note that in (c) fold height follows a similar trend to the summed fault heave profile, while in (f) the heave deficit in the transfer zone (e) is not reflected in the fold profile.

incorporates the folding component of deformation. Such is the case with the Type 2 linkage comprising *ff* 11 and *ff* 12 (Fig. 5.9). Here, fault planes overlap exclusively below the level of the branch line between the faults (Fig. 5.9b) such that horizons above this level are connected through the transfer zone by a hw-hw transfer fold (Fig. 5.9a and 5.5c). The lateral tip regions of both faults are downwards tapering, creating concave-up tip lines (Fig. 5.9f). As a result, fault traces drawn with respect to shallower horizons will display less along strike overlap than those at depth. Horizon m4, used here to demonstrate displacement transfer, is located stratigraphically above the level of the branch line of *ff* 11 and 12 and hence the fault traces do not overlap laterally (Fig. 5.9a) resulting in fault heave decreasing to zero within the transfer zone (Fig. 5.9c). This deficit is represented by irregularity in the aggregate strike projection (Fig. 5.9e) in the form of a depression in heave contours within the linkage zone. The bulk shortening estimate decreases in a similar manner to a minimum of approximately 98 m at a point where horizon m4 is deformed by folding alone (Fig. 5.9c). Regardless of this reduction in both fault heave and shortening, the depth to the fold crest is consistent at around 4.3 km (Fig. 5.9d) and even shows a small increase at 8.5 km along strike, the point of zero fault heave.

5.6.3.2. Dip-parallel displacement transfer

An interesting observation within the Frontal Array is that fault heave deficits within linkage zones are commonly aligned up or down regional dip with corresponding maxima on other structures. An excellent structure to illustrate this concept is *ff* 10 located approximately 3 km updip of the *ff* 11/12 linkage zone (Fig. 5.10b and 5.11) described in the previous section. Fault and fold 10 comprises a forethrust with a maximum fault heave in excess of 800 m and a fold amplitude of up to 480 m. It is only partially imaged due to the limits of the survey area. Superficially, the morphology of horizon m4, in the hangingwall anticline of *ff* 10, correlates with the linkage zone as the structural culmination of *ff* 10 is aligned with the fault tips (w.r.t. horizon m4) of *ff* 11 and 12 (Fig. 5.10b), assuming the transport direction on the faults has occurred perpendicular to fault strike. This relationship is reinforced by the fault heave contours of the strike projected profiles (Fig. 5.10c and d). The deficit in fault heave in the *ff* 11/12 linkage zone defined by depressed contours between c. 22 and 26 km along strike (Fig. 5.10c) coincides with a balancing zone of maximum

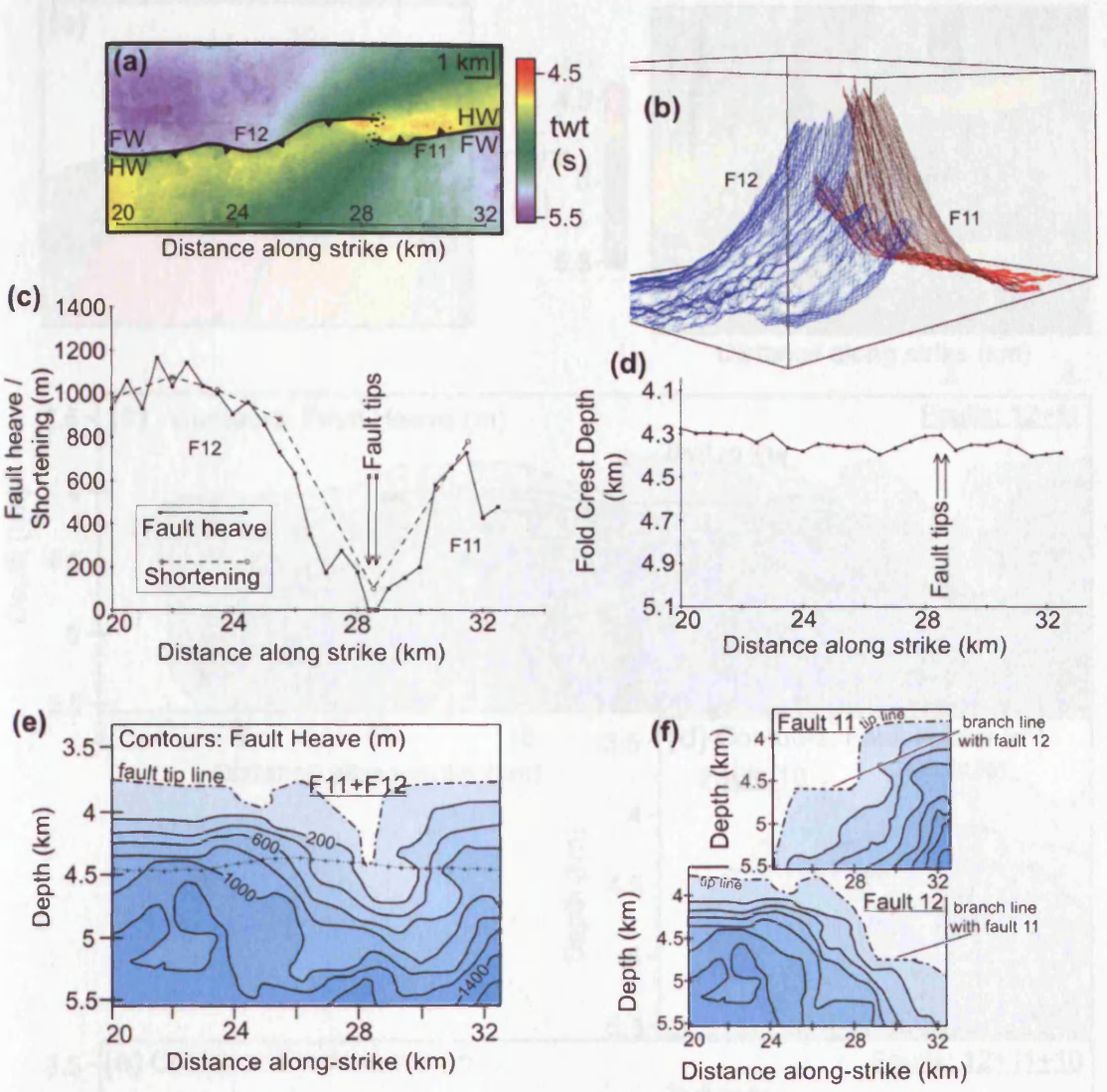

Figure 5.9: Analysis of the distribution of fault heave in a Type 2 antithetic thrust fault linkage zone (as defined in Chapter 3). Linkage occurs between faults and folds 11 (backthrust) and 12 (forethrust). **(a)** Topographic map of horizon m4 in the region of the transfer zone presented in two-way-time (s). FW: footwall. HW: hangingwall. **(b)** 3D visualisation of the transfer zone. Fault surfaces continue in and out of the page. **(c)** Heave – distance plot for faults through the transfer zone measured on horizon m4. Note that faults do not overlap with respect to horizon m4 due to its stratigraphic level and hence heave reduces to zero at around 28.5 km along strike. In a Type 2 linkage fault overlap varies with depth (see Figure 3.11). **(d)** Along strike variation in the depth to the fold crest on horizon m4. Note that fold height is maintained along strike. **(e)** and **(f)** Strike projected contour plots of fault heave. (e) Cumulative fault heave contoured profile (summation of faults 11 and 12). Stratigraphic level of m4 shown by joined 'cross' symbols. (f) Individual fault heave contoured profiles. Note that scale is reduced on these plots. Lateral tip regions of faults form typical downwards-tapering, 'depressed' tip lines of a Type 2 linkage (see Figure 3.8).

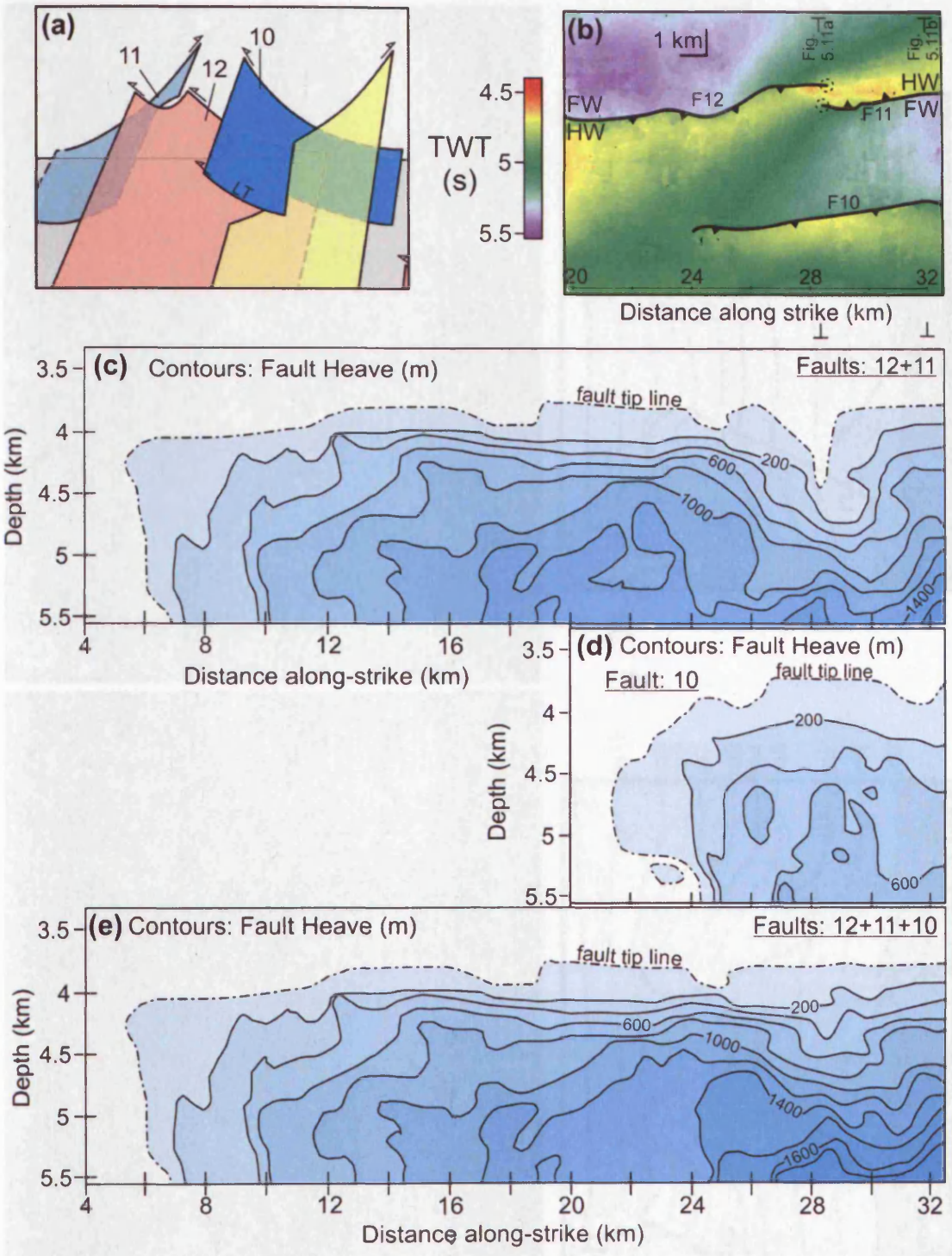

Figure 5.10: Complementary heave distribution patterns on a structure located up regional dip from the zone of heave deficit in the transfer zone featured in Figure 5.9. **(a)** Conceptual 3D geometry of faults10, 11 and 12. Taken from Figure 5.4. **(b)** Topographic map of horizon m4 in the region of the transfer zone presented in two-way-time (s). FW: footwall. HW: hangingwall. **(c)** Aggregate strike projected contour plot of heave values for faults 11 and 12. Deficit in heave in the transfer zone is expressed as irregularities in the distribution of heave and 'depressed' contour lines between 26 and 31 km along strike. **(d)** Individual fault heave contoured profile of Fault 10. The shape and location of the zone of maximum heave is aligned with the minimum recorded in (c). **(e)** Aggregate strike projected contour plot of heave values for faults 10, 11 and 12. The addition of Fault 10 into the aggregated profile increases the regularity of contours between 26 and 31 km along strike and produces a profile closer to that of Fold A in Chapter 4 (Fig. 4.5).

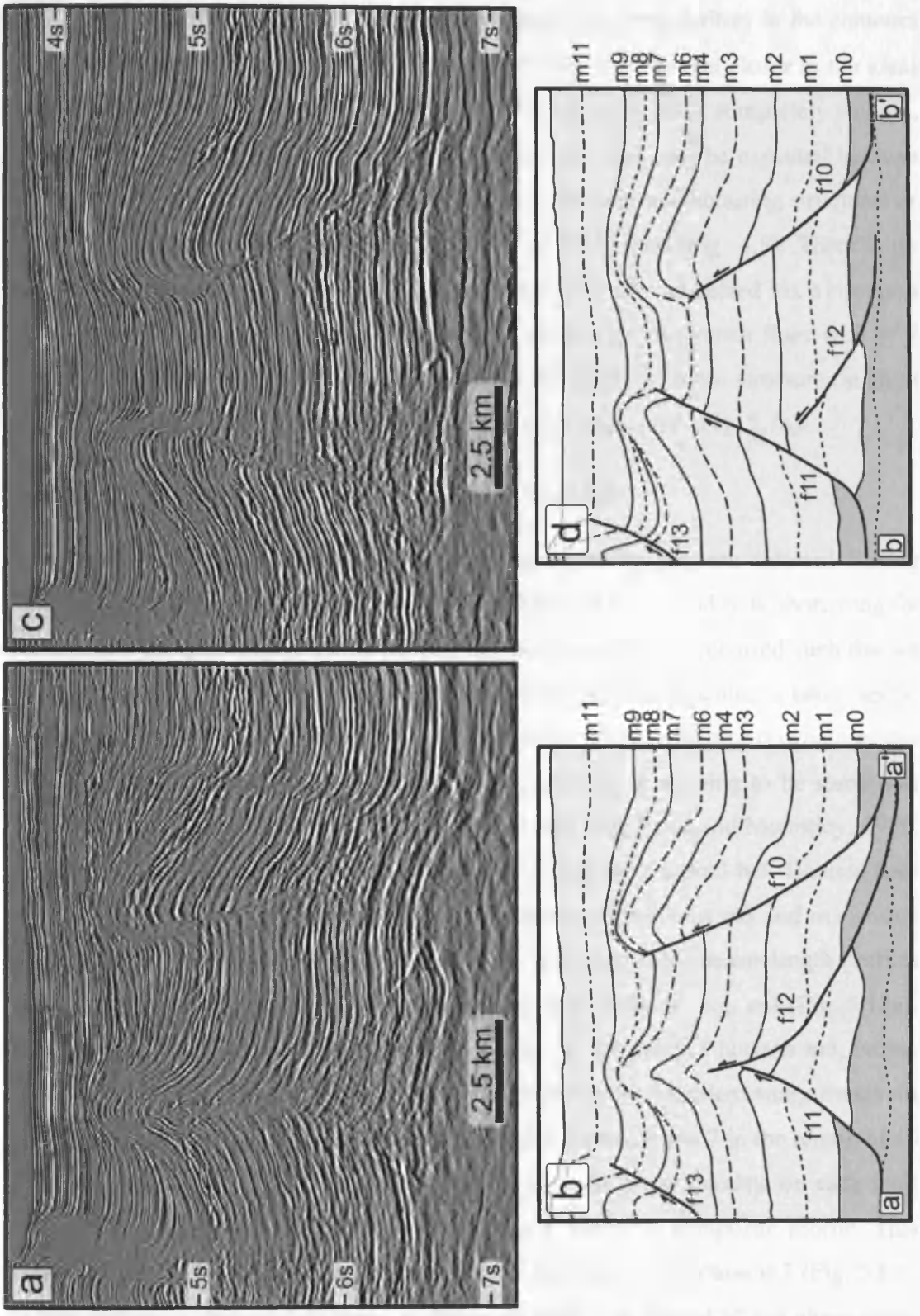

Figure 5.11: Example seismic sections through the linkage zone of Faults 11 and 12 oriented perpendicular to fault strike. Locations of lines are given in Figure 5.10. **(a)** Seismic section through the centre of the transfer zone. **(b)** Interpretation of (a). Note the vertical extent of faults 11 and 12, the shape of the folds and the amount of heave on Fault 10 on horizon m4. Faults 11 and 12 have approx. equal displacement, one fold is symmetric and Fault 10 displays increased heave on horizon m4 compared to (d). **(c)** Seismic section along strike from the centre of the transfer zone. **(d)** Interpretation of (c). In this case *ff*11 is dominant, folds are asymmetric and Fault 10 has reduced heave on horizon m4 compared to (b).

fault heave on *ff* 10 (Fig. 5.10d). When aggregated, the irregularities in the contours related to the transfer zone are smoothed (Fig. 5.10e) and brought closer to the ideal profile of a single non-linking fault (Fig. 4.5). The result is not a completely smooth, ideal profile however, and some irregularities remain. This may be expected because further displacement transfer may have occurred with other neighbouring structures or be accommodated by variations in the amount of fold strain (Fig. 4.5). There is no hard linkage between *ff* 11/12 and *ff* 10 but rather they are connected via a common detachment level (Fig. 5.11) and along strike, indirectly, via branch lines with *ff* 7 (Fig. 5.4). Analysis of sedimentary packages on the flanks of these structures suggest that *ff* 10, 11 and 12 all initiated at approximately the same time (Fig. 5.7a).

5.6.4. Distribution of shortening in a fold and thrust belt

Following the description of displacement transfer between selected linking structures, it is interesting to consider the distribution of heave and bulk shortening for the fold and thrust belt as a whole. If displacement transfer has occurred such that an along strike decrease in the amount of deformation on one structure is taken up by another structure (e.g. Dahlstrom, 1970), either along strike, updip or downdip across the array, then it is reasonable to predict values of bulk shortening to be somewhat consistent along the length of the fold and thrust belt (e.g. Price and Mountjoy, 1970; Liu and Dixon, 1991). The degree to which this is true for the fold belt featured here varies with depth and is highlighted by a comparison of horizons m6 and m3 within (i) the Frontal Array and (ii) the entire fold belt. It is clear from heave-length profiles that aggregate values are more irregular along deeper horizons, e.g. m3 (Fig. 5.13a), than on shallower examples, e.g. m6 (Fig. 5.12a). In the case of horizon m6, lateral variations in heave along individual faults are mirrored by complementary trends on neighbouring faults. This can be demonstrated with faults 12 and 7 in the region of 10 and 25 km along strike (Fig. 5.12f). A number of local heave maxima on each fault correspond with minima on the other producing a smoother composite profile. This relationship is not replicated for values of heave measured on horizon m3 (Fig. 5.13). In this instance a dramatic decrease in heave on fault 7 at around 12 km along strike (Fig. 5.13d) is not accompanied by a complementary trend on fault 12 (Fig. 5.13b) and is reflected in an irregular aggregate heave profile (Fig. 5.13a).

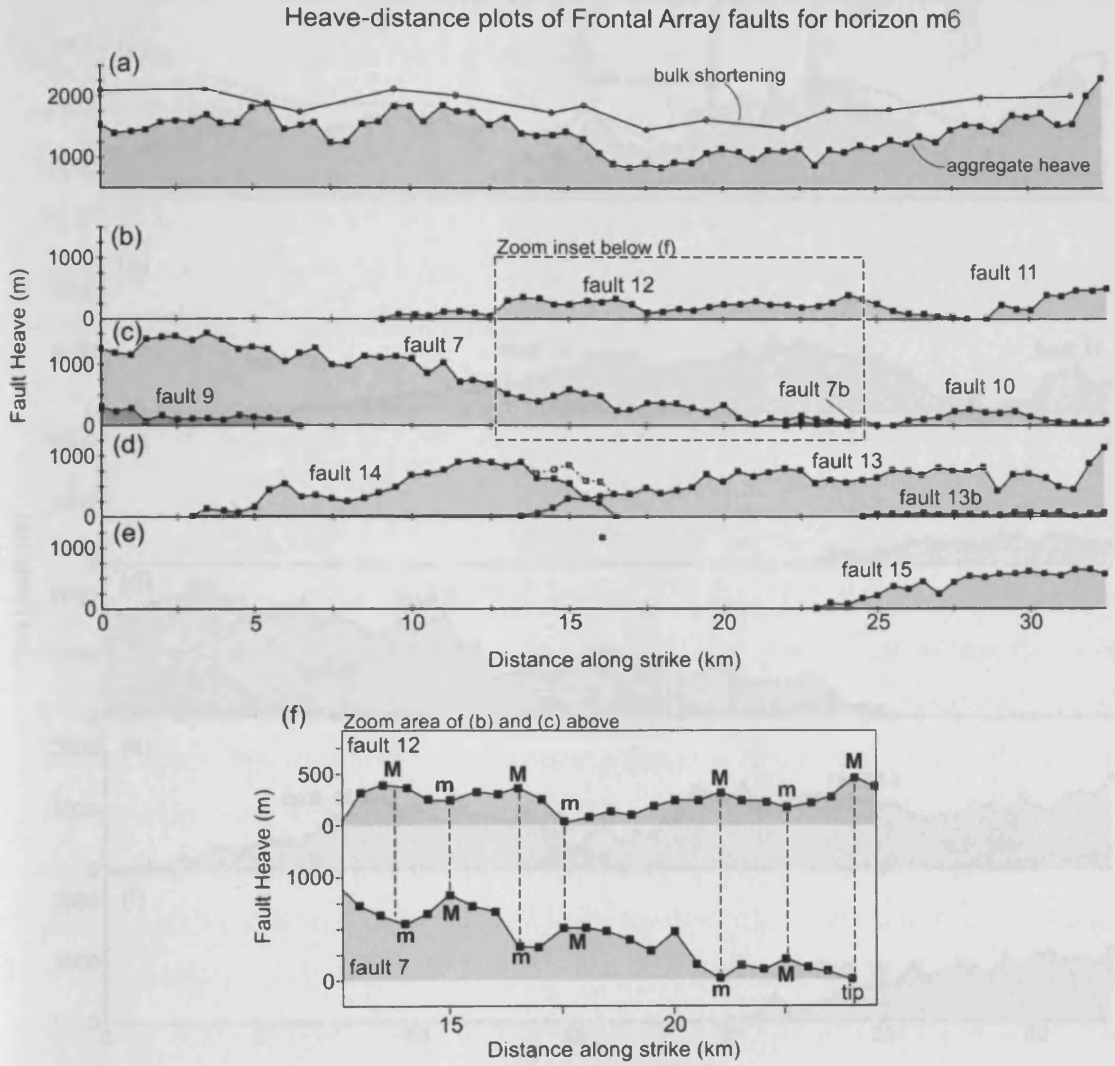

Figure 5.12: Heave-distance graphs for faults of the Frontal Array measured on the *syn-kinematic horizon* ***m6***. **(a)** Aggregated heave-distance graph of all faults in the Frontal Array (Faults 7 to 15). Profile of bulk shortening values across the Frontal Array is also presented. **(b)** to **(e)** Individual heave-distance plots for Faults 7 to 15. (b) Faults 11 and 12. (c) Faults 7, 7b, 9 and 10. (d) Faults 13, 13b and 14. (e) Fault 15. Note that not all faults have heave profiles (e.g. Fault 8) as not all faults offset the shallower syn-kinematic horizons. **(f)** Zoomed plot of part of the heave-distance profiles of Faults 7 and 12 to show complementary along strike trends in fault heave.

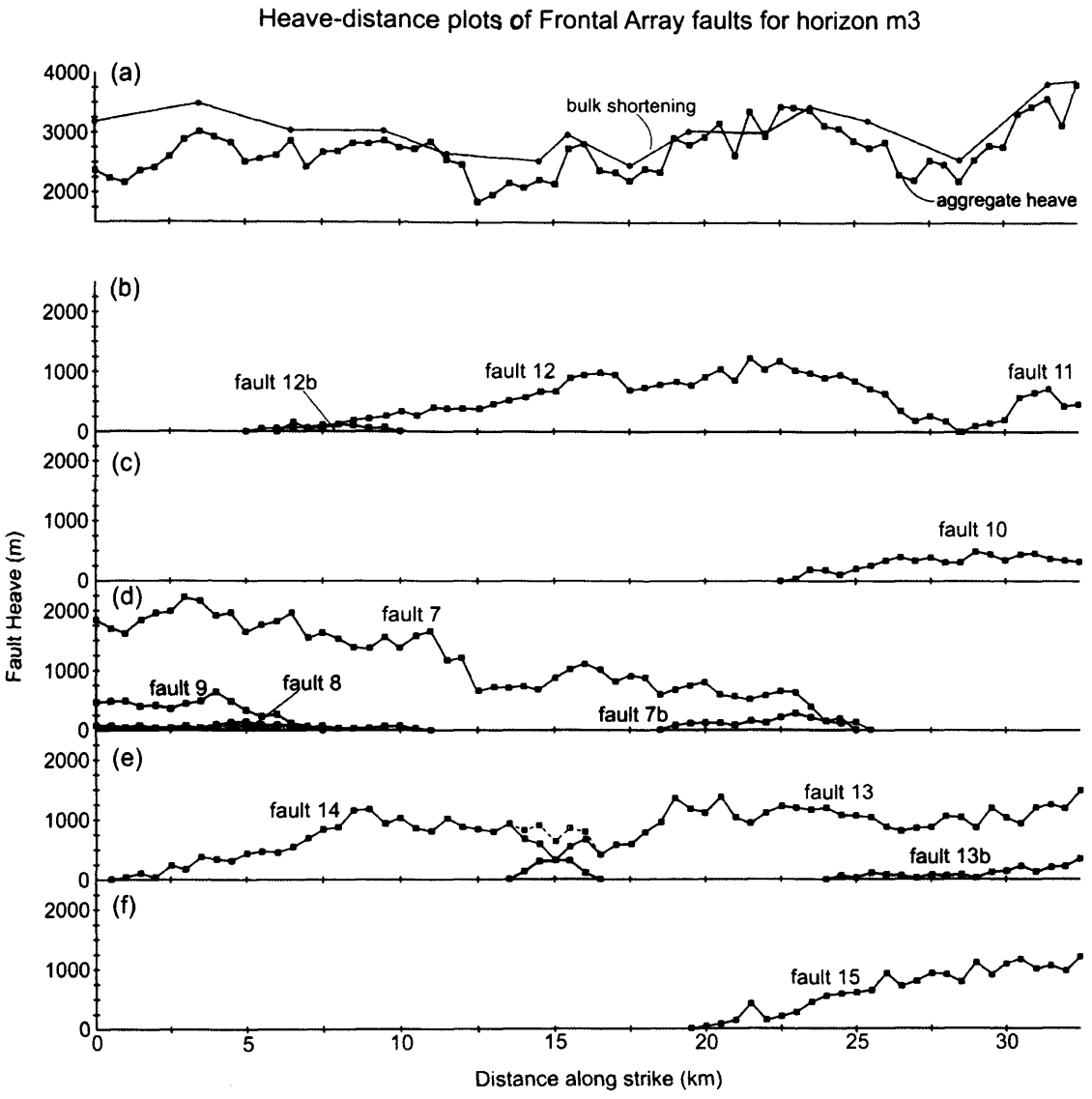

Figure 5.13: Heave-distance graphs for faults of the Frontal Array measured on the *pre-kinematic horizon* ***m3***. **(a)** Aggregated heave-distance graph of all faults in the Frontal Array (Faults 7 to 15). Profile of bulk shortening values across the Frontal Array is also presented. **(b)** to **(f)** Individual heave-distance plots for Faults 7 to 15. (b) Faults 11, 12 and 12b. (c) Fault 10. (d) Faults 7, 7b, 8 and 9. (e) Faults 13, 13b and 14. (f) Fault 15.

Measurements of bulk shortening are also more consistent along strike than those of aggregate fault heave. This is most pronounced on the m6 horizon (Fig. 5.12a). An overall shortfall in heave between 15 and 27 km along strike is less significant in the shortening curve and would suggest an increase in continuous strain in this area, as described in Chapter 4 for an isolated fold (Fig. 4.5). Shorter wavelength, more pronounced variations in fault heave on horizon m3 correspond to a similar trend in shortening (Fig. 5.13a) resulting in more pronounced maxima and minima.

This contrast in the distribution of deformation at various stratigraphic levels within the Frontal Array is more clearly demonstrated on strike projected contour plots of aggregate heave and bulk shortening (Fig. 5.14). The most pronounced feature of these profiles is the dissimilarity between the regular, evenly spaced sub-horizontal contours above a depth of around 4.25 km and the irregular contours below. The boundary between these two regions is approximately parallel with stratigraphy and coincides with the delineation of pre- and syn-kinematic sequences. This boundary line is defined as the stratigraphic level of fold onset of the first structure(s) to nucleate within the Frontal Array, i.e. *ff* 10 and 11 (Fig. 5.7). Lateral displacement gradients within the syn-kinematic sequence are extremely low and heave is preserved along strike (Fig. 5.14a). Numerous maxima and minima within the pre-kinematic units reflect a variable trend in both heave and shortening along strike. The significance of the distribution and regularity of shortening in relation to the timing of fold growth is discussed in a later section.

5.7. Discussion

Previous descriptions of isolated thrust-related folds (e.g. Rowan, 1997; Higgins et al., in review) have provided insight into the growth history of single structures from initially discrete segments (Chapter 4). The section of a 70 km wide deep water fold and thrust belt featured in this study provides an exceptional opportunity to apply the hypotheses derived from simpler structures to a more complex fold and fault array. The analysis of the distribution of shortening within an area comprising numerous synthetic and antithetic fault linkages allows conclusions to be drawn on the nature of displacement transfer between interlinking faulted folds. A remarkable aspect of this study stems from the degree of synchronous growth

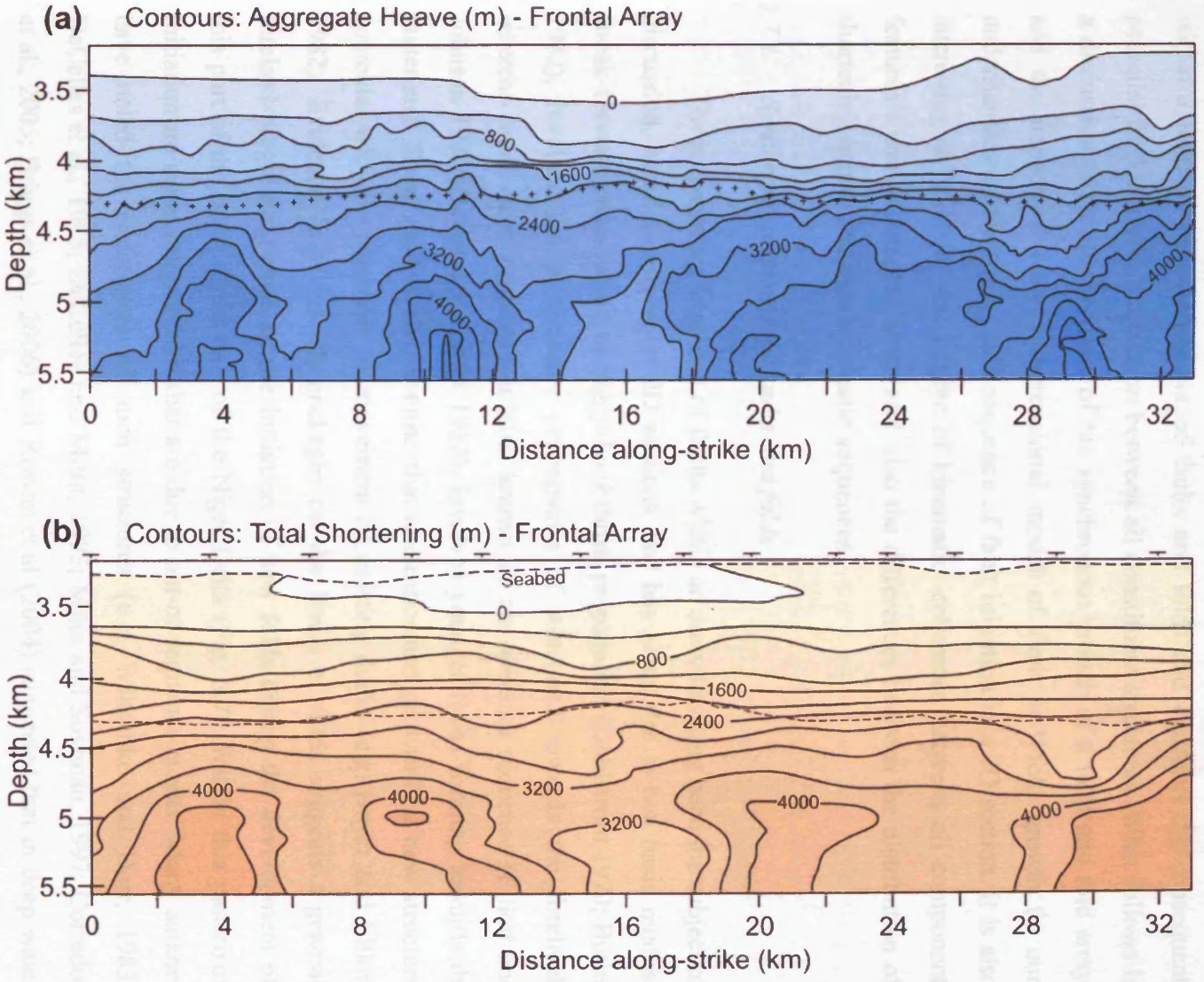

Figure 5.14: Strike projections of aggregated fault heave and bulk shortening for the Frontal Array. **(a)** Distribution of fault heave. Cross symbols indicate the sampling points of horizon m4, which represents the stratigraphic level of the onset of folding within the Frontal Array (i.e. is the boundary between pre- and syn-kinematic units). Note that above horizon m4 contours are regular, sub-horizontal and sub-parallel with stratigraphy. Below horizon m4 contours are irregular and record several locations of heave maxima. **(b)** Distribution of bulk shortening within the Frontal Array. Dashed line indicates the location of horizon m4. Contours show a similar pattern with regards pre- and syn-kinematic units to heave contours in (a). Further discussion on the shape of contours is given in the text.

within a foreland-propagating set of faults and folds and concerns the consequent potential for kinematic interaction between all constituent structures. What follows is a discussion of the implications of the synchronous growth of a fault and fold array and the impact of a three dimensional model of fault and fold growth for our understanding of the timing and sequence of fault initiation in a 2D section. It is also interesting to consider the degree of kinematic coherence between all component features within a complex array and also the differences between the distribution of shortening in pre- and syn-kinematic sequences.

5.7.1. Synchronous growth of faults and folds

The propagating sequence of faults within an array has long been the subject of discussion, based largely upon 2D sections, and has given rise to two basic models. Break-forward propagation, or *piggy-back* thrust propagation (Dahlstrom 1970; Butler 1982), involves the progressive propagation of structures towards the foreland, whereas break-back propagation, also known as an *overstep* sequence (Elliott and Johnson 1980; Boyer and Elliott 1982), involves younger faults forming towards the hinterland. These models also assume that nucleation and growth of a new structure coincides with the cessation of movement on existing faults (e.g. Boyer and Elliot, 1982). Evidence from growth packages on the limbs of folds suggests a general foreland-progressing trend in the initiation of new folds during the development of this part of the outer thrust belt of the Niger Delta (Fig. 5.7). Within this pattern of initiation are some irregularities that are due to out-of-sequence events. Many authors have noted the occurrence of such structures (e.g. Wiltschko and Dorr, 1983; DeCelles et al., 1995; DeCelles and Mitra, 1995; Mitra and Sussman, 1997; Corredor et al., 2005; Briggs et al., 2006) and Rowan et al (2004) suggested that in deep water settings this could reflect the nature of shale-detached fold belts which rely on overpressure to accommodate gravitational collapse (e.g. Wu and Bally, 2000). Pore fluid pressures in the shale units can fluctuate locally due to processes such as dewatering following fault movement, dehydration reactions, the production of hydrocarbons (Rowan et al., 2004) or disequilibrium compaction. Observations of the onset and cessation of folding also reveal a history of synchronous growth of faults and folds in the study area (Fig. 5.7), a finding supported by displacement transfer between faults and folds in the Frontal Array (Fig 5.12). This statement does not

account for the possibility of changes in individual rates of shortening accumulation during the lifespan of a given fault and fold and hence does not describe which folds grew when and by how much within a period of contemporaneous growth. Rowan et al (2004), for instance, argue that episodic movement is common in shale based deformation. It does show however, that during the progression of deformation into the foreland, the inception of each new structure did not coincide with the cessation of movement on older elements (Fig. 5.7). Synchronous growth of features in a fault array underlines the potential for geometric and kinematic coherence between structures. This coherence would be expressed as a more complex kinematic history with the possibility of closely spaced fold and faults experiencing stress perturbations from propagating neighbouring structures.

Given the three-dimensional nature of fault propagation (e.g. Suppe, 1983; Cooper et al., 2003), the order in which a fault appears in any given cross section may not reflect the order in which fault surfaces nucleated within the array (Walsh and Watterson, 1991). Chapter 4 demonstrated that numerous folds and faults can nucleate at approximately the same time and propagate along strike to link into a through-going structure (Fig. 4.16). Nucleation sites were shown to be close to, but not necessarily directly at, areas of maximum fault heave in the present day (Fig. 4.14). The seismic survey featured in this chapter is located towards the foreland from this isolated structure in Chapter 4 and images faults that propagated within the same stratigraphic sequence, at a similar time, detach on the same regional decollement and form very similar linkage geometries. If we therefore apply this model of growth to the Frontal Array, the position at which a dip-parallel 2D section is located along the length of the fold and thrust belt may affect the apparent order of thrust nucleation recorded within that section. The along strike interaction and displacement distribution of fault and folds *(ff)* 10, 11 and 12 (Figs. 5.10 and 5.11), for instance, suggest three initially spatially distinct thrusts formed at roughly the same time (Fig. 5.7) and grew laterally towards each other. If this is the case, then sections through and to one side of the *ff* 11/12 linkage would record different sequences of thrust initiation (assuming sufficient stratigraphic dating resolution). Growth strata on a section that passes through the linkage zone indicate that Fault 10 predates Faults 11 and 12 (given that Fault 10 nucleated close to the area of maximum heave) (Fig. 5.11a). Fault and folds 11 and 12 would predate *ff* 10 on sections either side (e.g. Fig. 5.11b) containing the lateral tips of fault 10.

It can also be tempting to predict, from a 2D section, the temporal relationship between a detaching thrust fault and an intersecting antithetic fault located exclusively within the hangingwall and forming a branch point at its lower tip (e.g. Fig. 5.3b). The three-dimensional geometries of antithetic fault linkages described in Chapter 3 (Fig. 3.11) and the evidence for the lateral propagation of linking thrusts from chapter 4 (Fig. 4.14) suggests the relative timing of fault surfaces is difficult to discern from 2D sections.

5.7.2. Response of fold height and fold shape to fault linkage

Davis et al (2005) noted a relationship between the length of the lateral overlap of linking faults and the efficiency of displacement transfer, such that greater overlaps produce smoother aggregate displacement profiles with little or no deficit within the transfer zone. A similar correlation is observed in this portion of the Niger Delta exemplified by the comparison of two Type 1 linkages (Fig. 5.8). The first example (Fig. 5.8a) has a lateral overlap of around 7 km, described in Chapter 4, and displays heave values that sum close to the ideal profile of a single fault. The second example, involving *ff* 13 and 14 (Fig. 5.8d), has half the lateral overlap and has a deficit in fault heave within the zone of overlap (Fig. 5.8e). One of the most interesting observations made in this study, however, is the lack of correlation between fold crest height and deficits in fault heave (Fig. 5.8c and f). This is noted on all types of linkages and also applies to instances of shortening deficit (Fig. 5.9c and d). Simpler structures display a close relationship between shortening (or heave) and the amplitude of the fold, as in the case of the single fault and fold from Higgins et al. (2007) (Fig. 3.4) and the isolated fold in Chapter 4 (Fig. 4.6). Therefore it is hypothesised that fold shape must be modified within zones of antithetic linkage to allow for the preservation of fold height. This premise appears accurate for the *ff* 11/12 linkage where horizon m3, for example, forms a classic asymmetric hangingwall anticline away from the zone of linkage (Fig. 5.11b) but describes a tight, symmetric fold with a low inter-limb angle at the central position (Fig. 5.11a). This change in shape enables lower heave and shortening values to be associated with elevated fold crests and therefore maintain fold amplitudes along strike. In this case the fold shape may be controlled by the two thrusts faults that abut at depth producing a 'bell-shaped' fold in the overburden (Fig.

5.11a). It can be concluded therefore, that in areas of fault linkage, fold height or fold amplitude are not necessarily indicative of the amount of shortening accommodated by a particular horizon and that continuous deformation (i.e. folding) does not always compensate for deficits in fault displacement.

5.7.3. Kinematic coherency of a fold and thrust belt

The synchronous growth of all structures within the fold and thrust belt (Fig. 5.7) indicates there is potential for the system to be kinematically coherent (Walsh and Watterson, 1991). In such a scenario the timing and distribution of displacement on one element of the fold and fault belt is related to the timing and distribution of deformation on all other parts of the array. The development of contemporaneous structures is essential for kinematic coherence and therefore it may be applicable to areas deforming as a critical-taper wedge, if the nucleation of structures in the foreland can be associated with continued accumulation of displacement on early faults in the hinterland (e.g. Davis et al., 1983).

The study of selected examples of linking faults and folds demonstrates the transfer of displacement both along strike and in a dip-parallel direction. The minimum in shortening located within the *ff* 11/12 transfer zone has been shown to correspond with a maximum on the neighbouring updip structure, *ff* 10 (Fig. 5.10). Based on criteria for kinematic interaction, cited as complementary modifications to fault displacement patterns from a reference standard (e.g. Barnett et al., 1987; Walsh and Watterson, 1991) and the observation of relay structures (Muraoka and Kamata, 1983; Larsen, 1988; Huggins et al., 1995), it can be concluded that the transfer of displacement, and of shortening, between these structures has occurred both along strike and in a dip-parallel direction. The aggregation of heave on these three faults (Fig. 5.10e) improves the regularity of contours within the *ff* 11/12 transfer zone and produces a profile closer to that of a single structure. This process does not however fully restore the deficit observed. Fault and fold 10 was the most likely candidate for dip-parallel displacement transfer as it is located immediately updip (Fig. 5.5) and displayed complementary geomorphology. It is conceivable that displacement transfer may have occurred between all features of the Frontal Array, and indeed the fold belt

as a whole, as all grew synchronously and are connected via common detachments and/or the hard-linkage of antithetic faults.

It is interesting to firstly consider the kinematic interaction of the faults in the Frontal Array, apart from the rest of the fold belt, as it is an excellent example of a complex folded sequence comprising a set of thrusts that are connected via common basal detachments but are also hard-linked into a single system via antithetic fault linkages above the detachment (Fig. 5.4). The aggregation of heave values for *all* faults in the Frontal Array produces sub-horizontal contours in the shallow section (<4.25 km depth) on the strike projection (Fig. 5.14a). This suggests that as heave decreases on one structure there is a corresponding complementary increase on another. This is most clearly demonstrated at lateral tip regions of linking faults within a single through-going fold such as the *ff* 13/14 interaction approximately 15 km along strike (Fig. 5.12d). Complementary heave profiles also occur away from fault tips within the Frontal Array. Faults 7 and 12 are hard-linked via branch lines that almost span the complete width of the survey (Fig. 5.4) and show opposite trends in fault heave along their entire length within the shallow section (Fig. 5.12f). Small amplitude irregularities in fault heave on each fault is mirrored by the other, such that local maxima on one trace corresponds, in a dip-parallel direction, with minima on the counterpart fault (Fig. 5.12f). Aggregation along shallow horizons within the Frontal Array therefore produces relatively consistent values of fault heave along strike and sub-horizontal contours on strike projections that demonstrate very low lateral heave gradients. Minor undulations in heave contours are less pronounced on the shortening profile (Fig. 5.14b) again suggesting continuous strain compensates for variations in discontinuous deformation. Within the deeper section (>4.25 km depth) the distribution of aggregate heave and bulk shortening is more irregular and contours do not follow the sub-horizontal patterns above (Fig. 5.14). The significance of this is discussed in the subsequent section.

The inclusion of all structures in the fold and thrust belt in the aggregation produces a similar profile to that of the Frontal Array with sub-horizontal contours characterising the shallow section (<4.5 km) (Fig. 5.15). All faults in this scenario are linked via common detachments. The uniform, regular and sub-horizontal nature of contours within the shallow section (< 4.5 km depth, Fig. 5.15) suggests displacement transfer has occurred between all structures during synchronous growth. Contours are

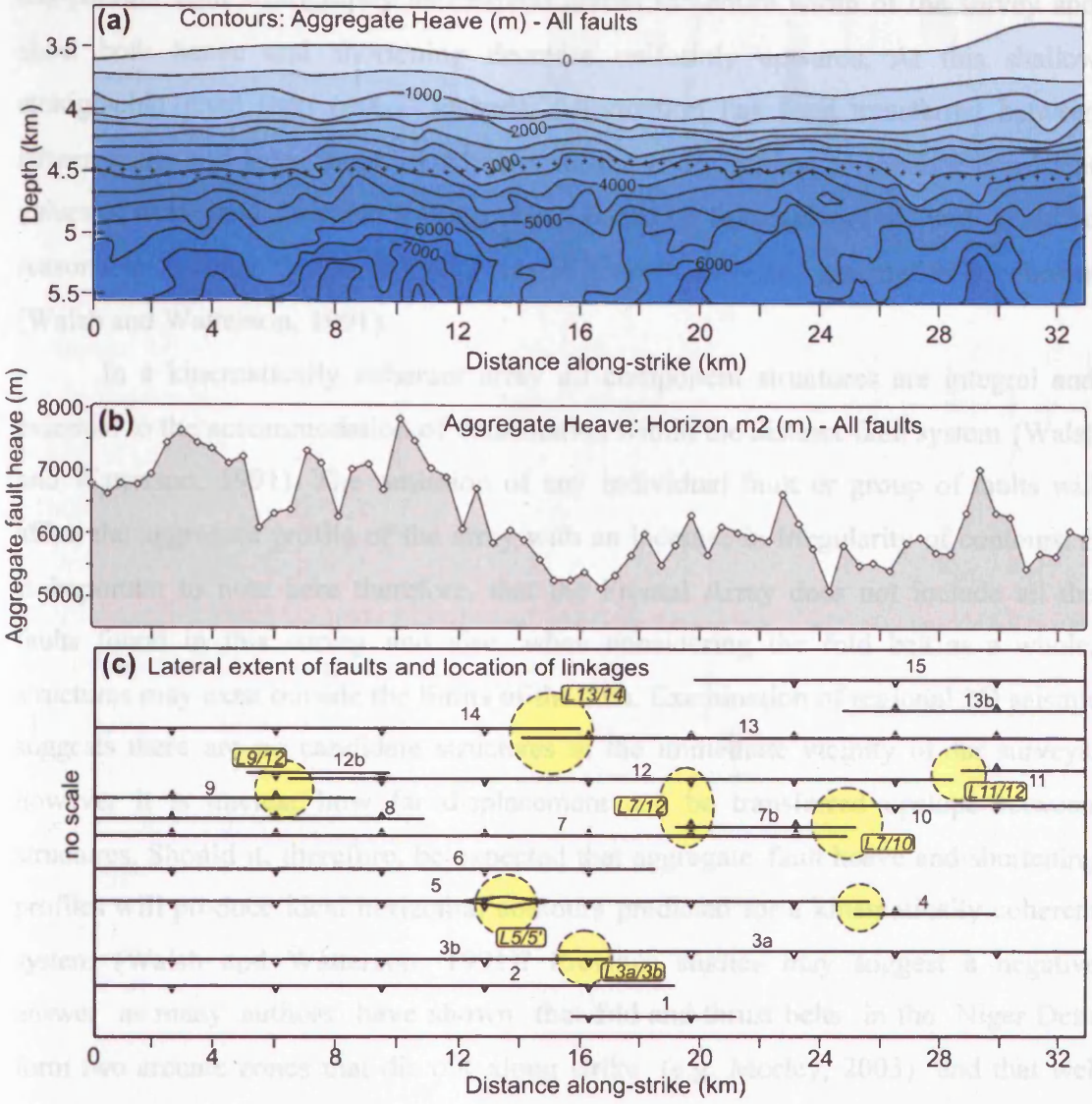

Figure 5.15: Distribution of fault heave within the fold belt and its relationship with fault linkage points. **(a)** Strike projected contour plot of aggregate fault heave for all faults within the fold belt (Faults 1 to 15). Cross symbols indicate the sampling points of horizon m3, which represents the stratigraphic level of the onset of folding within the fold belt (i.e. is the boundary between pre- and syn-kinematic units). Above horizon m3 contours are regular, sub-horizontal and sub-parallel with stratigraphy. Below horizon m3 contours are irregular and record several locations of heave maxima. Note that the level of fold onset here is stratigraphically below that given in Figure 5.14 as Folds 3a and 5 initiated earlier than those in the Frontal Array (see Fig. 5.7). **(b)** Aggregate heave-distance graph for all faults showing along strike variations in summed heave measured on the pre-kinematic horizon m2. **(c)** Graph to show lateral extent of thrust faults in the fold belt. Locations of major along strike linkage zones are indicated by yellow ellipses (e.g. *L13/14* refers to the linkage between faults and folds 13 and 14). Spacing between fault traces are not representative of true distances.

sub-parallel with stratigraphy and extend across the entire width of the survey and show both heave and shortening decrease uniformly upwards. At this shallow stratigraphic level then (m4 – seabed), deformation has been transferred between fifteen faults and folds, none of which span the entire survey, to produce consistent values of heave and shortening along strike. Based on this evidence alone it would be reasonable to conclude the Frontal Array is geometrically and kinematically coherent (Walsh and Watterson, 1991).

In a kinematically coherent array all component structures are integral and essential to the accommodation of deformation within the distinct fault system (Walsh and Watterson, 1991). The omission of any individual fault or group of faults will affect the aggregate profile of the array with an increase in irregularity of contours. It is important to note here therefore, that the Frontal Array does not include all the faults found in this survey and also, when considering the fold belt as a whole, structures may exist outside the limits of the data. Examination of regional 2D seismic suggests there are no candidate structures in the immediate vicinity of our surveys, however it is unclear how far displacement can be transferred upslope between structures. Should it, therefore, be expected that aggregate fault heave and shortening profiles will produce ideal horizontal contours predicted for a kinematically coherent system (Walsh and Watterson, 1991)? Previous studies may suggest a negative answer as many authors have shown that fold-and-thrust belts in the Niger Delta form two arcuate zones that die out along strike (e.g. Morley, 2003) and that well developed imbricate zones can pass laterally into regions of low shortening where only a few imbricates, pop-ups and triangle zones are developed (Morley and Guerin, 1996; Hooper et al., 2002). These changes in fold belt geometry and shortening may be due to variations in the thickness of mobile shale substratum (Morley, 2003) that could significantly affect aggregate profiles of displacement. Despite these observations however, it is clear that faults and folds comprising this section of the outer thrust belt show complementary trends in heave and shortening that demonstrate displacement transfer between numerous elements and move aggregate profiles of the distribution of deformation closer towards that of a single structure.

5.7.4. Controls on the distribution of bulk shortening

It is worth considering the relationship between the timing of sedimentation relative to the onset of folding and the distribution of shortening within the stratigraphic section. Displacement transfer between neighbouring faults and folds, both along strike and in a dip-parallel direction, can lead to relatively consistent values of bulk shortening along strike and cumulative profile projections should therefore be characterised by sub-horizontal contours. We discussed in previous sections how this is the case for values of heave recorded on shallow stratigraphic horizons (4.25 km) within this seismic survey. Below this level however (~4.25 km), contours are not sub-horizontal and display several maxima and minima along strike in both heave and shortening (Figs. 5.14 and 5.15). Childs et al. (2003) described similar distributions on syn-sedimentary normal faults in the Gulf of Mexico and noted that on individual faults the boundary between sub-horizontal and, in their case, sub-vertical contours demarcates the syn- and post-sedimentary regions of the fault plane. To apply this observation to a compressional regime, fault heave distributions are discussed with respect to pre- and syn-kinematic stratigraphy for three structural case studies: i) a singly faulted fold, ii) a potential synthetic thrust fault linkage zone and iii) the fold belt as a whole.

Fault and fold *(ff)* 3a comprises a single forethrust and an oceanward-vergent hangingwall anticline (Fig. 5.16). Some of the fault and fold is located outside of the survey boundaries and hence only one lateral tip is imaged. Fault and fold 3a links synthetically with *ff* 3b along strike, however this is considered to be at an early stage of linkage as folding reduces to zero at a saddle point within the relay zone (Fig. 5.1) and fault heave gradients remain constant towards the linkage zone. Fault heave contours on the majority of the fault length (c. 14 – 33 km along strike) are taken to represent an example of the distribution of displacement on a single fault during fold growth. Fault heave contours above a depth of approximately 4.5 km are sub-horizontal, sub-parallel and closely spaced (Fig. 5.16). Below this depth contours become more irregular to become sub-vertical close to the detachment, at around 5.75 km depth. The boundary between these two areas coincides with the stratigraphic level of the onset of folding (Fig. 5.16, dashed line), which delineates the syn-kinematic sediments above from the pre-kinematic sequence below. The change in character of heave contour shape is clearly demonstrated by the 800 m contour (Fig.

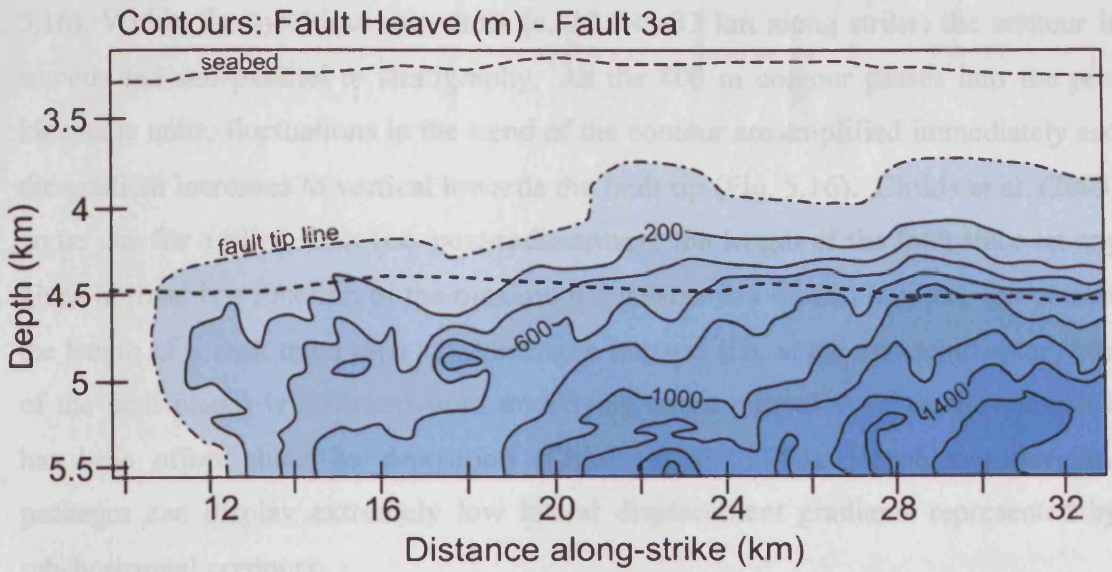

Figure 5.16: Strike projected contour plot showing the distribution of heave on Fault 3a. Fault tip line joins the points of zero fault heave observable on seismic data. Base of the plot is the level of the detachment. Dashed line indicates the depth of horizon m3, which represents the stratigraphic level of the onset of deformation for Fold 3a (i.e. is the boundary between pre- and syn-kinematic units). Contour display increased regularity above the level of m3 than below.

5.16). Within the syn-kinematic units (c. 27.5 to 33 km along strike) the contour is smooth and sub-parallel to stratigraphy. As the 800 m contour passes into the pre-kinematic units, fluctuations in the trend of the contour are amplified immediately and the gradient increases to vertical towards the fault tip (Fig. 5.16). Childs et al. (2003) argue that for a blind fault (i.e. post-sedimentary) the length of the fault trace on any given horizon is a function of the maximum displacement on that horizon. In contrast, the length of a fault trace on a syn-kinematic horizon (i.e. at the syn-sedimentary part of the fault plane) is inherited from underlying strata regardless of the how much it has been offset since its deposition (Childs et al., 2003). Hence syn-kinematic packages can display extremely low lateral displacement gradients represented by sub-horizontal contours.

Fault 5 displays a similar heave distribution to fault 3a with smooth, sub-horizontal contours within the syn-kinematic package and irregular contours below (Fig. 5.17a). The stratigraphic level of fold onset again coincides with the boundary between these two areas and also intersects the points of maximum curvature of heave contours (Fig. 5.17a). In contrast to fault 3a, fault 5 exhibits two distinct areas of heave maxima in the pre-kinematic section separated by a significant minimum. This pattern is not reflected in syn-kinematic contours which remain sub-parallel with stratigraphy throughout (Fig. 5.17a). Two dip-parallel seismic sections located through the maximum at c. 19 km along strike (Fig. 5.17b, c and e), and the minimum at c. the 14 km position (Fig. 5.17d and f), show varying fault plane geometries. The former section (w – w') comprises a clear single fault plane reflection (at the resolution of seismic) (Fig. 5.17c and e). The latter section (v – v') exhibits two fault planes separated by a distance of approximately 300 m (Fig. 5.17d and f). The two surfaces converge on a branch line at c. 5.75 s twt, seen as a branch point in section (Fig. 5.17d). This geometry is limited in extent from c. 12 km to 15 km along strike (Fig. 5.17g). One interpretation of such geometry could be that this is a breached synthetic relay zone and that two initially distinct faults have linked to form Fault 5 and the associated, single through-going fold. If correct, the minimum in fault heave seen in the pre-kinematic units (Fig. 5.17a), records the location of the original relay zone. Childs et al (2003) also noted that, as with blind faults, much of the complexities seen in syn-sedimentary faults is due to fault interaction, linkage and capture most commonly associated with a relay zone. Deficits in heave and shortening

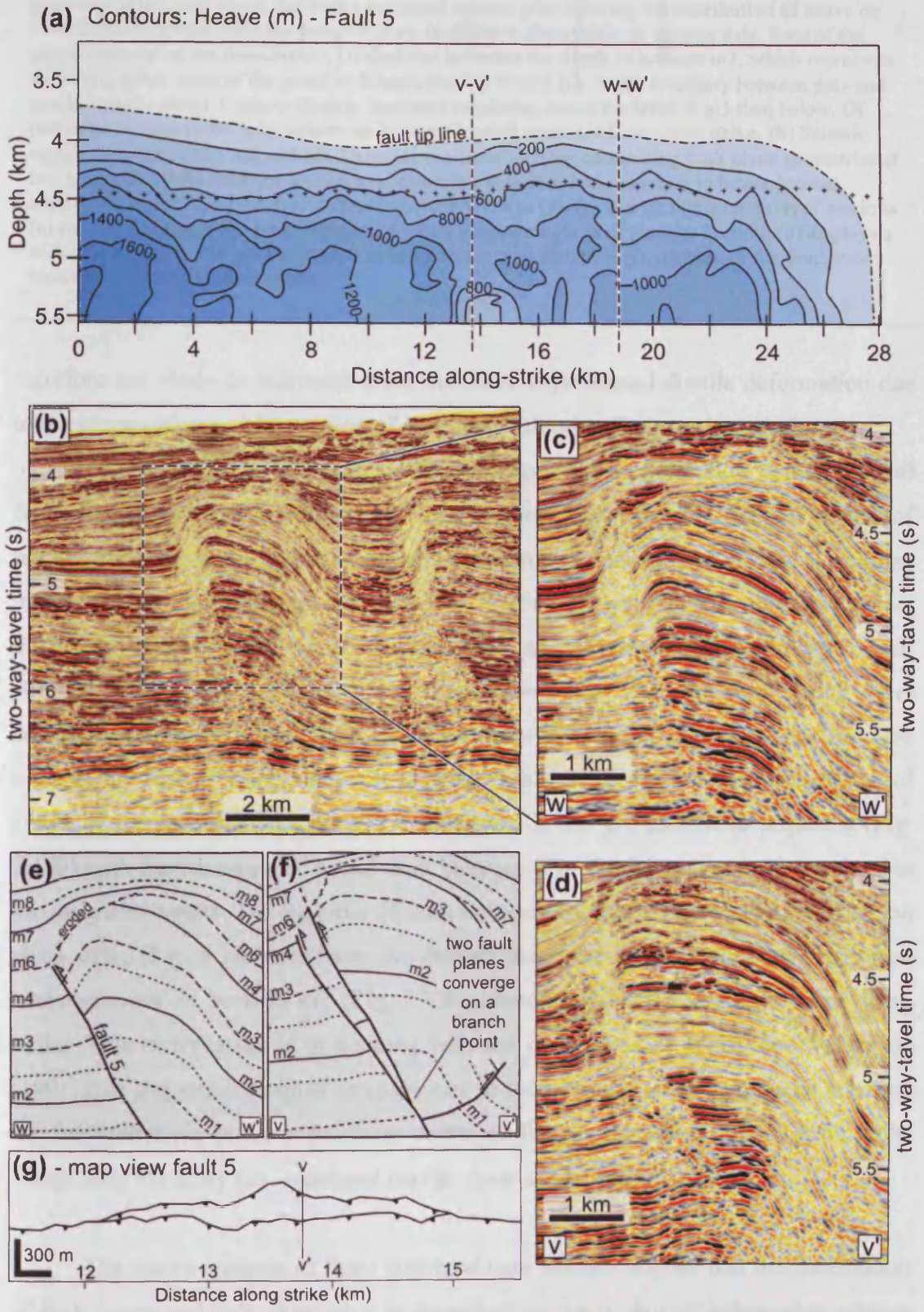

Figure 5.17: see next page for caption

Figure 5.17: Analysis of the relationship between the distribution of heave on Fault 5 and the geometry of the fault plane. **(a)** Strike projected contour plot showing the distribution of heave on Fault 5. Fault tip line joins the points of zero fault heave observable on seismic data. Base of the plot is the level of the detachment. Dashed line indicates the depth of horizon m3, which represents the stratigraphic level of the onset of deformation for Fold 5 (i.e. is the boundary between pre- and syn-kinematic units). Contour display increased regularity above the level of m3 than below. Of particular interest is the local minimum in heave located approx. 14 km along strike. **(b)** Seismic section through Fold 5. **(c)** and **(d)** Zoomed in seismic sections contrasting fault plane geometries at two points along the fold. (c) section v-v' coincides with the local minimum in heave located approx. 14 km along strike. Locations of sections given in (a). **(e)** and **(f)** Interpretations of sections (c) and (d). (e) shows the interpretation of a well imaged single fault plane reflection. (d) displays a wider fault zone (~300 m) interpreted as two distinct fault planes in (f). **(g)** Map of the fault traces between 12 and 15 k along strike.

therefore are likely to represent areas that have experienced ductile deformation due to the propagation and interaction of fault tips with other faults or boundaries.

The distribution of heave on the aggregate strike projection comprising *all* faults in the fold belt has been described previously and displays similar pattern of regular, sub-horizontal contours in the syn-kinematic package and irregular contours in the underlying pre-kinematic units (Fig. 5.15a). The similarities in displacement distribution between the entire fold belt and an individual syn-sedimentary fault (Childs et al., 2003) support the hypothesis that this suite of faults have accommodated deformation in a manner similar to a single structure and therefore upholds the idea of a kinematically coherent fold and thrust belt. The correlation of zones of heave deficit measured on a horizon in the pre-kinematic sequence (Fig. 5.15b) with the locations of major fault linkages (Fig. 5.15c) produces interesting but inconclusive results. The majority of fault linkages are located between 12 and 30 km along strike (Fig. 5.15c) and form two clusters that correspond with the two main fault heave minima on horizon m2 (Fig. 5.15b) situated around 16 km and 26 km along strike. This observation is in keeping with the conclusion of Walsh and Watterson (1991) that suggested residual irregularities in the contours of an aggregated coherent normal fault array occur at positions corresponding to the lateral tips of main faults comprising the array (i.e. increased ductile shear at tips and relays).

The above analysis of three structural case studies implies that the distribution of fault heave and bulk shortening is dependent on the timing of deformation relative to deposition of sedimentary layers. Irregularities in aggregate displacement distributions in pre-kinematic packages correspond to locations of fault linkage and associated relay structures and are therefore likely to be related to early fault

interaction during the development of the fold belt. Smooth, sub-horizontal contours within the syn-kinematic units, both on individual structures and aggregated profiles, reflect extremely low lateral displacement gradients due to fault length being determined by upward propagation of the fault to the free surface, rather than the maximum displacement on the fault (Childs et al., 2003). Displacement transfer within the syn-kinematic units, where heave-length profiles are devoid of the perturbations caused by increased lateral tip gradients, produces cumulative profiles that are consistent along strike and suggest the faults and folds have behave in a kinematically coherent manner during the synchronous growth of the fold and thrust belt.

5.8. Conclusions

1. A general foreland-propagating sequence of thrusting is overprinted by some out-of-sequence nucleation of faults and folds. Overlap in the duration of activity on all structures demonstrates firstly, that all faults were active for a significant period of the deformation history and secondly, that the initiation of new folds does not coincide with cessation of movement on older features.
2. Transfer zones with similar fault plane and stratal geometries display along strike heave profiles that either resemble that of a single fault and fold (i.e. regular contours within the linkage zone) or exhibit a net deficit (i.e. an irregular contours within the linkage zone). There is a positive correlation between the lateral extent of a transfer zone and the efficiency of displacement transfer.
3. The plunge of through-going folds, associated with antithetic transfer zones, is maintained along strike through the zones of linkage, regardless of variations in heave and shortening. Fold shape appears to be modified within transfer structures to maintain fold amplitude. The reasons for a conservation of fold height through linkage zones is unclear.
4. Deficits in heave and shortening within transfer zones correspond to complementary morphologies and fault profiles of structures located up and downdip indicating dip-parallel transfer of displacement via common detachments.

5. Aggregate heave and bulk shortening profiles of a fault and fold array have regular, sub-horizontal contours within the shallow section. Deeper horizons maintain irregularities. indicating kinematic coherency
6. Sub-horizontal contours correspond to the syn-kinematic sequence with irregularities remaining on the pre-kinematic sediments on individual faults, along strike linking fault pairs and the fold belt as a whole.
7. Irregularities in pre-kinematic package correspond to locations of maximum fault heaves and present day linkage zones.

Chapter 6

CHAPTER 6

6 SUMMARY AND DISCUSSION

6.1 Introduction

This thesis has used the 3D seismic reflection analysis of a deep water fold and thrust belt to investigate the nature and distribution of strain in a toe-of-slope compressional setting and to describe the complex fault plane and stratal geometries that result from fold and thrust linkage. The previous chapters are structured so as to represent a logical progression of thought from the linkage and interaction of fold and fault pairs, to considering a fold belt as a whole. This has provided new insights into the development and growth history of structures in gravity-driven fold belts on passive margins. This chapter aims to draw together the conclusions from Chapters 3, 4 and 5 to summarise the findings of this study (Fig. 6.1). A discussion follows that develops the themes of fault and fold segment linkage in the compressional domain, and the controls on locations and geometry of linkages. The potential errors uncertainties of strain measurements are also summarised along with their impact on the findings of this project. The chapter concludes with a consideration of the limitations of the study and some suggestions for future research.

6.2 Summary of results

6.2.1 Geometry and characteristics of thrust fault antithetic linkages (Chapter 3)

Chapter 3 presented a descriptive classification for along strike antithetic thrust fault linkage zones based on observations of fault surface and stratal geometries. Few studies, prior to this thesis, had investigated the geometry of transfer structures associated with linking thrust faults and only the en echelon overlap of synthetic thrusts (e.g. Dahlstrom, 1970), interactions within triangle zones (e.g. Pennock et al., 1989; Couzens and Wiltschko, 1996) and tear faults separating thrust surfaces (e.g. McClay, 1992) had been described. This work therefore represents the first 3D description of antithetic thrust linkages and was facilitated by the versatile imaging potential of modern 3D seismic data. This classification of fault interaction has implications on our understanding of fold belt development that is expanded on in

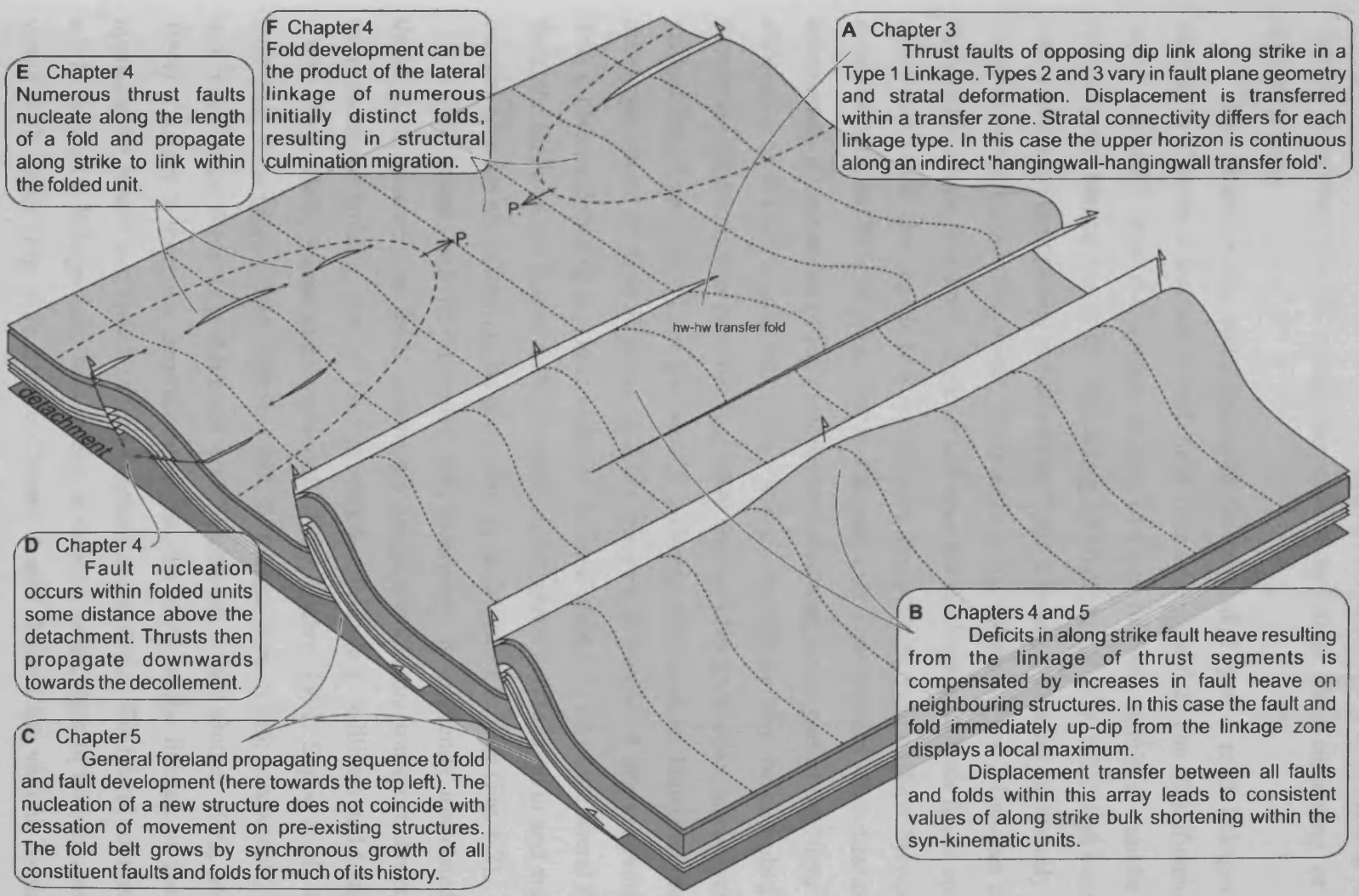

Figure 6.1: A schematic structural diagram of part of a deep water fold and thrust belt to summarise and illustrate some of the main findings of this project. See text for further discussion.

Chapters 4 and 5. The conclusions drawn on the connectivity of stratal reflections through transfer zones should also have significant application to modelling of fluid flow in a system that is compartmentalised by either flow-enhancing or flow-inhibiting faults.

The characteristic and diagnostic features of Types 1 to 3 linkages were defined in Chapter 3 and are summarised here in Figure 6.2. The classification was based primarily upon the vertical extent of fault surfaces within a transfer zone relative to the branch line of the interacting antithetic faults (Fig. 6.2). High resolution interpretation of fault planes indicated that Type 1 linkages overlap exclusively above the level of the branch line within the transfer zone, whereas Type 2 linkages overlap exclusively below this level. Type 3 linkages are distinctive as both faults continue above and below the branch line resulting in cross-cutting relationships between the constituent faults. This is presented in Chapter 3 as a preliminary classification that incorporates all variations of fault interactions observed in this part of the Niger Delta, although it is acknowledged that further linkage geometries may be described upon further investigation. It is possible that these end member geometries are the result of gradual evolution rather than genetically different mechanisms. However the well developed nature of fault linkages in folds featured in Chapter 4 argue against this. This is discussed further in a later section. The stratigraphic level of the lateral tip of a fault, the shape of the lateral fault tip regions and stratal deformation in and around a transfer zone are also shown to be distinctive in each type of linkage (Fig. 6.2).

Fold shape, and in particular fold symmetry, is inherently associated with thrust plane geometry as folds commonly verge towards the transport direction in many modes of faulting, such as fault propagation folds (e.g. Williams and Chapman, 1983; Mitra, 1990; Suppe and Medwedeff, 1990; Erslev, 1991; Suppe et al., 1992), fault bend folds (Rich, 1934; Suppe, 1983; Wiltschko et al., 1985; Medwedeff, 1992) and break-thrust folds (e.g. Mitchell and Woodward, 1988; Butler, 1992; Morley, 1994). Chapter 3 therefore demonstrated that the along strike linkage of faults of opposing dip results in a switch in fold vergence along strike. The lateral continuity of a fold through a linkage zone was shown to depend on the type of transfer zone and varied with depth (Fig. 6.2). Hence Chapter 3 also defined the various connective transfer structures associated with antithetic fault interaction including 'hangingwall-hangingwall transfer folds' and 'footwall-footwall corridors' (Fig. 6.2).

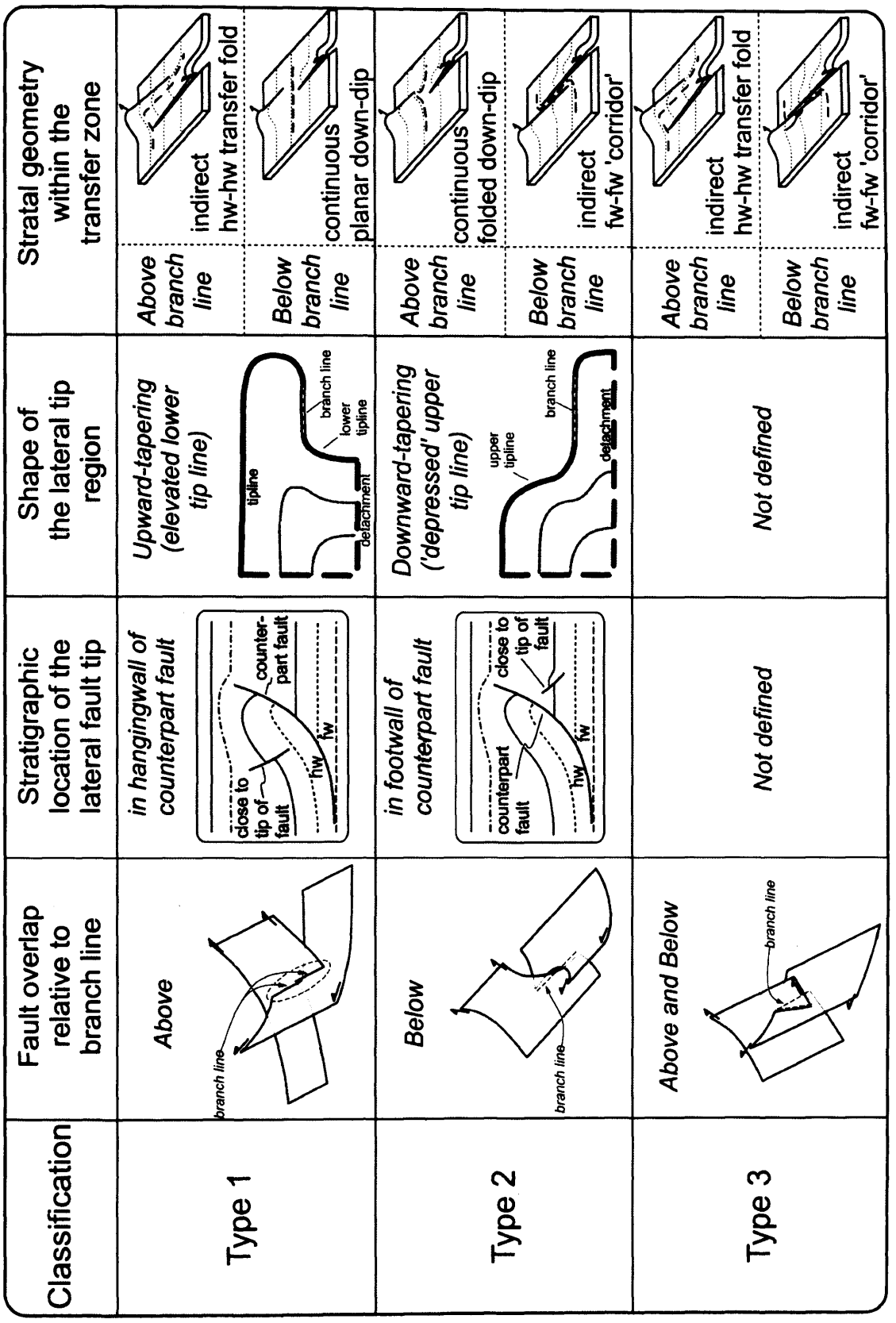

Figure 6.2 : A summary of the distinctive and defining characteristics of the classification scheme of antithetic thrust fault linkages presented in Chapter 3.

The findings of Chapter 3 were compared with examples of antithetic fault linkage in different geological settings within published literature to demonstrate the application of this research. The chapter concluded with a discussion that considered possible modes of structural evolution (i.e. fold-first or fault-first). This question was further investigated in Chapter 4.

6.2.2 Fold growth by segment linkage (Chapter 4)

Chapter 4 sought to build upon the descriptions of fault linkages in chapter 3, all of which were located in a tightly spaced fold belt, by investigating a single isolated fold (Fold B) that comprised numerous linking forethrusts and backthrusts. A case study involving the quantification of the development of this relatively simple structure allowed conclusions to be drawn on fold growth that was later applied to the more complex and closely spaced fold belt in Chapter 5. Chapter 4 took investigative and presentation techniques developed in the study of extensional faults and adapted them for use in compressional regimes. Strike projected contour plots for instance, allow the distribution of fault displacement to be mapped in great detail on a fault surface. Inferences of fault interaction from these plots are made with reference to a singly-faulted non-linking fold. Many of these methods had not been applied to thrusted fold belts and hence it provides a unique look at their development.

The research undertaken in Chapter 4 focussed on four main subjects. The first consisted of describing in detail the internal structural geometry of faults and stratigraphic horizons within the single fold. A clear definition of the constituent structures within Fold B established the type of linkages involved in forming this fold and validated the classification model in Chapter 3. It also provided a basis for the second focus of Chapter 4, that of quantifying the distribution of fault and fold strain both on individual thrusts within the fold and for the structure as a whole. Comparisons of the heave and shortening profiles produced information on displacement transfer between constituent faults and the kinematic relationship between them. Results showed that individual structures displayed irregular displacement profiles indicative of kinematic linkage with neighbouring structures. The fold as a whole had a shortening profile similar to that of simpler, non-linking structures and also blind faults from extensional studies. This suggested efficient displacement transfer between numerous linking faults that accommodated shortening as a coherent unit. The third subject of study looked at the response in the magnitude

of fold strain to along strike variations in the amount of fault heave which were shown to fluctuate along strike. The amount of shortening, and indeed fold shape, were shown to increase in areas of fault heave deficit compensating to some extent for the shortfall. Finally the growth history of Fold B was investigated using innovative techniques that charted the spatial extent of syn-kinematic stratigraphy in three-dimensions. It was shown that Fold B, although exhibiting a single structural culmination at the present day, was initially made up of a number of folds with local structural highs (Fig. 6.1). Correlation of this pattern with the location and extent of the major thrust surfaces indicated that this single fold was the product of the along strike linkage and amalgamation of both faults and folds.

6.2.3 Distribution of deformation in a kinematically coherent fault and fold array (Chapter 5)

The model of fold growth by segment linkage proposed in Chapter 4, based on the study of a single isolated fold, was applied to the fold and thrust belt in **Chapter 5**. The main objective of this chapter was to gain a better understanding of the distribution of strain within a fold and thrust belt and its relation to the growth and interaction of propagating faults and folds. The methods employed in Chapter 4 to chart fold growth through time could not be applied here due to the close down-dip spacing of hangingwall anticlines in the fold belt, along with channelised deposits in the limb of folds and in synclines that disrupt regional reflections. Hence the application of results from Chapter 4 was key to achieving this goal.

Chapter 5 was structured around a number of lines of investigation. Firstly the relative timing of individual faults and folds was established from a broad study of growth strata on folds limbs. Results agreed with established models of a progressive foreland propagating sequence to thrust faults (e.g. Dahlstrom, 1970) but also displayed evidence of out-of-sequence events (e.g. Wiltschko and Dorr, 1983; Corredor et al., 2005). Contrary to current models however was the degree of overlap of the durations of fold growth, and therefore findings in this chapter demonstrate a significant period of synchronous development of all structures in the fold belt.

Through the mapping of fault heave on all thrusts in the fold belt, the scale of displacement transfer between contemporaneous structures was investigated. Displacement transfer was demonstrated not only to have occurred between faults and folds along strike, as in Chapter 4, but also in a dip-parallel direction (Fig. 6.1). This

was evident due to complementary trends in horizon morphology and heave and shortening profiles that, when aggregated, produced smoother profiles of deformation. The summation of heave and shortening values of all structures in the fold belt demonstrated a conservation of the amount of deformation along strike within the syn-kinematic units. Extremely low lateral heave gradients suggest efficient displacement transfer between all constituent structures. Chapter 5 therefore shows that all elements of a fold belt can be kinematically linked during growth. Irregularities in the distribution of deformation in pre-kinematic units corroborate findings of Chapter 4 that the folds are the product of along strike linkage of discreet segments. Evidence suggests that displacement minima on heave profiles of through-going faults record the locations of early linkages and transfer zones.

In summary, the various styles of antithetic thrust fault linkages described geometrically in Chapter 3 have been showed to transfer displacement efficiently along strike in Chapter 4 such that numerous faults, aligned along strike, can grow and accommodate displacement as a single structure. The study of the full width of a fold belt in Chapter 5 however demonstrated a more three-dimensional transfer of displacement as local deficits in shortening at linkage zones are compensated for within the array. Geometric and kinematic coherence of the fold and fault array is possible due to the synchronous growth of its constituent structures. Stratal geometries around transfer zones outlined in Chapter 3 show that fault linkages can be characterised by through-going fold crests that maintain structural elevation or display a local apex (Fig. 6.1). Given the evidence in Chapters 4 and 5 for fold growth by the lateral propagation and interaction of discrete segments it is concluded that present structural highs are the result of culmination migration through time. What follows is a discussion of segment linkage in the compressional domain and the controls on the style and location of such linkages.

6.3 Discussion

6.3.1 Segment linkage in the compressional domain

The concept of segment linkage of thrust faults and folds has been discussed over the past few decades for a range of structural settings and experimental arrangements. Ellis and Dunlap (1988), for example, described displacement patterns on thrust systems of varying maturity and size and presented a hypothesis of large fault development through pervasive footwall deformation and fault linkage. Liu and Dixon (1991) used their centrifuge models of thrust propagation to highlight the importance of folds in controlling the nucleation and linkage of multiple, initially discrete faults. Rowan (1997) utilised 2D seismic data to discuss the three-dimensional geometry and evolution of a segmented detachment fold in the deep water Gulf of Mexico. More recently, Davis et al. (2005) investigated fault-growth and fault-segmentation models through the analysis of the geometry and scaling of fault segments in an active thrust fault zone in New Zealand. Despite the advancements in this area, research into normal fault growth processes has resulted in a greater understanding of extensional systems compared to compressional settings. This thesis represents the first study to fully utilise 3D seismic data in examining thrust fault growth by segment linkage. This high-resolution 3D data have allowed the detailed distribution of fault heave on individual and linking thrust faults to be imaged for the first time. It also allows our findings from well constrained natural geological examples of thrust fault growth by segment linkage to be compared with modelled laboratory results. This section therefore contrasts the results of Liu and Dixon (1991) with the evidence presented in Chapters 3, 4 and 5.

Liu and Dixon (1991) and Dixon and Liu (1991) presented experimental investigations into the along strike structural variation in a fold and thrust belt, the three-dimensional interaction and propagation of thrust faults in duplex structures, and the mechanisms of displacement transfer between adjacent thrust faults and folds. In these studies they contrast their findings with the natural geological example of the central Appalachians (Liu and Dixon 1991). Although this proved a useful exercise, the capacity to view 3D seismic data on unlimited planes and sections allows for more rigorous testing of experimental models. The conclusions drawn from the models in discussion here are centred around four main topics: i) the order of initiation and

propagation of faults and folds, ii) the mechanisms of fault and fold nucleation and growth, iii) the structural variability of a fold belt along strike, and iv) displacement transfer between structures (Dixon and Liu, 1991; Liu and Dixon 1991). Each of these themes shall be considered in turn below.

The methods by which the sequence of fold and thrust initiation was determined differed between this thesis and the research by Dixon and Liu (1991). The progressive evolution of the centrifuge model was monitored by cutting profiles parallel to the shortening direction at regular stages during deformation (Dixon and Liu 1991). In this thesis the timing and duration of fold and fault activity was ascertained from growth packages on the limbs of folds within syn-kinematic units (e.g. Fig. 5.7). The results from the experimental model agree with many findings in this study (Fig. 6.3). Dixon and Liu (1991) describe the early stages of deformation as being characterised by harmonic buckle-fold trains in competent units. These folds were observed to have nucleated serially from hinterland to foreland and grew progressively in amplitude (Fig. 6.3a). The authors also documented the nucleation of thrusts in the front limb of the folds at a later stage of deformation, although they display the same sequence of nucleation as the folds. This supports results presented in Chapter 5 of this thesis that showed an overall foreland progressing trend to fold initiation (Fig. 6.3c). In contrast, however, folds in the deep water Niger Delta also display some out-of-sequence events within this trend, an observation supported by other authors who describe thrusting in this region (e.g. Morley, 2003; Rowan et al., 2004; Corredor et al., 2005; Briggs et al., 2006). This pattern is not observed in the modelling study (Dixon and Liu 1991) (Fig. 6.3a and b). Another similarity between this 3D seismic research and the laboratory study is the conclusion that the nucleation of new faults does into coincide with cessation of movement on the older structures, despite a successive move towards the foreland (Fig. 6.3). This is in contrast to simple models of thrust fault development in fold belts (e.g. Dahlstrom 1970; Butler 1982; Elliot and Johnson 1980; Boyer and Elliot 1982) and argues for the synchronous growth of numerous structures within a fold belt. Dixon and Liu (1991) state that "this agrees with the critical Coulomb wedge model of Davis et al (1983) which involves the continued accumulation of displacement on early faults in the hinterland".

The mechanisms by which faults and folds nucleate and propagate are easier to establish using experimental studies where deformation can be observed taking place,

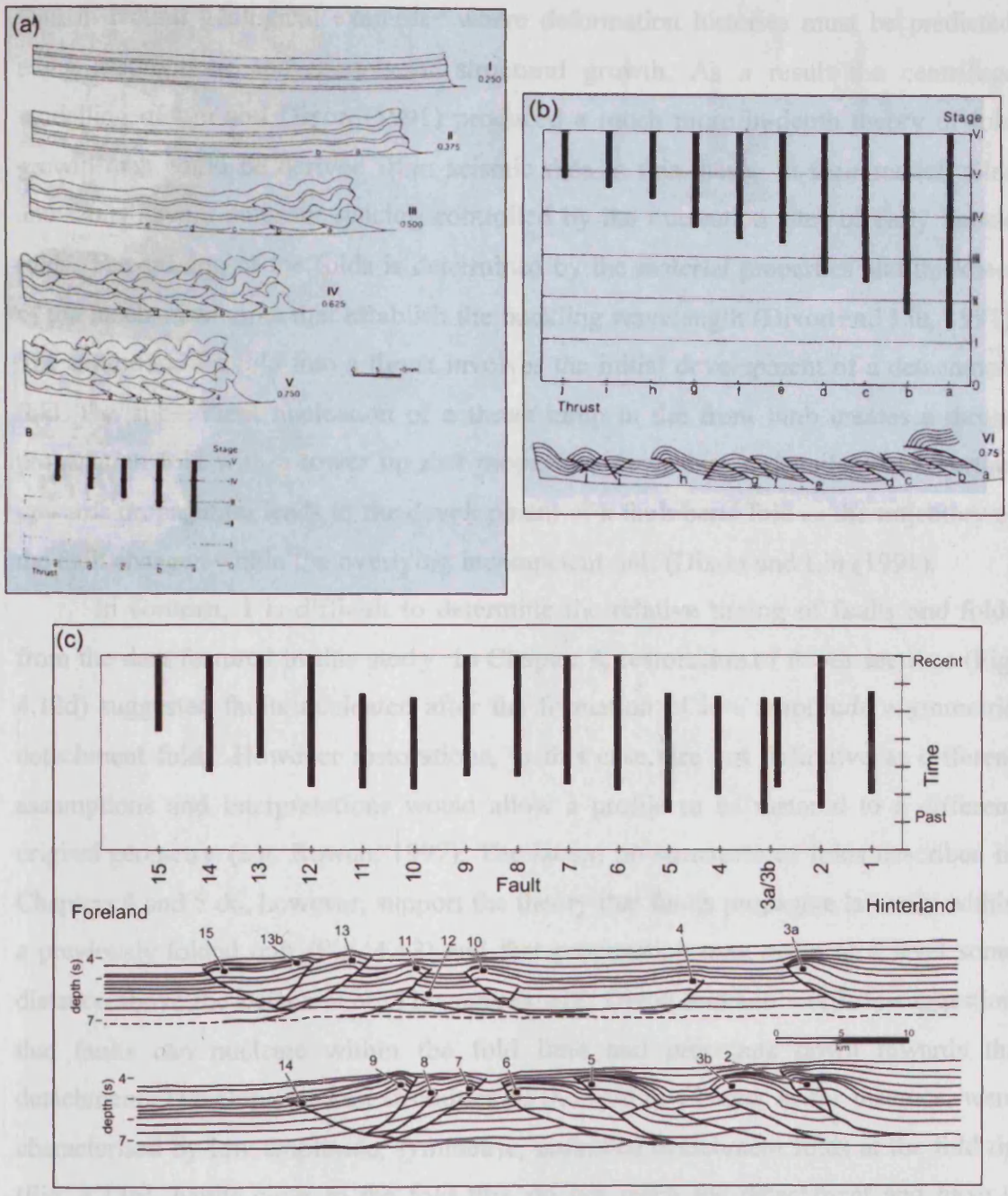

Figure 6.3: Comparison of results in this thesis regarding the sequence and duration thrust fault and fold propagation with experimental modelling results from Dixon and Liu (1991). **(a)** and **(b)** Line drawings of model sections and bar chart showing the stage of initiation and duration of displacement of faults in two experimental centrifuge models. Note that the fault ramps nucleate serially from hinterland to foreland, and not a single thrust dies during the deformation. Taken from *Dixon and Liu (1991).* **(c)** Findings from this thesis (Chapter 5) showing the sequence of initiation and duration of faults and folds in a deep water fold belt of the Niger Delta. Two line cross-sections are presented as not all faults are present in any one dip-parallel section. Note the similarities with the modelling results in (a) and (b). A general foreland-propagating sequence of fault initiation and a significant period of synchronous growth. However out-of-sequence events occur within this pattern and not all faults continue to the present day.

than in natural geological examples where deformation histories must be predicted using assumptions and models of structural growth. As a result the centrifuge modelling of Liu and Dixon (1991) produced a much more in-depth theory of fold growth than could be derived from seismic data in this thesis. In their models folds and faults have a constant spacing controlled by the nucleation sites of early buckle folds. The spacing of the folds is determined by the material properties and thickness of the mechanical units that establish the buckling wavelength (Dixon and Liu, 1991). The evolution of a fold into a thrust involves the initial development of a detachment fold. The subsequent nucleation of a thrust ramp in the front limb creates a thrust-propagation fold with a lower tip that propagates down into a decollement. Further upwards propagation leads to the development of a fault bend fold as the trajectory of the fault changes within the overlying incompetent unit (Dixon and Liu (1991).

In contrast, it is difficult to determine the relative timing of faults and folds from the data featured in this study. In Chapter 4, restoration of depth sections (Fig. 4.12d) suggested faults nucleated after the formation of low amplitude asymmetric detachment folds. However restorations, in this case, are not definitive as different assumptions and interpretations would allow a profile to be restored to a different original geometry (e.g. Rowan, 1997). The lateral tip structures of folds described in Chapters 4 and 5 do, however, support the theory that faults propagate laterally within a previously folded unit (Fig. 4.13) and that propagation may occur at a level some distance above the detachment. This agrees with Dixon and Liu's (1991) suggestion that faults can nucleate within the fold limb and propagate down towards the detachment. The along strike extremities of the fold in Chapter 4, for instance, were characterised by low amplitude, symmetric, unfaulted detachment folds at the fold tip (Fig. 4.13b). Faults close to the fold tips do not reach the detachment and have a maximum displacement located within the Agbada Fm (i.e. above the detachment). This relationship between faulting and folding towards the lateral tips is clearly demonstrated on Fault 15 in Figure 6.4. Fault 15 is the youngest (Fig. 5.7) and most distal (Fig. 5.1) fault in the fold and thrust belt featured in this study. It is only partially imaged as it intersects the limits of the seismic survey. The imaged fault segment is located in the hangingwall stratigraphy of Fault 13 and hence the lower tip line of Fault 15 forms a branch line with Fault 13 for much of its length (Fig. 5.4). One of the interesting attributes of Fault 15 is that maximum fault heave values are

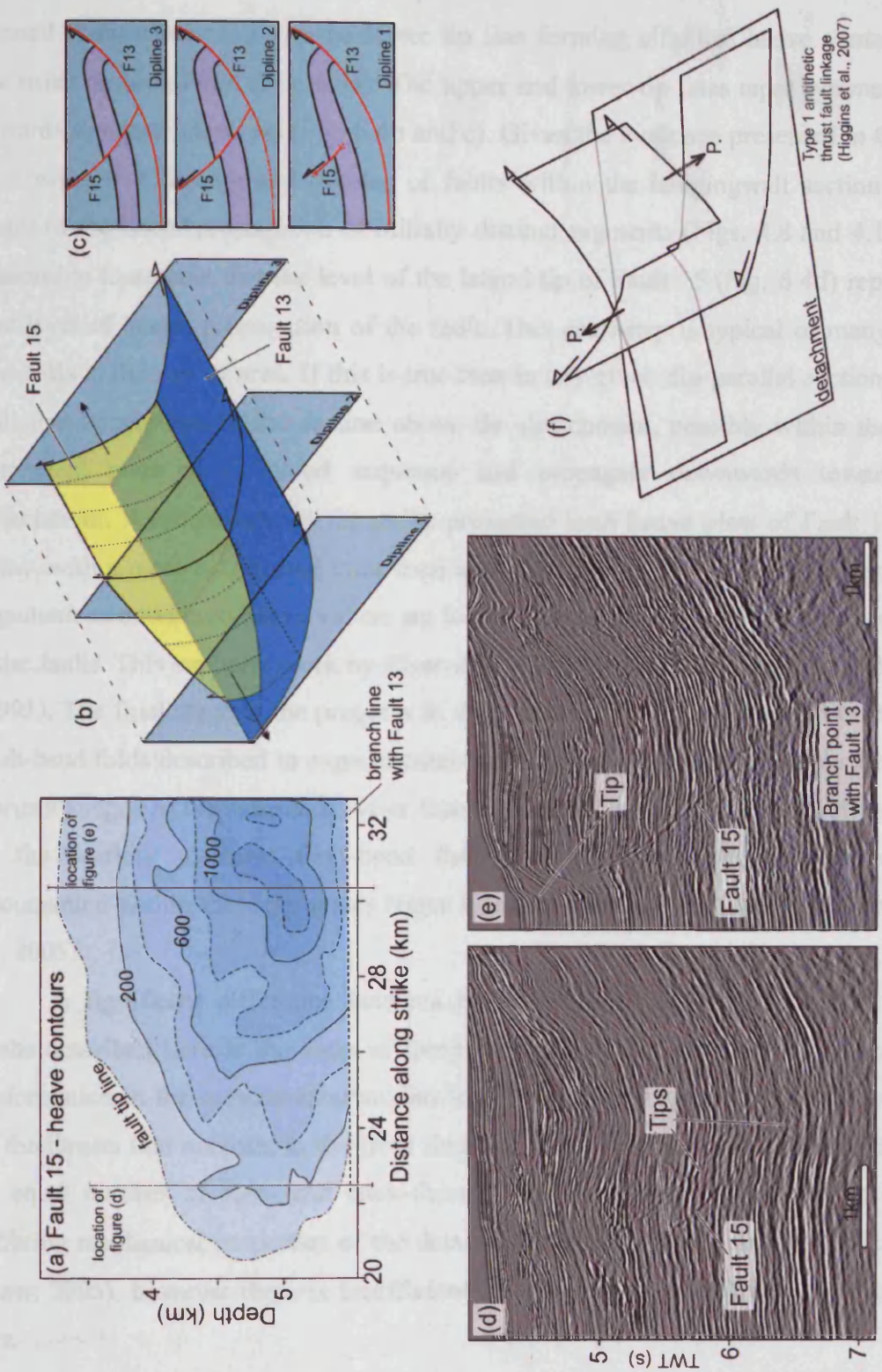

Figure 6.4: Profile of fault and fold 15 from Chapter 5 as an illustrative example of the stratigraphic level of lateral propagation of many faults in this study. **(a)** Strike projection contour plot of fault heave values. Note the elliptical shape of the contours and the location of the zone of maximum heave some distance above the lower tip line (branch line with fault 13). **(b)** Schematic block diagram of the structural characteristics of Fault 15 (yellow). Note that towards the lateral tip of the fault the lower tip line changes from forming a branch line with fault 13 (blue) and climbs stratigraphy to a central lateral tip. This is also evident in figure (a). **(c)** Schematic cross sections relating to figure (b). **(d)** and **(e)** Seismic sections of Fault 15. Locations are shown on figure (a). Note the lesser vertical extent of the fault in the section closer to the lateral fault tip. **(f)** Schematic diagram of a Type 1 antithetic thrust linkage showing propagation of faults in the hangingwalls. P. indicates propagation direction.

located some distance above the lower tip line forming elliptical heave contours on the strike projected plot (Fig. 6.4a). The upper and lower tip lines taper symmetrically towards a central lateral tip (Fig. 6.4b and c). Given the evidence presented in Chapter 4 showing that linkage and overlap of faults within the hangingwall section was a result of the lateral propagation of initially distinct segments (Figs. 4.8 and 4.11) it is reasonable to assume that the level of the lateral tip of Fault 15 (Fig. 6.4d) represents that level of lateral propagation of the fault. This geometry is typical of many faults and folds in the survey area. If this is true then in any given dip-parallel section a fault will first appear within the section above the detachment, possibly within the more competent units of a folded sequence and propagate downwards towards the detachment. A comparison of the strike projected fault heave plots of Fault 15 (Fig. 6.4a) with a more established fault such as Fault 12 (Fig. 5.10c) lends weight to this argument as maximum heave values are located closer (or even in) the detachment on older faults. This supports work by Eisenstadt and De Paor (1987) and Liu and Dixon (1991). The final stage in the progress in deformation, from fault-propagation folds to fault-bend folds described in experimental models above, is not observed in this study. Thrusts imaged in the seismic surveys features here do not reach an upper detachment or the seafloor to form fault-bend folds, however such structures have been documented within the deep water Niger Delta by previous authors (e.g. Corredor et al., 2005).

A significant difference between the models of Liu and Dixon (1991) and faults described here is the ratio of forethrusts to backthrusts observed in the data. Deformation in the experimental studies lead to an evenly spaced synthetic sequence of forethrusts that nucleate in the front limbs of folds. Sections featured here can have an equal number of fore- and back-thrusts (Fig. 5.2). This is likely to be due to differing mechanical properties of the detachment layers in each case (e.g. Bilotti and Shaw, 2005), however there is insufficient information from well data to investigate this.

One of the main conclusions of this thesis has been that displacement and shortening transfer occurs between fault and fold pairs along strike (Chapter 4) and between all structures within a kinematically coherent fold and fault array (Chapter 5) such that numerous faults accommodate shortening as if a single structure. Liu and Dixon (1991) record similar observations in their modelled study of the along strike variability of a fold and thrust belt. They state that "displacement transfer occurs

between pairs of en-echelon thrust faults, between pairs of imbricate thrusts, and between thrust faults and folds. The transfer accommodates structural change along strike while the total transverse shortening stays relatively constant". This contrasts to some degree with the findings of this thesis as consistent values of transverse shortening were only observed in syn-kinematic packages, with pre-kinematic units displaying irregular along strike bulk shortening profiles. Almost all faults within Liu and Dixon's model were of a similar direction of dip and hence the transfer of displacement associated with antithetic interaction cannot be compared. Points of linkage between the synthetic forethrusts were identified by deficits in along strike profiles of displacement, while points of maximum displacement were assumed to represent points of fault nucleation (Liu and Dixon, 1991). Detailed analyses of syn-kinematic growth strata in Chapters 4 and 5 of this thesis question the validity of these conclusions. Although linkage zones within the Niger Delta can be characterised by deficits in heave and shortening, they can also interact to produce smooth aggregate profiles through a transfer zone (Fig. 5.8). In addition to this, the point of nucleation of a fault does not always correspond to maximum values of displacement. It was not possible to demonstrate the site of fault nucleation with any degree of accuracy in this study, however Chapter 4 demonstrated the along strike linkage a two initially distinct faults and folds into a single through-going thrust with a maximum heave value at the point of original linkage (Figure 4.14). This must necessarily have involved an along strike migration the points of maximum heave and shortening. It has also been discussed in this section that the location of maximum displacement can migrate vertically on a fault plane during fold and thrust growth.

Many of the findings of the experimental studies of Liu and Dixon (1991) and Dixon and Liu (1991) are supported by the findings in this thesis. In general, the modelling studies produced much simpler results than those from seismic data, such as a clearer sequence of thrust nucleation (Fig. 6.3) and a consistent direction of fault dip. This is possibly due to a greater degree of heterogeneities in the natural geological examples, both in the nature of the detachment and variations in mechanical stratigraphy (Fig. 1.10). The possible controls on the range of structural linkages styles observed in the deep water Niger Delta are discussed in the following section.

6.3.2 Controls on location and geometry of linkages

The classification scheme of antithetic thrust fault linkages presented in Chapter 3 was based upon a geometrical analysis of fault plane interactions and stratal deformation within transfer zones (Fig. 6.2). This represented a purely descriptive study of fault linkage and hence Chapters 4 and 5 aimed to build on this work and investigated the kinematic relationships and history of the constituent structures. Despite the research in previous chapters, it remains unclear what controls the type of antithetic thrust fault linkage manifest at each transfer zone. It could be that linkages develop through types 1-3 (Higgins et al., 2007) (Fig. 6.2) during the accumulation of displacement such that the classification represents a gradual evolution rather than genetically different mechanisms. However the well developed nature of the F1/F2 fault linkage in fold B, described in Chapter 4, argues against this (Fig. 4.8). The faults are kinematically coherent, accommodate large amounts of displacement, produce a smooth aggregated profile and appear to have a stable geometrical relationship (Fig. 4.10). This Type 1 linkage zone (F1/F2) has efficiently transferred displacement between component thrusts, at all stratal levels, to allow the fold to act as a single structure and it is unlikely, if propagation continued, to deviate from this relationship. This section therefore aims to discuss the possible controls on the varying geometries and displacement characteristics of the three types of linkage outlined in Chapter 3 (Fig. 6.2).

One possible control on the mechanism of antithetic fault linkage could be the stratigraphic level of the line of fault intersection of the linking faults. All the faults in fold B maintain a near uniform dip following the ramp out of the detachment (Fig. 4.7), such that the level of intersection of antithetic faults will, in turn, be controlled by the along strike alignment of the faults themselves (Fig. 6.5a). When combined with the stratigraphic level of lateral fault propagation (Fig. 6.5b to e), this may determine whether approaching faults overlap in the hangingwalls (Type 1), footwalls (Type 2) of by fault-on-fault offset (Type 3) (Fig. 6.2).

As has been previously discussed, fold tip structures, away from linkage zones, suggest that faults may propagate laterally at a stratigraphic level some distance above the detachment (Figs. 4.13). In figure 6.5b two faults of opposing dip have approximately equal maximum displacement values located near the h3 horizon. They converge on a point of intersection, or branch point, at the level of horizon h2 in

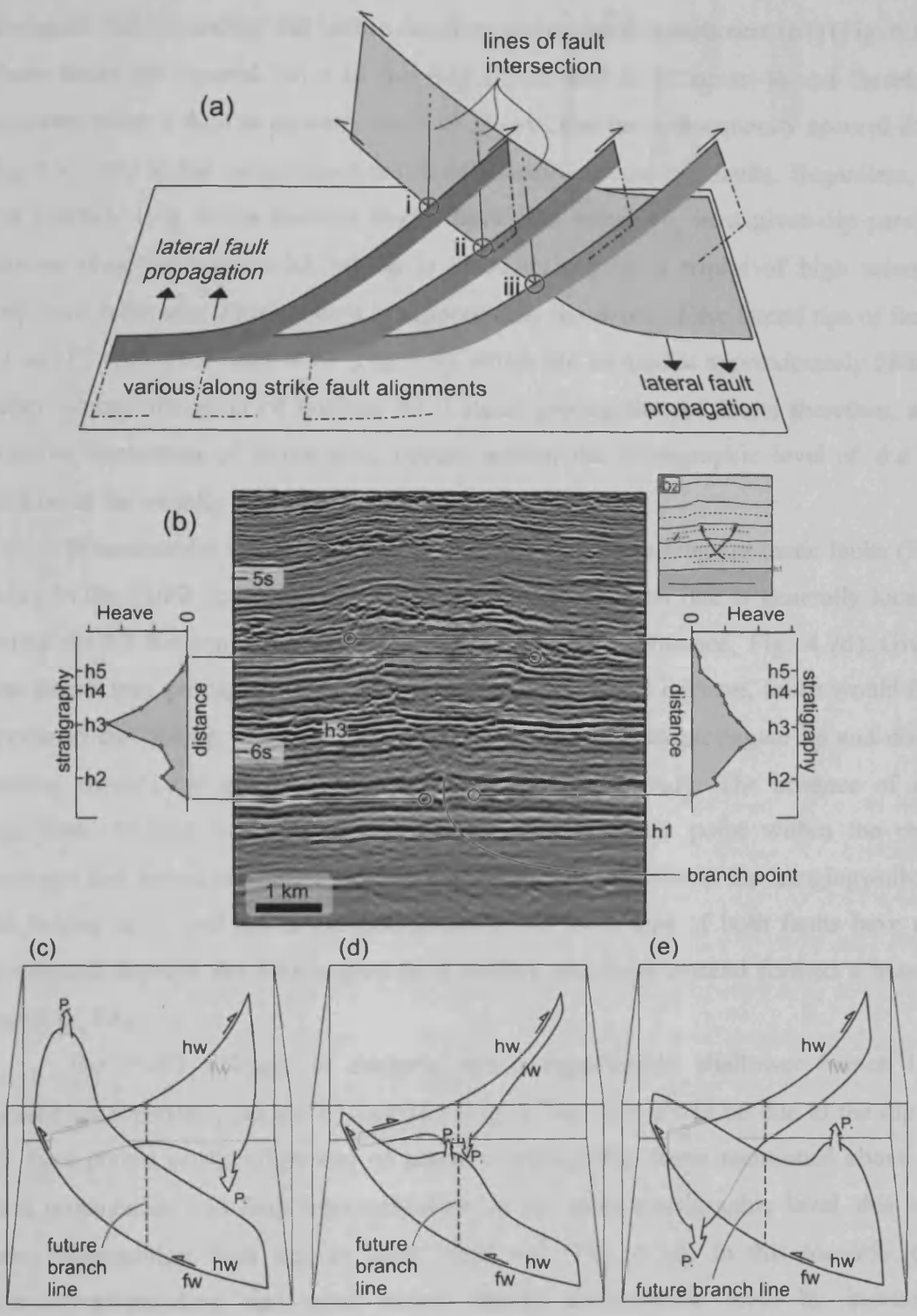

Figure 6.5: Illustration of a possible control on the types of linkages described in Chapter 3. **(a)** Schematic diagram demonstrating the effect of along strike alignment of thrust faults with essentially planar, uniform dips on the level of a branch line (line of intersection). i. ii. and iii. indicate the level of branch lines for three linkages with varying alignments. **(b)** Analysis of fold tip structures featured in Figure 4.13. Two thrusts of opposing dip are located close to the lateral tip of Fold B (Chapter 4). Heave-distance profiles show that the point of maximum heave is located close to horizon h3 on both faults. Horizon h3 is characterised by higher seismic amplitudes than surrounding reflections. **(c)**, **(d)** and **(e)** Schematic block diagrams to show various stratigraphic levels of lateral fault propagation on linking antithetic faults. The alignment of faults does not change in each diagram. (c) Propagation high in the section, towards hangingwall rocks. May lead to Type 1 linkage. (d) Propagation in the mid-section, towards branch line. May lead to Type 3 linkage. (e) Propagation lower in the section, towards footwall rocks. May lead to Type 2 linkage. hw: hangingwall. fw:footwall. P.: propagation direction.

conjugate-fashion and tip out before reaching the regional detachment (h1) (Fig. 6.5b). These faults are located close to the fold tip of fold B (Chapter 4) and therefore represent either a fault at an early stage of growth that has subsequently accrued little displacement, or the more recent result of laterally advancing faults. Regardless, in this example (Fig. 6.5b) faulting would have first appeared, in a given dip-parallel section, close to horizon h3 which is characterised by a triplet of high seismic amplitude reflectors. This concept is supported by the depth of the lateral tips of faults F1 and F2 within the relay zone (Fig. 4.9), which are located at approximately 5800m depth, around the level of horizon h3. Lateral propagation of faults therefore, and possibly nucleation of faults also, occurs around the stratigraphic level of the h3 horizon in the vicinity of this fold.

Now consider the depth of the branch point of the linking antithetic faults (Fig. 6.5a). In the F1/F2 linkage (Type 1) the depth of the branch line is generally located below the h2 horizon (with respect to the hangingwall sequence, Fig. 4.7d). Given that thrusts may propagate along strike at the level of the h3 horizon, faults would first appear in the linking fault hangingwall (Fig. 6.5c) and then propagate up and down section towards the surface and a branch point respectively. The absence of any significant faulting in the footwall of either fault at any point within the relay indicates that lateral propagation has occurred exclusively within the hangingwalls of the linking faults and not at the detachment. The lower tips of both faults have not propagated through the counterpart fault surface and have instead formed a branch line (Fig. 4.8).

The F3/F2 linkage, in contrast, has a significantly shallower branch line located approximately on the h3 horizon (Fig. 4.7b). This could be due to the dip of the fault planes or the alignment of laterally propagating faults mentioned above. If fault propagation and fault intersection are at the same stratigraphic level, this will cause approaching fault tips to meet 'head on' (Fig. 6.5d). In this scenario, the laterally propagating tips must either change stratigraphic level by increased advancement of the fault tip line above or below horizon h3, thus forming a Type 1 or Type 2 linkage, or otherwise cross-cut the counterpart fault surface (i.e. Type 3) (Fig. 6.2).

This relationship between the depth of a propagating tip and the alongstrike alignment of faults may control linkage geometries. Many authors have suggested that faults may nucleate within the more competent units of a heterogeneous sequence (e.g.

Eisenstadt and De Paor, 1987 Liu and Dixon). Horizon h3 is characterised by a high amplitude seismic triplet (Fig. 6.5b) and is regional in extent. Relatively high seismic amplitudes can indicate a change in lithology (e.g. Brown, 1999). In the setting of the deep water Niger Delta high amplitude reflections commonly occur within a background of lower amplitude seismic facies and may indicate coarser-grained turbidites associated with aggrading or migrating channel axes (e.g. Kastens and Shor, 1985; Deptuck et al., 2003). The seismic facies associated with the high amplitude, continuous, triple reflection of horizon h3 may indicate a more competent unit compared to sediments above and below. A lack of well data, however, means this is unverifiable and remains speculative. Taking a broader view, if coarser grained sediments are confined to stacked channel-levee systems (e.g. Deptuck et al., 2003) mechanical stratigraphy within a fold is expected to vary along strike and hence the level at which fault nucleate, propagate and, ergo, link may also be laterally inconsistent.

6.4 Implications for fold belt evolution and hydrocarbon exploration

The research presented in this thesis includes novel geometric and kinematic observations that help to further our understanding of fold and thrust belt evolution. The utilisation of 3D seismic data have enabled one of the first detailed descriptions of the distribution of strain on thrust fault surfaces and within compressional folds. The conclusions of this study are made with reference to the gravity-driven fold and thrust belt of the deep water Niger Delta. Chapter 3 discussed the possible application of some of the findings of this thesis to other geological locations and settings around the world. Similar structural geometries are recorded in studies of other passive margins but also have been described in with orogenic belts. It should be noted however that while there are significant similarities between gravity-driven thrust belts and the classic orogenic thrust belts, there are also significant differences in mechanism and structural style (see section 2.4). It may be wise to consider passive margin thrust belts as related to, but in many ways dissimilar to constructive margins. Deep water fold belts are a relatively new area of geological investigation and therefore this thesis complements established thrust fault literature based predominantly on onshore orogenic belts. Further discussion of the shared and unique characteristics of each geological setting should lead to a better understanding of both

types. The implications of this study involve a number of geological topics including aspects of basin analysis, deep water sediment dispersal and hydrocarbon exploration. These are discussed below.

Sedimentation patterns provide fundamental control on deformation in gravity-driven fold belts on passive margins (e.g. Rowan, 2004). Numerous studies have documented the linked structural system of updip extension and downdip contraction that accommodates gravitational collapse above regional décollements (e.g. Morley and Guerin, 1996; Wu and Bally, 2000; Morgan, 2003; Rowan et al., 2004). Analyses of such systems have focussed on both the landward extensional domain and the basinward contractional domain and provide quantitative estimates of translation magnitude (Jackson and Hudec, 2005). Many questions remain however over displacement transfer within the translational domain, and the disparities between net values of extension and contraction (e.g. Ings and Shimeld, 2006). Detailed analyses of the along strike variability of downdip contraction within deep water fold belts, such as that presented here in Chapter 5, provide important information that can be applied to such issues.

A brief description of the effect of structural development on deep water sediment dispersal was presented in Chapter 1 (Fig. 1.16). This can be summarised in by the observation that low relief structures create structural highs and lows which become influential in focussing submarine flows (Hooper et al., 2002). Given the findings of Chapters 4 that documented the growth of a single fold by the along strike linkage of several initially distinct folds, this concept of channel diversion can be expanded further. The evidence for the migration and amalgamation of structural culminations (Fig. 4.16a) suggests that undeformed areas between advancing fold and fault tips (Fig. 6.1) will develop into saddle points of a through-going fold following linkage (Fig. 6.6a) and may even become a local culmination as deformation proceeds (Fig. 3.3). One effect on channel systems may be to focus sediment pathways through narrow channels for significant periods of time. This is demonstrated in Figure 6.6. In this case two thrust faults of similar dip interact along strike forming a synthetic linkage zone (Fig. 6.6a). Displacement is transferred between the structures within a transfer zone characterised by a significant minimum in fault displacement and topography, labelled point '*s*' (Fig. 6.6). Three channels located at various stratigraphic levels are oriented perpendicular to fault strike and intersect the fault at

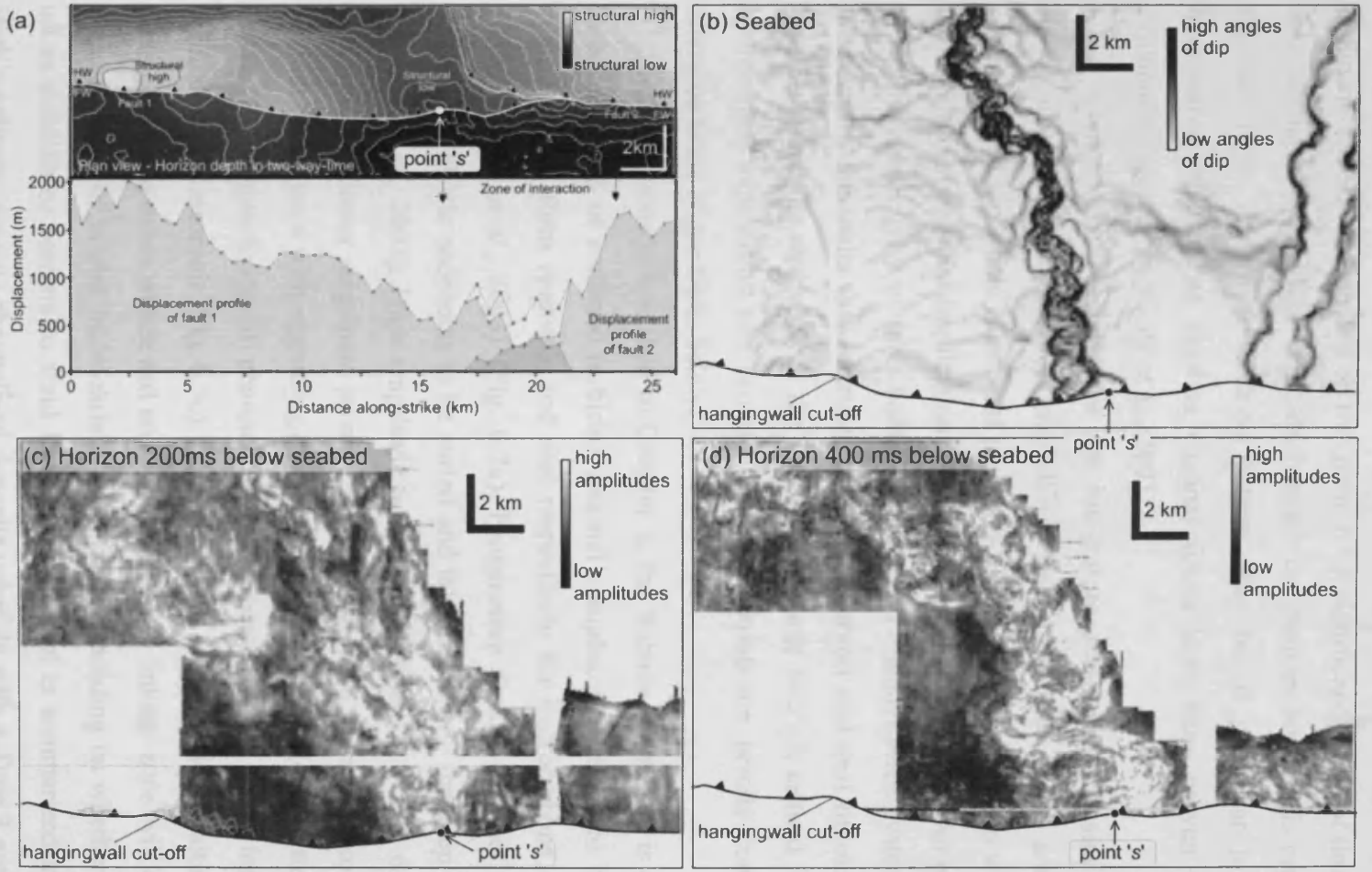

Figure 6.6: Demonstration of 'channel-funnelling' due to interaction and lateral propagation of folds. **(a)** Topographic map of horizon m4 showing a saddle point (*'s'*) between two linking forethrusts and folds. Also included is displacement-distance plot of individual and cumulative along strike fault displacement profiles. Note that the saddle point corresponds to the minimum in fault displacement. **(b)** Dip map of the present day seabed. Channel flows sub-parallel with regional dip of the delta and intersects the fault at a right angle close to the saddle point. **(c)** and **(d)** Amplitude extraction maps of sediments 200 milliseconds and 400 milliseconds below the seabed. The channels imaged in (b), (c) and (d) all have distinct morphological characteristics, but all insect the fault linkage at point *'s'*.

the saddle point '*s*' (Fig. 6.6b, c and d). The high amplitude channelised deposits can be seen to narrow towards the saddle point (Fig. 6.6c) as if being funnelled by the topography of the linking folds. The channels are imaged in Figure 6.6 show how sediments have been focussed on this point for a significant period of time resulting in the stacking of channelised deposits beneath the transfer zone. This organisation of channels in to a vertical stacking pattern may be of particular interest to the hydrocarbon industry as sinuous channel forms have been proven to be viable exploration targets (e.g. Kolla et al., 2001).

Complex fault geometries are integral to sedimentary basins and have a significant impact on reservoir modelling. The three-dimensional analysis of the geometric and kinematic history of part of a highly prospective deep water fold and thrust belt has important implications for the hydrocarbon industry. An understanding of (a) the connectivity of sand bodies in a stacked channel-levee system (b) the 3D geometry of the faults that intersect potential reservoir and seal lithologies and (c) how faults link the reservoirs to the underlying source rocks is critical for successful hydrocarbon exploration and production. These points are briefly considered with reference to the Niger Delta below.

As previously described in Chapter 2, the Agbada Formation is characterised by a succession of confined turbidite channel complexes, surrounded by deepwater mudstones that form reservoir and seal respectively for hydrocarbons (e.g. Davies, 2003; Deptuck et al., 2003) (Fig. 6.7a). Prospective sinuous channel forms act as conduits for clastic sediments to be sorted and transported into the deep water setting (Deptuck et al., 2003). High amplitude reflections (labeled 'r' – Fig. 6.7b) within a background of lower amplitude seismic facies are thought to indicate coarser-grained turbidites associated with aggrading or migrating channel axes (e.g. Kastens and Shor, 1985). The connectivity of channel deposits therefore has great impact on the production of a reservoir (Fig. 6.7c) The density and complexity of faulting of stacked channel-levee systems within and around an antithetic linkage zone will consequently either enhance of inhibit hydrocarbon production depending on whether fault planes act as conduits or barriers to fluid flow. This concept is summarized in Figure 6.7. High amplitude, sinuous channelised deposits coincide with a Type 3 antithetic thrust fault linkage (Chapter 3). A cross-section through the linkage zone shows movement on both the forethrust and backthrust has resulted in the repeated offset of one fault by

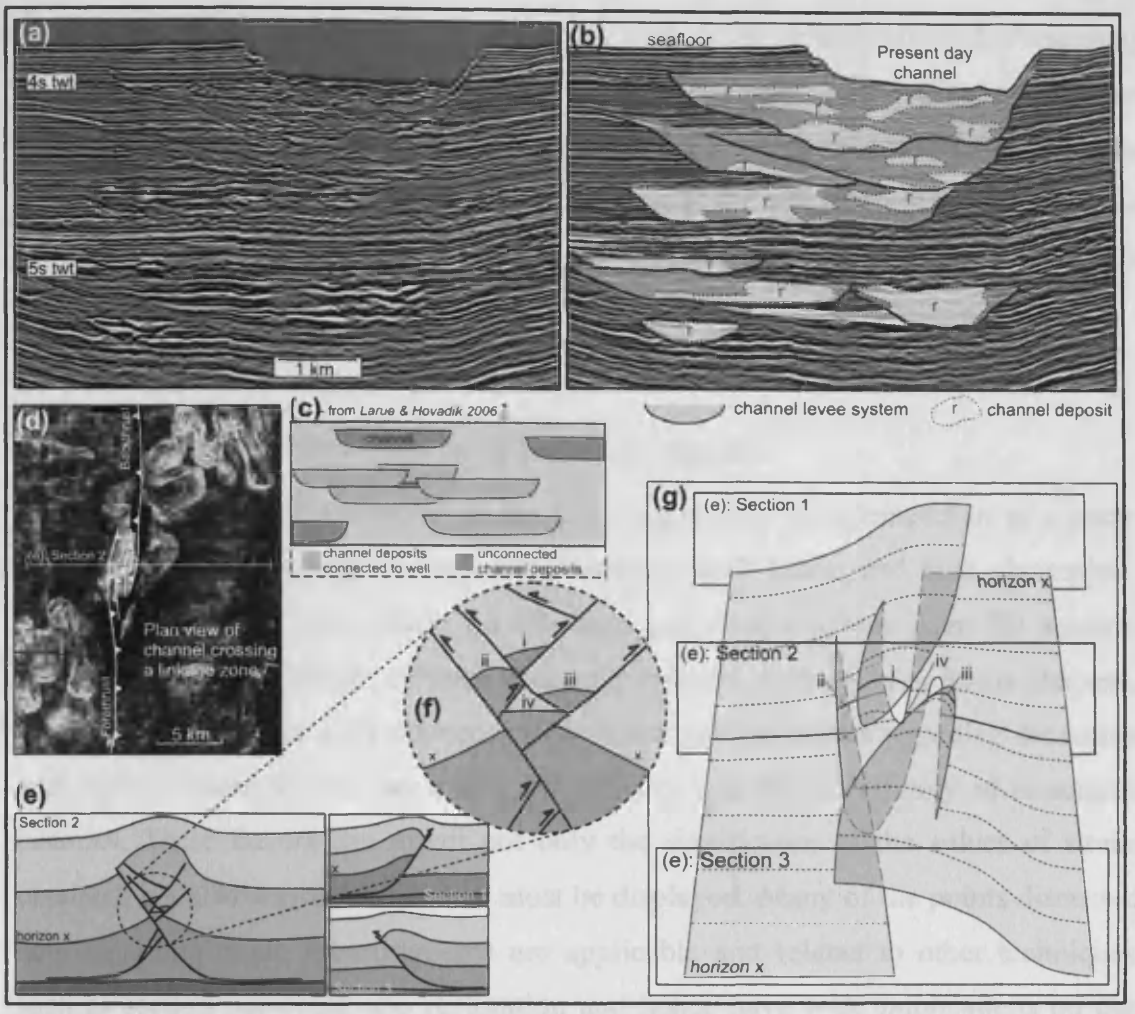

Figure 6.7: Implications of complex fault networks of a Type 3 antithetic thrust fault linkage on reservoir connectivity in a deep water Channel Levee Complex. **(a)** 3D seismic crossline imaging a stacked channel levee complex. **(b)** Interpreted section highlighting high amplitude reflections. **(c)** Figure adapted from *Larue and Hovadik (2006)* describing connectivity of channel deposits in a deep water setting. **(d)** Amplitude extraction map of horizon 'x' containing a meandering, buried channel crossing a Type 3 antithetic thrust fault linkage (Chapter 3). High amplitudes are light; lows amps dark. **(e)** Sketch cross sections to show variations in complexity of fault networks from simpler structures (sections 1 & 3) into a more complex Type 3 antithetic thrust fault linkage (section 2). **(f)** Zoom on section 2 in (e) to detail cross-cutting faults causing an interconnected fault network and repetition of horizon 'x'. **(g)** 3D model for horizon 'x' of the Type 3 linkage to show the complex trap geometries in and around the linkage zone.

the other creating an intricate fault network (Fig. 6.7e, cross section 2). Assuming faults in this area act as conduits for fluid flow (e.g. Morgan, 2003) this may increase both the link between source and trap and, potentially, the connectivity of sand bodies within the channel-levee. A greater understanding of the range of geometries of thrust fault linkages presented in Chapter 3 will also aide the generation of reservoir models in an area of structural complexity (Fig. 6.7g).

6.5 Errors and uncertainties in strain measurements

Strain analysis of sediments in the deep water fold belt featured in this study involved the measurement of fault displacement, fault heave and bulk shortening. Strain measurements were made on 2D time and depth sections from 3D seismic surveys. The methodologies of these measurements are outlined in previous chapters. These techniques come with inherent assumptions and limitations regarding the nature and style of deformation, the scaling of the data and the uncertainty of structural histories. These factors can affect not only the significance of the values of strain obtained, but also way in which data must be displayed. Many of the points discussed here regarding strain measurements are applicable and related to other techniques such as section balancing and restoration and hence have wide implications on our approach to structural analysis. This chapter therefore considers the possible errors and uncertainties introduced during the course of a study.

6.5.1 Fault measurements

The three components of fault movement are commonly referred to as the *displacement* (the distance of movement along the fault plane), *throw* (the vertical offset of a faulted sequence) and *heave* (the horizontal offset of faulted rocks). Measurements of all of these components are affected by the orientation of the plane of reference relative to the direction of movement of hangingwall strata. Measurements must be made on planes parallel to fault propagation direction otherwise 'apparent' values of displacement will be recorded. Fault displacement and throw are also influenced by time to depth conversion of seismic data. This is discussed in greater detail in Chapter 1 along with a consideration of seismic resolution. For the purposes of this study fault heave was predominantly recorded in order to minimise the influence of inaccurate depth conversion. True values of fault

heave and throw may also be altered by post-kinematic rotations of sediments, by process such as differential compaction, subsidence or a second phase of deformation. Fault displacement is unaffected in this case.

A major limiting factor on the reliability of values of fault movement in areas such as the deep water Niger Delta is the stratigraphic interpretation of seismic reflections across large displacement fault planes. The simplest method of horizon correlation involves interpreting a seismic reflection around the lateral tip of a fault, effectively making a direct link between hangingwall and footwall sediments. This was not possible on many faults in the Niger Delta due to the limited extent of the seismic surveys. In this case, other methods such as channel matching were employed (see section 1.3.4) to ensure a rigorous stratigraphic framework.

6.5.2 Bulk shortening measurements and assumptions

In this study, shortening measurements were made with reference to eleven interpreted seismic horizons using a simple line-length comparison methodology (Fig. 4.3). All methods of shortening calculation have inherent limitations and assumptions that must be considered. Much of the uncertainty is due to the assumptions that are necessary for the construction and restoration of balanced cross-sections (e.g. Dahlstrom 1969, Woodward et al., 1986) such as plane strain, conservation of bed length and area and isometric folding. The process of section balancing was developed to test the validity of cross-sections and structural interpretations in areas of insufficient seismic data (Woodward et al., 1985). The use of high resolution 3D seismic data therefore helps to produces more credible interpretations, but error can still be introduced in the conversion from time to depth for example. Sequential structural restorations, although an excellent tool for the estimation of orogenic contraction (e.g. Hossack, 1990), were generally not suitable for the purposes of this study and are discussed below. In this section the validity of methods regarding the estimation shortening values is considered.

Plane strain and isometric folding

The notion of 'plane strain' assumes that strain can be completely described by changes in size and shape in a single orientation of plane through a body (Twiss and Moores, 1992). That is to say that no deformation occurs normal to that plane. The assumption of plane strain is commonly used during the analysis of deformation as it

is an easier concept to understand and generalisations to three-dimensions do not always increase insight into the geometric characteristics of deformation (Twiss and Moores, 1992). As a result the majority of strain calculations in this study are performed on 2D sections. It is often invalid to assume plane strain in many natural geological settings however. The geometric changes across a thrust-belt that most affect the restoration of cross-sections are changes in folding styles and mechanisms. An understanding of the style of folding can validate the use of plane strain as, for example, parallel folds limit displacement to within a single transport plane. The preservation of section area presupposes parallel folding and preservation of bed lengths (Woodward et al 1985). When non-parallel or non-flexural slip folding occurs because of cleavage formation, then folding deviates from isometric bending (Lisle 1992) and it does not strictly maintain bed length in 3 dimensions. Hence Shackleton and Cooke (2007) state that "during the development of non-cylindrical folds a component of out-of-plane motion may develop where material displacement vectors deviate from the transport plane" thereby invalidating assumptions of plane strain. The majority of large scale folds in deep water fold and thrust belts, such as the Niger Delta, adhere to the former description and form simple structures where curvature is predominantly perpendicular to the fold axis. The amount of bedding curvature parallel to the fold axis is minimal so such non-plane strains are likely to be very small (Mason 1997). For folds where these conditions do not apply, measurements should always lead to minimum estimates of shortening (Hossack 1979). Measurements of deformation made on 2D lines are also dependent on the orientation of that plane relative to the transport direction of faults and folds (e.g. Cooper, 1983). Price (1981) suggested that section lines within 30° of the transport direction are close enough for most section constructions (less than 15% error), however others have suggested +/- 5° error is more reasonable (Woodward et al. 1986). All faults and folds featured in this study lie within this margin of error.

Ductile thickening during deformation

Given the assumptions above, balanced geological cross-sections are commonly drawn with the condition that the area of section has not changed during deformation (Hossack, 1979). In areas where most of the folds have been formed by flexural slip, the thickness of the beds measured normal to the bedding, as well as bed lengths, also remain constant (Dahlstrom 1969). This conventional section balancing

procedure can under- or over-estimate the true shortening values however, due to ductile deformation (Cooper and Trayner 1986). Strain within a thrust sheet is known to occur by a combination of rigid-body translation, internal rotation (i.e. folding) and distortion (layer-parallel shortening, LPS) mechanisms (Geiser, 1988). Some authors have attempted to account for this by the construction of balanced cross sections that incorporate strain not described by large scale features (e.g. cleavage, veins) in areas of penetratively deformed rocks (e.g. Mason, 1997). Ductile deformation in the internal zone of an orogenic belt, for instance, renders balancing dubious and shortening estimations are best carried out on highly competent beds, such as sandstone (Cooper and Trayner 1986).

To justify the use of balanced cross sections to calculate shortening, published studies cite a number of observations such as: i) comparable bed thicknesses of deformed strata in the fold belt and undeformed strata in the foreland (Dahlstrom, 1969), ii) a lack of penetrative deformation in outcrop (e.g. Mason, 1997), or iii) high stratigraphic competence contrasts that make deformation by flexural slip likely. Ductile strain may also be estimated from the position of the study area, such as external or internal parts of an orogenic belt (Woodward 1987). Thrust-zone strains and cleavage in the external zones, for instance are usually restricted to the lower 30-70 m of thrust sheets, so that they are negligible (<1% area) for practical purposes (Woodward et al., 1987). In gravitational fold belts, the amount of deformation is significantly less than in orogenic or accretionary fold belts (Rowan 2004).

The comparison of bed thicknesses between deformed and undeformed areas in the study area showed that the majority of units thin naturally downslope due to the nature of deposition in a prograding delta. Predicted thicknesses within the deformed section were therefore projected from parts of the section up and down dip of the fold belt. Thicknesses were also only compared within the pre-kinematic units within the Agbada Formation, as growth packages thin towards and over fold crests. No significant thickness increases within the deformed sector of the section, that would indicate ductile deformation during fold growth, were observed. Limitations in estimating bed thicknesses related to seismic resolution are minimised by considering larger packages of sediments. It was not possible to investigate the amount of penetrative deformation in the area due to a lack of published or released well data in the region. Few boreholes have been drilled in this part of the deep water Niger Delta at the time of submission of this thesis.

The sediments of the Agbada Formation comprise alternating layers of sand, silt and clays laid down in delta-front environments (e.g. Doust and Omatsola 1990). Competence contrasts between these layers may result in a predominance of flexural slip folding, however it is not clear if this is the case from data presented here. Corredor et al. (2005) inferred the predominance of flexural slip folding in the Niger Delta during sequential structural restorations of 2D seismic lines. Without such inferences the structural restorations are invalid. This also supports the assumptions for plane strain outlined above as beds in flexural slip folds with axes normal to the section will suffer no shortening or elongation along the axes.

The possible errors induced in shortening measurements caused by ductile deformation and layer-parallel shortening would result in estimations in bulk strain from balanced sections to be minimum values (Hossack, 1979). In addition to this it is reasonable to predict some forms of ductile deformation, if active in this area, to be consistent throughout the study area. Pre-thrust and -fold layer-parallel shortening, for instance, involves the bulk thickening of a layer prior to fold of fault initiation (e.g. Geiser, 1988) and would affect the entire 3D seismic surveys. This would result in absolute values of shortening recorded in this study to be erroneous but would not affect relative changes in displacement or the distribution of shortening within the fold belt, which is the main focus of this thesis.

Velocity models

Estimations of shortening made on time seismic data either using measurements of horizon line lengths, or based on sequential restorations of a balanced section, must necessarily follow the process of depth conversion. Previously in this chapter it was shown that fault heave is unaffected by post-migration depth conversion methods and so can be calculated from time sections. The true geometry and dimensions of a fold, on the other hand, can only be measured on a depth section. The values of shortening calculated by line-length comparisons across a fold will therefore be dependent on the velocity model used during the depth conversion. This is demonstrated using a simple, conceptual fold in Figure 6.8a. The folded strata are assigned a velocity V_1 and are surrounded by sediments of velocity V_2. The four scenarios describe the depth conversion effects of varying the ratio between V1 and V_2. If $V_1=V_2$ then fold geometries will resemble the time section (Fig. 6.8a). As the

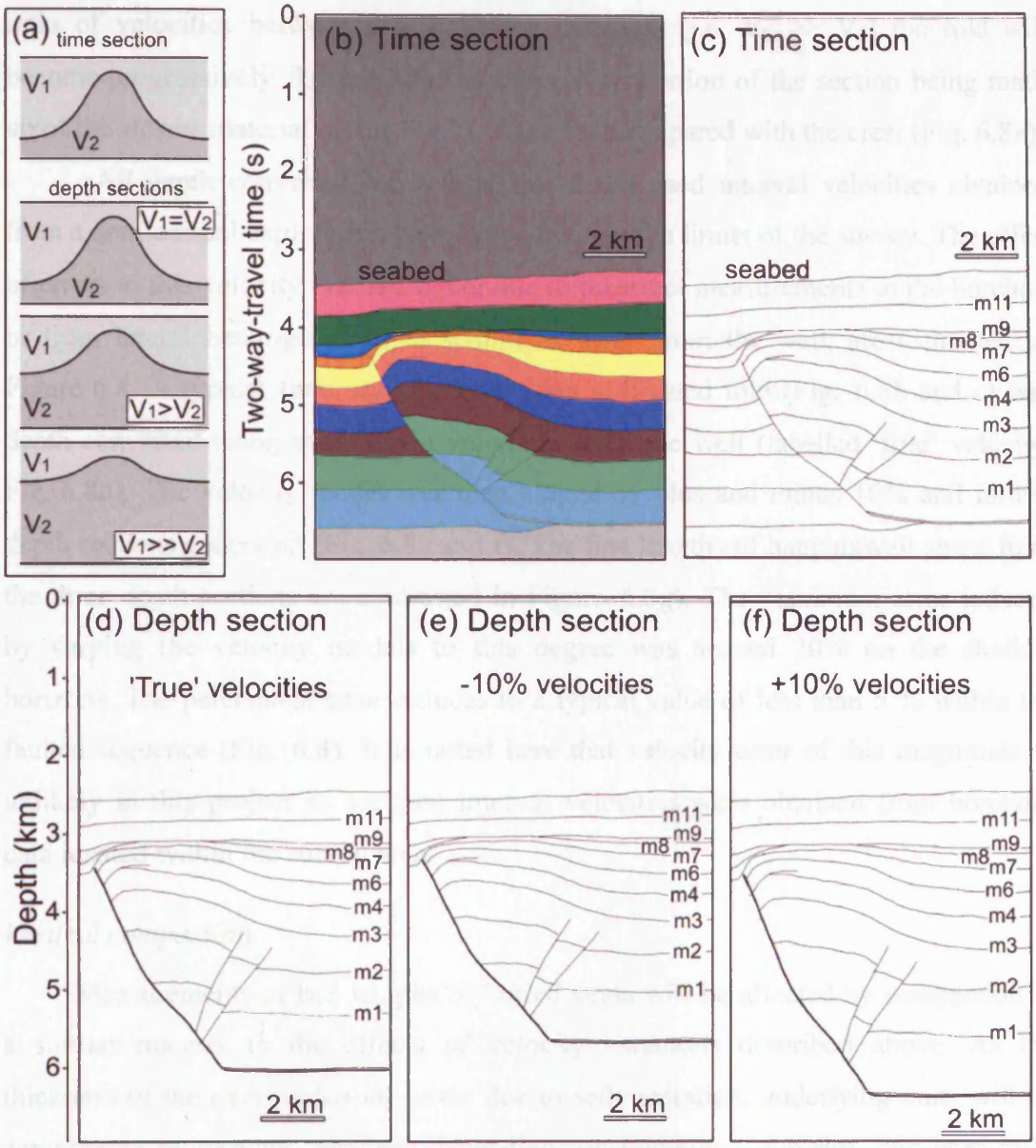

(g)

Hangingwall horizon shortening values and error				
Horizon	'True' *V* (m)	-10% *V* (m)	+10% *V* (m)	Max % change
m11	3	3	3	n/a
m9	8	7	9	13
m8	30	24	36	20
m7	82	66	98	20
m6	274	260	287	5
m4	421	403	441	5
m3	630	616	645	2
m2	1164	1153	1177	1
m1	1813	1802	1824	<1

Figure 6.8: Error analysis of an inaccurate velocity model on depth conversion and shortening measurements. **(a)** Illustration of changing fold shapes during depth conversion due to different velocity models. **(b)** and **(c)** Typical time sections interpreted from seismic data. **(d)** Depth converted section using velocity model based on borehole data. **(e)** and **(f)** Depth converted hangingwall sections using velocity model from (d) altered by +/- 10%. **(g)** Measurements of shortening using line-length comparison method for each of the three depth sections. The maximum percentage error between calculations from (d) and those made on (e) or (f) and displayed.

ratio of velocities between the sediments increases (i.e. $V_1 >> V_2$) the fold will become progressively flattened due to a larger proportion of the section being made up of the slower material on the flanks of the fold compared with the crest (Fig. 6.8a).

All depth converted sections in this thesis used interval velocities obtained from a confidential exploration well located within the limits of the survey. The effect of errors to this velocity models, either due to incorrect measurements in the borehole or from lateral heterogeneities in sediments away from the well, are estimated in Figure 6.8. A typical time section comprising a thrusted fold (Fig. 6.8b and c) was depth converted using the interval velocities from the well (labelled 'true' velocity, Fig. 6.8d). The velocity model was then altered by plus and minus 10% and further depth sections generated (Fig. 6.8e and f). The line lengths of hangingwall strata from the three depth sections are contrasted in Figure 6.8g). The maximum error induced by varying the velocity models to this degree was around 20% on the shallow horizons. The percentage error reduces to a typical value of less than 5 % within the faulted sequence (Fig. 6.8). It is noted here that velocity error of this magnitude is unlikely in this project as accurate interval velocities were obtained from borehole data located within the survey area.

Vertical compaction

Measurements of bed lengths of buried strata will be affected by compaction in a similar manner to the effects of velocity variations described above. As the thickness of the overburden increases due to sedimentation, underlying units will be compressed by varying amounts depending on lithology, porosity and pore fluid (e.g. Brown, 1999). Deposition of syn-kinematic strata during fold development can also lead to growth strata thinning towards and onto the crest. This can in turn result in differential compaction as the greater thickness of sediments on the flanks of the fold causes greater compaction beneath increasing fold amplitude. This is all accounted for during the process of back-stripping and structural restoration (e.g. Corredor et al., 2005). This section assesses the possible errors induced in this thesis during the measurement of shortening by line-length comparisons without decompacting sections. Figure 6.9 presents an example depth section of a thrusted fold which is decompacted to the m3 horizon using lithology characteristics, such as porosity, from a confidential exploration borehole within the study area. No attempt at restoration is made here so that the effect of

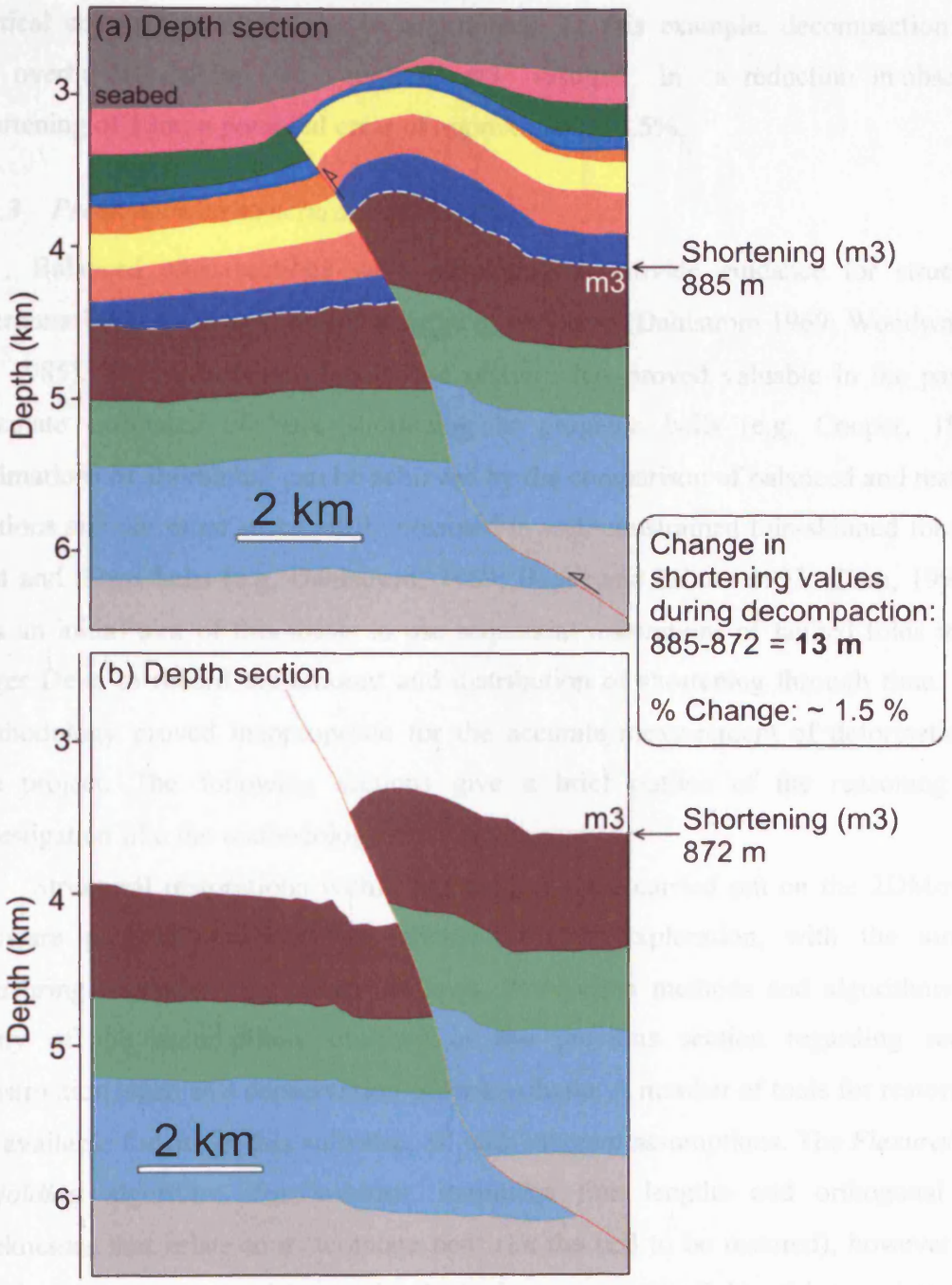

Figure 6.9: Demonstration of the effect of decompaction on shortening values obtained using the line-length comparison methodology. **(a)** Typical depth converted section through a thrusted fold in the deep water Niger Delta. Shortening of the m3 horizon is calculated to be 885 metres. **(b)** Decompacted section down to the m3 horizon. Decompaction was performed using 2DMove software and information on lithological properties of the overburden obtained from a nearby borehole. No attempted at structural restoration was made in order to highlight the effect of decompaction alone on shortening values. Shortening of horizon m3 following decompaction of the overburden was calculated as 872 metres, a change 13 metres or c. 1.5%.

vertical compaction alone can be ascertained. In this example, decompaction of the overburden down to horizon m3 resulted in a reduction in observed shortening of 13m, a potential error of approximately 1.5%.

6.5.3 Problems with structural restorations

Balanced cross-sections were developed to provide guidance for structural interpretations in areas of limited seismic or well data (Dahlstrom 1969; Woodward et al., 1985). The restoration of balanced sections has proved valuable in the past to calculate estimates of bulk shortening in orogenic belts (e.g. Cooper, 1983). Estimations of shortening can be achieved by the comparison of balanced and restored sections and are more successfully obtained in well-constrained thin-skinned foreland fold and thrust belts (e.g. Dahlstrom, 1969; Boyer and Elliott, 1992; Chen, 1999). It was an initial aim of this thesis to use sequential restorations of faulted folds in the Niger Delta to record the amount and distribution of shortening through time. This methodology proved inappropriate for the accurate measurement of deformation in this project. The following sections give a brief outline of the reasoning and investigation into the methodology used in this study.

Structural restorations within this project were carried out on the 2DMove^{TM} software program provided by Midland Valley Exploration, with the aim of measuring shortening on numerous lines. Restoration methods and algorithms use many of the assumptions outlined in the previous section regarding section construction, such as a conservation of rock volume. A number of tools for restoration are available for use in this software, all with inherent assumptions. The *Flexural Slip Unfolding* algorithm, for instance, maintains line lengths and orthogonal bed thicknesses that relate to a 'template bed' (i.e the bed to be restored), however line lengths are not preserved in passive beds that are not parallel to this template (Fig. 6.10). Therefore, although restoration may produce realistic geometries and true values of shortening on the template bed, any further stage of restoration will be using bed-lengths that no longer reflect the original interpreted section. Flexural unfolding may cope well in the folded part of the section (i.e. the shallow section of the hangingwall), and not so well in the less folded part (i.e. the deeper section) (Fig. 6.11). *Fault Parallel Flow* also assumes a predominance of deformation by flexural slip between layers, however the key parameters for this algorithm are the geometry

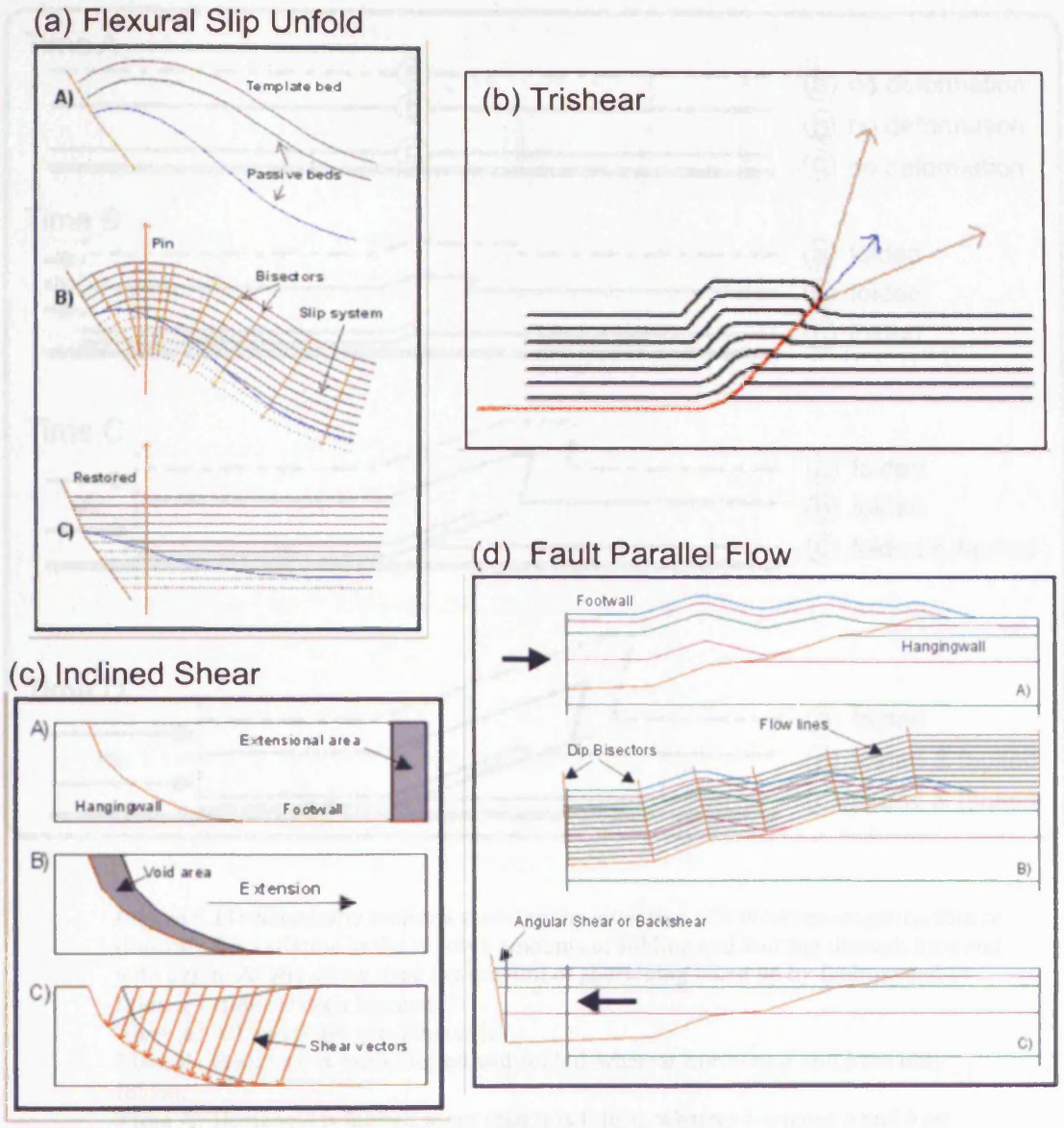

Figure 6.10: Summary of the restoration tools available in the 2DMove™ software. **(a)** Flexural Slip Unfolding algorithm- maintains line lengths and orthogonal bed thicknesses that relate to a 'template bed' (i.e. the bed to be restored). Line lengths are not preserved in passive beds that are not parallel to this template. **(b)** Trishear algorithm - attempts to deal with folding ahead of a propagating fault tip through the definition of a trishear zone. Outside of the trishear zone beds in the hangingwall are deformed using Fault Parallel Flow methodology. **(c)** Inclined Shear algorithm. **(d)** Fault Parallel Flow - assumes deformation by flexural slip between layers. Key parameters for this algorithm are the geometry of the fault plane at depth, the angular relationship between bedding and a fault plane and the 'angular shear' factor. Particles are restored along lines parallel to a fault plane. Images presented here are taken from the 2DMove™ software *help* package provided by Midland Valley exploration.

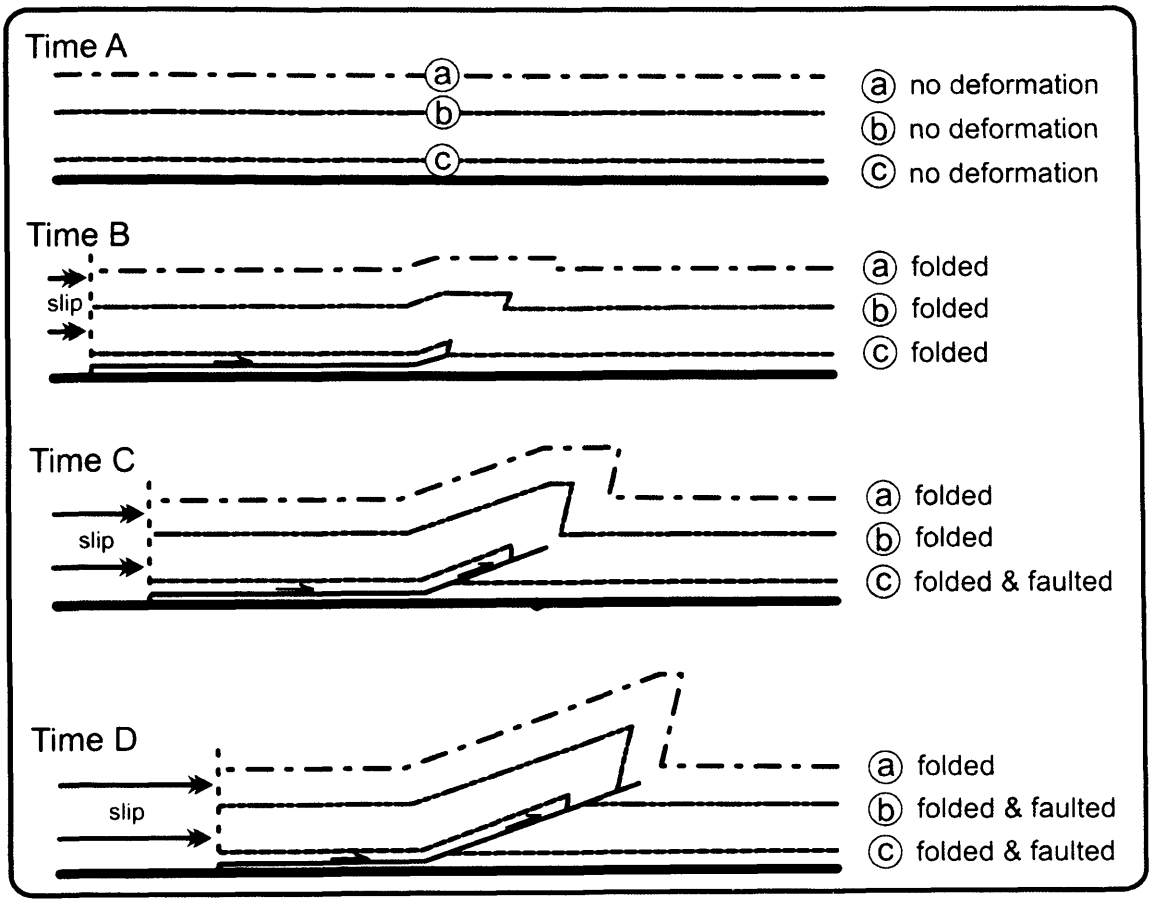

Figure 6.11: Schematic sections showing the evolution of a thrust-propagation fold to illustrate the variation in the relative amounts of folding and faulting through time and with depth. At any given time the amount of shortening taken up by faulting and/or folding varies for each horizon.
Time A: All layers are pre-kinematic.
Time B: Horizon *c* is both faulted and folded, whereas horizons *a* and *b* are only folded.
Time C: Horizon *c* is faulted more than it is folded, whereas horizons *a* and *b* are only folded.
Time D: Horizons *c* and *b* are faulted and folded, whereas horizon *a* is only folded.

of the fault plane at depth, the angular relationship between bedding and a fault plane and the 'angular shear' factor. Particles are restored along lines parallel to a fault plane and hence only honour the assumption of inter-bed slip if bedding is also sub-parallel with the fault, (i.e. long hangingwall-flat sections). Commonly, sections in this study display a high angle between bedding and fault planes (e.g. Fig. 6.9a) and hence this method would effectively be modelling inclined simple shear in the hangingwall. One limitation of *Inclined Shear* algorithms is a change in bed thickness on restored sections which can be problematic when trying to recognise fold growth. Finally, the *Trishear* algorithm attempts to deal with folding ahead of a propagating fault tip through the definition of a trishear zone (e.g. Erslev, 1991) (Fig. 6.10). Unfortunately, outside the trishear zone beds in the hangingwall are deformed using *Fault Parallel Flow* methodology and are thus affected by similar limitations.

A summary of the effects of structural restoration algorithms on restored sections is presented in Figure 6.12 which applies these tools to synthetic sections. This is not intended to reflect a realistic geological scenario, but instead aims to use simple geometric structures to assess the adaptations made to beds during the restoration process. Many of the limitations described above are confirmed by this exercise. *Fault parallel flow*, *trishear* and *inclined* shear all cause an increasing change in bed thickness with depth (Fig. 6.12b, c and d), even on a synthetic section where all hangingwall strata are parallel (Fig. 6.12a). *Flexural slip unfold* successfully restores parallel beds in the first synthetic section (Fig. 6.12d), however when folding of the shallow section is introduced (Fig. 6.12b) this results in deeper beds being restored down the fault, past original positions (Fig. 6.12h).

In general, many structural restoration techniques use one method for the restoration of deformation by folding (e.g. flexural slip unfold), and another to move hangingwall stratigraphy along a fault plane (e.g. fault parallel flow). Each method is designed using assumptions specific to the task being performed, and hence can induce error on the other mechanism. This is problematic as the relative amounts of faulting and folding during the development of a fault propagation fold, for instance, can be shown to vary with depth and through time for any given horizon (Fig. 6.11).

The measurement of shortening on sequential restorations of a folded and faulted cross section also produces uncertainties due to the errors induced by the restoration algorithms mentioned above. If the restoration of the uppermost bed leads

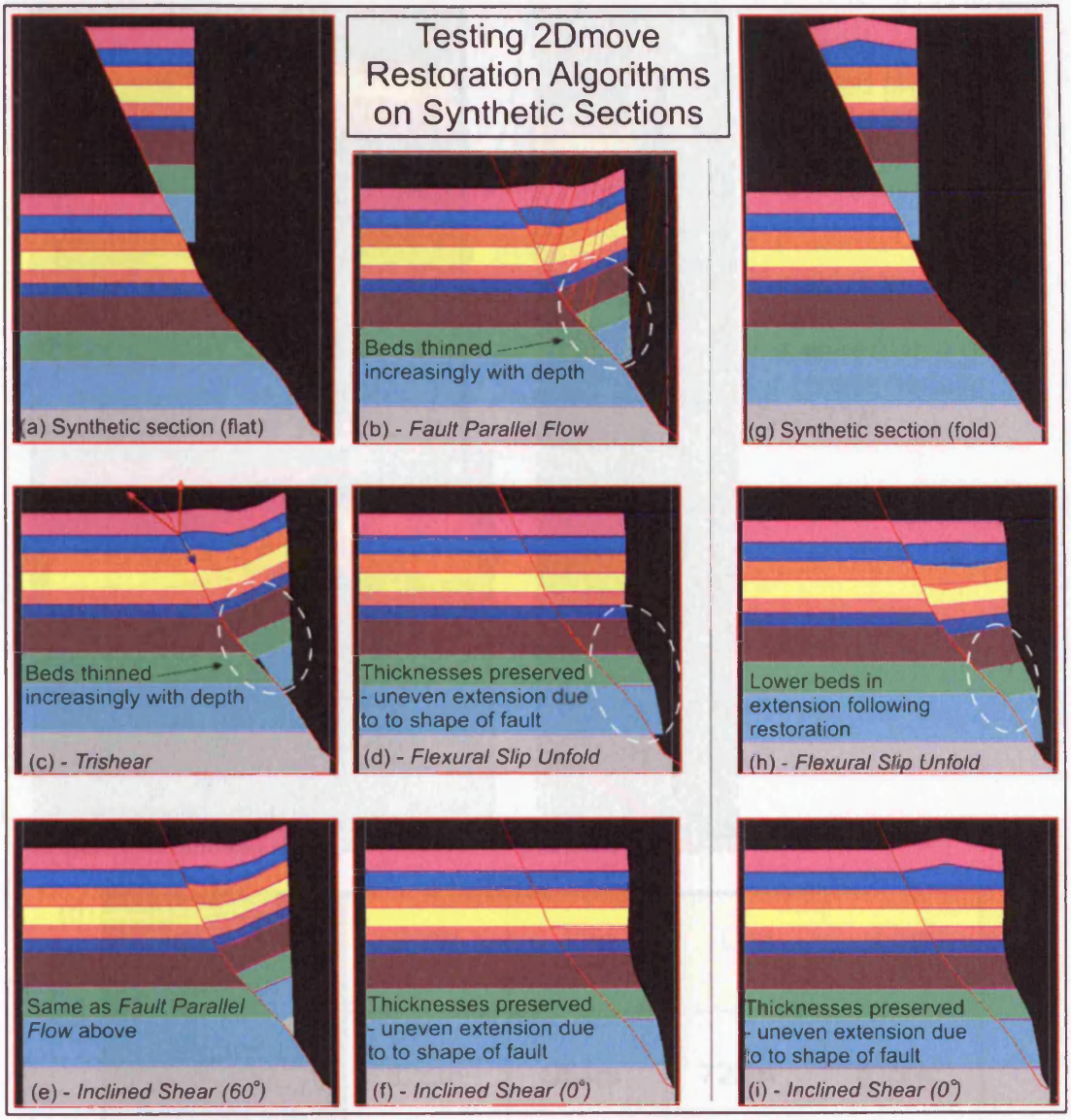

Figure 6.12: Two synthetic sections are presented in order to test the algorithms of structural restoration; the first **(a)** with parallel, uniform hangingwall beds, the second **(g)** with folded shallow hangingwall strata.
Restorations of the first synthetic section. **(b)** *Fault parallel flow*: Beds are thinned increasingly with depth. **(c)** *Trishear*: Very similar to (b) as outside the trishear zone, beds in the hangingwall are deformed using *Fault Parallel Flow*. **(d)** *Flexural slip unfold*: Thicknesses are preserved as all beds in the hangingwall were parallel. Additional extension at the base of the section due to the shape of the fault. **(e)** *Inclined Shear (60°)*: Thins hangingwall strata and 'under-restores' the base of the section. **(f)** *Inclined Shear (0°)*: Thicknesses preserved – effectively a simple 'fault-slide'.
Restorations of the second synthetic section. **(h)** *Flexural slip unfold*: Lower beds put into extensional geometry following restoration due to non-parallel horizons in the original hangingwall section. **(i)** *Inclined Shear (0°)*: Thicknesses preserved – effectively a simple 'fault-slide'.

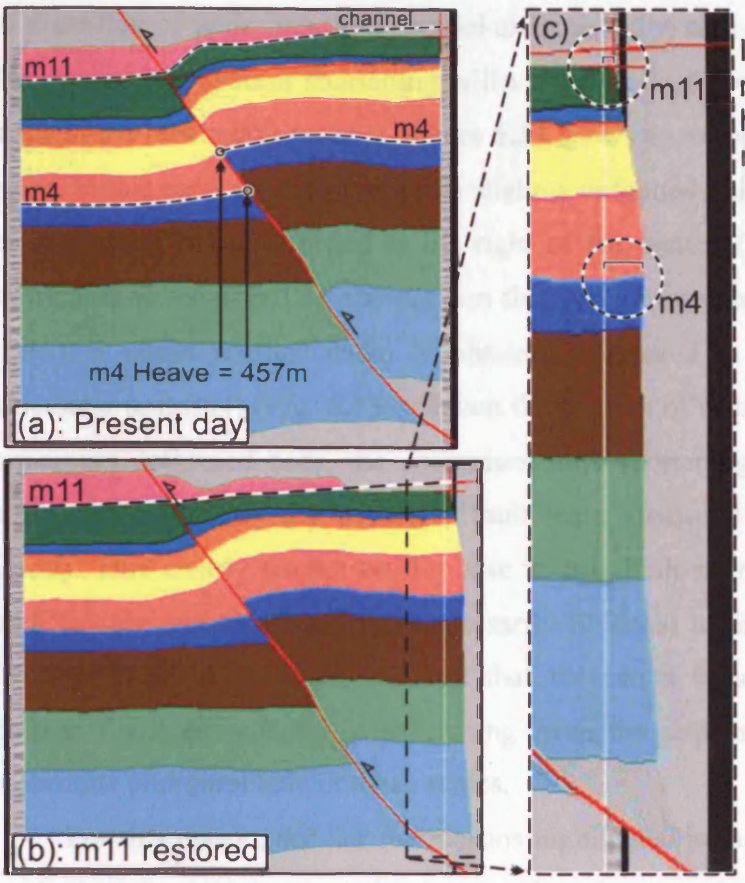

(d)

Shortening on horizon m4 by..	Line 1	Line 2	Line 3	Line 4
..sequential restoration	328m	954m	725m	618m
..line length comparison	612m	956m	1248m	1197m
..present day fault heave	502m	726m	940m	760m

Figure 6.13: Quantification of errors in shortening measurements induced limitations in structural restoration methods. **(a)** Typical depth converted section showing a thrusted fold. **(b)** Structural restoration of horizon m11 in (a) back to paleo-seabed geometry. Flexural slip unfold algorithms was applied in this case. Amount of shortening was measured as the amount of section protruding outside the section width (right) following restoration. **(c)** Zoom on part of (b) to show inconsistent amounts of shortening with depth following restoration. Horizon m11 suggests 112 metres of shortening have been restored during this step. Horizon m4 (a pre-kinematic horizon) suggests 373 metres have been restored during this step. **(d)** Table contrasting maximum shortening values of horizon m4 on four seismic lines using sequential restoration and line-length comparison methods. Present day measurements of fault heave on the m4 horizon are also included. Note that maximum values of bulk shortening, calculated by the restoration method, are commonly less than fault heave.

to distortion of underling, non-parallel units, as in the case of *flexural slip unfold* then the amount of apparent shortening will vary with depth on each horizon and at each stage in the restoration process. Figure 6.13 shows an example section to illustrate this point. In this case, the unfolding of a shallow unfaulted unit results in various amounts of shortening being recorded to the right of the section (Fig. 6.13). If the value of shortening is measured on the horizon that was restored to its depositional geometry (m11), a much smaller value is obtained compared to that measured on a pre-kinematic unit (m4) (Fig. 6.13c). When the process of restoration is continued for the remaining deformed beds, the *maximum* bulk shortening of pre-kinematic units is commonly lower than the amount of fault heave measured on the original section (Fig. 6.13d). This clearly cannot be the case as true bulk shortening, which incorporates both folding and faulting, must necessarily be equal to or greater than the value of faulting alone. It is suggested here that the errors induced during the restoration process make estimations of shortening from the sequential restoration of sections inaccurate and unreliable at these scales.

For this reason, and for the reasons highlighted in the earlier sections, a simpler method of shortening calculation by *line-length comparisons* was utilised to estimate bulk shortening within the deep water Niger Delta.

6.5.4 Line-length comparison method

The above assumptions, limitations and uncertainties associated with structural restorations and strain measurements lead to the decision with regards this thesis to calculate shortening values by a method of simple line-length comparisons. The methodology of this process is highlighted in the Chapters 4 and 5 (Fig. 4.3). This method has the advantages of allowing time-efficient calculations that facilitate higher-definition plots of the distribution of shortening. It is less prone to errors induced by restoration algorithms and assumptions. Potential error does exist with method in the form of vertical compaction and erroneous velocity models used in depth conversion. In this study these uncertainties are considered to be within acceptable limits as both are typically less than 5% error (Fig. 6.9) and data from the velocity model was obtained direct from borehole data within the survey limits. Potential errors are also most likely to affect the absolute values of shortening. This study has been most concerned with along strike variations and trends in deformation and it is suggested that the limitations associated with this method, such as vertical

compaction, velocity errors and pre-thrust ductile thickening, are likely to be relatively consistent throughout the survey area thereby minimising the effect on shortening distribution.

6.6 Project limitations and further research

The work presented in this thesis is a comprehensive study, based on 3D seismic data, of the geometry and interaction of structural components of part of the deep water fold and thrust belt of the Niger Delta. The utilisation of 3D data have produced high-definition mapping and measurement of strain within a fold belt that was previously unattainable. However, whilst this project provides fresh insight into fold belt characteristics and development, some of the interpretations and conclusions made here have been partially hindered by a number of limitations. The final part of this chapter now considers the project limitations with reference to future paths of research that may overcome these difficulties.

A significant limitation throughout this research has been the incomplete coverage of the study area by the seismic surveys. Although the data sets utilised in this study covered a combined area of c. 5000 square kilometres only part of the outer fold and thrust belt is imaged (Fig. 1.1). The lengths of both folds and faults generally exceeded the width of the survey and only partial profiles were obtained (Chapters 3 and 5). More extensive, regional 2D seismic datasets are inherently unsuitable for high-resolution mapping of faults due to wide spacing of seismic lines. The acquisition of expensive 3D seismic data over this part of the Niger Delta is driven by pioneering hydrocarbon exploration in deep waters, and hence for future work to provide a more complete study of fault and fold characteristics is dependent on the production and release of more data.

Another significant limitation imposed on this project has been the paucity of well data in this part of the Niger Delta. This is due in part to the high costs of drilling boreholes in such deep water. As the outer thrust belt of the Niger Delta represents an emerging prospective area for hydrocarbons, the majority of wells that have been drilled remain confidential and therefore are not released for academic study. The single well used in this study had the benefit of being located within the survey area allowing direct comparison between measured interval velocities and seismic reflections. These values were applied in this study during depth conversion and back-

stripping, but the well information could not be included. There is also very little information available on the nature of the detachment in the outer most parts of the Niger Delta. Very few wells have been able to pierce the Akata Formation due to intense over-pressures. As more well data becomes available from the ongoing exploration activity of industry, the additional information on mechanical and lithological heterogeneities, the characteristics of the decollement and a more accurate velocity model will enable clearer conclusions to be drawn on fault and fold development.

Within this discussion section the consideration of the controls on fault and fold linkage geometries highlighted the potential effect of the dip and lateral alignment of linking faults (section 6.3.2). Interesting questions that arise from such a hypothesis include what controls the locations of fault and fold nucleation? Do pre-existing structures play an important role in more recent structural growth? Can the nature and distribution of over-pressure and mobility of the shales in the detachment unit be described? Do these characteristics vary spatially or temporally? Due to the time constraints of a PhD project these pertinent uncertainties could not be investigated in any real depth. It is known for instance that the part of the Niger Delta featured in this thesis overlies a basement sequence with dramatic horizontal variation in character and thickness associated with the Charcot fracture zone (e.g. Davies, 2005). It is the opinion of the author that an appreciation of the relationship between the deformation manifest in pre-delta rocks and more recent sediments would be a useful and fruitful avenue for future research.

Chapter 7

CHAPTER 7

7 CONCLUSIONS

This study has been one of the first to use 3D seismic data to describe detailed distributions of strain within a fold and thrust belt. The preceding chapters have demonstrated that this novel approach has provided important insight into the geometry, interaction and kinematic relationship of compressional structures that accommodate deformation in a toe-of-slope deltaic setting. Although investigations into thrust fault development and linkage have been the focus of geological interest for several decades through extensive field studies of orogenic belts, new generation seismic data allow for three-dimensional observations and conclusions to be drawn, that will complement established models of thrust growth. Whilst this project focused on one geographic area it is anticipated that the findings are relevant and applicable to fold and thrust belts worldwide. The primary conclusions of this PhD project, and specific summarising statements drawn from each of the previous chapters, are listed below.

7.1 General Conclusions

- The Niger Delta is an ideal setting to investigate the initiation and development of folds and thrusts as numerous 3D seismic surveys have been acquired during recent hydrocarbon exploration, thrust fault and stratal geometries are well imaged down to significant depths and patterns of sedimentation recorded in the stratigraphic column chart fold and fault development through time.
- 3D seismic data provides a unique opportunity to explore the characteristics of fold belts from a number of angles, including detailed analysis of fault plane geometries, high-resolution mapping of the spatial extent of syn-kinematic growth strata and high-density measurements of the distribution of fault and fold strain.

7.2 Antithetic fault linkages in a deep water fold and thrust belt

- The portion of the deep water fold belt featured in this project is comprised of comparable numbers of thrust faults of opposing dip. This has provided the basis for this study to document both synthetic and antithetic fault linkages.
- Along strike linkage of thrust faults of opposing dip in the Niger Delta results in the along strike switch in the vergence of associated hangingwall anticlines.
- Along strike antithetic thrust fault linkages occur in a number of distinct structural styles and geometries that comprise all permutations of antithetic fault interactions observed in this thesis.
- Antithetic thrust fault linkages can be classified based primarily upon the vertical extent of fault surfaces within a transfer zone relative to the branch line of the interacting antithetic faults. The classification comprised three sub-divisions.
- Type 1 antithetic thrust fault linkages are defined by faults that overlap exclusively above the level of the branch line of the antithetic thrusts within the transfer zone.
- In Type 2 linkages faults overlap exclusively below the level of the branch line of the antithetic thrusts within the transfer zone.
- Type 3 linkages are defined by both faults continuing above and below the branch line in the transfer zone resulting in cross-cutting relationships between the constituent faults.
- Stratal deformation and connectivity across an antithetic linkage zone varies with each type of interaction and with depth. Displacement is transferred between linking faults and folds through a number of transfer structures.
- In a Type 1 linkage sediments above the branch line form a 'pop-up' structure and are connected via an indirect 'hangingwall-hangingwall transfer fold'. Below the branch line beds are continuous and planar in the downdip direction.
- Distinctive tight folds characterise deformation above the branch line in a Type 2 linkage, whereas below this level strata are connected via an indirect, undeformed footwall-footwall 'corridor'.
- Strata above the branch line in Type 3 linkages form indirect hangingwall-hangingwall transfer folds, while those below form indirect, undeformed

footwall-footwall 'corridors'. An increase in horizon repetition is commonly evident in the mid section, close to the branch line.

- Examples of antithetic linkages are also interpreted from literature from studies of fold belts in the Canadian Arctic and Pakistan.

7.3 Fold and thrust growth by segment linkage

- The fault heave and bulk shortening profiles along a single, isolated faulted fold of a deep water fold and thrust belt represents the first quantitative study of thrust faults to use strike-projected contour plots.
- Measurements of growth sequences and detailed fault plane geometries described numerous faults of similar and opposing dip linking along strike to create a through-going fold.
- The distribution of bulk shortening along faulted folds that comprise either a single thrust fault or numerous linked thrusts can be simple, systematic and similar to that observed for extensional fault displacement.
- Individual heave profiles of overlapping, linked faults show modification of contours away from systematic patterns. Displacement transfer occurs between overlapping faults leading to more regular profiles on aggregated plots.
- Deficits in fault heave, both in the form of perturbations on non-linking or aggregated profiles and displacement minima within linkage zones, are compensated to some degree by an increase in the amount of fold strain. Fold amplitude or fold crest elevation is largely unaffected by minor variations in fault heave.
- The geometry and distribution of syn-kinematic growth strata indicates that the evolution of a fold involved the nucleation and amalgamation of three smaller folds and culminations. At least eight thrusts initiated along the length of the early folds before lateral propagation and along strike synthetic linkage eventually created four major faults of opposing dip. Lateral fault propagation produced synthetic and antithetic thrust fault linkages.
- There is little conclusive data in this study to determine if folding preceded faulting or vice-versa.

- The distribution of syn-kinematic sediments can be used to show that the along strike length of fold B was established relatively early albeit as three separate culminations.
- Folds coalescence along strike results in culmination migration to a central, single apex.
- Initial offset by a propagating tip commonly occurs above the level of the detachment. The point maximum fault heave subsequently moves downwards, to either the level of the detachment or the point of intersection with another fault.
- Folds can accommodate shortening as a coherent unit, producing displacement and shortening profiles similar to that comprising a single fault. This suggesting component faults have been kinematically linked throughout development.

7.4 Synchronous growth of a fold and thrust belt

- The use of 3D seismic data has demonstrated a kinematic relationship between all faults and folds within a fold belt.
- A general foreland-propagating sequence of thrusting is overprinted by some out-of-sequence nucleation of faults and folds. Overlap in the duration of activity on all structures demonstrates firstly, that all faults were active for a significant period of the deformation history and secondly, that the initiation of new folds does not coincide with cessation of movement on older features.
- Transfer zones with similar fault plane and stratal geometries display along strike heave profiles that either resemble that of a single fault and fold (i.e. regular contours within the linkage zone) or exhibit a net deficit (i.e. an irregular contours within the linkage zone). There is a positive correlation between the lateral extent of a transfer zone and the efficiency of displacement transfer.
- The plunge of through-going folds, associated with antithetic transfer zones, is maintained along strike through the zones of linkage, regardless of variations in heave and shortening. Fold shape is modified within transfer structures to maintain fold amplitude.
- Deficits in heave and shortening within transfer zones correspond to complementary morphologies and fault profiles of structures located up and

downdip indicating dip-parallel transfer of displacement via common detachments.

- Aggregate heave and bulk shortening profiles of a fault and fold array have regular, sub-horizontal contours within the shallow section. Deeper horizons maintain irregularities indicating kinematic coherency.
- Sub-horizontal contours correspond to the syn-kinematic sequence with irregularities remaining on the pre-kinematic sediments on individual faults, along strike linking fault pairs and the fold belt as a whole.
- Irregularities in pre-kinematic package correspond to locations of maximum fault heaves and present day linkage zones.
- The synchronous growth of structures within a fold belt, along with the evidence of efficient displacement transfer between all constituent features, suggests a three-dimensional nature to kinematic interaction of faults and folds.

8 REFERENCES

Aamir, A., Siddiqui, M., 2006. Interpretation and visualisation of thrust sheets in a triangle zone in eastern Potwar, Pakistan. The Leading Edge 25, 24-37.

Anders, M. H., Schlische, R. W., 1994. Overlapping faults, intrabasin highs, and the growth of normal faults. Journal of Geology 102, 165-180.

Armstrong, F. C., Oriel, S. S., 1965. Tectonic development of Idaho-Wyoming thrust belt. AAPG Bulletin 49, 1847-1866.

Armstrong, P. A., Bartley, J. M., 1993. Displacement and deformation associated with a lateral thrust termination, southern Golden Gate Range, southern Nevada, U.S.A. Journal of Structural Geology 15, 721-736.

Aydin, A., 1988. Discontinuities along thrust faults and the cleavage duplexes. In: Mitra G, W. S. F. (Eds.), Geometries and mechanism of thrusting, with special reference to the Appalachians. Special Paper - Geological Society of America 222, 223-232.

Barnett, J. A. M., Mortimer, J., Rippon, J. H., Walsh, J. J., Watterson, J., 1987. Displacement geometry in the volume containing a single normal fault. AAPG Bulletin 71, 925-937.

Bilotti, F., Shaw, J., 2005. Deep-water Niger Delta fold and thrust belt modeled as a critical-taper wedge: The influence of elevated basal fluid pressure on structural styles. AAPG Bulletin 89, 1475-1491.

Boyer, S., Elliot, D., 1982. Thrust Systems. AAPG Bulletin 66, 1196-1230.

Briggs, S. E., Davies, R. J., Cartwright, J. A., Morgan, R., 2006. Multiple detachment levels and their control on fold styles in the compressional domain of the deepwater west Niger Delta. Basin Research 18, 435-450.

Brown, A. R., 1999. Interpretation of Three-Dimensional Seismic Data. AAPG Memoir 42, SEG Investigations in Geophysics.

Burbank, D. W., Anderson, R. S., 2001. Tectonic Geomorphology. Blackwell Science, Massachusetts.

Butler, R., 1982. The terminology of structures in thrust belts. Journal of Structural Geology 4, 239-245.

Butler, R., Coward, M. P., Harwood, G. M., Knipe, R. J., 1987. Salt control on thrust geometry, structural style and gravitational collapse along the Himalayan mountain front in the Salt Range of northern Pakistan. In: Lerche, I., O'Brien, J. J. (Eds.), Dynamical geology of salt and related structures. Academic Press, Orlando, 339-418.

Butler, R. W. H., 1992. Structural evolution of the western Chartreuse fold and thrust system, NW French Subalpine Chains. In: McClay, K. R. (Eds.), Thrust Tectonics. Chapman and Hall, New York, 287-297.

Cartwright, J., Trudgill, B., Mansfield, C., 1995. Fault growth by segment linkage: an explanation for scatter in maximum displacement and trace length data from the Canyonlands Grabens of SE Utah. Journal of Structural Geology 17, 1319-1326.

Cartwright, J. A., Trudgill, B., 1994. Relay-ramp forms and normal-fault linkages, Canyonlands National Park, Utah. Geological Society of America Bulletin 106, 1143-1157.

Cartwright, J. A., Huuse, M., 2005. 3D seismic technology; the geological "Hubble". Basin Research 17, 1-20.

Chester, J. S., 2003. Mechanical stratigraphy and fault-fold interaction, Abaroska thrust sheet, Salt River Range, Wyoming. Journal of Structural Geology 25, 1171-1192.

Childs, C., Easton, S. J., Vendeville, B. C., Jackson, M. P. A., Lin, S. T., Walsh, J. J., Watterson, J., 1993. Kinematic analysis of faults in a physical model of growth faulting above a viscous salt analogue. Tectonophysics 228, 313-329.

Childs, C., Watterson, J., Walsh, J. J., 1995. Fault overlap zones within developing normal fault systems. Journal of the Geological Society, London 152, 535-549.

Childs, C., Nicol, A., Walsh, J. J., Watterson, J., 2003. The growth and propagation of synsedimentary faults. Journal of Structural Geology 25, 633-648.

Cobbold, P. R., Szatmari, P., Demerican, L. S., Coelho, D., Rossello, E. A., 1995. Seismic and experimental evidence for thin-skinned horizontal shortening by convergent radial glidingon evaporites, deep-water Santos Basin, Brasil. In: Jackson, M. P. A., Roberts, D. G., Snelson, S. (Eds.), Salt tectonics: a global perspective: AAPG Memoir 65, 305-321.

Cobbold, P. R., Mourgues, R., Boyd, K., 2004. Mechanism of thin-skinned detachment in the Amazon Fan: assessing the importance of fluid overpressure and hydrocarbon generation. Marine and Petroleum Geology 21, 1013-1025.

Cohen, H., McClay, K., 1996. Sedimentation and shale tectonics of the northwestern Niger Delta front. Basin Research 13, 313-328.

Connors, C. D., Denson, D. B., Kristiansen, G., Angstadt, D. M., 1998. Compressive anticlines of the mid-outer slope, central Niger Delta (abs). AAPG Bulletin 82, 1903.

Cooper, K., Hardy, S., Gawthorpe, R., 2003. Stratigraphic and structural expression of the lateral growth of thrust fault-propagation folds: results and implications from kinematic modelling. Basin Research 15, 165-182.

Corredor, F., Shaw, J., Bilotti, F., 2005. Structural styles in the deep-water fold and thrust belts of the Niger Delta. AAPG Bulletin 89, 753-780.

Couzens, B. A., Wiltschko, D. V., 1996. The control of mechanical stratigraphy on the formation of triangle zones. Bulletin of Canadian Petroleum Geology 44, 165-179.

Cowie, P. A., Scholz, C. H., 1992. Physical explanation for the displacement–length relationship of faults using a post-yield fracture mechanics model. Journal of Structural Geology 14, 1133-1148.

Currie, J. B., Patnode, H. W., Trump, R. P., 1962. Development of folds in sedimentary strata. Geological Society of America Bulletin 73, 655-674.

Dahlstrom, C. D. A., 1969. Balanced cross sections. Canadian Journal of Earth Sciences 6, 743-757.

Dahlstrom, C. D. A., 1970. Structural Geology in the Eastern Margin of the Canadian Rocky Mountains. Bulletin of Canadian Petroleum Geology 18, 332-406.

Dahlstrom, C. D. A., 1990. Geometric constraints derived from the law of conservation of volume and applied to evolutionary models for detachment folding. AAPG Bulletin 74, 336-344.

Damuth, J., 1994. Neogene gravity tectonics and depositional processes on the deep Niger Delta continental margin. Marine and Petroleum Geology 11, 320-346.

Davies, R., 2003. Kilometer-scale fluidization structures formed during early burial of a deep-water slope channel on the Niger Delta. Geology 31, 949-952.

Davis, D., Suppe, J., Dahlen, F. A., 1983. Mechanics of fold-and-thrust belts and accretionary wedges. Journal of Geophysical Research 88, 1153-1172.

Davis, D. M., Engelder, T., 1985. The role of salt in fold-and-thrust belts. Tectonophysics 119, 67-88.

Davis, K., Burbank, D. W., Fisher, D., Wallace, S., Nobes, D., 2005. Thrust-fault growth and segment linkage in the active Ostler fault zone, New Zealand. Journal of Structural Geology 27, 1528-1546.

Dawers, N., Anders, M., 1995. Displacement-length scaling and fault linkage. Journal of Structural Geology 17, 607-614.

DeCelles, P. G., Lawton, T. F., Mitra, G., 1995. Thrust timing, growth of structural culminations, and synorogenic sedimentation in the type Sevier orogenic belt, Western United States. Geology (Boulder) 23, 699-702.

DeCelles, P. G., Mitra, G., 1995. History of the Sevier orogenic wedge in terms of critical taper models, northeast Utah and southwest Wyoming. Geological Society of America Bulletin 107, 454-462.

Deptuck, M., Steffens, G., Barton, M., Pirmez, P., 2003. Architecture and evolution of upper fan channel-belts on the Niger Delta slope and in the Arabian Sea. Marine and Petroleum Geology 20, 649-676.

Dixon, D., Liu, S., 1991. Centrifuge modelling of the propagation of thrust faults. In: McClay, K. (Eds.), Thrust Tectonics. Chapman & Hall, London, 53-70.

Douglas, R. J. W., 1958. Mount Head map area, Alberta: Canada. Geol. Survey Mem. 291, 241.

Doust, H., Omatsola, E., 1990. Niger Delta. In: Edwards, J., Santagrossi, P. (Eds.), Divergent/passive margin basins: AAPG Memoir 48, 201-238.

Eisenstadt, G., De Paor, D., 1987. Alternative model of thrust-fault propagation. Geology 15, 630-633.

Elliot, D., 1976. The energy balance and deformation mechanisms of thrust sheets. Phil. Trans. R. Soc. Lond. A. 283, 289-312.

Ellis, M., Dunlap, W., 1988. Displacement variation along thrust faults: implications for the development of large faults. Journal of Structural Geology 10, 183-192.

Erickson, S. G., 1996. Influence of mechanical stratigraphy on folding vs faulting. Journal of Structural Geology 18, 443-450.

Erslev, E. A., 1991. Trishear fault-propagation folding. Geology (Boulder) 19, 617-620.

Evamy, B. D., Haremboure, J., Kamerling, P., Knapp, W. A., Molloy, F. A., Rowlands, P. H., 1978. Hydrocarbon habitat of Tertiary Niger Delta. AAPG Bulletin 62, 1-39.

Fischer, M. P., Woodward, N. B., Mitchell, M. M., 1992. The kinematics of break-thrust folds. Journal of Structural Geology 14, 451-460.

Fischer, M. P., Jackson, P. B., 1999. Stratigraphic controls on deformation patterns in fault-related folds: a detachment fold example from the Sierra Madre Oriental, northeast Mexico. Journal of Structural Geology 21, 613-633.

Fort, X., Brun, J.-P. C. F., 2004. Salt tectonics on the Angolan margin, synsedimentary deformation processes. AAPG Bulletin 88, 1523-1544.

Gawthorpe, R. L., Hurst, J. M., 1993. Transfer zones in extensional basins: their structural style and influence on drainage development and stratigraphy. Journal of the Geological Society, London 150, 1137-1152.

Gillespie, P. A., Walsh, J. J., Watterson, J., 1992. Limitations of dimension and displacement data from single faults and the consequences for data analysis and interpretation. Journal of Structural Geology 14, 1157-1172.

Granier, T., 1985. Origin damping and pattern of development of faults in granite. Tectonics 4, 721-737.

Groshong, R. H., Epard, J.-L., 1994. The role of strain in area-constant detachment folding. Journal of Structural Geology 16, 613-618.

Gupta, A., Scholz, C., 2000. A model of normal fault interaction based on observations and theory. Journal of Structural Geology 22, 865-879.

Gwinn, V., 1964. Thin-skinned tectonics in the Plateau and northwestern Valley and Ridge provinces of the central Appalachians. Geological Society of America Bulletin 75, 863-900.

Hardy, S., Poblet, J., 1994. Geometric and numerical model of progressive limb rotation in detachment folds. Geology 22, 371-374.

Hardy, S., Poblet, J., 1995. The velocity description of deformation; Paper 2, Sediment geometries associated with fault-bend and fault-propagation folds. Marine and Petroleum Geology 12, 165-176.

Hardy, S., Poblet, J., McClay, K., Waltham, D., 1995. Mathmatical modelling of growth strata associated with fault-related fold structures. In: Buchanan, P. G., Nieuwland, D. A. (Eds.), Modern Developments in Structural Interpretation, Validation and Modelling 99. Geol. Soc. London Spec. Publ., 265-282.

Hardy, S., Poblet, J., McClay, K., Waltham, D., 1996. Mathematical modelling of growth strata associated with fault-related fold structures. In: Buchanan, P. G., Nieuwland, D. A. (Eds.), Modern developments in structural interpretation, validation and modelling Geological Society Special Publications 99. Geological Society of London, London, 265-282.

Harrison, J. C., Bally, A. W., 1988. Cross-sections of the Parry Islands Fold Belt on Melville Island, Canadian Arctic Islands: implications for the timing and kinematic history of some thin-skinned decollement systems. Bulletin of Canadian Petroleum Geology 36, 311-332.

Hart, B. S., 1999. Definition of subsurface stratigraphy, structure and rock properties from 3-D seismic data. Earth Science Reviews 47, 497-518.

Hedlund, C. A., Anastasio, D. J., Fisher, D. M., 1994. Kinematics of fault-related folding in a duplex, Lost River Range, Idaho, U.S.A. Journal of Structural Geology 16, 571-584.

Heinio, P. 2007. 3D seismic analysis of sedimentary processes on deepwater continental margins. Unpublished PhD Thesis, Cardiff University.

Higgins, S., Davies, R. J., Clarke, B., 2007. Antithetic fault linkages in a deep water fold and thrust belt. Journal of Structural Geology 29, 1900-1914.

Higgins, S., Clarke, B., Davies, R. J., Cartwright, J. A., in review. Internal architecture and growth history of a thrust-related anticline in a deep water fold belt. Journal of Structural Geology.

Homza, T. X., Wallace, W. K., 1995. Geometric and kinematic models for detachment folds with fixed and variable detachment depths. Journal of Structural Geology 17, 575-588.

Hooper, R., Fitzsimmons, R., Grant, N., Vendeville, B., 2002. The role of deformation in controlling depositional patterns in the south-central Niger Delta, West Africa. Journal of Structural Geology 24, 847-859.

Hossack, J. R., 1979. The use of balanced cross-sections in the calculation of orogenic contraction: A review. Journal of the Geological Society, London 136, 705-711.

Hubbert, M. K., Rubey, W., 1959. Role of fluid pressure in mechanics of over-thrust faulting, Parts I and II. Geological Society of America Bulletin 70, 115-205.

Hudec, M. R., Jackson, M. P. A., 2002. Structural segmentation, inversion, and salt tectonics on a passive margin; evolution of the inner Kwanza Basin, Angola. Geological Society of America Bulletin 114, 1222-1244.

Huggins, P., Watterson, J., Walsh, J. J., Childs, C., 1995. Relay zone geometry and displacement transfer between normal faults recorded in coal-mine plans. Journal of Structural Geology 17, 1741-1755.

Ingram, G., Chisholm, T., Grant, C., Hedlund, C., Stuart-Smith, P., Teasdale, J., 2004. Deepwater North West Borneo: hydrocarbon accumulation in an active fold and thrust belt. Marine and Petroleum Geology 21, 879-887.

Jamison, W. R., 1987. Geometric analysis of fold development in overthrust terranes. Journal of Structural Geology 9, 207-219.

Johnson, A. M., Fletcher, R. C., 1994. Folding of viscous layers; mechanical analysis and interpretation of structures in deformed rock. Columbia University Press, New York.

Jubril, M. A., Shaw, H. F., Fallick, A. E., 1998. Stable isotope and geochemical evidence of formation pore fluid evolution during diagenesis of Tertiary sandstones and mudrocks of the Niger Delta. Journal of African Earth Sciences 27, 417-435.

Kastens, K. A., Shor, A. N., 1985. Depositional Processes of a Meandering Channel on Mississippi Fan. AAPG Bulletin 69, 190-202.

Kearey, P., Brooks, M., Hill, I., 2002. An introduction to geophysical exploration. Blackwell Science.

Knox, G. J., Omatsola, E. M. 1989. Development of the Cenozoic Niger Delta in terms of the 'Escalator Regression' model and impact on hydrocarbon distribution. In: Proceedings KNGMG Symposium 'Coastal Lowlands, Geology and Geotechnology', 181-202.

Kolla, V., Bourges, P., Urruty, J.-M., Safa, P., 2001. Evolution of deep-water Tertiary sinuous channels offshore Angola (west Africa) and implication for reservoir architecture. AAPG Bulletin 85, 1373-1405.

Larsen, P.-H., 1988. Relay structures in the Lower Permian basement-involved extension system, East Greenland. Journal of Structural Geology 10, 3-8.

Larue, D., Hovadik, J., 2006. Connectivity of channelized reservoirs: a modelling approach. Petroleum Geoscience 12, 291-308.

Lebel, D., Mountjoy, E., 1995. Numerical modeling of propagation and overlap of thrust faults, with application to the thrust-fold belt of central Alberta. Journal of Structural Geology 17, 631-646.

Lehner, P., Ruiter, P., 1977. Structural History of Atlantic Margin of Africa. AAPG Bulletin 61, 961-981.

Letouzey, J., Colletta, B., Vially, R., Chermette, J. C., 1995. Evolution of salt-related structures in compressional settings. In: Jackson, M. P. A., Roberts, D. G., Snelson, S. (Eds.), Salt tectonics: a global perspective: AAPG Memoir 65, 41-60.

Lisle, R. J., 1992. Constant bed-length folding: three-dimensional geometrical implications. Journal of Structural Geology 14, 245-252.

Liu, S., Dixon, D., 1991. Centrifuge modelling of thrust faulting: structural variation along strike in fold-thrust belts. Tectonophysics 188, 39-62.

Mandl, G., Crans, W., 1981. Gravitational gliding in deltas. In: McClay, K. R., Price, N. J. (Eds.), Thrust and Nappe Tectonics. Geological Society Special Publication No.9, London, 41-54.

Manighetti, I., King, G., Gaudemer, Y., Scholz, C., Doubre, C., 2001. Slip accumulation and lateral propagation of active normal faults in Afar. Journal of Geophysical Research 106, 13667-13696.

Martel, S. J., Pollard, D. D., Segall, P., 1988. Development of simple strike-slip fault zones, Mount Abbot quadrangle, Sierra Nevada, California. Geological Society of America Bulletin 100, 1451-1465.

Marton, L. G., Tari, G. C., Laehmann, C. T., 2000. Evolution of the Angolan passive margin, West Africa, with emphasis on post-salt structural styles. Atlantic rifts and continental margins 115, 129-149.

Mascle, J., Blarez, E., Marinho, M., 1988. The shallow structures of the Guinea and Ivory Coast-Ghana transform margins; their bearing on the Equatorial Atlantic Mesozoic evolution. Tectonophysics 155, 193-209.

Mason, R. A., 1997. Structure of the Alice anticline, Papua New Guinea: serial balanced cross-sections and their restoration. Journal of Structural Geology 19, 719-734.

McClay, K., Dooley, T., Lewis, G., 1998. Analog modeling of progradational delta systems. Geology 26, 771-774.

McClay, K. R., 1992. Glossary of thrust tectonics terms. In: McClay, K. R. (Eds.), Thrust Tectonics. Chapman & Hall, London, 419-433.

Medwedeff, D. A., 1989. Growth Fault-Bend Folding at Southeast Lost Hills, San Joaquin Valley, California. AAPG Bulletin 73, 54-67.

Medwedeff, D. A., 1992. Geometry and kinematics of an active, laterally propagating wedge thrust, Wheeler Ridge, California. In: Mitra, S., Fisher, G. (Eds.), Structural Geology of Fold and Thrust Belts 5. The John Hopkins Studies in Earth and Space Sciences, 3-28.

Meyer, V., Nicol, A., Childs, C., Walsh, J. J., Watterson, J., 2002. Progressive localisation of strain during the evolution of a normal fault population. Journal of Structural Geology 24, 1215-1231.

Miall, A. D., 1992. Exxon global cycle chart: An event for every occasion? Geology 20, 787-790.

Mitchell, M. M., Woodward, N. B., 1988. Kink detachment fold in the southwest Montana fold and thrust belt. Geology 16, 162-165.

Mitra, G., Sussman, A. V., 1997. Structural evolution of connecting splay duplexes and their implications for critical taper: an example based on geometry and kinematics of the Canyon Range culmination, Sevier Belt, central Utah. Journal of Structural Geology 19, 503-521.

Mitra, G., 2002. Structural models of faulted detachment folds. AAPG Bulletin 86, 1673-1694.

Mitra, S., Namson, J. S., 1989. Equal-area balancing. American Journal of Science 289, 563-599.

Mitra, S., 1990. Fault-Propagation Folds: Geometry, Kinematic Evolution and Hydrocarbon Traps. AAPG Bulletin 74, 921-945.

Morgan, R., 2003. Prospectivity in ultradeep water; the case for petroleum generation and migration within the outer parts of the Niger Delta apron. In: Arthur, T., MacGregor Duncan, S., Cameron, N. R. (Eds.), Petroleum geology of Africa; new themes and developing technologies. Geological Society of London.

Morgan, R., 2004. Structural controls on the positioning of submarine channels on the lower slopes of the Niger Delta. In: Davies, R., Cartwright, J., Stewart, S., Lappin, A., Underhill, J. (Eds.), 3D Seismic Technology: Application to the Exploration of Sedimentary Basins 29. Geological Society, London, Memoirs, 45-51.

Morley, C., Guerin, G., 1996. Comparison of gravity-driven deformation styles and behaviour associated with mobile shales and salt. Tectonics 15, 1154-1170.

Morley, C. K., Nelson, R., Patton, T., Munn, S., 1990. Transfer Zones in the East African Rift System and Their Relevance to Hydrocarbon Exploration in Rifts. AAPG Bulletin 74, 1234-1253.

Morley, C. K., 1994. Fold-generated imbricates: examples from the Caledonides of Southern Norway. Journal of Structural Geology 16, 619-631.

Morley, C. K., 2003. Mobile shale related deformation in large deltas developed on passive and active margins. In: Van-Rensbergen, P., Hillis, R. R., Maltman, A. J., Morley, C. K. (Eds.), Subsurface Sediment Mobilisation 216. Geological Society, London, Special Publications, 335-357.

Muraoka, H., Kamata, H., 1983. Displacement distribution along minor fault traces. Journal of Structural Geology 5, 483-495.

Nicol, A., Walsh, J. J., Watterson, J., Bretan, P. G., 1995. Three-dimensional geometry and growth of conjugate normal faults. Journal of Structural Geology 17, 847-862.

Nicol, A., Watterson, J., Walsh, J. J., Childs, C., 1996. The shapes, major axis orientations and displacement patterns of fault surfaces. Journal of Structural Geology 18, 235-248.

Nicol, A., Gillespie, P., Childs, C., Walsh, J., 2002. Relay zones between mesoscopic thrust faults in layered sedimentary sequences. Journal of Structural Geology 24, 709-727.

Nürnberg, D., Müller, R. D., 1991. The tectonic evolution of the South Atlantic from Late Jurassic to present. Tectonophysics 191, 27-53.

O'Keefe, F. X., Stearns, D. W., 1982. Characteristics of displacement transfer zones associated with thrust faults. In: Powers, R. B. (Eds.), Geologic Studies of the Cordilleran Thrust Belt 1. Rocky Mountain Association of Geologists, Denver, Colorado, 219-233.

Onuoha, K., Ofoegbu, C., 1988. Subsidence and evolution of Nigeria's continental margin: implications of data from Afowo-1 well. Marine and Petroleum Geology 5, 175-181.

Peacock, D. C. P., Sanderson, D. J., 1991. Displacements, segment linkage and relay ramps in normal fault zones. Journal of Structural Geology 13, 721-733.

Peacock, D. C. P., Sanderson, D. J., 1994. Geometry and Development of Relay Ramps in Normal Fault Systems. AAPG Bulletin 78, 147-165.

Peacock, D. C. P., Knipe, R. J., Sanderson, D. J., 2000. Glossary of normal faults. Journal of Structural Geology 22, 291-305.

Peel, F., Travis, C. J., Hossack, J. R., 1995. Genetic structural provinces and salt tectonics of the Cenozoic offshore US Gulf of Mexico: a preliminary analysis. In: Jackson, M. P. A., Roberts, D. G., Snelson, S. (Eds.), Salt tectonics: a global perspective: AAPG Memoir 65, 153-175.

Pennock, E. S., Lillie, R. J., Zaman, A. S. H., Yousaf, M., 1989. Structural interpretation of seismic reflection data from Eastern Salt Range and Potwar Plateau, Pakistan. AAPG Bulletin 73, 841-857.

Pfiffner, O. A., 1985. Displacements along thrust faults. Eclogae geol. Helv. 78, 313-333.

Pierce, W. G., 1966. Jura tectonics as a decollement. Geological Society of America Bulletin 77, 1265-1276.

Poblet, J., McClay, K., 1996. Geometry and kinematics of single-layer detachment folds. AAPG Bulletin 80, 1085-1109.

Poblet, J., McClay, K., Storti, F., Munoz, J. A., 1997. Geometries of syntectonic sediments associated with single-layer detachment folds. Journal of Structural Geology 19, 369-381.

Pollard, D. D., Aydin, A., 1984. Propagation and linkage of oceanic ridge segments. Journal of Geophysical Research 89, 10017-10028.

Pollard, D. D., Segall, P., 1987. Theoretical displacements and stresses near fractures in rock: with applications to faults, joints, veins, dykes and solution surfaces. In: Atkinson, B. (Eds.), Fracture mechanics of rock. Academic Press, London, 277-349.

Price, R. A., Mountjoy, E. W., 1970. Geologic structure of the Canadian Rocky Mountains between Bow and Athabasca Rivers - a progress report. Geological Association of Canada, Special Paper number 6, 7-25.

Rafini, S., Mercier, E., 2002. Forward modelling of foreland basins progressive unconformities. Sedimentary Geology 146, 75-89.

Ravaglia, A., Turrini, C., Seno, S., 2004. Mechanical stratigraphy as a factor controlling the development of a sandbox transfer zone: a three-dimensional analysis. Journal of Structural Geology 26, 2269-2283.

Riba, O., 1976. Syntectonic unconformities in the Alto Cardener, Spanish Pyrenees: a genetic interpretation. Sedimentary Geology 15, 213-233.

Rich, J. L., 1934. Mechanics of low-angle overthrust faulting as illustrated by Cumberland thrust block, Virginia, Kentucky, and Tennessee. Bulletin of the American Association of Petroleum Geologists 18, 1584-1596.

Rippon, J. H., 1985. Contoured patterns of the throw and hade of normal faults in the Coal Measures (Westphalian) of north-east Derbyshire. Proceedings of the Yorkshire Geological Society 45, 147-161.

Rowan, M., Peel, F., Vendeville, B., 2004. Gravity-driven Fold Belts on Passive Margins. In: McClay, K. (Eds.), Thrust tectonics and hydrocarbon systems: AAPG Memoir 82, 157-182.

Rowan, M. G., 1997. Three-dimensional geometry and evolution of a segmented detachment fold, Mississippi Fan foldbelt, Gulf of Mexico. Journal of Structural Geology 19, 463-480.

Rowan, M. G., Trudgill, B. D., Fiduk, J. C., 2000. Deep water, salt-cored fold belts: lessons from the Mississippi Fan and Perdido fold belts, northern Gulf of Mexico. In: Mohriak, W., Talwnai, M. (Eds.), Atlantic rfts and continental margins: American Geophysical Union Geophysical Monograph 115, 173-191.

Saugy, E., Eyer, A., 2003. Fifty years of exploration in the Niger Delta (west Africa). In: Halbouty, M. T. (Eds.), Giant oil and gas fields of the decade 1990-1999, American Association of Petroleum Geologists Memoir 78, 211-226.

Schlische, R. W., Young, S. S., Ackermann, R. V., Gupta, A., 1996. Geometry and scaling relations of a population of very small rift-related normal faults. Geology 24, 683-686.

Scholz, C. H., Cowie, P. A., 1990. Determination of total strain from faulting using slip measurements. Geology 15, 495-497.

Segall, P., Pollard, D. D., 1980. Mechanics of discontinuous faults. Journal of Geophysical Research B 85, 4337-4350.

Shaw, J. H., Novoa, E., Connors, C. D., 2004. Structural controls on growth stratigraphy in contractional fault-related folds. In: McClay, K. (Eds.), Thrust tectonics and hydrocarbon systems: AAPG Memoir 82, 407-419.

Sheriff, R. E., Geldart, L. P., 1995. Exploration seismology. Cambridge University Press, Cambridge.

Short, K., Stauble, A., 1967. Outline of Geology of Niger Delta. AAPG Bulletin 51, 761-779.

Simm, R., White, R., 2002. Phase, polarity and the interpreter's wavelet. First Break 20, 277-281.

Storti, F., Poblet, J., 1997. Growth stratal architectures associated to decollement folds and fault-propagation folds; inferences on fold kinematics. In: Cloetingh, S., Fernandez, M., Munoz, J. A., Sassi, W., Horvath, F. (Eds.), Structural controls on sedimentary basin formation. Tectonophysics 282; 1-4. Elsevier, Amsterdam, Netherlands, 353-373.

Suppe, J., 1983. Geometry and kinematics of fault-bend folding. American Journal of Science 283, 684-721.

Suppe, J., Medwedeff, D. A. 1984. Fault-propagation folding. In: The Geological Society of America, 97th annual meeting 16. Geological Society of America.

Suppe, J., 1985. Principles of Structural Geology. Prentice Hall, Englewood Cliffs, New Jersey.

Suppe, J., Medwedeff, D. A., 1990. Geometry and kinematics of fault-propagation folding. Eclogae Geologicae Helvetiae 83, 409-454.

Suppe, J., Chou, G. T., Hook, S. C., 1992. Rates of folding and faulting determined from growth strata. In: McClay, K. R. (Eds.), Thrust tectonics. Chapman and Hall, London, 105-121.

Tearpock, D., Bischke, R. E., 1991. Applied Subsurface Geological Mapping. Prentice Hall PTR, New Jersey.

Thorbjornsen, K. L., Dunne, W. M., 1997. Origin of a thrust-related fold: geometric vs kinematic tests. Journal of Structural Geology 19, 303-319.

Toto, E. A., Kellogg, J. N., 1992. Structure of the Sinu-San Jacinto fold belt - An active accretionary prism in northern Colombia. Journal of South American Earth Sciences 5, 211-222.

Trudgill, B. D., Cartwright, J. A., 1994. Relay ramp forms and normal fault linkages, Canyonlands National Park, Utah. Geological Society of America Bulletin 106, 1143-1157.

Urai, J. L., Spiers, C. J., Zwart, H. J., Lister, G. S., 1989. Water weakening effects in rocksalt during long term creep. Nature 324, 554-557.

Walsh, J. J., Watterson, J., 1987. Distributions of cumulative displacement and seismic slip on a single normal fault surface. Journal of Structural Geology 9, 1039-1046.

Walsh, J. J., Watterson, J., 1991. Geometric and kinematic coherence and scale effects in normal fault systems. In: Roberts, A. M., Yielding, G., Freeman, B. (Eds.), The Geometry of Normal Faults. Geological Society Special Publication 56, 193-203.

Walsh, J. J., Watterson, J., Bailey, W. R., Childs, C., 1999. Fault relays, bends and branch-lines. Journal of Structural Geology 21, 1019-1026.

Walsh, J. J., Nicol, A., Childs, C., 2002. An alternative model for the growth of faults. Journal of Structural Geology 24, 1669-1675.

Walsh, J. J., Bailey, W. R., Childs, C., Nicol, A., Bonson, C. G., 2003. Formation of segmented normal faults: a 3-D perspective. Journal of Structural Geology 25, 1251-1262.

Watterson, J., 1986. Fault dimensions, displacements and growth. Pure & Applied Geophysics 124, 365-373.

Weijermars, R., Jackson, M. P. A., Vendeville, B. C., 1993. Rheological and tectonic modelling of salt provinces. Tectonophysics 217, 143-174.

Weimar, P., Buffler, R. T., 1992. Structural geology and evolution of the Mississippi Fan fold belt, deep Gulf of Mexico. AAPG Bulletin 76, 225-251.

Whiteman, A. J., 1982. Nigeria; its petroleum geology, resources and potential. Grahan and Trotman, London.

Wickham, J., 1995. Fault displacement-gradient folds and the structure at Lost Hills, California (U.S.A). Journal of Structural Geology 17, 1293-1302.

Wilkerson, M. S., Medwedeff, D. A., Marshak, S., 1991. Geometrical modeling of fault-related folds: a pseudo-three-dimensional approach. Journal of Structural Geology 13, 801-812.

Williams, G., Chapman, T., 1983. Strains developed in the hangingwalls of thrusts due to their slip/propagation rate: a dislocation model. Journal of Structural Geology 5, 563-571.

Willis, B., 1893. Mechanics of Appalachian Structure. U.S. Geological Survey Annual Report 13, 217-281.

Wiltschko, D. V., Dorr, J. A., 1983. Timing of Deformation in Overthrust Belt and Foreland of Idaho, Wyoming and Utah. AAPG Bulletin 67, 1304-1322.

Wiltschko, D. V., Medwedeff, D. A., Millson, H. E., 1985. Distribution and mechanisms of strain within rocks of the northwest ramp of Pine Mountain block, southern Appalachian foreland: A field test of theory. Geological Society of America Bulletin 96, 426-435.

Woodward, N. B., Rutherford, E., 1989. Structural lithic units in external orogenic zones. Tectonophysics 158, 247-267.

Woodward, N. B., 1992. Deformation styles and geometric evolution of some Idaho-Wyoming thrust belt structures. In: Mitra, S., Fisher, G. (Eds.), Structural

Geology of Fold and Thrust Belts 5. The John Hopkins Studies in Earth and Space Sciences.

Wu, S., Bally, A. W., 2000. Slope tectonics; comparisons and contrasts of structural styles of salt and shale tectonics of the northern Gulf of Mexico with shale tectonics of offshore Nigeria in Gulf of Guinea. In: Mohriak Webster, U., Talwani, M. (Eds.), Atlantic rifts and continental margins. American Geophysical Union. Washington, DC, United States. 2000.

APPENDICES

The core chapters presented in this thesis have been written as scientific papers and are therefore structured and formatted with publication in mind. The following appendices provide lists, figures and data to demonstrate the full extent of the body of work summarised in the papers. A caption is included with each of the figures, giving a brief description of its significance, but they are not referred to in the text. A digital copy of the complete thesis is also included in the final appendix.

Appendix 1 - List of mapped seismic horizons and interpreted faults.
Appendix 2 - Supplementary figures of major horizons and fault geometries.
Appendix 3 - Fault heave data and depth plot points from Chapter 4.
Appendix 4 - Fault heave data and depth plot points from Chapter 5.
Appendix 5 - Digital copy of this thesis on CD.

APPENDIX 1: List of mapped seismic horizons and faults

A list of all seismic horizons mapped and all faults picked are given below. Each one is noted by the name corresponding to the Geoframe IESX project smh_niger_int.

Horizon List

Name	ID	Name	ID	Name	ID
rjd_trash3	[2520624]	smh_A4_PioneerHW	[2916831]	smh_ChanF_l2_onis_HW	[2503406]
smh_A10_onis_HW	[2439594]	smh_A4_tini_FW	[2453616]	smh_ChanG_Bs_onis_HW	[2503412]
smh_A11_onis_FW	[2755168]	smh_A5_onis_HW	[2439224]	smh_ChanG_l1_onis_HW	[2503418]
smh_A11_onis_HW	[2653816]	smh_A6_onis_HW	[2439218]	smh_ChanG_l2_onis_HW	[2503424]
smh_A1_bast_FW	[2545600]	smh_A6_onis_HWZ	[2442196]	smh_ChanG_l3_onis_HW	[2503629]
smh_A1_blast_HW	[2687712]	smh_A6U_onis_FW	[2457088]	smh_ChanI_Bs_onis_HW	[2502409]
smh_A1_bndy_HW	[2443660]	smh_A6U_onis_FWZ	[2461008]	smh_ChanI_l1_onis_HW	[2500698]
[illegible]	[illegible]	smh_A6X_onis_FW	[2443353]	smh_ChanI_l2_onis_HW	[2502477]
smh_A1_bndy_Sub	[2754032]	smh_A7_onis_FW	[2443359]	smh_ChanI_l3_onis_HW	[2502483]
smh_A1_buki_HW	[2651255]	smh_A7_onis_HW	[2439586]	smh_ChanJ_Bs_onis_FW	[2504658]
smh_A1_kaba_FW	[2651249]	smh_A7a_2DM	[2826437]	smh_ChanJ_Bs_onis_HW	[2502146]
smh_A1_onis_FW	[2434825]	smh_A7b_2DM	[2826645]	smh_ChanJ_l1_onis_FW	[2500753]
smh_A1_onis_FWZ	[2437664]	smh_A8_onis_FW	[2443648]	smh_ChanJ_l1_onis_HW	[2499785]
smh_A1_onis_HW	[2434640]	smh_A8_onis_HW	[2441644]	smh_ChanJ_l2_onis_FW	[2501397]
smh_A1_onis_HWc	[2434818]	smh_A9_onis_FW	[2443461]	smh_ChanJ_l2_onis_HW	[2500528]
smh_A1_onis_HWcZ	[2437751]	smh_A9_onis_HW	[2441778]	smh_ChanJ_l3_onis_HW	[2500759]
smh_A1_onis_HWZ	[2437745]	smh_B1_onis_FW	[2484626]	smh_ChanL_Bs	[2561128]
smh_A1_Pioneer_FW	[2687718]	smh_base_debris	[2653622]	smh_ChanM_l1_onis_HW	[2592685]
smh_A1_tini_FW	[2452642]	smh_bellfold_onlap	[2653808]	smh_ChanM_l2_onis_HW	[2592691]
smh_A1_transE1_HW	[2573432]	smh_BellOnlap_1	[2657014]	smh_ChanM_l3_onis_HW	[2592697]
smh_A1b	[2857187]	smh_BellOnlap_2	[2657020]	smh_ChBs1_A2_onis_FW	[2477624]
smh_A2_5_kaba_HW	[2652128]	smh_BellOnlap_3	[2657008]	smh_ChBs1_A2_onis_HW	[2476258]
smh_A2_Aparo_HW	[2580514]	smh_BellOnlap_4	[2657026]	smh_ChBs2_A2_onis_FW	[2480146]
smh_A2_blast_FW	[2545606]	smh_BellOnlap_5	[2657168]	smh_ChBs3_A2_onis_FW	[2480220]
smh_A2_blast_HW	[2552594]	smh_BellOnlap_6	[2657174]	smh_ChBs4_A2_onis_FW	[2480152]
smh_A2_bndy_HW	[2452272]	smh_BellOnlap_6b	[2657406]	smh_ChBs5_A2_onis_FW	[2480736]
smh_A2_bndy_HWc	[2683264]	smh_BellOnlap_7	[2657180]	smh_ChBs6_A2_onis_FW	[2480742]
smh_A2_onis_FW	[2441632]	smh_BellOnlap_8	[2657400]	smh_ChTp1_A2_onis_FW	[2477618]
smh_A2_onis_FW+150ms	[2479494]	smh_BellOnlap_9	[2657394]	smh_ChTp1_A2_onis_HW	[2476418]
smh_A2_onis_FW+225ms	[2479500]	smh_Bf_onis_FW	[2508308]	smh_ChTp2_A2_onis_FW	[2480208]
smh_A2_onis_FW+300ms	[2479506]	smh_Bf_onis_HW	[2508184]	smh_ChTp3_A2_onis_FW	[2480214]
smh_A2_onis_FW+75ms	[2479488]	smh_Bf_onis_HW	[2508184]	smh_ChTp4_A2_onis_FW	[2480386]
smh_A2_onis_FW-150ms	[2479518]	smh_Bh_Aparo_HW	[2586449]	smh_debris1_aparo	[2462686]
smh_A2_onis_FW-225ms	[2479524]	smh_Bh_onis_FW	[2586461]	smh_deleteme1	[2644226]
smh_A2_onis_FW-300ms	[2479530]	smh_Bh_onis_HW	[2586455]	smh_explore1_onis_FW	[2459632]
smh_A2_onis_FW-75ms	[2479512]	smh_Bho_onis_HW	[2586473]	smh_explore2_onis_FW	[2459638]
smh_A2_onis_HW	[2439280]	smh_Bl_onis_FW	[2508178]	smh_fault1_export	[2818610]
smh_A2_onis_HW+150ms	[2479990]	smh_Bj_onis_FW	[2592656]	smh_fault2_export	[2818616]
smh_A2_onis_HW+225ms	[2479996]	smh_Bj_onis_HW	[2503808]	smh_fault3_export	[2818622]
smh_A2_onis_HW+300ms	[2480002]	smh_BL_Aparo_HW	[2586479]	smh_FoldOnset	[2634734]
smh_A2_onis_HW+75ms	[2479984]	smh_BL_Aparo_HW_XXX	[2581122]	smh_MidAkata_Detach	[2706768]
smh_A2_onis_HW-150ms	[2480014]	smh_BL_onis_FW	[2586467]	smh_Roller1	[2724405]
smh_A2_onis_HW-225ms	[2480020]	smh_BL_onis_FW_XXX	[2586437]	smh_Roller2	[2726867]
smh_A2_onis_HW-300ms	[2480026]	smh_BL_onis_HW	[2586415]	smh_Roller4	[2724411]
smh_A2_onis_HW-301ms	[2480034]	smh_Bm_Aparo_HW	[2586443]	smh_Roller5	[2726775]
smh_A2_onis_HW-75ms	[2480008]	smh_Bm_Aparo_HW_XXX	[2586497]	smh_Roller6	[2726781]
smh_A2_tini_FW	[2452648]	smh_Bm_onis_FW	[2504664]	smh_seabed_depth	[2762761]
smh_A2_transE1_HW	[2573426]	smh_Bm_onis_HW	[2586491]	smh_seabed_onis	[2441638]
smh_A2b	[2857037]	smh_Bn_Aparo_HW_XXX	[2586503]	smh_stato1_onis_FW	[2454310]
smh_A3_bndy_HW	[2443666]	smh_Bn_onis_FW	[2586485]	smh_stato1_onis_HW	[2454304]
smh_A3_onis_FW	[2443347]	smh_Bn_onis_FW_XXX	[2586515]	smh_temp_copyA3_2	[2701373]
smh_A3_onis_HW	[2439206]	smh_Bn_onis_HW	[2586509]	smh_temp_copyA3_3	[2701491]
smh_A3b_Blast_HW	[2826651]	smh_ChanF_Bs_onis_FW	[2508190]	smh_temp_copyA3_4	[2701497]
smh_A4_ALL	[2910900]	smh_ChanF_Bs_onis_HW	[2503394]	smh_temp_copyA3_5	[2710480]
smh_A4_Aparo_FW	[2825767]	smh_ChanF_l1_onis_HW	[2503400]	smh_TpAkar_All	[2701367]
smh_A4_Bandy_HW	[2778726]	smh_ChanF_l2_onis_HW	[2503406]	smh_TpAkar_bndy_HW	[2446892]
smh_A4_Blast_HW	[2690364]	smh_ChanG_Bs_onis_HW	[2503412]	smh_TpAkar_front	[2595042]
smh_A4_Blast_HWc	[2690686]	smh_ChanG_l1_onis_HW	[2503418]	smh_TpAkar_kaba_HW	[2595048]
smh_A4_depth	[2762838]	smh_ChanG_l2_onis_HW	[2503424]	smh_TpAkar_Levelled	[2848770]
smh_A4_KabaBack_HW	[2825760]	smh_ChanG_l3_onis_HW	[2503629]	smh_TpAkar_onis_FW	[2446866]
smh_A4_OnlS_HW	[2825793]	smh_ChanI_Bs_onis_HW	[2502489]	smh_TpAkar_onis_HW	[2446880]
smh_A4_PioneerFW	[2916933]	smh_ChanI_l1_onis_HW	[2500698]	smh_TpAkar_Smooth	[2848191]

Fault List

Name	ID
f	[2433862]
smh_aparo_1	[2454816]
smh_bandy_1	[2443654]
smh_bandy_detachment	[2674560]
smh_bandy_MidInt	[2674789]
smh_blast_1	[2552600]
smh_blast_2	[2691504]
smh_blast_3	[2778720]
smh_brisk	[2928675]
smh_brisk_b	[2928669]
smh_Buki_1	[2547736]
smh_Front_1	[2567170]
smh_Kaba_1	[2547730]
smh_Kaba_2	[2776864]
smh_Kaba_back_1	[2547742]
smh_Kaba_back_2	[2547796]
smh_ogin_1	[2455584]
smh_ogin_2	[2561486]
smh_ogin_back1	[2457584]
smh_ogin_synlink	[3009567]
smh_onis_1	[2434652]
smh_onis_2	[2730718]
smh_onis_back1	[2434646]
smh_onis_back2	[2732068]
smh_onis_back_Etrans	[2732060]
smh_onis_ext1	[2441784]
smh_onis_extfollow	[2441790]
smh_pioneer_1	[2569124]
smh_tini_1	[2452278]
smh_tini_back	[2452284]
smh_transE_1a	[2730594]
smh_transE_1b	[2748623]
smh_transfer1	[2730486]
smh_transfer1b	[2730492]

APPENDIX 2: Supplementary figures

Figures APP1.0 – APP1.19 provide example time maps and seismic sections of major interpreted horizons used in this study for structural description and strain measurements. Each map is followed by an inline and a crossline from the relevant seismic survey.

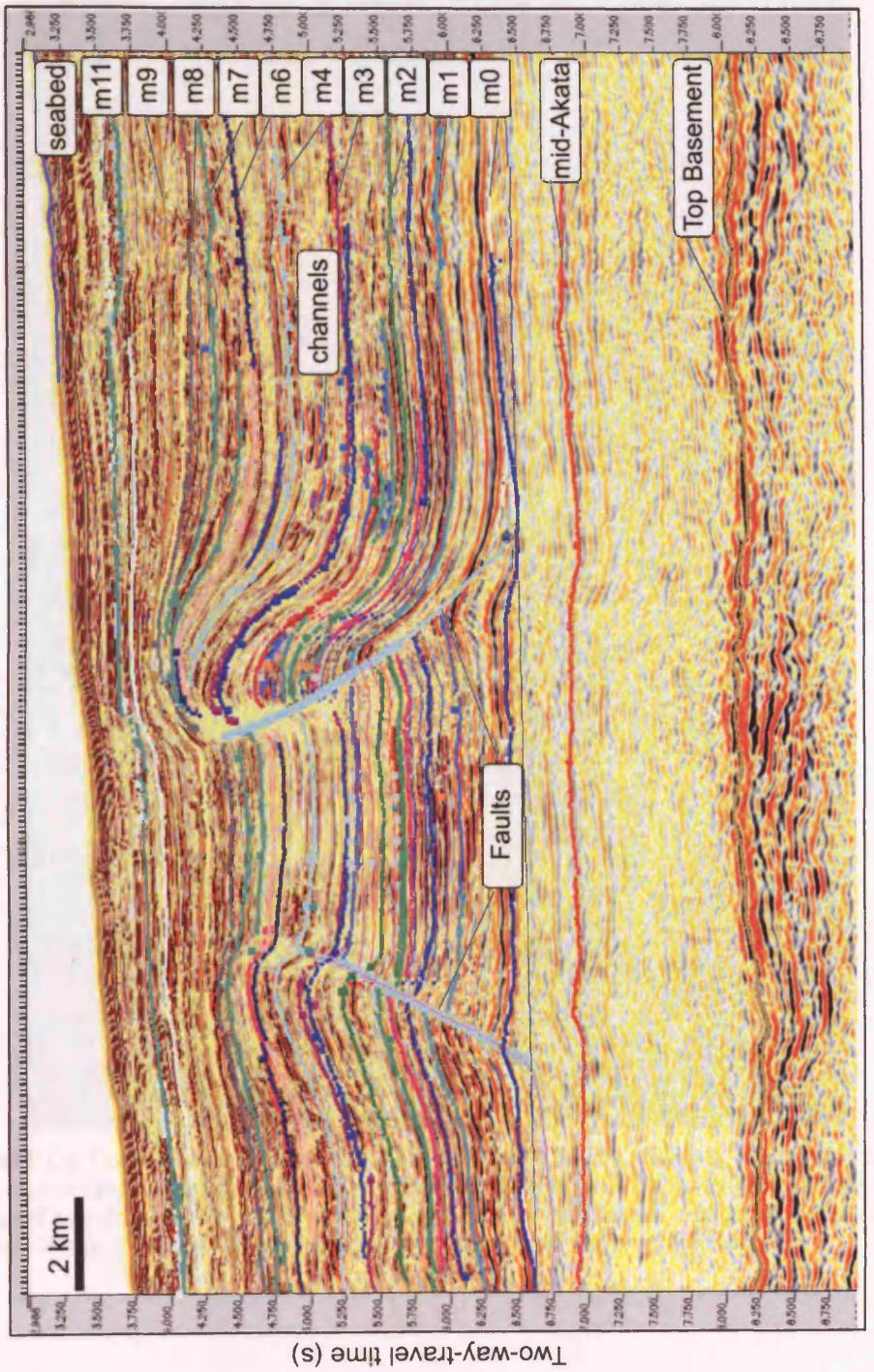

Figure APP1.0: Seismic section showing all of the interpreted horizons used in this thesis. See list in Appendix 1. Not all horizons were mapped to the full extent of the data set as some correspond to channel forms, levees and erosional features. The main horizons used in this thesis (m0 – m11) are labelled and are featured in the following Figures.

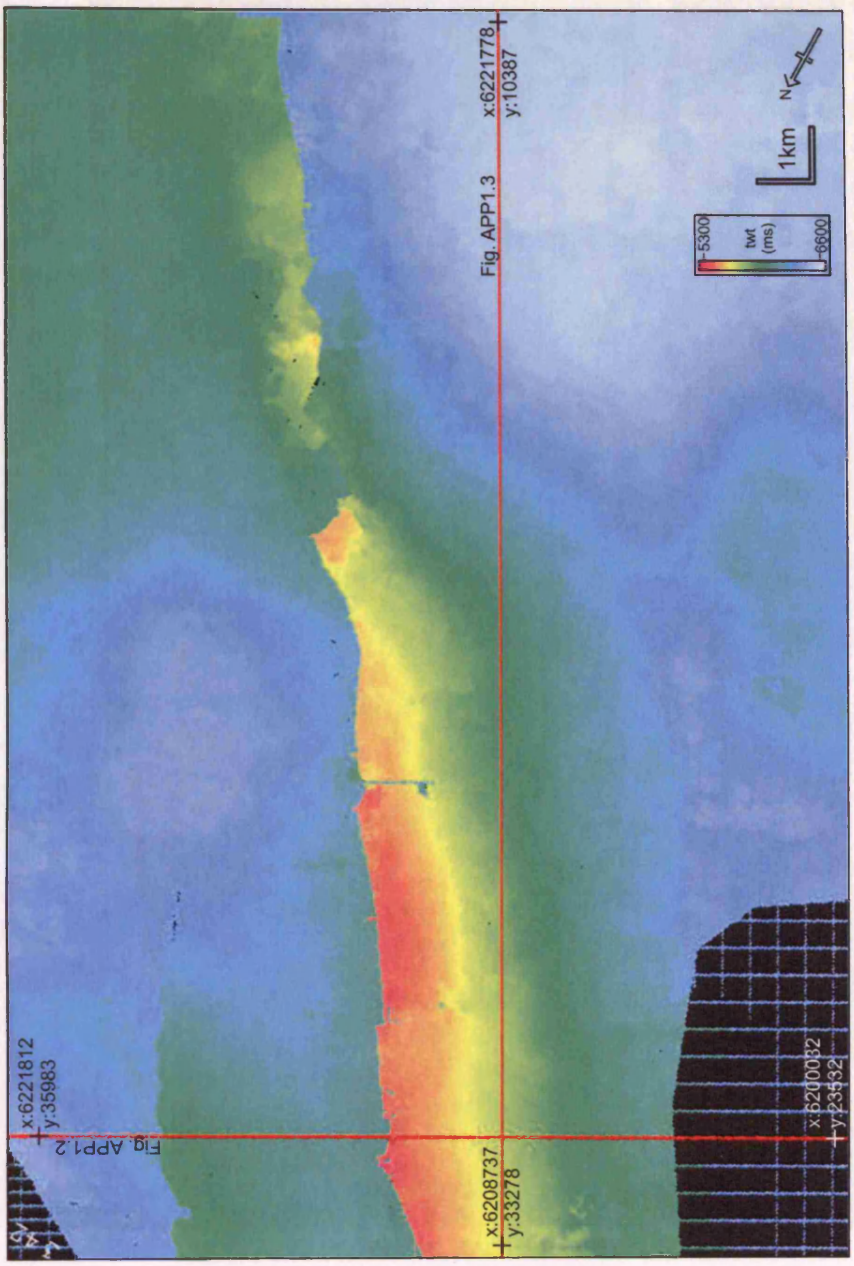

Figure APP1.1: Example seismic time map of **Horizon m1** in seismic survey A, presented in two-way-travel time (ms). Locations of two seismic sections (an inline and a crossline) in following figures are indicated by red lines. The world coordinates of the ends of the seismic sections are given as *x* and *y* in metres. Warm colours represent structural highs, cool colours show structural lows.

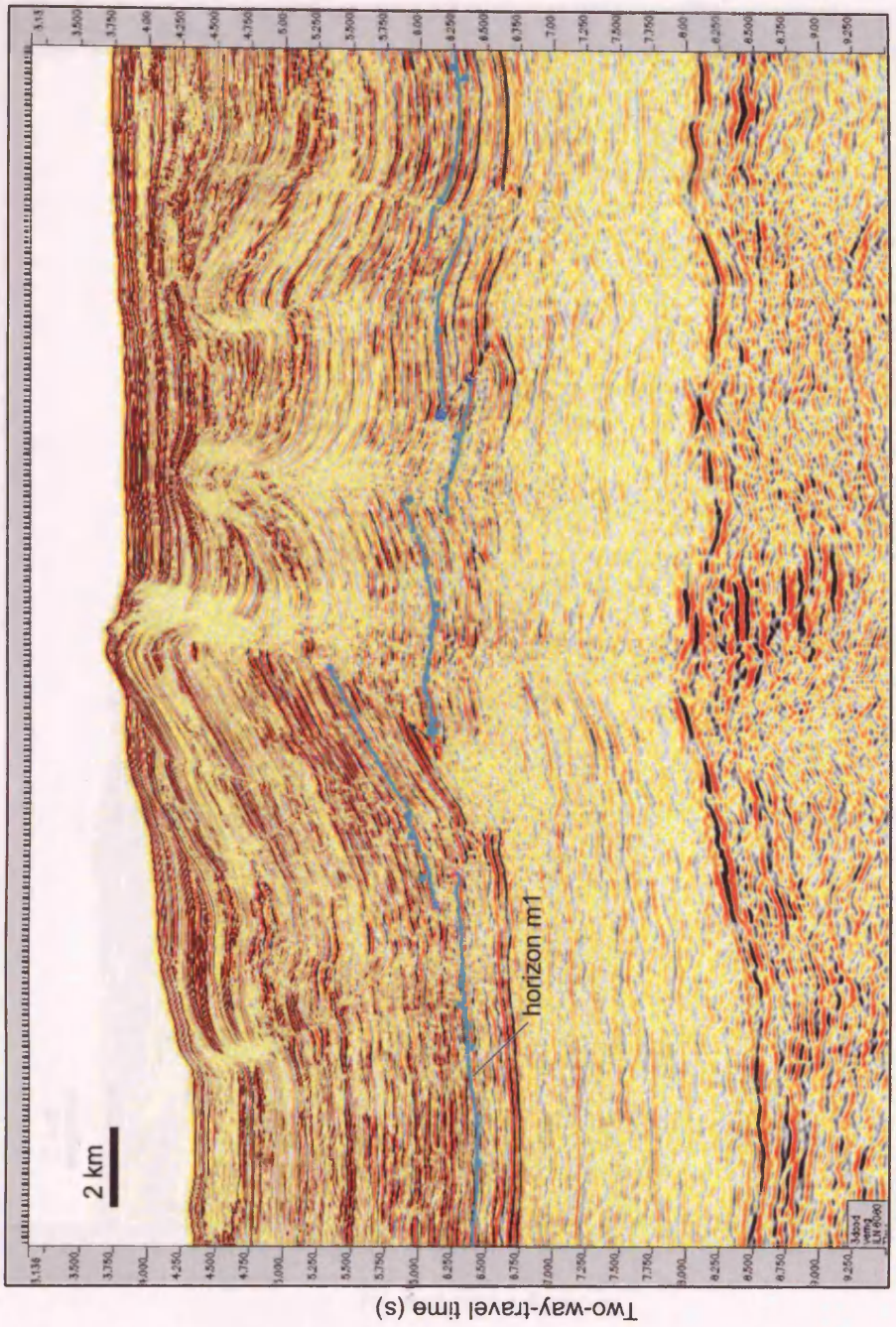

Figure APP1.2: Seismic section (inline) oriented perpendicular to fault strike showing an example of Horizon m1 interpretation. For location and coordinates of section see Figure APP1.1.

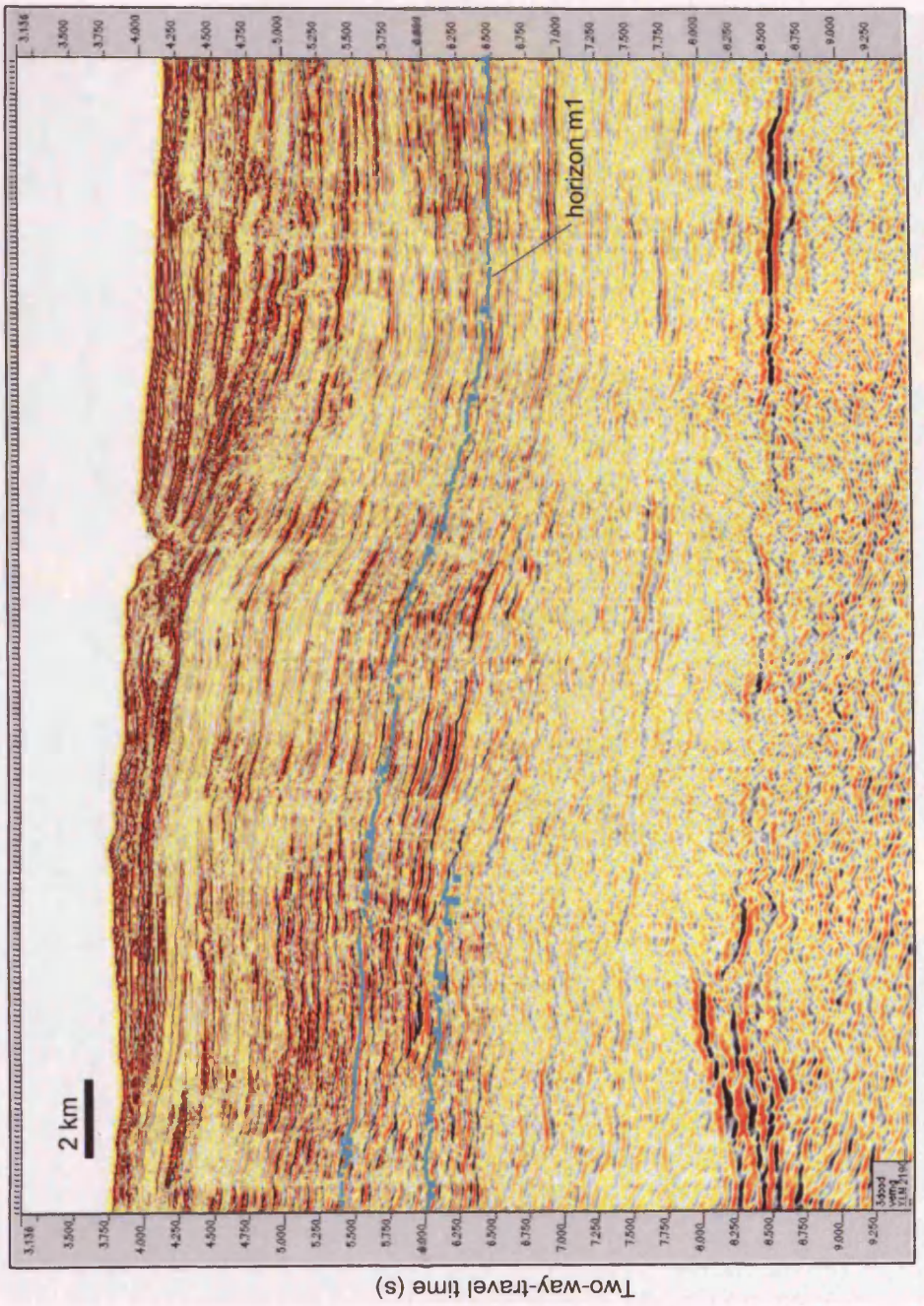

Figure APP1.3: Seismic section (crossline) oriented sub-parallel to fault strike showing an example of Horizon m1 interpretation. For location and coordinates of section see Figure APP1.1.

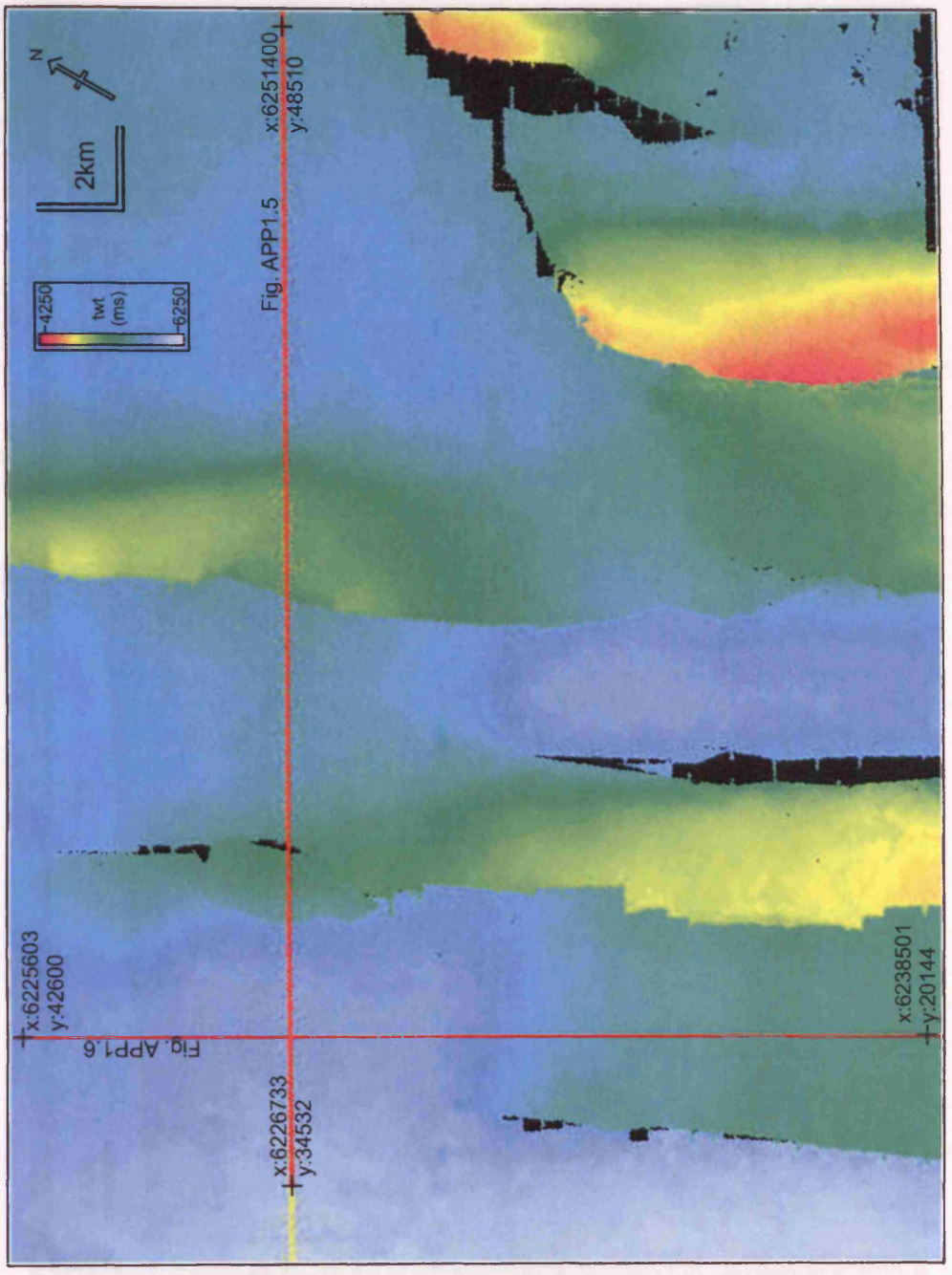

Figure APP1.4: Example seismic time map of **Horizon m2** in seismic survey A, presented in two-way-travel time (ms). Locations of two seismic sections (an inline and a crossline) in following figures are indicated by red lines. The world coordinates of the ends of the seismic sections are given as *x* and *y* in metres. Warm colours represent structural highs, cool colours show structural lows.

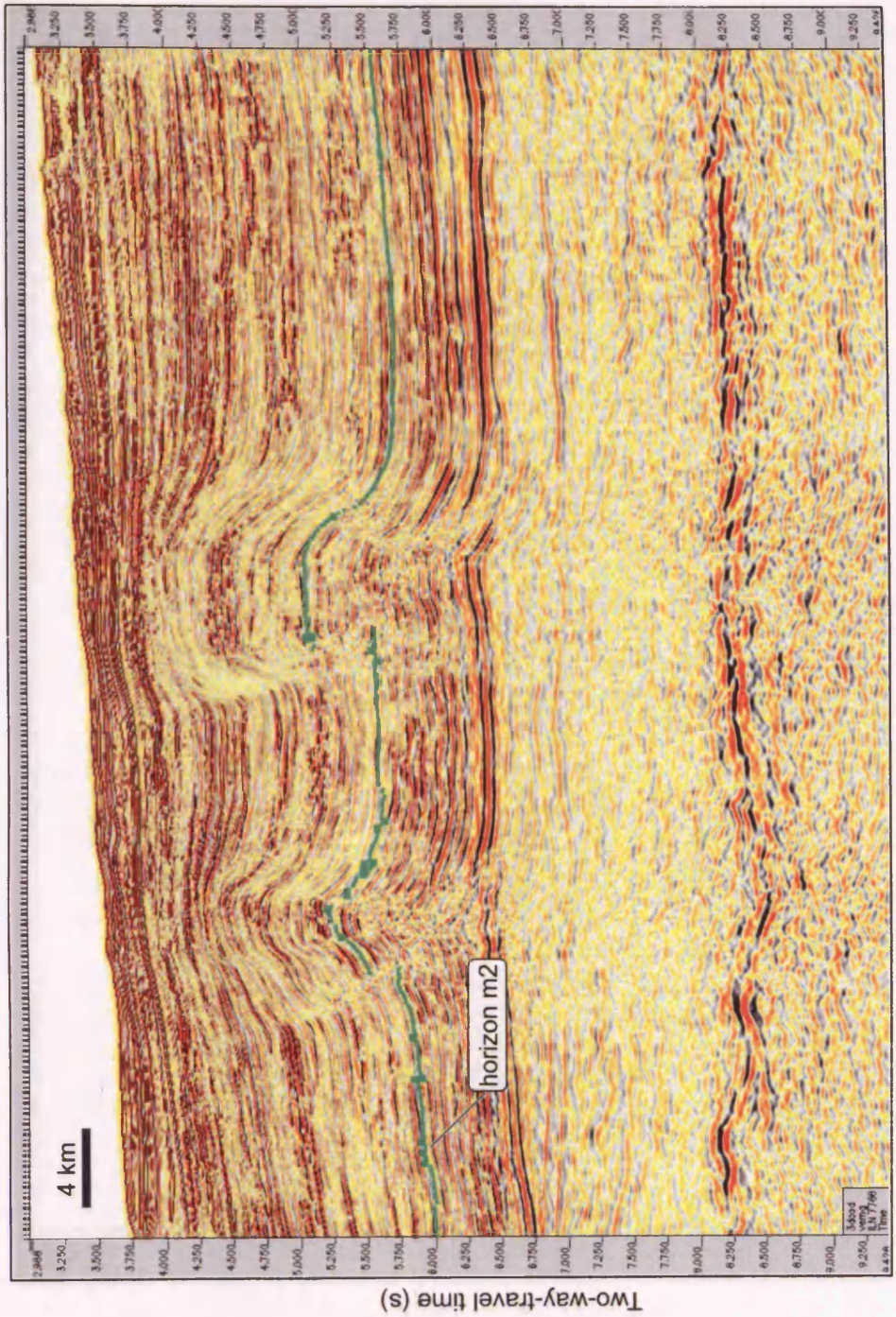

Figure APP1.5: Seismic section (inline) oriented perpendicular to fault strike showing an example of Horizon m2 interpretation. For location and coordinates of section see Figure APP1.4.

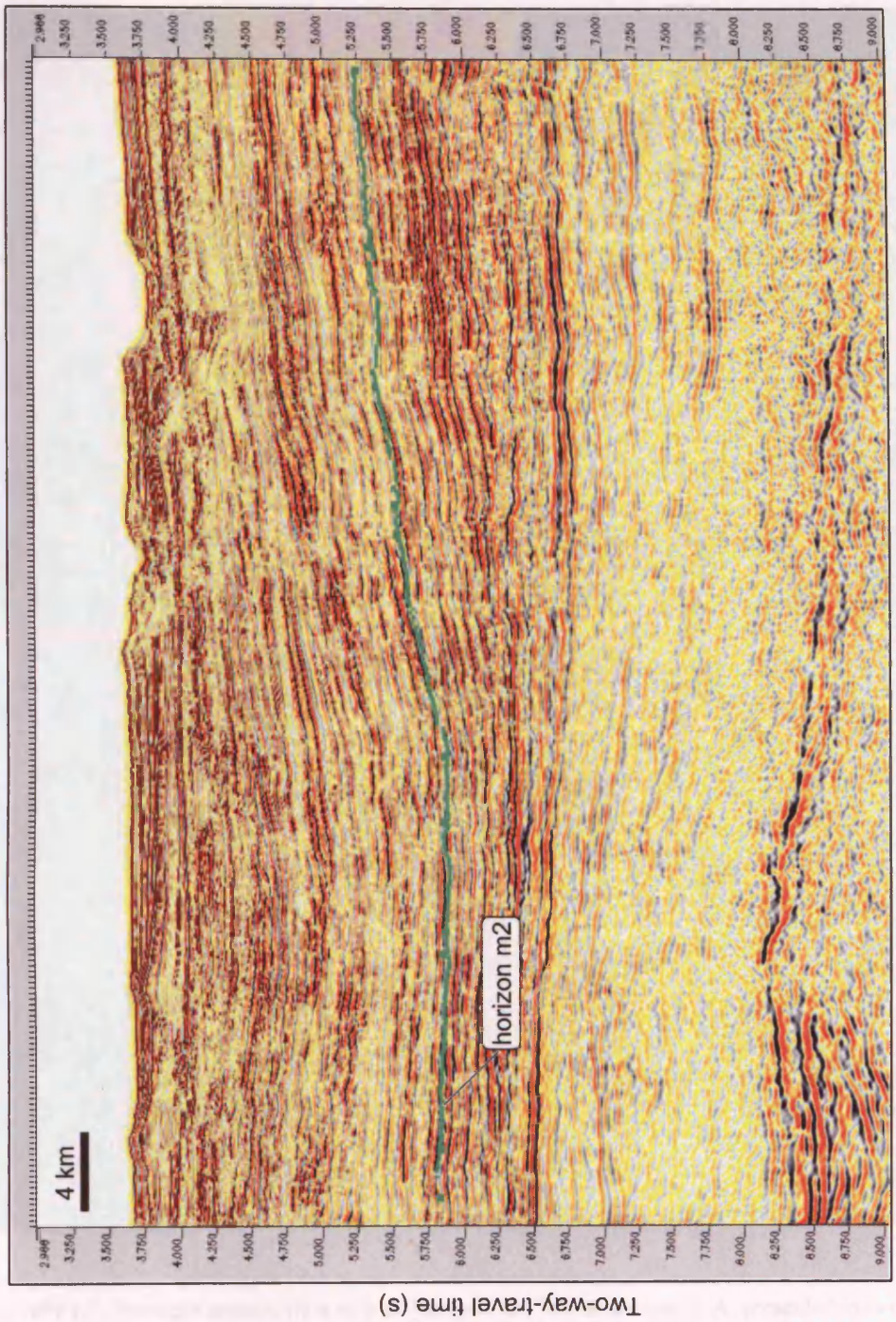

Figure APP1.6: Seismic section (crossline) oriented sub-parallel to fault strike showing an example of Horizon m2 interpretation. For location and coordinates of section see Figure APP1.4.

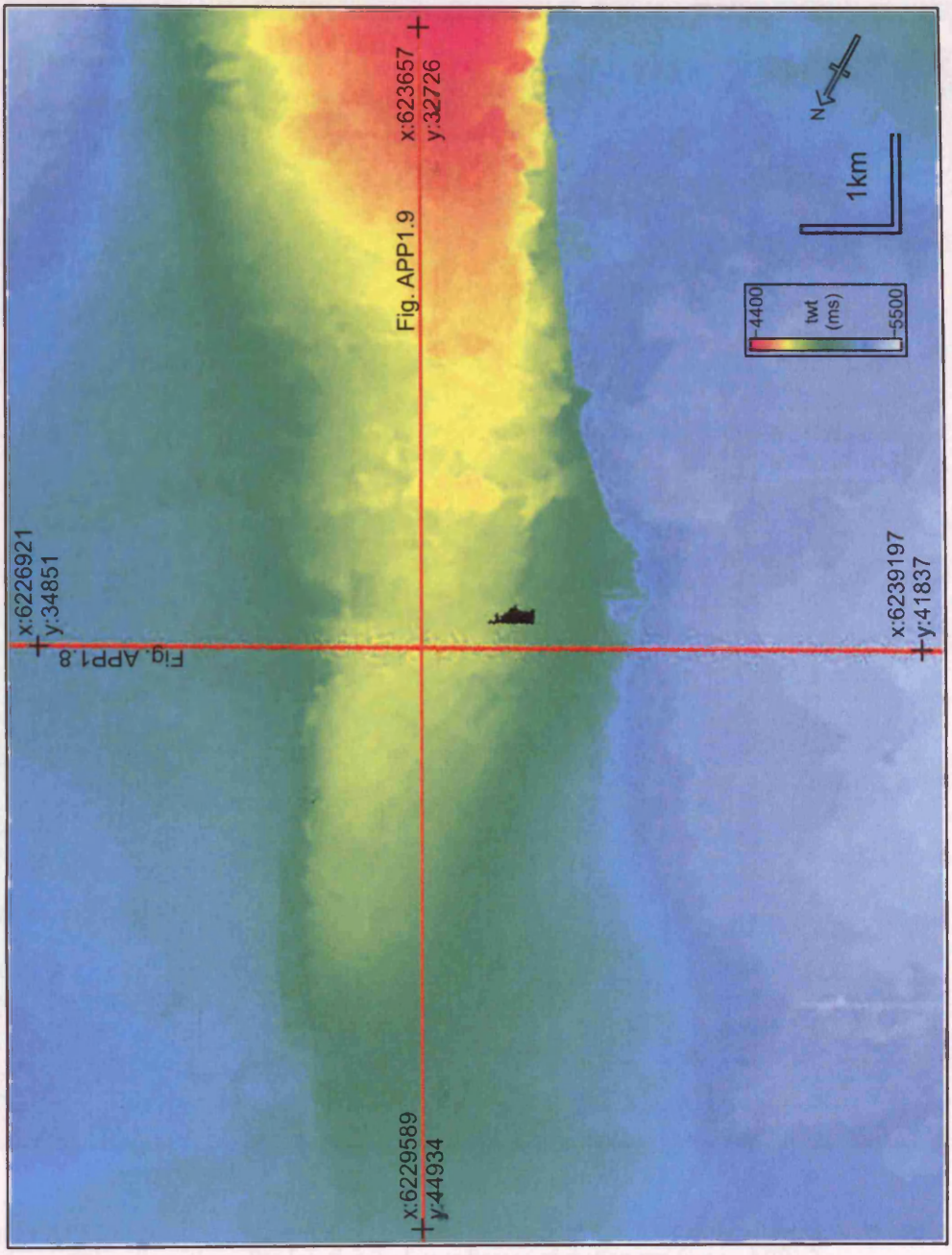

Figure APP1.7: Example seismic time map of **Horizon m3** in seismic survey A, presented in two-way-travel time (ms). Locations of two seismic sections (an inline and a crossline) in following figures are indicated by red lines. The world coordinates of the ends of the seismic sections are given as *x* and *y* in metres. Warm colours represent structural highs, cool colours show structural lows.

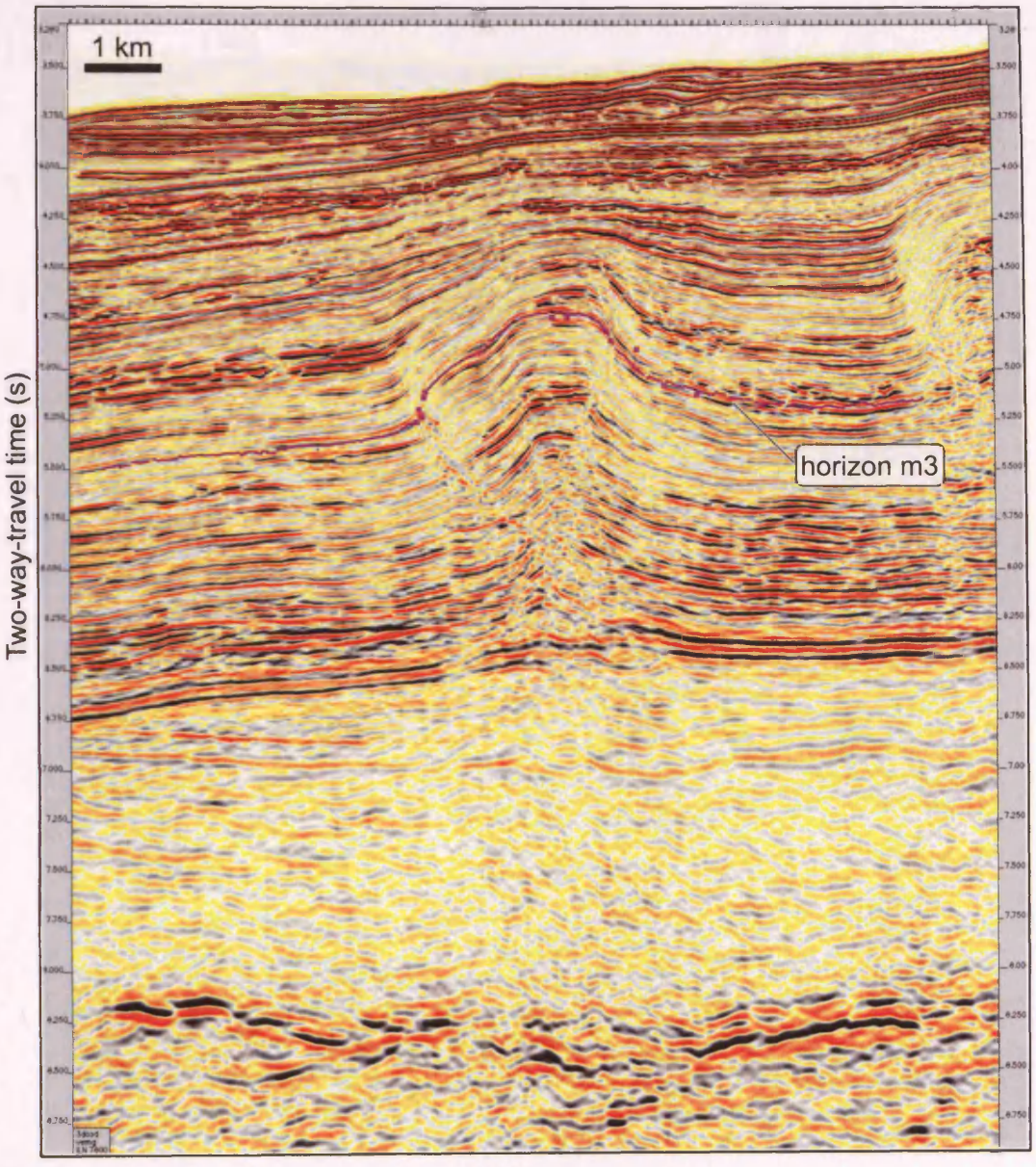

Figure APP1.8: Seismic section (inline) oriented perpendicular to fault strike showing an example of Horizon m3 interpretation. For location and coordinates of section see Figure APP1.7.

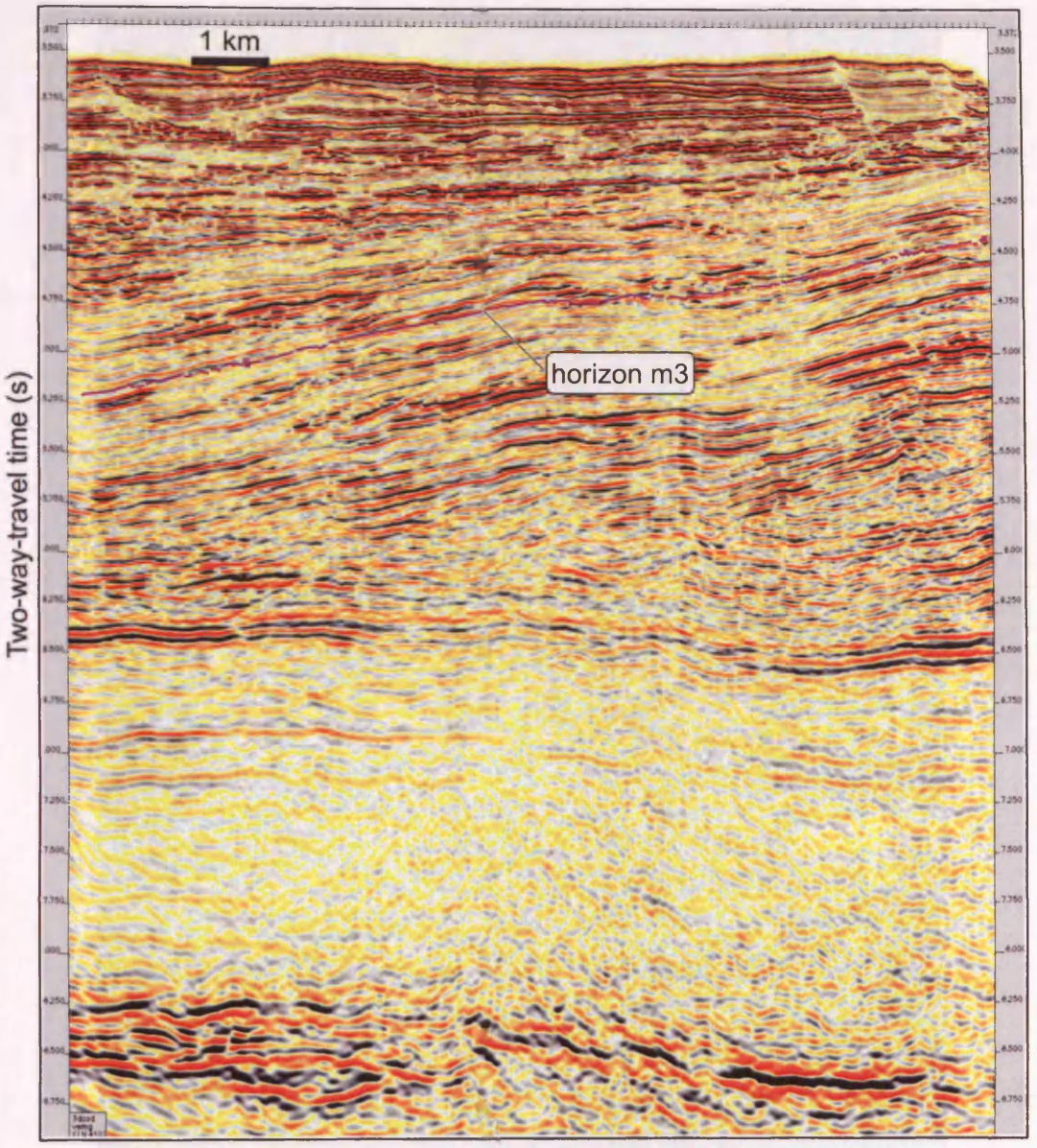

Figure APP1.9: Seismic section (crossline) oriented sub-parallel to fault strike showing an example of Horizon m3 interpretation. For location and coordinates of section see Figure APP1.7.

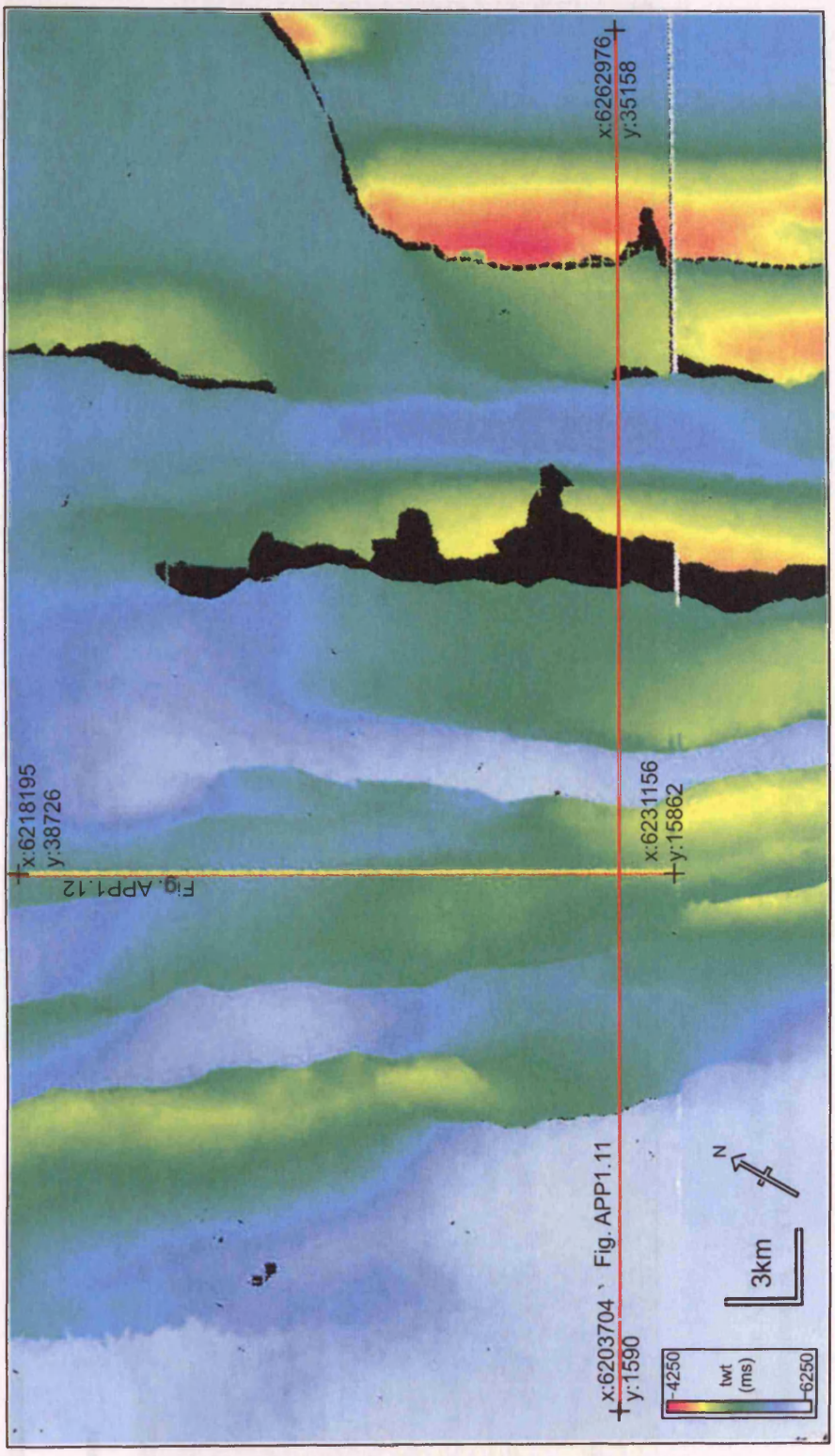

Figure APP1.10: Example seismic time map of **Horizon m4** in seismic survey A, presented in two-way-travel time (ms). Locations of two seismic sections (an inline and a crossline) in following figures are indicated by red lines. The world coordinates of the ends of the seismic sections are given as *x* and *y* in metres. Warm colours represent structural highs, cool colours show structural lows.

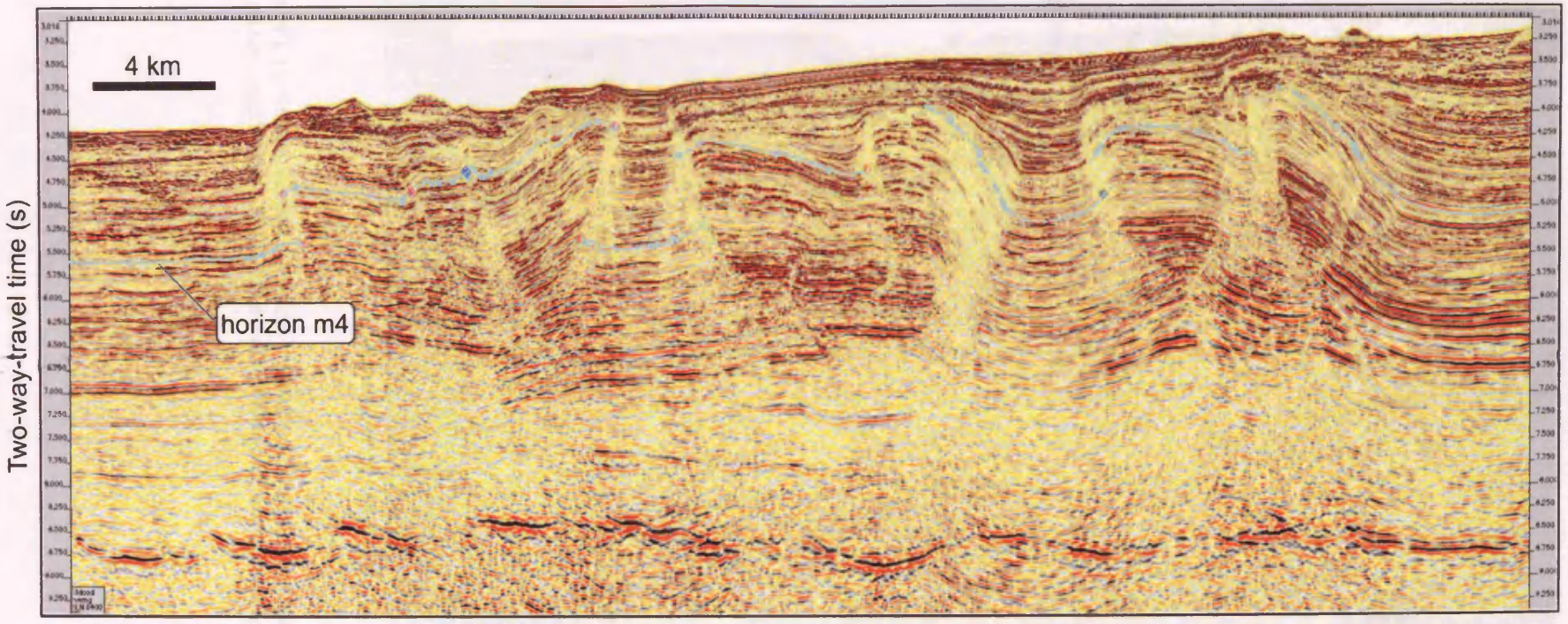

Figure APP1.11: Seismic section (inline) oriented perpendicular to fault strike showing an example of Horizon m4 interpretation. For location and coordinates of section see Figure APP1.10.

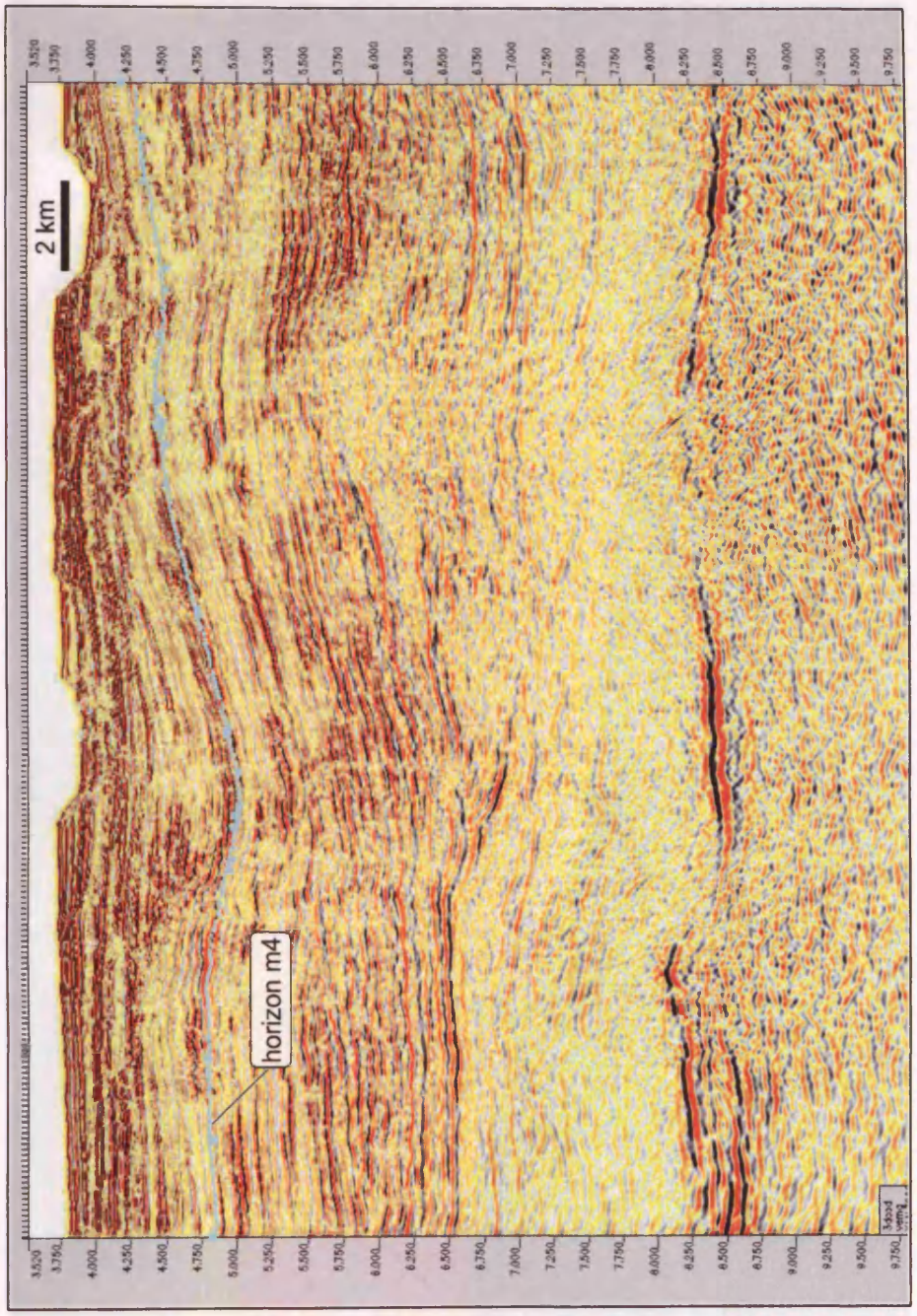

Figure APP1.12: Seismic section (crossline) oriented sub-parallel to fault strike showing an example of Horizon m4 interpretation. For location and coordinates of section see Figure APP1.10.

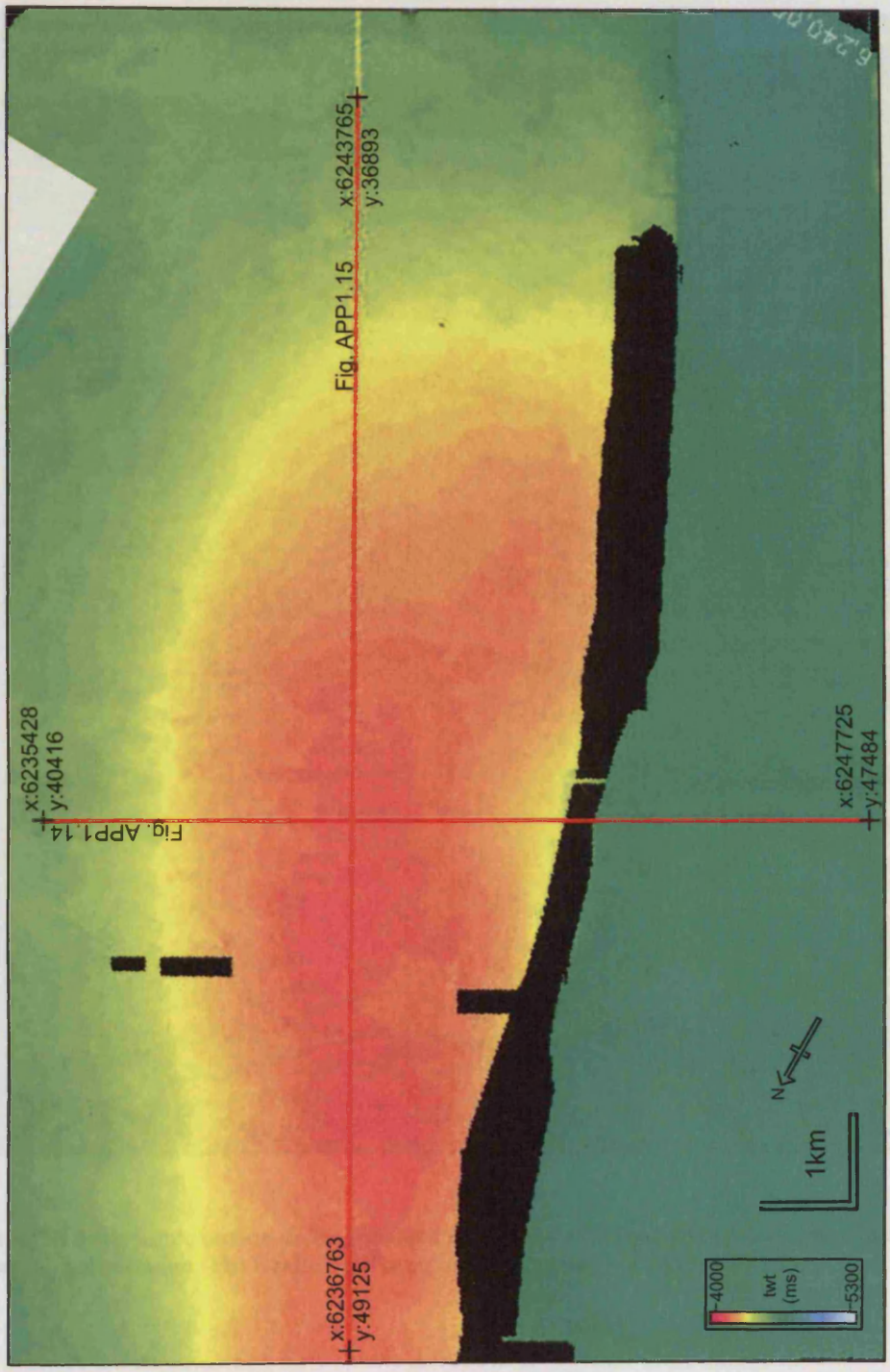

Figure APP1.13: Example seismic time map of **Horizon m6** in seismic survey A, presented in two-way-travel time (ms). Locations of two seismic sections (an inline and a crossline) in following figures are indicated by red lines. The world coordinates of the ends of the seismic sections are given as *x* and *y* in metres. Warm colours represent structural highs, cool colours show structural lows.

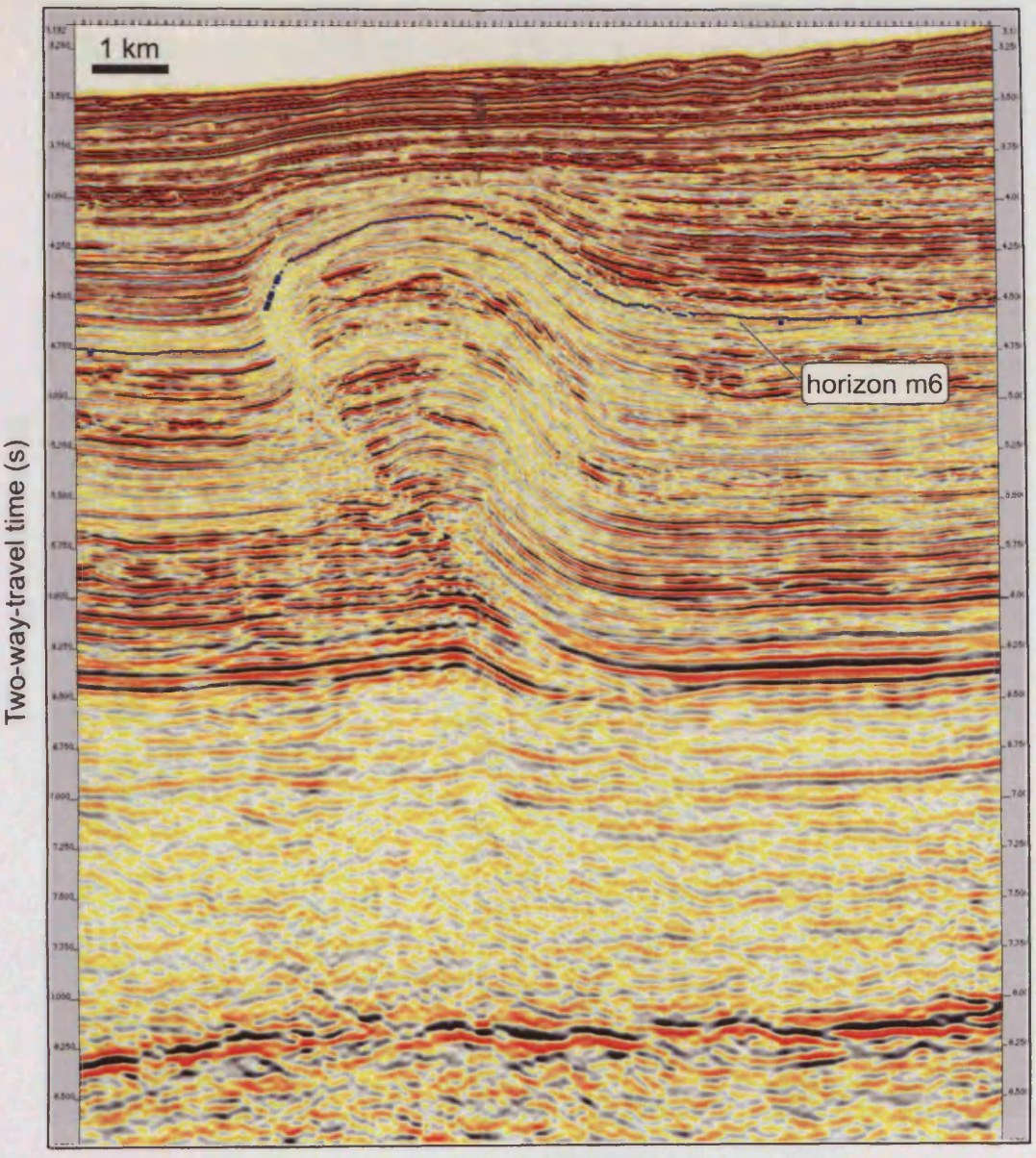

Figure APP1.14: Seismic section (inline) oriented perpendicular to fault strike showing an example of Horizon m6 interpretation. For location and coordinates of section see Figure APP1.13.

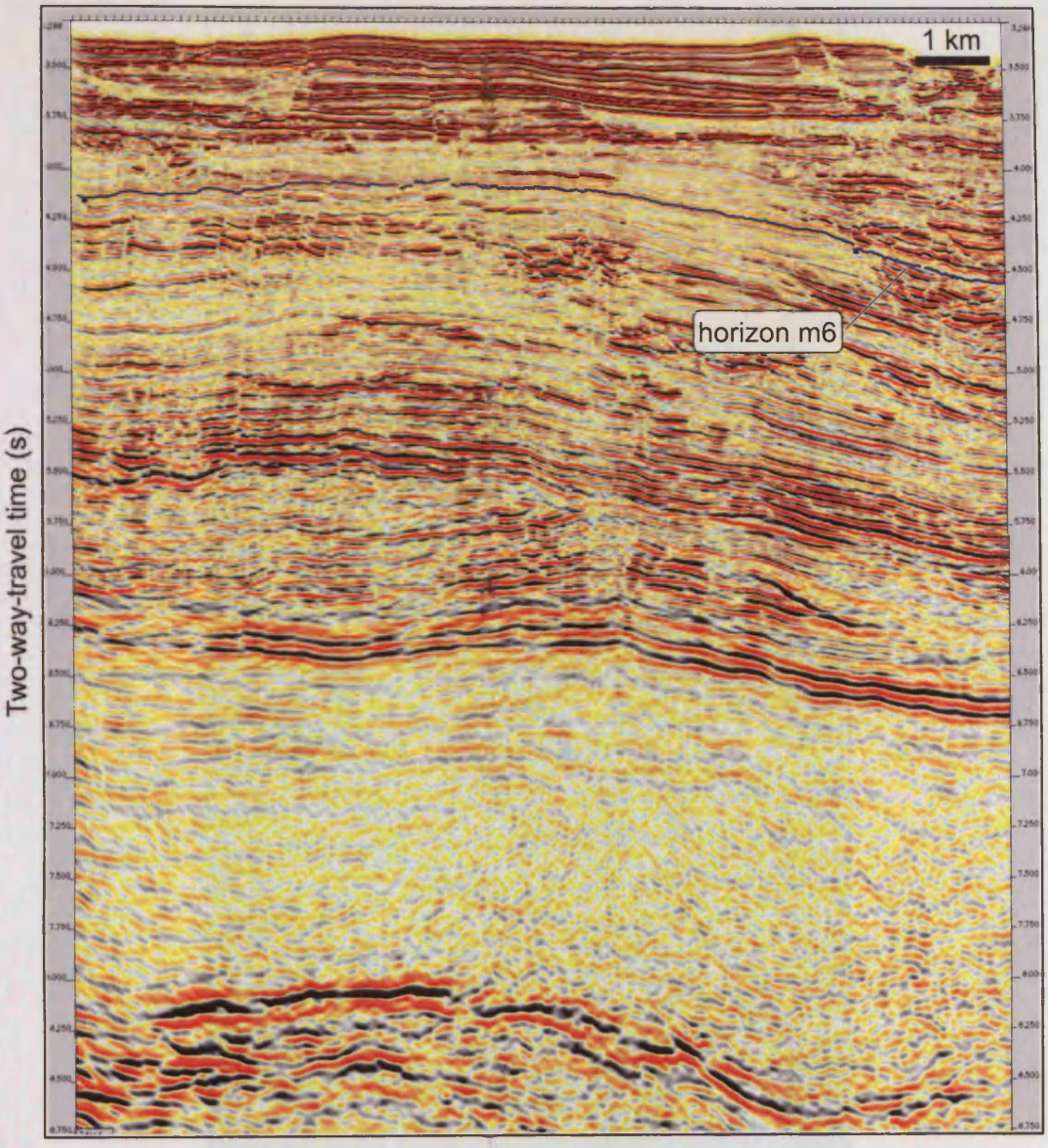

Figure APP1.15: Seismic section (crossline) oriented sub-parallel to fault strike showing an example of Horizon m6 interpretation. For location and coordinates of section see Figure APP1.13.

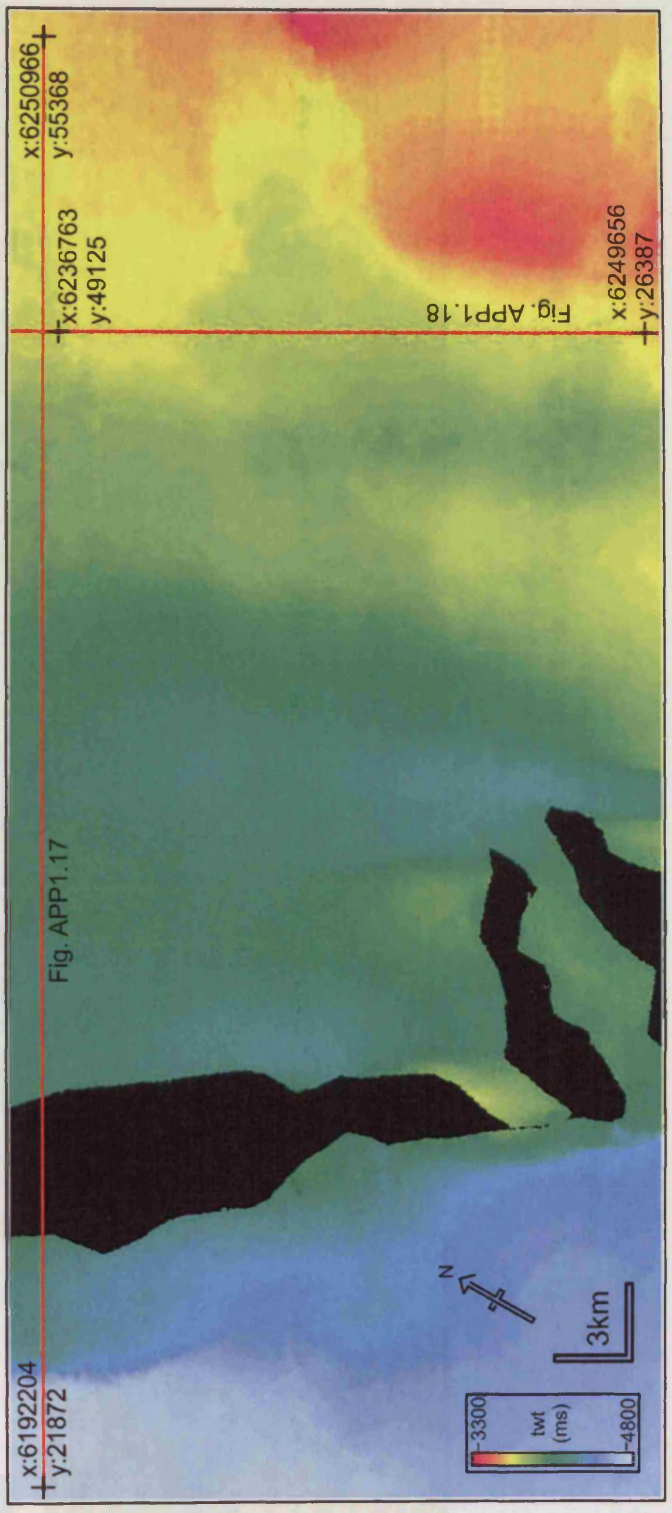

Figure APP1.16: Example seismic time map of **Horizon m11** in seismic survey A, presented in two-way-travel time (ms). Locations of two seismic sections (an inline and a crossline) in following figures are indicated by red lines. The world coordinates of the ends of the seismic sections are given as *x* and *y* in metres. Warm colours represent structural highs, cool colours show structural lows.

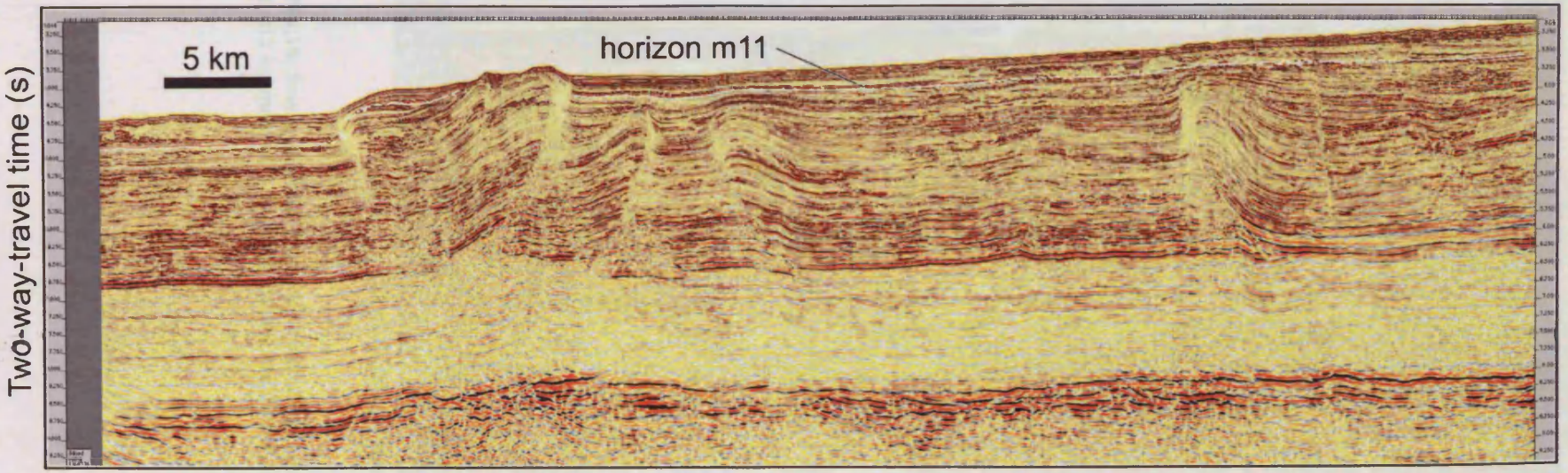

Figure APP1.17: Seismic section (inline) oriented perpendicular to fault strike showing an example of Horizon m11 interpretation. For location and coordinates of section see Figure APP1.16.

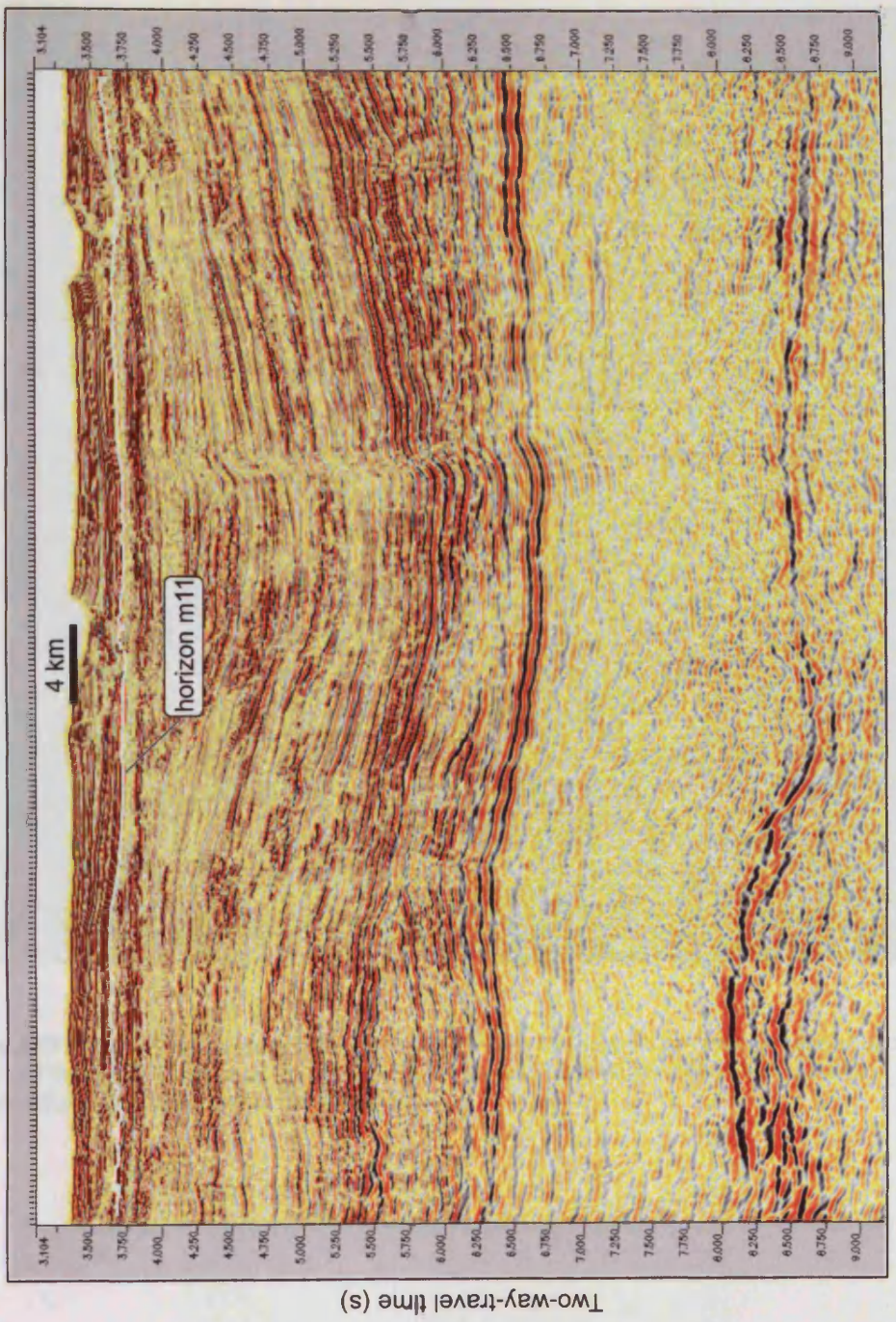

Figure APP1.18: Seismic section (crossline) oriented sub-parallel to fault strike showing an example of Horizon m11 interpretation. For location and coordinates of section see Figure APP1.16.

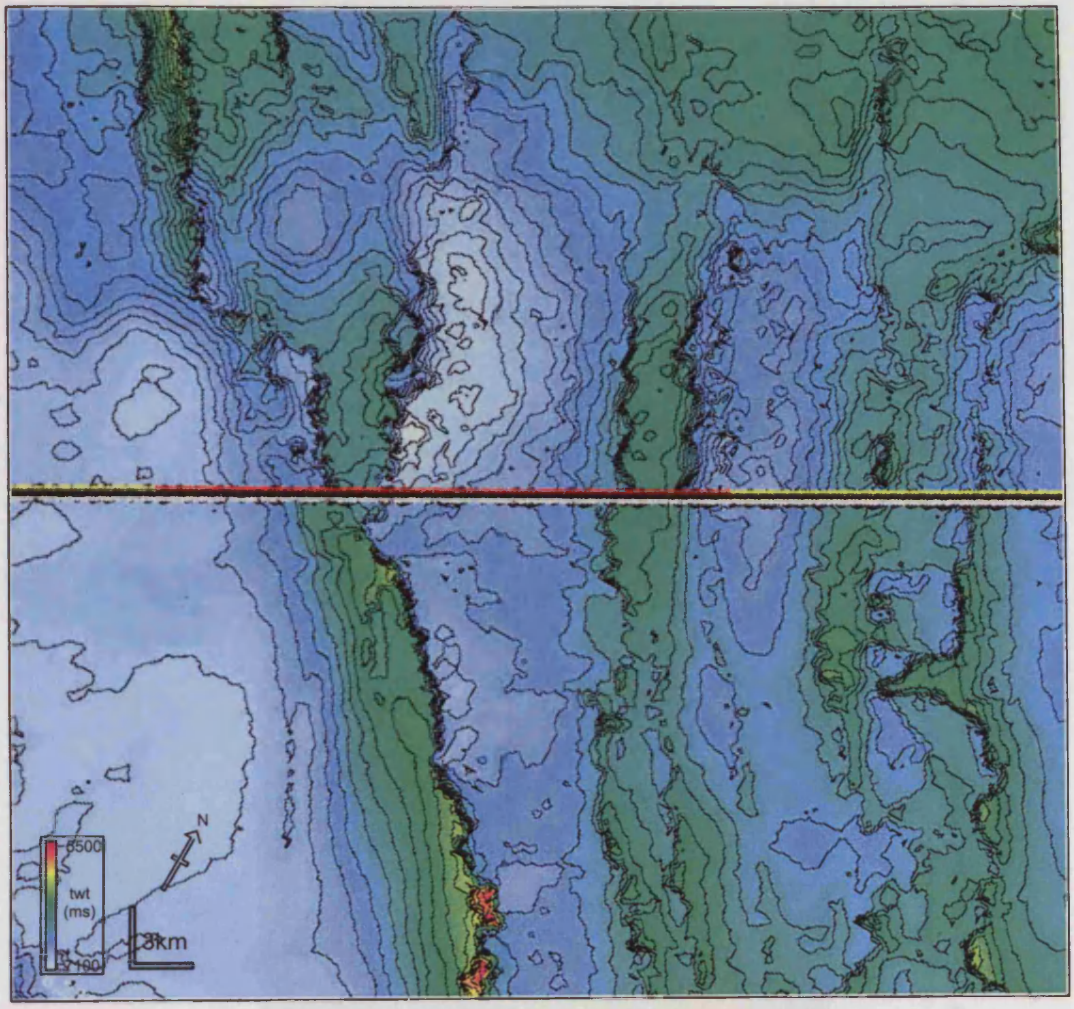

Figure APP1.19: Example seismic time map of **Horizon m0** in seismic survey A, presented in two-way-travel time (ms). Horizon m0 is the Agbada-Akata Fm interface. Warm colours represent structural highs, cool colours show structural lows.

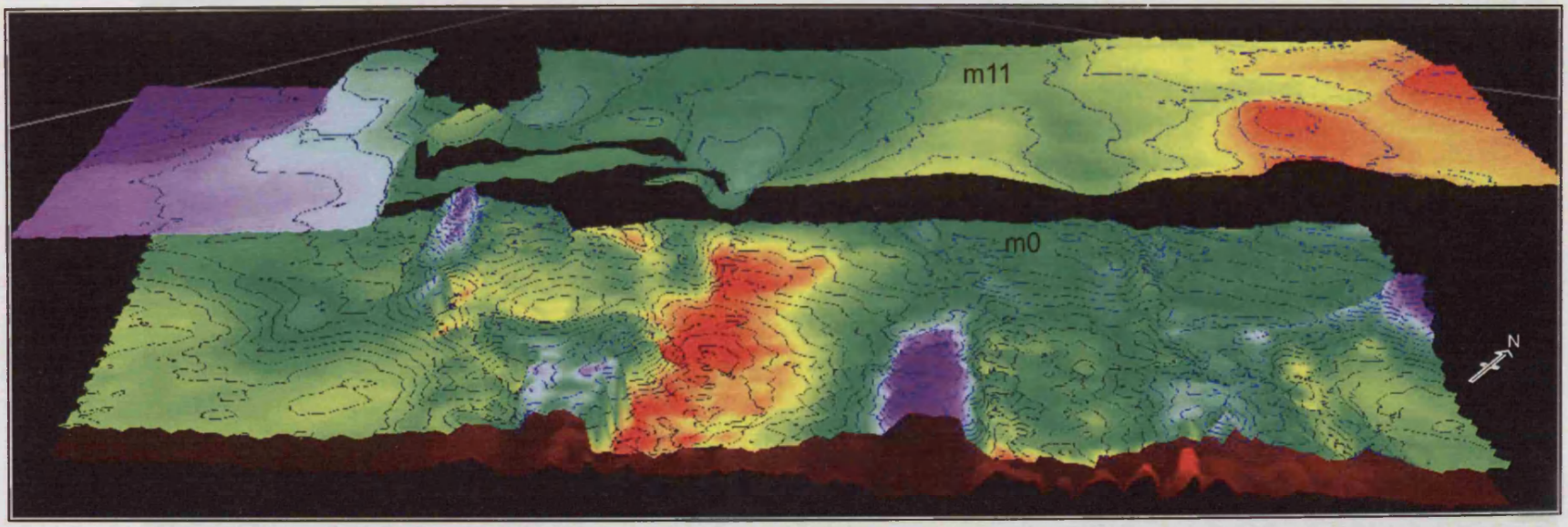

Figure APP1.20: 3D visualisation of Horizons m11 and m0 using IESX Geoviz™ software to show changing structural geometries with depth. 3D visualisations were used in this study to better understand stratal geometries associated with thrust faults. A mid-Akata reflection is also imaged as the lowermost red surface.

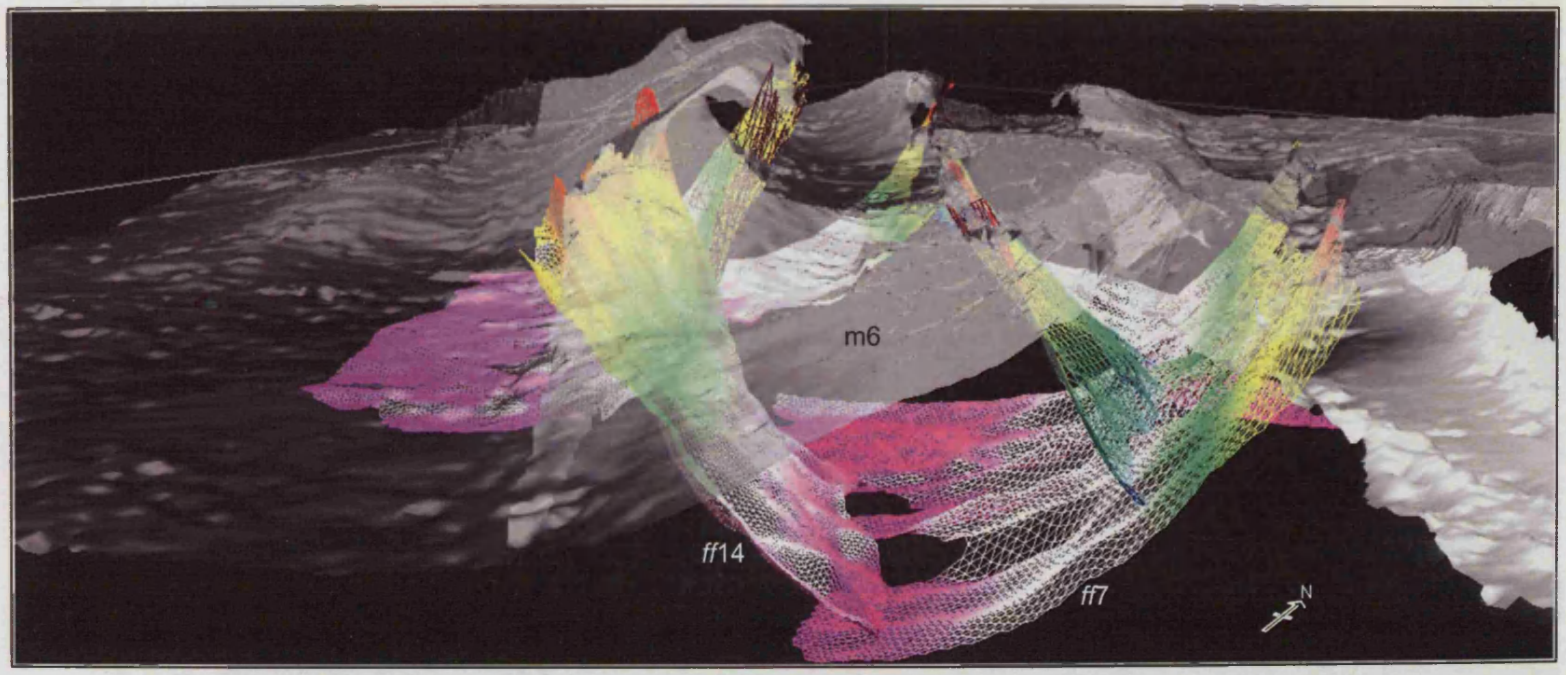

Figure APP1.21: 3D visualisation of Horizons m6 using IESX Geoviz™ software. Horizon m6 is shown as a partially transparent white surface. 3D visualisations were used in this study to better understand stratal geometries associated with thrust faults. *ff*: denotes fault numbers referred to in Chapter 5. The colour of faults corresponds to the depth in the section of a given point on the fault surface.

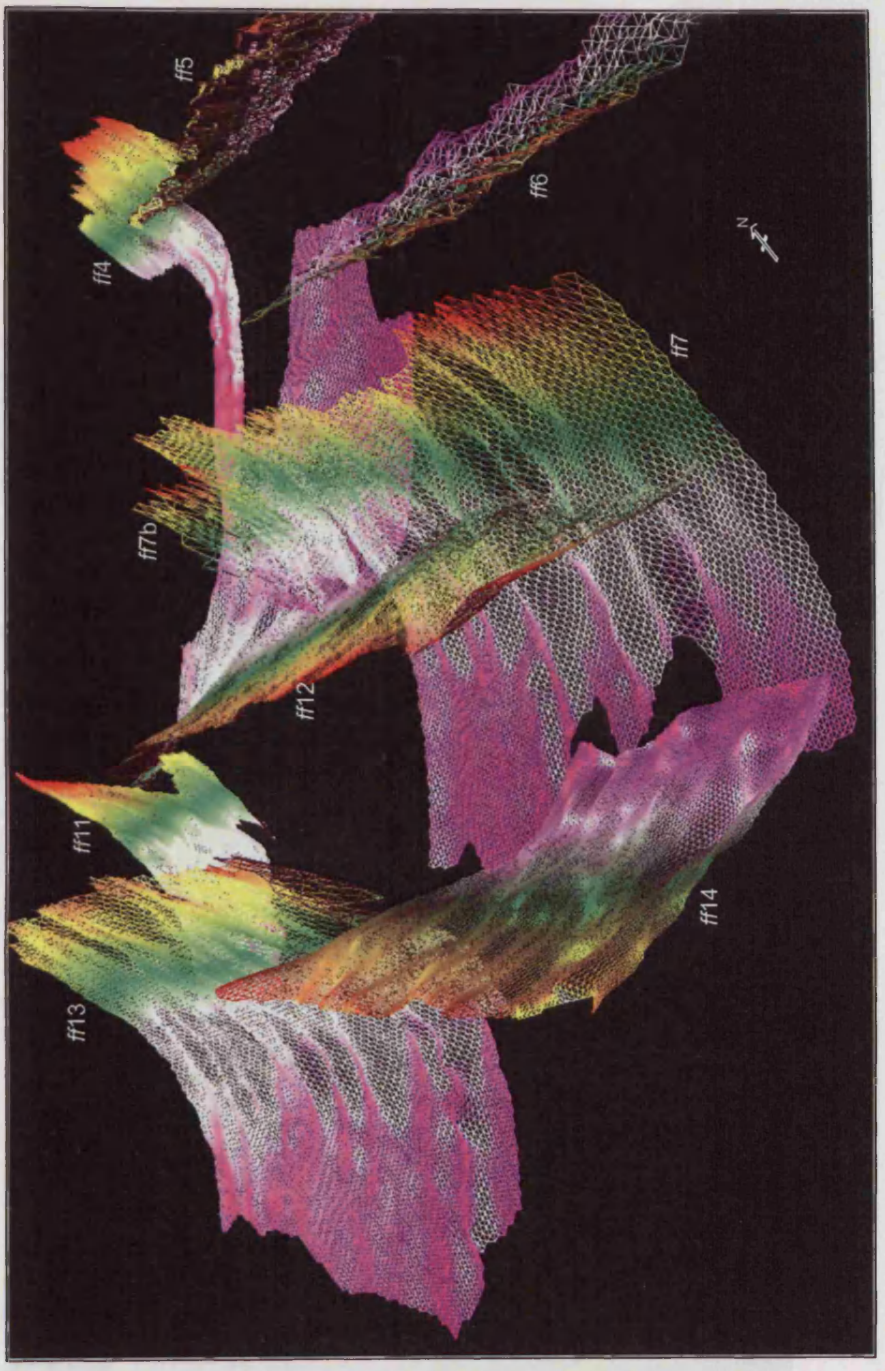

Figure APP1.22: 3D visualisation of selected faults from Chapter 5, imaged using IESX Geoviz™ software. 3D visualisations were used in this study to describe and classify fault plane geometries. *ff*: denotes fault numbers referred to in Chapter 5. The colour of faults corresponds to the depth in the section of a given point on the fault surface.

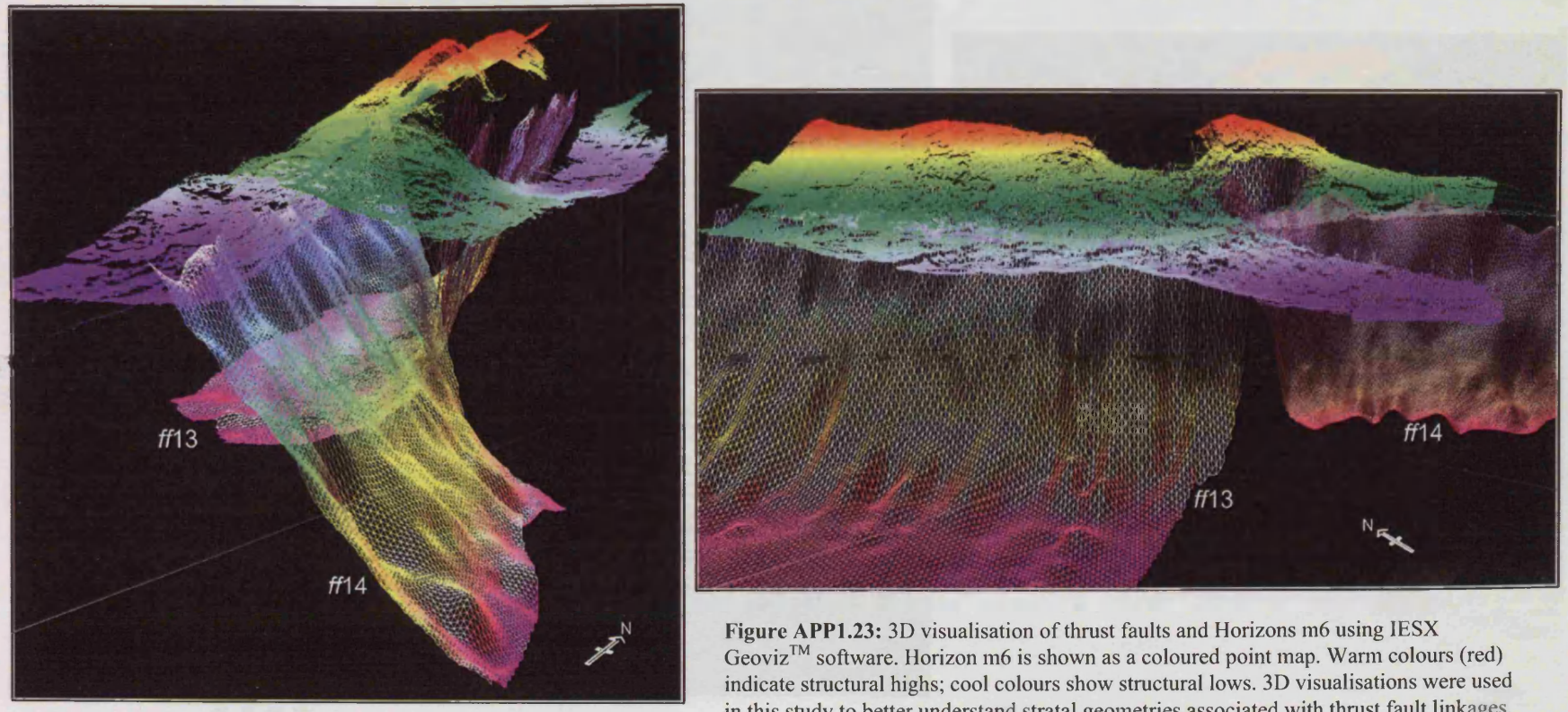

Figure APP1.23: 3D visualisation of thrust faults and Horizons m6 using IESX Geoviz™ software. Horizon m6 is shown as a coloured point map. Warm colours (red) indicate structural highs; cool colours show structural lows. 3D visualisations were used in this study to better understand stratal geometries associated with thrust fault linkages. In this case faults 13 and 14 are linking along strike (see Fig. 3.7). *ff*: denotes fault numbers referred to in Chapter 5.

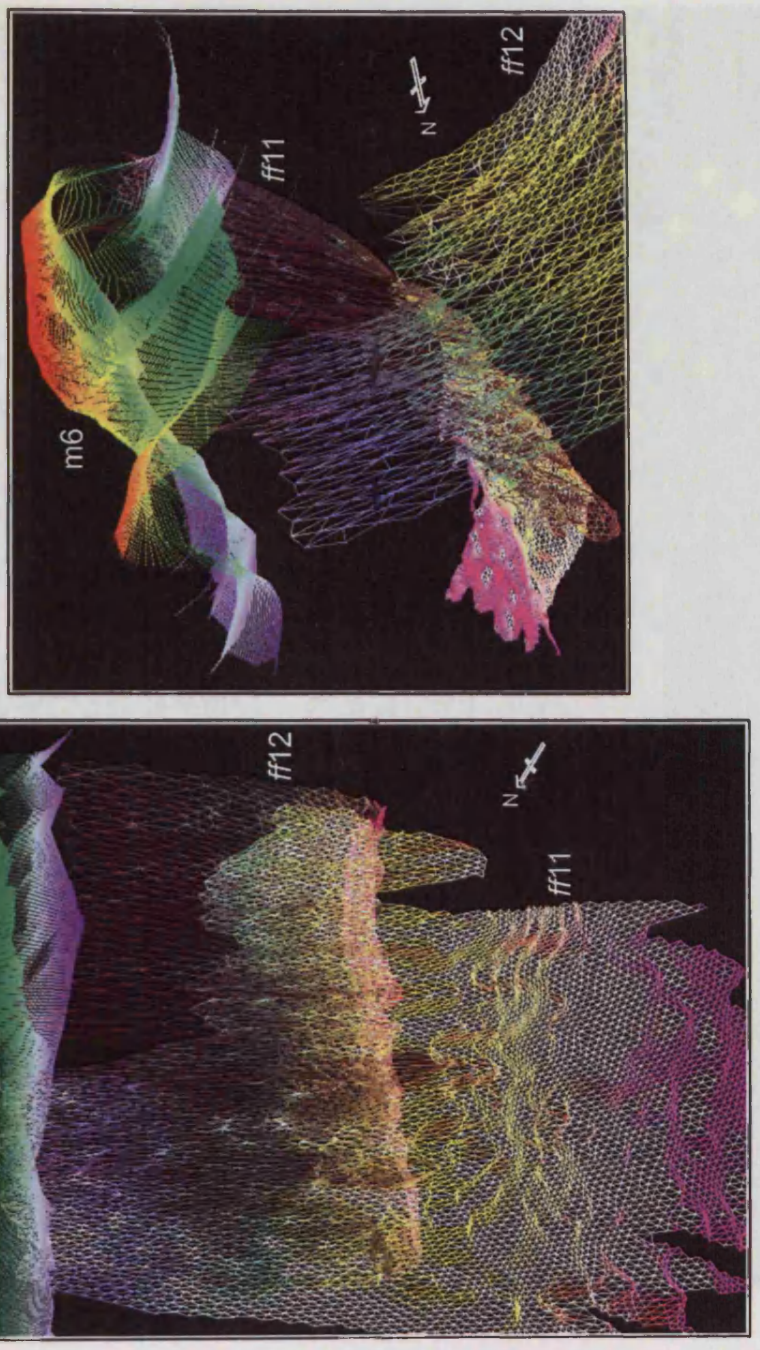

Figure APP1.24: 3D visualisation of thrust faults and Horizons m6 using IESX Geoviz^{TM} software. Horizon m6 is shown as a coloured point map. Warm colours (red) indicate structural highs; cool colours show structural lows. 3D visualisations were used in this study to better understand stratal geometries associated with thrust fault linkages. In this case faults 11 and 12 are linking along strike (see Fig. 3.9). *ff*: denotes fault numbers referred to in Chapter 5.

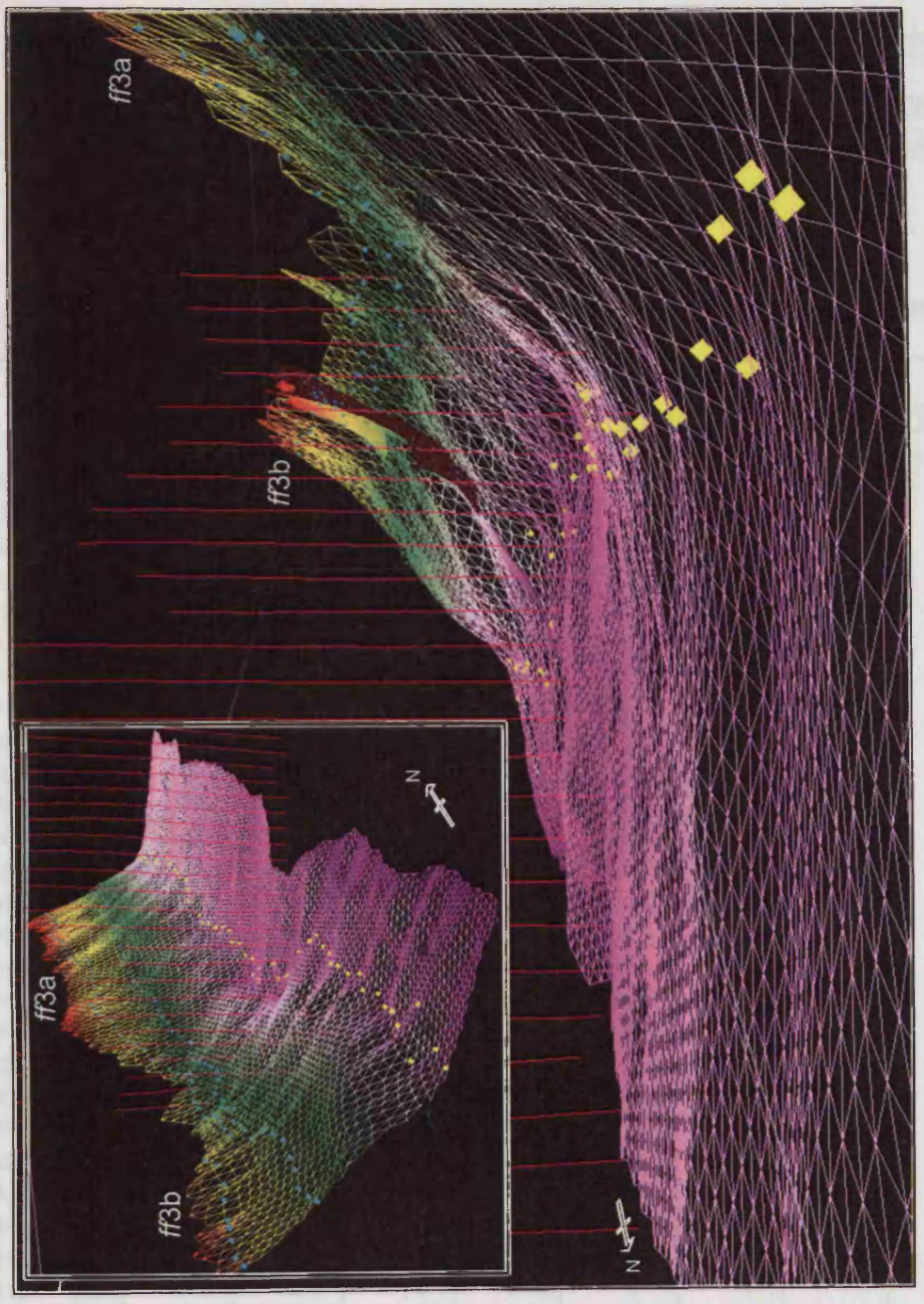

Figure APP1.25: 3D visualisation of synthetic thrust faults using IESX Geoviz^{TM} software. 3D visualisations were used in this study to better understand fault linkage geometries. In this case faults 3a and 3b are linking along strike (see Fig. 5.1). *ff*: denotes fault numbers referred to in Chapter 5. The colour of faults corresponds to the depth in the section of a given point on the fault surface. Yellow dots represent the base of the thrust ramp. Blue dots represent hangingwall cutoffs for a given horizon. Note the position of the base of the ramp coincides with a low in displacement (indicated by blue dots).

APPENDIX 3 - Fault heave values (F1, F2, F2b and F3) from seismic survey B. (Chapter 4)
Measurements were made on sequential inlines oriented perpendicular to fault and fold strike.
Spacing between lines: 350 m

Depth to data point points used to plot heave values for each of the major horizons.

	Depth to data points on each seismic line for each horizon (m)										
Line #	h1	h2	h3	h4	h5	h6	h7	h8	h9	h10	cb
0	6500	6252	5956	5764	5564	5388	5132	4924	4448	4036	3636
1	6500	6251	5956	5764	5564	5387	5131	4923	4447	4035	3632
2	6499	6250	5956	5765	5565	5386	5131	4922	4446	4035	3629
3	6499	6249	5956	5765	5565	5386	5130	4921	4445	4034	3625
4	6499	6249	5955	5766	5565	5385	5129	4920	4444	4034	3622
5	6498	6248	5955	5766	5566	5384	5129	4919	4444	4033	3618
6	6498	6247	5955	5767	5566	5383	5128	4918	4443	4033	3615
7	6498	6246	5955	5767	5566	5383	5127	4917	4442	4032	3611
8	6497	6245	5955	5768	5566	5382	5127	4917	4441	4032	3608
9	6497	6244	5955	5768	5567	5381	5126	4916	4440	4031	3604
10	6496	6244	5955	5768	5567	5380	5125	4915	4439	4031	3601
11	6496	6243	5955	5769	5567	5380	5125	4914	4438	4030	3597
12	6496	6242	5954	5769	5568	5379	5124	4913	4437	4030	3594
13	6495	6241	5954	5770	5568	5378	5123	4912	4436	4029	3590
14	6495	6240	5954	5770	5568	5377	5123	4911	4436	4029	3587
15	6495	6239	5954	5771	5569	5377	5122	4910	4435	4028	3583
16	6494	6238	5954	5771	5569	5376	5121	4909	4434	4027	3580
17	6494	6238	5954	5772	5569	5375	5121	4908	4433	4027	3576
18	6494	6237	5954	5772	5570	5374	5120	4907	4432	4026	3573
19	6493	6236	5953	5772	5570	5374	5119	4906	4431	4026	3569
20	6493	6235	5953	5773	5570	5373	5119	4905	4430	4025	3566
21	6493	6234	5953	5773	5571	5372	5118	4904	4429	4025	3562
22	6492	6233	5953	5774	5571	5371	5117	4903	4428	4024	3559
23	6492	6233	5953	5774	5571	5371	5117	4903	4428	4024	3555
24	6491	6232	5953	5775	5571	5370	5116	4902	4427	4023	3552
25	6491	6231	5953	5775	5572	5369	5115	4901	4426	4023	3548
26	6491	6230	5953	5776	5572	5368	5115	4900	4425	4022	3545
27	6490	6229	5952	5776	5572	5368	5114	4899	4424	4022	3541
28	6490	6228	5952	5776	5573	5367	5113	4898	4423	4021	3538
29	6490	6228	5952	5777	5573	5366	5113	4897	4422	4021	3534
30	6489	6227	5952	5777	5573	5365	5112	4896	4421	4020	3531
31	6489	6226	5952	5778	5574	5365	5111	4895	4420	4019	3527
32	6489	6225	5952	5778	5574	5364	5111	4894	4420	4019	3524
33	6488	6224	5952	5779	5574	5363	5110	4893	4419	4018	3520
34	6488	6223	5951	5779	5575	5362	5109	4892	4418	4018	3517
35	6488	6222	5951	5780	5575	5362	5109	4891	4417	4017	3513
36	6487	6222	5951	5780	5575	5361	5108	4890	4416	4017	3510
37	6487	6221	5951	5780	5576	5360	5107	4889	4415	4016	3506
38	6486	6220	5951	5781	5576	5359	5107	4889	4414	4016	3503
39	6486	6219	5951	5781	5576	5359	5106	4888	4413	4015	3499
40	6486	6218	5951	5782	5576	5358	5105	4887	4412	4015	3496
41	6485	6217	5951	5782	5577	5357	5105	4886	4412	4014	3492
42	6485	6217	5950	5783	5577	5356	5104	4885	4411	4014	3489

43	6485	6216	5950	5783	5577	5356	5103	4884	4410	4013	3485
44	6484	6215	5950	5784	5578	5355	5103	4883	4409	4013	3482
45	6484	6214	5950	5784	5578	5354	5102	4882	4408	4012	3478
46	6484	6213	5950	5784	5578	5353	5101	4881	4407	4011	3474
47	6483	6212	5950	5785	5579	5352	5101	4880	4406	4011	3471
48	6483	6211	5950	5785	5579	5352	5100	4879	4405	4010	3467
49	6483	6211	5949	5786	5579	5351	5099	4878	4404	4010	3464
50	6482	6210	5949	5786	5580	5350	5099	4877	4404	4009	3460
51	6482	6209	5949	5787	5580	5349	5098	4876	4403	4009	3457
52	6482	6208	5949	5787	5580	5349	5097	4875	4402	4008	3453
53	6481	6207	5949	5788	5580	5348	5097	4875	4401	4008	3450
54	6481	6206	5949	5788	5581	5347	5096	4874	4400	4007	3446
55	6480	6206	5949	5788	5581	5346	5095	4873	4399	4007	3443
56	6480	6205	5949	5789	5581	5346	5095	4872	4398	4006	3439
57	6480	6204	5948	5789	5582	5345	5094	4871	4397	4006	3436
58	6479	6203	5948	5790	5582	5344	5093	4870	4396	4005	3432
59	6479	6202	5948	5790	5582	5343	5093	4869	4396	4005	3429
60	6479	6201	5948	5791	5583	5343	5092	4868	4395	4004	3425
61	6478	6200	5948	5791	5583	5342	5091	4867	4394	4003	3422
62	6478	6200	5948	5792	5583	5341	5091	4866	4393	4003	3418
63	6478	6199	5948	5792	5584	5340	5090	4865	4392	4002	3415
64	6477	6198	5947	5792	5584	5340	5089	4864	4391	4002	3411
65	6477	6197	5947	5793	5584	5339	5089	4863	4390	4001	3408
66	6477	6196	5947	5793	5585	5338	5088	4862	4389	4001	3404
67	6476	6195	5947	5794	5585	5337	5087	4861	4388	4000	3401
68	6476	6195	5947	5794	5585	5337	5087	4861	4388	4000	3397
69	6475	6194	5947	5795	5585	5336	5086	4860	4387	3999	3394
70	6475	6193	5947	5795	5586	5335	5085	4859	4386	3999	3390
71	6475	6192	5947	5796	5586	5334	5085	4858	4385	3998	3387
72	6474	6191	5946	5796	5586	5334	5084	4857	4384	3998	3383
73	6474	6190	5946	5796	5587	5333	5083	4856	4383	3997	3380
74	6474	6190	5946	5797	5587	5332	5083	4855	4382	3997	3376
75	6473	6189	5946	5797	5587	5331	5082	4854	4381	3996	3373
76	6473	6188	5946	5798	5588	5331	5081	4853	4380	3995	3369
77	6473	6187	5946	5798	5588	5330	5081	4852	4380	3995	3366
78	6472	6186	5946	5799	5588	5329	5080	4851	4379	3994	3362
79	6472	6185	5945	5799	5589	5328	5079	4850	4378	3994	3359
80	6472	6184	5945	5800	5589	5328	5079	4849	4377	3993	3355
81	6471	6184	5945	5800	5589	5327	5078	4848	4376	3993	3352
82	6471	6183	5945	5800	5590	5326	5077	4847	4375	3992	3348
83	6470	6182	5945	5801	5590	5325	5077	4847	4374	3992	3345
84	6470	6181	5945	5801	5590	5325	5076	4846	4373	3991	3341
85	6470	6180	5945	5802	5590	5324	5075	4845	4372	3991	3338
86	6469	6179	5945	5802	5591	5323	5075	4844	4372	3990	3334
87	6469	6179	5944	5803	5591	5322	5074	4843	4371	3990	3331
88	6469	6178	5944	5803	5591	5322	5073	4842	4370	3989	3327
89	6468	6177	5944	5804	5592	5321	5073	4841	4369	3989	3324
90	6468	6176	5944	5804	5592	5320	5072	4840	4368	3988	3320

Heave values for Fault F1.

	Fault heave values (m) measured on 11 horizons (fault F1)										
Line #	h1	h2	h3	h4	h5	h6	h7	h8	h9	h10	Seabed
0	0	0	0	0	0	0	0	0	0	0	0
1	0	0	55	0	0	0	0	0	0	0	0
2	0	50	100	63	0	0	0	0	0	0	0
3	0	75	59	99	75	43	0	0	0	0	0
4	0	137	125	162	100	25	0	0	0	0	0
5	0	150	138	163	87	62	0	0	0	0	0
6	0	125	195	112	113	87	0	0	0	0	0
7	0	62	226	162	163	125	0	0	0	0	0
8	0	200	251	163	170	125	0	0	0	0	0
9	0	245	200	126	188	137	0	0	0	0	0
10	0	111	150	87	114	125	0	0	0	0	0
11	0	100	113	50	124	87	0	0	0	0	0
12	0	137	75	62	38	50	25	0	0	0	0
13	0	112	75	51	25	50	13	0	0	0	0
14	0	162	50	43	37	50	38	0	0	0	0
15	0	162	50	50	63	38	26	0	0	0	0
16	0	126	37	38	50	25	25	0	0	0	0
17	0	158	38	62	62	12	51	0	0	0	0
18	0	206	50	13	75	62	38	0	0	0	0
19	0	287	63	38	12	25	26	0	0	0	0
20	0	425	99	75	62	37	0	0	0	0	0
21	0	425	237	87	62	0	0	0	0	0	0
22	0	363	325	212	125	25	0	0	0	0	0
23	0	451	400	250	112	13	0	0	0	0	0
24	700	400	351	263	195	101	0	0	0	0	0
25	424	442	388	287	263	87	25	0	0	0	0
26	38	513	363	237	263	112	37	0	0	0	0
27	286	500	375	287	300	114	0	0	0	0	0
28	412	563	376	350	325	126	38	0	0	0	0
29	475	488	375	251	226	225	25	0	0	0	0
30	237	537	388	200	187	150	38	0	0	0	0
31	0	600	438	275	237	150	0	0	0	0	0
32	0	565	400	251	224	87	0	0	0	0	0
33	236	401	400	150	188	50	0	0	0	0	0
34	0	226	338	212	162	100	0	0	0	0	0
35	0	251	325	250	187	137	0	0	0	0	0
36	0	263	325	175	150	112	0	0	0	0	0
37	0	363	300	238	225	63	0	0	0	0	0
38	0	300	326	250	287	113	0	0	0	0	0
39	0	338	287	238	251	125	0	0	0	0	0
40	0	253	275	188	201	137	0	0	0	0	0
41	0	262	251	225	201	163	0	0	0	0	0
42	0	149	187	162	100	75	0	0	0	0	0
43	0	150	187	112	138	75	0	0	0	0	0
44	0	137	150	62	113	88	0	0	0	0	0
45	0	75	137	62	112	113	0	0	0	0	0
46	0	0	137	62	112	62	0	0	0	0	0
47	0	0	124	0	62	0	0	0	0	0	0
48	0	0	87	0	37	0	0	0	0	0	0
49	0	0	50	0	0	0	0	0	0	0	0

50	0	0	0	0	0	0	0	0	0	0	0
51	0	0	0	0	0	0	0	0	0	0	0
52	0	0	0	0	0	0	0	0	0	0	0
53	0	0	0	0	0	0	0	0	0	0	0
54	0	0	0	0	0	0	0	0	0	0	0
55	0	0	0	0	0	0	0	0	0	0	0
56	0	0	0	0	0	0	0	0	0	0	0
57	0	0	0	0	0	0	0	0	0	0	0
58	0	0	0	0	0	0	0	0	0	0	0
59	0	0	0	0	0	0	0	0	0	0	0
60	0	0	0	0	0	0	0	0	0	0	0
61	0	0	0	0	0	0	0	0	0	0	0
62	0	0	0	0	0	0	0	0	0	0	0
63	0	0	0	0	0	0	0	0	0	0	0
64	0	0	0	0	0	0	0	0	0	0	0
65	0	0	0	0	0	0	0	0	0	0	0
66	0	0	0	0	0	0	0	0	0	0	0
67	0	0	0	0	0	0	0	0	0	0	0
68	0	0	0	0	0	0	0	0	0	0	0
69	0	0	0	0	0	0	0	0	0	0	0
70	0	0	0	0	0	0	0	0	0	0	0
71	0	0	0	0	0	0	0	0	0	0	0
72	0	0	0	0	0	0	0	0	0	0	0
73	0	0	0	0	0	0	0	0	0	0	0
74	0	0	0	0	0	0	0	0	0	0	0
75	0	0	0	0	0	0	0	0	0	0	0
76	0	0	0	0	0	0	0	0	0	0	0
77	0	0	0	0	0	0	0	0	0	0	0
78	0	0	0	0	0	0	0	0	0	0	0
79	0	0	0	0	0	0	0	0	0	0	0
80	0	0	0	0	0	0	0	0	0	0	0
81	0	0	0	0	0	0	0	0	0	0	0
82	0	0	0	0	0	0	0	0	0	0	0
83	0	0	0	0	0	0	0	0	0	0	0
84	0	0	0	0	0	0	0	0	0	0	0
85	0	0	0	0	0	0	0	0	0	0	0
86	0	0	0	0	0	0	0	0	0	0	0
87	0	0	0	0	0	0	0	0	0	0	0
88	0	0	0	0	0	0	0	0	0	0	0
89	0	0	0	0	0	0	0	0	0	0	0
90	0	0	0	0	0	0	0	0	0	0	0

Heave values for Fault F2.

	Fault heave values (m) measured on 11 horizons (fault F2)										
Line #	h1	h2	h3	h4	h5	h6	h7	h8	h9	h10	Seabed
0	0	0	0	0	0	0	0	0	0	0	0
1	0	0	0	0	0	0	0	0	0	0	0
2	0	0	0	0	0	0	0	0	0	0	0
3	0	0	0	0	0	0	0	0	0	0	0
4	0	0	0	0	0	0	0	0	0	0	0
5	0	0	0	0	0	0	0	0	0	0	0
6	0	0	0	0	0	0	0	0	0	0	0
7	0	0	0	0	0	0	0	0	0	0	0
8	0	0	0	0	0	0	0	0	0	0	0
9	0	0	0	0	0	0	0	0	0	0	0
10	0	0	0	0	0	0	0	0	0	0	0
11	0	0	0	0	0	0	0	0	0	0	0
12	0	0	0	0	0	0	0	0	0	0	0
13	0	0	0	0	0	0	0	0	0	0	0
14	0	0	0	0	0	0	0	0	0	0	0
15	0	0	0	0	0	0	0	0	0	0	0
16	0	0	0	0	0	0	0	0	0	0	0
17	0	0	0	0	0	0	0	0	0	0	0
18	0	0	0	0	0	0	0	0	0	0	0
19	0	0	0	0	0	0	0	0	0	0	0
20	0	0	0	0	0	0	0	0	0	0	0
21	0	0	0	0	0	0	0	0	0	0	0
22	0	0	0	0	0	0	0	0	0	0	0
23	0	0	0	0	0	0	0	0	0	0	0
24	0	0	0	0	0	0	0	0	0	0	0
25	0	0	0	0	0	0	0	0	0	0	0
26	0	0	100	38	0	0	0	0	0	0	0
27	0	25	138	25	12	0	0	0	0	0	0
28	0	50	125	0	0	0	0	0	0	0	0
29	0	125	125	37	24	0	0	0	0	0	0
30	0	201	150	38	25	0	0	0	0	0	0
31	0	88	112	100	124	0	0	0	0	0	0
32	0	162	163	50	125	0	0	0	0	0	0
33	0	183	195	100	99	0	0	0	0	0	0
34	0	476	350	275	200	0	0	0	0	0	0
35	351	388	338	287	231	50	0	0	0	0	0
36	337	450	338	300	251	75	0	0	0	0	0
37	363	363	337	362	188	100	62	0	0	0	0
38	513	538	388	275	188	113	0	0	0	0	0
39	462	637	500	251	200	138	0	0	0	0	0
40	562	838	737	300	263	238	0	0	0	0	0
41	563	813	687	437	401	188	0	0	0	0	0
42	951	888	750	500	476	226	0	0	0	0	0
43	607	888	725	450	363	188	0	0	0	0	0
44	975	1051	800	488	488	325	88	0	0	0	0
45	723	950	875	588	488	350	150	37	0	0	0
46	1263	975	813	575	438	288	187	101	0	0	0
47	1326	863	863	675	376	226	76	0	0	0	0
48	838	776	825	538	340	275	150	75	0	0	0
49	1643	762	850	425	350	325	226	75	0	0	0

50	475	626	800	375	476	337	126	98	0	0	0
51	500	751	800	377	312	275	226	100	0	0	0
52	553	708	725	662	530	333	250	70	0	0	0
53	581	788	643	506	451	425	288	126	0	0	0
54	395	513	552	412	357	424	188	0	0	0	0
55	365	561	465	328	345	258	95	0	0	0	0
56	313	475	535	325	251	188	25	0	0	0	0
57	363	613	434	175	263	138	75	0	0	0	0
58	476	450	354	113	150	62	50	0	0	0	0
59	126	388	288	100	87	100	0	0	0	0	0
60	0	330	195	200	87	0	0	0	0	0	0
61	0	199	149	138	87	0	0	0	0	0	0
62	0	251	107	75	37	0	0	0	0	0	0
63	0	250	75	0	0	0	0	0	0	0	0
64	0	150	13	0	0	0	0	0	0	0	0
65	0	137	0	0	0	0	0	0	0	0	0
66	0	0	0	0	0	0	0	0	0	0	0
67	0	0	0	0	0	0	0	0	0	0	0
68	0	0	0	0	0	0	0	0	0	0	0
69	0	0	0	0	0	0	0	0	0	0	0
70	0	0	0	0	0	0	0	0	0	0	0
71	0	0	0	0	0	0	0	0	0	0	0
72	0	0	0	0	0	0	0	0	0	0	0
73	0	0	0	0	0	0	0	0	0	0	0
74	0	0	0	0	0	0	0	0	0	0	0
75	0	0	0	0	0	0	0	0	0	0	0
76	0	0	0	0	0	0	0	0	0	0	0
77	0	0	0	0	0	0	0	0	0	0	0
78	0	0	0	0	0	0	0	0	0	0	0
79	0	0	0	0	0	0	0	0	0	0	0
80	0	0	0	0	0	0	0	0	0	0	0
81	0	0	0	0	0	0	0	0	0	0	0
82	0	0	0	0	0	0	0	0	0	0	0
83	0	0	0	0	0	0	0	0	0	0	0
84	0	0	0	0	0	0	0	0	0	0	0
85	0	0	0	0	0	0	0	0	0	0	0
86	0	0	0	0	0	0	0	0	0	0	0
87	0	0	0	0	0	0	0	0	0	0	0
88	0	0	0	0	0	0	0	0	0	0	0
89	0	0	0	0	0	0	0	0	0	0	0
90	0	0	0	0	0	0	0	0	0	0	0
	0	0	0	0	0	0	0	0	0	0	0

Heave values for Fault F2b.

	Fault heave values (m) measured on 11 horizons (fault F2b)										
Line #	h1	h2	h3	h4	h5	h6	h7	h8	h9	h10	Seabed
0	0	0	0	0	0	0	0	0	0	0	0
1	0	0	0	0	0	0	0	0	0	0	0
2	0	0	0	0	0	0	0	0	0	0	0
3	0	0	0	0	0	0	0	0	0	0	0
4	0	0	0	0	0	0	0	0	0	0	0
5	0	0	0	0	0	0	0	0	0	0	0
6	0	0	0	0	0	0	0	0	0	0	0
7	0	0	0	0	0	0	0	0	0	0	0
8	0	0	0	0	0	0	0	0	0	0	0
9	0	0	0	0	0	0	0	0	0	0	0
10	0	0	0	0	0	0	0	0	0	0	0
11	0	0	0	0	0	0	0	0	0	0	0
12	0	0	0	0	0	0	0	0	0	0	0
13	0	0	0	0	0	0	0	0	0	0	0
14	0	0	0	0	0	0	0	0	0	0	0
15	0	0	0	0	0	0	0	0	0	0	0
16	0	0	50	21	0	0	0	0	0	0	0
17	0	62	125	68	0	0	0	0	0	0	0
18	0	43	138	45	75	0	0	0	0	0	0
19	0	70	200	158	87	37	0	0	0	0	0
20	0	65	200	205	118	50	0	0	0	0	0
21	0	100	138	138	75	25	0	0	0	0	0
22	0	71	78	100	62	50	0	0	0	0	0
23	0	50	37	50	38	0	0	0	0	0	0
24	0	0	124	55	75	58	0	0	0	0	0
25	0	0	115	75	76	50	0	0	0	0	0
26	0	0	150	124	138	62	0	0	0	0	0
27	0	62	99	75	100	58	0	0	0	0	0
28	0	91	112	87	162	62	25	0	0	0	0
29	0	62	95	82	99	50	0	0	0	0	0
30	0	0	113	62	63	0	0	0	0	0	0
31	0	0	112	70	138	75	0	0	0	0	0
32	0	0	50	38	21	38	0	0	0	0	0
33	0	0	0	0	0	0	0	0	0	0	0
34	0	0	0	0	0	0	0	0	0	0	0
35	0	0	0	0	0	0	0	0	0	0	0
36	0	0	0	0	0	0	0	0	0	0	0
37	0	0	0	0	0	0	0	0	0	0	0
38	0	0	0	0	0	0	0	0	0	0	0
39	0	0	0	0	0	0	0	0	0	0	0
40	0	0	0	0	0	0	0	0	0	0	0
41	0	0	0	0	0	0	0	0	0	0	0
42	0	0	0	0	0	0	0	0	0	0	0
43	0	0	0	0	0	0	0	0	0	0	0
44	0	0	0	0	0	0	0	0	0	0	0
45	0	0	0	0	0	0	0	0	0	0	0
46	0	0	0	0	0	0	0	0	0	0	0

No heave values on lines 47 to 90.

Heave values for Fault F3.

	Fault heave values (m) measured on 11 horizons (fault F3)										
Line #	h1	h2	h3	h4	h5	h6	h7	h8	h9	h10	Seabed
0	0	0	0	0	0	0	0	0	0	0	0
1	0	0	0	0	0	0	0	0	0	0	0
2	0	0	0	0	0	0	0	0	0	0	0
3	0	0	0	0	0	0	0	0	0	0	0
4	0	0	0	0	0	0	0	0	0	0	0
5	0	0	0	0	0	0	0	0	0	0	0
6	0	0	0	0	0	0	0	0	0	0	0
7	0	0	0	0	0	0	0	0	0	0	0
8	0	0	0	0	0	0	0	0	0	0	0
9	0	0	0	0	0	0	0	0	0	0	0
10	0	0	0	0	0	0	0	0	0	0	0
11	0	0	0	0	0	0	0	0	0	0	0
12	0	0	0	0	0	0	0	0	0	0	0
13	0	0	0	0	0	0	0	0	0	0	0
14	0	0	0	0	0	0	0	0	0	0	0
15	0	0	0	0	0	0	0	0	0	0	0
16	0	0	0	0	0	0	0	0	0	0	0
17	0	0	0	0	0	0	0	0	0	0	0
18	0	0	0	0	0	0	0	0	0	0	0
19	0	0	0	0	0	0	0	0	0	0	0
20	0	0	0	0	0	0	0	0	0	0	0
21	0	0	0	0	0	0	0	0	0	0	0
22	0	0	0	0	0	0	0	0	0	0	0
23	0	0	0	0	0	0	0	0	0	0	0
24	0	0	0	0	0	0	0	0	0	0	0
25	0	0	0	0	0	0	0	0	0	0	0
26	0	0	0	0	0	0	0	0	0	0	0
27	0	0	0	0	0	0	0	0	0	0	0
28	0	0	0	0	0	0	0	0	0	0	0
29	0	0	0	0	0	0	0	0	0	0	0
30	0	0	0	0	0	0	0	0	0	0	0
31	0	0	0	0	0	0	0	0	0	0	0
32	0	0	0	0	0	0	0	0	0	0	0
33	0	0	0	0	0	0	0	0	0	0	0
34	0	0	0	0	0	0	0	0	0	0	0
35	0	0	0	0	0	0	0	0	0	0	0
36	0	0	0	0	0	0	0	0	0	0	0
37	0	0	0	0	0	0	0	0	0	0	0
38	0	0	0	0	0	0	0	0	0	0	0
39	0	0	0	0	0	0	0	0	0	0	0
40	0	0	0	0	0	0	0	0	0	0	0
41	0	0	0	0	0	0	0	0	0	0	0
42	0	0	0	0	0	0	0	0	0	0	0
43	0	0	0	0	0	0	0	0	0	0	0
44	0	0	0	0	0	0	0	0	0	0	0
45	0	0	0	0	0	0	0	0	0	0	0
46	0	0	0	0	0	0	0	0	0	0	0
47	0	0	0	0	0	0	0	0	0	0	0
48	0	0	0	0	0	0	0	0	0	0	0

49	0	0	0	0	0	0	0	0	0	0	0
50	0	0	0	0	0	0	0	0	0	0	0
51	0	0	0	0	0	0	0	0	0	0	0
52	0	163	0	0	0	0	0	0	0	0	0
53	0	124	0	0	0	0	0	0	0	0	0
54	0	124	0	0	0	0	0	0	0	0	0
55	0	125	0	0	0	0	0	0	0	0	0
56	0	75	136	0	0	0	0	0	0	0	0
57	0	175	155	0	0	0	0	0	0	0	0
58	0	263	207	37	62	0	0	0	0	0	0
59	0	338	242	175	87	125	75	0	0	0	0
60	0	238	294	162	100	113	88	0	0	0	0
61	0	225	247	250	226	112	99	0	0	0	0
62	0	412	375	251	313	251	87	0	0	0	0
63	0	439	513	250	313	200	50	0	0	0	0
64	0	538	513	225	263	238	38	0	0	0	0
65	0	450	576	250	275	238	113	0	0	0	0
66	0	462	563	488	424	317	50	0	0	0	0
67	0	475	600	650	400	373	0	0	0	0	0
68	0	513	613	675	400	250	0	0	0	0	0
69	0	585	638	650	337	150	0	0	0	0	0
70	0	625	613	513	287	200	0	0	0	0	0
71	0	625	664	588	313	175	0	0	0	0	0
72	0	550	625	588	375	150	0	0	0	0	0
73	0	488	676	449	312	212	0	0	0	0	0
74	0	363	525	488	401	263	50	0	0	0	0
75	0	375	525	450	438	275	0	0	0	0	0
76	0	500	488	488	338	238	38	0	0	0	0
77	0	463	401	500	275	200	0	0	0	0	0
78	0	468	413	400	388	150	0	0	0	0	0
79	0	425	325	312	263	137	0	0	0	0	0
80	0	287	363	313	313	137	0	0	0	0	0
81	0	326	275	325	213	50	0	0	0	0	0
82	0	312	238	325	212	0	0	0	0	0	0
83	0	213	212	263	163	50	0	0	0	0	0
84	0	250	113	100	87	0	0	0	0	0	0
85	0	138	50	62	26	0	0	0	0	0	0
86	0	70	99	25	0	0	0	0	0	0	0
87	0	100	100	25	0	0	0	0	0	0	0
88	0	137	62	37	0	0	0	0	0	0	0
89	0	62	37	0	0	0	0	0	0	0	0
90	0	0	0	0	0	0	0	0	0	0	0

APPENDIX 4 - Fault heave values (faults 2 to 15) from seismic survey A (Chapter 5).
Measurements were made on sequential inlines oriented parallel with regional dip.
Measurements were made on lines spaced at 40 inlines (i.e. 500m).

			Fault heave (m)															
Inline	Hor	Depth (m)	2	3a	3b	4	5	6	7	7b	8	9	10	11	12	13	13b	14	15
8400	m1	5545		1502									830	1687	121	1398	173		1150
	m2	5015		1478									440	1349	0	1610	380		880
	m3	4530		958									331	477	0	1482	341		1201
	m4	4363		378									224	680	0	1377	122		1054
	m6	4226		220									49	488	0	1122	48		580
	m7	3979		47									13	241	0	930	46		551
	m8	3811		0									0	0	0	421	0		202
	m9	3732		0									0	0	0	348	0		98
	m11	3519		0									0	0	0	123	0		31
	seabed	3240		0									0	0	0	0	0		0
8360	m1	5536		1573		0							601	1431	180	1375	200		931
	m2	4995		1149		0							398	1144	44	1425	77		1361
	m3	4523		748		0							344	431	0	1175	231		962
	m4	4357		446		0							177	583	0	1025	162		957
	m6	4219		122		0							26	480	0	850	26		644
	m7	3970		0		0							0	222	0	750	46		608
	m8	3809		0		0							0	19	0	450	0		131
	m9	3730		0		0							0	0	0	400	0		49
	m11	3514		0		0							0	0	0	100	0		77
	seabed	3230		0		0							0	0	0	0	0		0
8320	m1	5529		1430		16							661	1281	281	1275	124		630
	m2	4998		144		50							452	931	0	1575	153		1134
	m3	4528		821		0							375	730	0	1250	202		1060
	m4	4341		324		0							301	699	0	1025	198		856
	m6	4220		69		0							22	484	0	425	0		652
	m7	3970		0		0							0	231	0	375	0		431
	m8	3807		0		0							0	0	0	275	0		105
	m9	3724		0		0							0	0	0	200	0		98
	m11	3515		0		0							0	0	0	0	0		67
	seabed	3235		0		0							0	0	0	0	0		0
8280	m1	5540		1427		98							731	1031	246	1150	82		1189
	m2	5003		1557		66							480	780	0	1425	134		1181
	m3	4511		902		0							477	648	0	1200	126		1005
	m4	4345		436		0							253	537	0	1075	155		806
	m6	4209		140		0							48	380	0	475	51		551
	m7	3961		22		0							0	177	0	450	0		569
	m8	3799		0		0							0	0	0	300	0		334
	m9	3720		0		0							0	0	0	225	0		203
	m11	3509		0		0							0	0	0	50	0		101
	seabed	3226		0		0							0	0	0	0	0		0
8240	m1	5519		1502		76							679	964	398	1400	186		708
	m2	5000		1340		66							443	631	119	1325	226		1261
	m3	4517		877		0							446	578	0	925	219		1148
	m4	4369		369		0							281	575	0	1000	157		771
	m6	4211		144		0							74	401	0	625	26		580
	m7	3968		119		0							29	176	0	675	0		631
	m8	3810		46		0							0	0	0	500	0		397
	m9	3726		0		0							0	0	0	325	0		249
	m11	3504		0		0							0	0	0	75	0		98

Continued...

			Fault heave (m)																
Inline	Hor	Depth (m)	2	3a	3b	4	5	6	7	7b	8	9	10	11	12	13	13b	14	15
	seabed	3224		0		0							0	0	0	0	0		0
8200	m1	5508		1830		112							649	798	374	1700	198		661
	m2	5010		1530		98							681	480	419	1425	144		1428
	m3	4524		998		0							349	198	0	1025	131		1078
	m4	4361		470		0							380	256	0	1025	97		930
	m6	4213		180		0							122	154	0	700	48		640
	m7	3962		146		0							26	49	0	525	26		664
	m8	3806		0		0							0	0	0	350	0		331
	m9	3728		0		0							0	0	0	225	0		180
	m11	3508		0		0							0	0	0	50	0		101
	seabed	3216		0		0							0	0	0	0	0		0
8160	m1	5501		1649		125							789	710	387	1875	130		887
	m2	5014		1482		102							551	306	349	1650	121		1130
	m3	4521		1022		12							451	161	0	1200	91		901
	m4	4343		570		0							350	224	0	1050	70		843
	m6	4204		349		0							222	170	0	675	62		580
	m7	3971		130		0							50	24	0	625	21		449
	m8	3810		72		0							0	15	0	375	0		283
	m9	3730		0		0							0	0	0	250	0		181
	m11	3507		0		0							0	0	0	75	0		80
	seabed	3206		0		0							0	0	0	0	0		0
8120	m1	5493		1842		214							675	630	704	2175	56		781
	m2	5022		1301		183							601	238	431	1875	29		1262
	m3	4524		1024		27							487	96	0	850	19		1108
	m4	4334		605		0							399	194	0	750	13		632
	m6	4197		301		0							202	251	0	400	0		581
	m7	3975		162		0							88	116	0	450	0		525
	m8	3810		139		0							0	13	0	375	0		306
	m9	3720		0		0							0	0	0	300	0		196
	m11	3506		0		0							0	0	0	0	0		91
	seabed	3192		0		0							0	0	0	0	0		0
8080	m1	5484		1600		304							811	441	892	1675	0		830
	m2	5020		1215		178							701	304	681	1575	0		1147
	m3	4508		1147		13							296	0	0	1025	62		779
	m4	4322		660		0							321	0	0	1075	22		653
	m6	4175		298		0							195	0	0	800	0		521
	m7	3980		72		0							71	0	0	600	0		485
	m8	3813		71		0							0	0	0	350	0		192
	m9	3728		0		0							0	0	0	250	0		67
	m11	3504		0		0							0	0	0	0	0		0
	seabed	3188		0		0							0	0	0	0	0		0
8040	m1	5512		1448		357							649	486	1088	1600	0		680
	m2	5020		1189		261							599	260	631	1375	0		1077
	m3	4512		960		27							311	0	181	1050	51		902
	m4	4325		687		0							432	0	149	900	78		756
	m6	4183		392		0							244	0	0	725	19		553
	m7	3971		130		0							47	0	0	500	0		451
	m8	3805		98		0							0	0	0	225	0		206
	m9	3736		0		0							0	0	0	125	0		73
	m11	3501		0		0							0	0	0	0	0		0
	seabed	3161		0		0							0	0	0	0	0		0
8000	m1	5504		1600		447	0						731	482	971	1650	0		522
	m2	5015		1485		361	0						499	143	783	1525	0		856

Continued...

			Fault heave (m)																
Inline	Hor	Depth (m)	2	3a	3b	4	5	6	7	7b	8	9	10	11	12	13	13b	14	15
	m3	4513		992		50	0						388	0	281	875	76		931
	m4	4331		502		0	0						296	0	283	1075	71		680
	m6	4181		180		0	0						216	0	30	750	34		453
	m7	3984		30		0	0						109	0	0	575	21		323
	m8	3806		0		0	0						0	0	0	275	0		155
	m9	3737		0		0	0						0	0	0	375	0		98
	m11	3498		0		0	0						0	0	0	0	0		0
	seabed	3175		0		0	0						0	0	0	0	0		0
7960	m1	5507		1598		400	97						949	281	998	1600	0		1003
	m2	5032		1330		254	0						441	144	874	1425	0		777
	m3	4494		732		23	0						351	0	181	850	28		801
	m4	4318		382		0	0						348	0	265	900	48		566
	m6	4165		78		0	0						122	0	46	800	26		245
	m7	3971		0		0	0						23	0	0	550	17		280
	m8	3792		0		0	0						0	0	0	300	0		77
	m9	3728		0		0	0						0	0	0	175	0		23
	m11	3492		0		0	0						0	0	0	0	0		0
	seabed	3179		0		0	0						0	0	0	0	0		0
7920	m1	5490		1528		534	117						381	262	966	1750	0		811
	m2	5021		1128		203	47						662	144	735	1625	57		932
	m3	4476		778		65	0						401	0	348	800	60		697
	m4	4331		360		25	0						451	0	381	800	54		556
	m6	4162		0		0	0						98	0	74	675	48		451
	m7	3978		0		0	0						0	0	71	500	26		303
	m8	3788		0		0	0						0	0	0	250	0		180
	m9	3704		0		0	0						0	0	0	150	0		151
	m11	3481		0		0	0						0	0	0	50	0		52
	seabed	3160		0		0	0						0	0	0	0	0		0
7880	m1	5486		1240		725	312						381	244	946	1550	0		530
	m2	5025		1081		231	123						648	149	987	1550	77		997
	m3	4457		932		0	0						351	0	635	875	68		930
	m4	4306		444		0	0						331	0	501	900	51		626
	m6	4134		78		0	0						77	0	76	725	26		333
	m7	3981		0		0	0						0	0	64	475	19		252
	m8	3775		0		0	0						0	0	0	400	0		131
	m9	3712		0		0	0						0	0	0	225	0		49
	m11	3490		0		0	0						0	0	0	50	0		0
	seabed	3157		0		0	0						0	0	0	0	0		0
7840	m1	5459		1280		567	298			0			502	268	1010	1450	0		352
	m2	5017		998		115	265			0			477	100	989	1250	0		707
	m3	4458		753		43	34			0			252	0	730	1025	102		631
	m4	4289		386		0	0			0			197	0	601	1000	51		561
	m6	4113		182		0	0			0			0	0	131	750	23		374
	m7	3978		0		0	0			0			0	0	0	450	0		211
	m8	3784		0		0	0			0			0	0	0	325	0		125
	m9	3700		0		0	0			0			0	0	0	150	0		80
	m11	3477		0		0	0			0			0	0	0	125	0		0
	seabed	3176		0		0	0			0			0	0	0	0	0		0
7800	m1	5455		1462		661	530		0	0			488	175	1081	1525	0		452
	m2	5007		968		83	312		0	240			374	98	1101	1200	0		598
	m3	4436		732		23	65		0	131			210	0	860	1050	18		601
	m4	4314		192		0	97		0	97			247	0	564	1025	41		451
	m6	4120		95		0	0		0	0			26	0	261	625	14		226

Continued...

			Fault heave (m)																
Inline	Hor	Depth (m)	2	3a	3b	4	5	6	7	7b	8	9	10	11	12	13	13b	14	15
	m7	3965		0		0	0		0	0			0	0	0	400	0		123
	m8	3765		0		0	0		0	0			0	0	0	325	0		80
	m9	3715		0		0	0		0	0			0	0	0	200	0		24
	m11	3468		0		0	0		0	0			0	0	0	100	0		0
	seabed	3269		0		0	0		0	0			0	0	0	0	0		0
7760	m1	5456		1230		583	761		230	0			0	0	1161	1475	0		302
	m2	4978		932		0	337		341	335			333	0	1200	1650	0		531
	m3	4439		756		0	181		198	115			101	0	948	1075	44		586
	m4	4284		301		0	80		30	104			49	0	830	975	43		326
	m6	4099		87		0	0		0	71			26	0	331	600	0		180
	m7	3974		0		0	0		0	0			0	0	0	300	0		151
	m8	3769		0		0	0		0	0			0	0	0	225	0		98
	m9	3706		0		0	0		0	0			0	0	0	175	0		0
	m11	3479		0		0	0		0	0			0	0	0	75	0		0
	seabed	3289		0		0	0		0	0			0	0	0	0	0		0
7720	m1	5459		1372		402	580		480	121			0		1301	1325	0		202
	m2	5013		880		0	375		231	224			198		1152	1475	0		580
	m3	4454		730		0	166		125	149			177		909	1200	0		551
	m4	4301		305		0	68		45	89			124		831	1000	0		374
	m6	4107		88		0	0		0	46			0		405	550	0		80
	m7	3984		0		0	0		0	0			0		19	325	0		69
	m8	3785		0		0	0		0	0			0		0	175	0		0
	m9	3720		0		0	0		0	0			0		0	75	0		0
	m11	3488		0		0	0		0	0			0		0	0	0		0
	seabed	3158		0		0	0		0	0			0		0	0	0		0
7680	m1	5471		1395		334	831		398	281			0		1144	1325			301
	m2	4990		882		0	651		649	374			34		1226	1275			444
	m3	4478		687		0	330		622	198			198		998	1150			431
	m4	4302		348		0	212		330	119			0		899	1050			323
	m6	4120		148		0	130		80	65			0		281	600			90
	m7	3989		51		0	0		49	0			0		0	400			0
	m8	3787		0		0	0		24	0			0		0	250			0
	m9	3706		0		0	0		0	0			0		0	100			0
	m11	3489		0		0	0		0	0			0		0	0			0
	seabed	3172		0		0	0		0	0			0		0	0			0
7640	m1	5487		1330		187	1182		398	475			0		1177	1350			181
	m2	4973		902		0	861		649	630			31		1350	1375			431
	m3	4474		525		0	502		616	269			22		1026	1200			267
	m4	4314		427		0	275		323	230			0		687	1000			223
	m6	4129		240		0	90		80	16			0		230	550			0
	m7	4003		56		0	0		49	0			0		98	350			0
	m8	3773		0		0	0		23	0			0		0	225			0
	m9	3724		0		0	0		0	0			0		0	100			0
	m11	3499		0		0	0		0	0			0		0	0			0
	seabed	3170		0		0	0		0	0			0		0	0			0
7600	m1	5485		1669		0	1045		593	498			0		1028	1450			130
	m2	4981		878		0	981		747	566			19		1064	1600			481
	m3	4478		502		0	351		623	195			0		1203	1225			210
	m4	4314		382		0	246		425	206			0		680	1000			131
	m6	4103		215		0	77		150	61			0		195	750			0
	m7	3994		106		0	0		39	0			0		34	500			0
	m8	3779		0		0	0		38	0			0		0	425			0
	m9	3724		0		0	0		0	0			0		0	200			0

Continued...

			Fault heave (m)																
Inline	Hor	Depth (m)	2	3a	3b	4	5	6	7	7b	8	9	10	11	12	13	13b	14	15
	m11	3505		0		0	0		0	0			0		0	0			0
	seabed	3172		0		0	0		0	0			0		0	0			0
7560	m1	5483		1498			1144	0	449	381			0		1131	1350			164
	m2	4972		880			802	0	607	647			39		1178	1025			229
	m3	4472		502			432	0	581	99			0		1028	1100			121
	m4	4317		349			301	0	600	87			0		698	1075			74
	m6	4103		182			100	0	77	0			0		244	775			0
	m7	4008		60			0	0	68	0			0		48	600			0
	m8	3776		0			0	0	14	0			0		0	350			0
	m9	3712		0			0	0	0	0			0		0	250			0
	m11	3506		0			0	0	0	0			0		0	0			0
	seabed	3164		0			0	0	0	0			0		0	0			0
7520	m1	5471		1289			1077	28	551	555			0		1197	1250			202
	m2	4973		956			1068	23	535	441			0		1344	925			452
	m3	4465		582			382	0	499	148			0		1264	925			543
	m4	4322		244			223	0	293	121			0		707	950			177
	m6	4126		146			92	0	97	0			0		251	725			44
	m7	4012		130			0	0	0	0			0		97	450			0
	m8	3770		92			0	0	0	0			0		0	225			0
	m9	3710		0			0	0	0	0			0		0	150			0
	m11	3519		0			0	0	0	0			0		0	0			0
	seabed	3163		0			0	0	0	0			0		0	0			0
7480	m1	5481		1298			1131	147	527	480					1178	1000			0
	m2	4959		880			953	98	556	551					1203	1200			230
	m3	4469		490			451	0	543	78					864	1025			131
	m4	4317		168			281	0	236	124					731	1050			52
	m6	4137		87			82	0	0	0					305	650			0
	m7	4012		0			0	0	14	0					81	525			0
	m8	3761		0			0	0	0	0					0	300			0
	m9	3714		0			0	0	0	0					0	175			0
	m11	3519		0			0	0	0	0					0	0			0
	seabed	3150		0			0	0	0	0					0	0			0
7440	m1	5438		1189			1102	198	898	440					1151	1225			0
	m2	4937		805			931	280	731	341					1203	1350			77
	m3	4457		466			552	0	580	111					1054	1375			75
	m4	4298		135			250	0	298	167					681	1200			44
	m6	4139		26			143	0	89	0					255	725			0
	m7	3998		0			0	0	48	0					46	475			0
	m8	3766		0			0	0	21	0					0	500			0
	m9	3707		0			0	0	0	0					0	375			0
	m11	3518		0			0	0	0	0					0	0			0
	seabed	3148		0			0	0	0	0					0	0			0
7400	m1	5415		1150			1245	631	830	0					1105	900			0
	m2	4930		782			851	130	798	131					1181	1175			99
	m3	4438		330			580	0	804	98					931	1100			31
	m4	4287		62			251	0	480	87					651	925			0
	m6	4116		0			99	0	331	0					243	550			0
	m7	3994		0			0	0	197	0					101	450			0
	m8	3760		0			0	0	101	0					0	325			0
	m9	3721		0			0	0	39	0					0	175			0
	m11	3523		0			0	0	0	0					0	0			0
	seabed	3151		0			0	0	0	0					0	0			0
7360	m1	5389	0	998			1131	445	1832	0					1449	1200			0

Continued...

			Fault heave (m)																
Inline	Hor	Depth (m)	2	3a	3b	4	5	6	7	7b	8	9	10	11	12	13	13b	14	15
	m2	4930	0	645			902	130	1119	101					1177	1125			0
	m3	4423	0	330			730	0	753	97					776	1175			0
	m4	4261	0	94			441	0	261	77					480	1025			0
	m6	4109	0	0			80	0	198	0					202	675			0
	m7	3991	0	0			0	0	180	0					39	425			0
	m8	3754	0	0			0	0	75	0					0	250			0
	m9	3702	0	0			0	0	0	0					0	150			0
	m11	3548	0	0			0	0	0	0					0	0			0
	seabed	3152	0	0			0	0	0	0					0	0			0
7320	m1	5378	549	887			1081	398	1431	0					1431	1225			
	m2	4931	119	802			880	310	1221	0					1249	1025			
	m3	4427	24	237			477	0	680	76					830	1350			
	m4	4227	0	0			330	0	509	0					624	1150			
	m6	4077	0	0			127	0	271	0					147	475			
	m7	3984	0	0			0	0	230	0					0	275			
	m8	3772	0	0			0	0	149	0					0	250			
	m9	3690	0	0			0	0	80	0					0	125			
	m11	3554	0	0			0	0	0	0					0	0			
	seabed	3150	0	0			0	0	0	0					0	0			
7280	m1	5346	969	780			1075	530	1530	0					1202	900			
	m2	4913	324	601			808	442	1131	0					1040	1175			
	m3	4411	616	105			431	80	580	0					810	950			
	m4	4225	148	0			202	0	481	0					603	775			
	m6	4066	48	0			54	0	329	0					164	425			
	m7	3975	0	0			39	0	180	0					0	350			
	m8	3770	0	0			0	0	83	0					0	275			
	m9	3697	0	0			0	0	69	0					0	175			
	m11	3558	0	0			0	0	0	0					0	0			
	seabed	3160	0	0			0	0	0	0					0	0			
7240	m1	5322	998	682			1132	780	1653						1130	775			
	m2	4921	894	481			730	346	1647						1174	950			
	m3	4410	774	63			446	130	881						756	775			
	m4	4174	321	0			275	0	605						523	650			
	m6	4058	171	0			197	0	356						126	350			
	m7	3968	123	0			0	0	154						0	225			
	m8	3764	0	0			0	0	98						0	200			
	m9	3688	0	0			0	0	47						0	100			
	m11	3560	0	0			0	0	0						0	0			
	seabed	3186	0	0			0	0	0						0	0			
7200	m1	5311	1473	667			1034	1054	998						1241	550			
	m2	4911	1274	998			1076	480	1487						1108	725			
	m3	4400	1001	0			512	83	889						707	425			
	m4	4196	601	0			201	0	553						539	400			
	m6	4037	360	0			100	0	351						94	450			
	m7	3959	224	0			0	0	223						0	225			
	m8	3777	49	0			0	0	127						0	200			
	m9	3689	0	0			0	0	47						0	150			
	m11	3580	0	0			0	0	0						0	0			
	seabed	3187	0	0			0	0	0						0	0			
7160	m1	5303	1750	730			887	1181	1143						1185	400			
	m2	4915	1274	500			1003	605	1523						1041	825			
	m3	4388	1023	0			661	230	788						961	575			
	m4	4208	748	0			261	0	487						647	500			

Continued...

			Fault heave (m)																
Inline	Hor	Depth (m)	2	3a	3b	4	5	6	7	7b	8	9	10	11	12	13	13b	14	15
	m6	4035	369	0			89	0	217						241	350			
	m7	3955	24	0			0	0	147						0	250			
	m8	3748	0	0			0	0	78						0	225			
	m9	3711	0	0			0	0	21						0	100			
	m11	3574	0	0			0	0	0						0	0			
	seabed	3184	0	0			0	0	0						0	0			
7120	m1	5319	1774	575			998	1102	961						1037	275		0	
	m2	4912	1373	342			969	581	1223						870	500		0	
	m3	4391	988	15			613	180	989						971	400		0	
	m4	4198	749	0			471	0	647						702	400		0	
	m6	4053	399	0			280	0	230						326	350		0	
	m7	3950	124	0			0	0	121						71	175		0	
	m8	3779	74	0			0	0	98						0	100		0	
	m9	3715	73	0			0	0	0						0	50		0	
	m11	3583	0	0			0	0	0						0	0		0	
	seabed	3188	0	0			0	0	0						0	0		0	
7080	m1	5335	1904	632			1001	1706	1180						1035	175		0	
	m2	4913	1649	442			848	734	1209						981	575		174	
	m3	4393	1022	87			571	254	1097						956	675		100	
	m4	4183	470	0			430	0	662						704	600		145	
	m6	4054	370	0			220	0	453						298	325		0	
	m7	3962	122	0			0	0	180						31	350		0	
	m8	3790	71	0			0	0	45						0	275		0	
	m9	3716	48	0			0	0	0						0	150		0	
	m11	3577	0	0			0	0	0						0	0		0	
	seabed	3196	0	0			0	0	0						0	0		0	
7040	m1	5334	1720	661	0		930	1481	1147						998	0		0	
	m2	4915	1470	608	0		1002	771	1143						945	550		331	
	m3	4398	1398	111	0		711	370	989						889	550		296	
	m4	4200	490	0	0		351	0	580						597	600		345	
	m6	4059	340	0	0		175	0	498						298	275		221	
	m7	3959	190	0	0		0	0	180						97	175		94	
	m8	3810	0	0	0		0	0	47						0	150		0	
	m9	3714	20	0	0		0	0	0						0	125		0	
	m11	3585	0	0	0		0	0	0						0	0		0	
	seabed	3204	0	0	0		0	0	0						0	0		0	
7000	m1	5348	1774	760	72		881	1554	1080						1071	0		80	
	m2	4939	1574	620	65		925	551	1253						997	400		331	
	m3	4417	1169	248	0		566	224	860						680	300		296	
	m4	4218	498	0	0		389	47	480						809	325		551	
	m6	4048	249	0	0		144	0	578						241	300		299	
	m7	3976	98	0	0		0	0	247						181	125		185	
	m8	3816	73	0	0		0	0	29						0	100		47	
	m9	3723	48	0	0		0	0	0						0	100		0	
	m11	3587	0	0	0		0	0	0						0	0		0	
	seabed	3210	0	0	0		0	0	0						0	0		0	
6960	m1	5355	2021	601	120		669	1487	1460						997	0		176	
	m2	4960	1873	441	70		952	701	1631						1087	0		330	
	m3	4429	971	97	0		651	298	652						680	300		601	
	m4	4229	398	0	0		330	203	547						700	275		714	
	m6	4048	170	0	0		254	23	445						244	125		542	
	m7	3980	120	0	0		0	0	142						143	25		281	
	m8	3824	48	0	0		0	0	89						0	0		246	

Continued...

			Fault heave (m)																
Inline	Hor	Depth (m)	2	3a	3b	4	5	6	7	7b	8	9	10	11	12	13	13b	14	15
	m9	3710	0	0	0		0	0	0						0	0		0	
	m11	3595	0	0	0		0	0	0						0	0		0	
	seabed	3212	0	0	0		0	0	0						0	0		0	
6920	m1	5345	2250	551	110		480	1478	1330						888	0		480	
	m2	4980	1650	498	143		989	1103	1189						931	0		701	
	m3	4449	875	87	0		530	554	730						571	125		652	
	m4	4244	525	0	0		331	146	500						426	125		775	
	m6	4066	249	0	0		256	19	366						332	50		626	
	m7	4002	190	0	0		0	0	0						19	0		443	
	m8	3831	45	0	0		0	0	0						0	0		350	
	m9	3722	22	0	0		0	0	0						0	0		0	
	m11	3606	0	0	0		0	0	0						0	0		0	
	seabed	3212	0	0	0		0	0	0						0	0		0	
6880	m1	5374	2305	352	125		580	1998	1587						980	0		551	
	m2	4980	1750	269	166		998	1258	919						931	0		769	
	m3	4470	1122	112	71		625	472	698						531	0		935	
	m4	4254	448	0	0		177	170	380						524	0		910	
	m6	4067	139	0	0		80	19	432						361	0		624	
	m7	4003	120	0	0		0	0	11						70	0		534	
	m8	3840	50	0	0		0	0	0						0	0		222	
	m9	3716	48	0	0		0	0	0						0	0		279	
	m11	3606	0	0	0		0	0	0						0	0		0	
	seabed	3207	0	0	0		0	0	0						0	0		0	
6840	m1	5379	2070	315	235		602	2203	1221						771			685	
	m2	4966	1690	265	181		980	1077	1114						931			960	
	m3	4488	1120	60	0		530	387	699						480			790	
	m4	4266	427	0	0		202	197	387						553			877	
	m6	4064	55	0	0		0	20	497						296			901	
	m7	4020	152	0	0		0	0	93						28			476	
	m8	3846	77	0	0		0	0	0						0			351	
	m9	3717	45	0	0		0	0	0						0			346	
	m11	3609	0	0	0		0	0	0						0			0	
	seabed	3207	0	0	0		0	0	0						0			0	
6800	m1	5388	1874	0	880		1047	2002	1247						698			1302	
	m2	4974	1454	318	245		980	1049	880						798			1001	
	m3	4480	1051	169	0		530	389	631						381			831	
	m4	4269	400	0	0		275	197	580						401			832	
	m6	4072	245	0	0		23	71	662						606			822	
	m7	4010	170	0	0		0	0	332						106			551	
	m8	3846	76	0	0		0	0	198						0			431	
	m9	3725	22	0	0		0	0	43						0			398	
	m11	3616	0	0	0		0	0	0						0			0	
	seabed	3220	0	0	0		0	0	0						0			0	
6760	m1	5377	1945	0	987		947	2097	1678						789			1041	
	m2	4990	1620	198	181		1225	1123	1623						853			1211	
	m3	4482	945	48	66		530	256	1189						377			880	
	m4	4282	402	0	0		288	154	798						404			953	
	m6	4070	305	0	0		154	0	743						98			897	
	m7	4008	101	0	0		0	0	423						0			680	
	m8	3843	52	0	0		0	0	276						0			501	
	m9	3714	0	0	0		0	0	123						0			333	
	m11	3616	0	0	0		0	0	0						0			0	
	seabed	3231	0	0	0		0	0	0						0			0	

Continued...

			Fault heave (m)																
Inline	Hor	Depth (m)	2	3a	3b	4	5	6	7	7b	8	9	10	11	12	13	13b	14	15
6720	m1	5398	2110	0	1021		1227	2156	1979						630			1380	
	m2	4994	1730	268	223		1402	1343	1576						649			1100	
	m3	4494	1080	0	0		461	347	1157						380			1031	
	m4	4269	430	0	0		302	225	780						202			1080	
	m6	4072	149	0	0		198	80	698						130			932	
	m7	4016	49	0	0		0	47	487						0			705	
	m8	3837	24	0	0		0	0	400						0			475	
	m9	3726	0	0	0		0	0	225						0			269	
	m11	3621	0	0	0		0	0	0						0			0	
	seabed	3242	0	0	0		0	0	0						0			0	
6680	m1	5418	1820	0	1275		1047	1943	2301			0			599			1284	
	m2	4991	1610	0	841		1080	1280	2115			0			640			1061	
	m3	4486	1250	0	323		630	480	1653			0			401			802	
	m4	4276	530	0	74		502	312	1229			0			331			931	
	m6	4074	280	0	0		131	87	1034			0			121			898	
	m7	4018	149	0	0		0	0	447			0			0			924	
	m8	3838	105	0	0		0	0	380			0			0			501	
	m9	3726	80	0	0		0	0	331			0			0			352	
	m11	3620	0	0	0		0	0	80			0			0			0	
	seabed	3251	0	0	0		0	0	0			0			0			0	
6640	m1	5420	1770		1532		1131	1989	2880			0			681			1401	
	m2	4980	1280		681		1124	1128	2231			0			580			1102	
	m3	4482	1110		310		650	556	1581			22			269			856	
	m4	4273	580		130		281	223	998			0			230			889	
	m6	4082	410		43		13	70	810			0			49			745	
	m7	4025	90		0		0	0	503			0			0			625	
	m8	3827	45		0		0	0	392			0			0			346	
	m9	3728	80		0		0	0	224			0			0			324	
	m11	3636	0		0		0	0	47			0			0			0	
	seabed	3271	0		0		0	0	0			0			0			0	
6600	m1	5408	1777		1421		1040	2103	2487			0			448			1444	
	m2	4995	1102		860		1123	1127	1981			24			751			1236	
	m3	4485	1024		721		597	523	1361			48			331			1019	
	m4	4276	456		345		288	356	1187			21			198			786	
	m6	4076	310		234		0	97	1078			0			77			686	
	m7	4024	162		0		0	24	630			0			0			551	
	m8	3825	48		0		0	0	504			0			0			451	
	m9	3731	72		0		0	0	431			0			0			398	
	m11	3637	0		0		0	0	80			0			0			98	
	seabed	3278	0		0		0	0	0			0			0			0	
6560	m1	5398	1840		1443		1002	1898	1887			0			243			1552	
	m2	4995	1170		1223		1145	1354	2045			101			451			1460	
	m3	4475	320		743		730	802	1550			48			261			937	
	m4	4277	253		320		280	432	1254			0			249			771	
	m6	4083	248		145		0	221	1132			0			68			674	
	m7	4018	140		76		0	74	581			0			0			651	
	m8	3826	70		0		0	0	456			0			0			480	
	m9	3718	72		0		0	0	297			0			0			369	
	m11	3636	0		0		0	0	39			0			0			201	
	seabed	3284	0		0		0	0	0			0			0			0	
6520	m1	5397	1778		1512		1302	2352	2138			0			177			1350	
	m2	4989	1270		1443		1260	1550	2043			0			245			1380	
	m3	4470	530		1065		730	1147	1345			24			225			1169	

Continued...

			Fault heave (m)																
Inline	Hor	Depth (m)	2	3a	3b	4	5	6	7	7b	8	9	10	11	12	13	13b	14	15
	m4	4282	380		343		361	574	1287			54			34			980	
	m6	4073	380		202		0	280	1103			0			0			471	
	m7	4010	158		95		0	102	631			0			0			349	
	m8	3833	0		0		0	14	498			0			0			346	
	m9	3728	0		0		0	0	377			0			0			155	
	m11	3636	0		0		0	0	34			0			0			91	
	seabed	3290	0		0		0	0	0			0			0			0	
6480	m1	5412	1720		1777		1330	2330	2300			0			461			990	
	m2	4988	1228		1465		1423	1532	1844			0			263			1074	
	m3	4481	710		930		841	1330	1366			26			181			1161	
	m4	4284	580		445		414	632	1187			51			80			1021	
	m6	4083	380		225		0	413	1123			0			0			410	
	m7	4016	52		103		0	131	651			0			0			431	
	m8	3823	0		0		0	180	554			0			0			349	
	m9	3719	0		0		0	25	476			0			0			341	
	m11	3623	0		0		0	0	80			0			0			160	
	seabed	3296	0		0		0	0	0			0			0			0	
6440	m1	5421	1860		1333		1228	2147	2443		0	0			249			530	
	m2	4979	1460		1302		1180	1670	1876		0	44			187			708	
	m3	4484	780		787		582	1031	1524		0	34			131			880	
	m4	4273	560		480		495	680	1223		0	21			97			849	
	m6	4077	402		235		118	304	961		0	0			0			310	
	m7	4007	27		155		0	130	680		0	0			0			205	
	m8	3823	0		34		0	98	552		0	0			0			174	
	m9	3715	0		0		0	47	430		0	0			0			46	
	m11	3630	0		0		0	0	80		0	0			0			0	
	seabed	3300	0		0		0	0	0		0	0			0			0	
6400	m1	5427	1824		1696		1168	2370	2511		0	0			243			430	
	m2	4999	1680		1115		1146	1632	2376		43	130			261			731	
	m3	4483	1010		835		780	1031	1621		0	49			77			820	
	m4	4280	530		460		375	830	1421		0	30			64			746	
	m6	4089	432		378		0	554	555		0	0			0			248	
	m7	4007	110		80		0	198	700		0	0			0			222	
	m8	3823	49		90		0	147	576		0	0			0			123	
	m9	3715	96		0		0	80	443		0	0			0			0	
	m11	3627	0		0		0	0	30		0	0			0			0	
	seabed	3304	0		0		0	0	0		0	0			0			0	
6360	m1	5423	2182		1553		1400	2581	2721		81	0			0			641	
	m2	5004	1992		1256		1131	1980	1280		122	44			197			711	
	m3	4507	1387		936		505	1275	1183		44	18			55			680	
	m4	4287	980		634		403	930	1102		98	0			78			649	
	m6	4086	611		445		0	552	768		21	0			0			301	
	m7	4018	180		165		0	249	589		0	0			0			251	
	m8	3813	130		0		0	139	480		0	0			0			131	
	m9	3721	98		0		0	89	98		0	0			0			21	
	m11	3628	0		0		0	31	13		0	0			0			0	
	seabed	3312	0		0		0	0	0		0	0			0			0	
6320	m1	5417	1980		1480		1298	2224	2524		161	0			0			651	
	m2	5025	1777		1253		1134	1709	2123		103	31			0			654	
	m3	4516	1229		865		680	1125	1953		98	70			152			520	
	m4	4273	905		465		300	856	1477		23	0			81			517	
	m6	4073	786		323		0	634	1180		0	0			18			344	
	m7	4015	256		97		0	280	707		0	0			0			260	

Continued...

Inline	Hor	Depth (m)	Fault heave (m) 2	3a	3b	4	5	6	7	7b	8	9	10	11	12	13	13b	14	15
	m8	3813	195		0		0	213	580		0	0			0			130	
	m9	3726	143		0		0	212	453		0	0			0			80	
	m11	3625	0		0		0	0	123		0	0			0			0	
	seabed	3314	0		0		0	0	0		0	0			0			0	
6280	m1	5448	1760		1636		1444	2190	2621		181	0			0			430	
	m2	4954	1689		1234		1261	1610	2378		223	19			0			415	
	m3	4533	1224		698		661	1143	1807		263	81			0			446	
	m4	4385	856		365		347	707	1409		171	41			0			441	
	m6	4167	731		231		249	530	1026		95	0			0			339	
	m7	4047	259		80		45	249	680		0	0			0			261	
	m8	3823	130		0		0	251	509		0	0			0			182	
	m9	3744	159		0		0	90	354		0	0			0			97	
	m11	3624	0		0		0	0	38		0	0			0			0	
	seabed	3291	0		0		0	0	0		0	0			0			0	
6240	m1	5455	1946		1661		1153	2453	2754		198	0						461	
	m2	4967	1999		1167		1234	1409	2254		224	0						552	
	m3	4535	1560		734		651	1075	1753		221	77						481	
	m4	4372	1232		134		606	780	1309		145	0						496	
	m6	4162	966		146		298	602	1223		97	0						544	
	m7	4055	152		0		98	275	909		0	0						356	
	m8	3838	97		0		0	180	654		0	0						223	
	m9	3740	146		0		0	139	534		0	0						180	
	m11	3624	0		0		0	0	78		0	0						0	
	seabed	3295	0		0		0	0	0		0	0						0	
6200	m1	5447	1810		1864		1447	2134	2809		581	0						374	
	m2	4982	1880		1413		1333	1809	2513		474	22						581	
	m3	4534	1502		617		607	1401	1625		331	130						431	
	m4	4348	1053		180		498	710	1525		224	0						530	
	m6	4169	758		95		280	403	1274		123	0						421	
	m7	4071	178		0		94	260	880		0	0						306	
	m8	3827	226		0		0	211	706		0	0						152	
	m9	3740	25		0		0	151	531		0	0						131	
	m11	3622	0		0		0	30	54		0	0						0	
	seabed	3281	0		0		0	0	0		0	0						0	
6160	m1	5442	2125		1674		1553	2105	3050		530	0						316	
	m2	4967	1926		1153		1408	1856	2850		498	29						498	
	m3	4536	1430		532		651	1309	1950		471	91						301	
	m4	4340	926		281		452	880	1525		392	0						380	
	m6	4161	758		174		382	447	1250		149	0						151	
	m7	4068	80		0		131	198	900		0	0						124	
	m8	3841	198		0		0	210	675		0	0						0	
	m9	3731	154		0		0	143	525		0	0						0	
	m11	3620	0		0		0	0	75		0	0						0	
	seabed	3272	0		0		0	0	0		0	0						0	
6120	m1	5404	2040		1531		1333	2425	3225		680	0						274	
	m2	4990	1710		1153		1243	1776	2800		581	92						401	
	m3	4539	1382		687		843	1367	1900		619	66						326	
	m4	4357	1179		431		430	580	1425		297	0						424	
	m6	4164	699		333		380	302	1400		80	0						71	
	m7	4063	0		0		80	130	1050		0	0						129	
	m8	3830	174		0		0	74	825		0	0						80	
	m9	3744	152		0		0	70	650		0	0						31	
	m11	3614	0		0		0	0	75		0	0						0	

Continued...

			Fault heave (m)																
Inline	Hor	Depth (m)	2	3a	3b	4	5	6	7	7b	8	9	10	11	12	13	13b	14	15
	seabed	3267	0		0		0	0	0		0	0						0	
6080	m1	5429	2080		1783		1446	2124	2889		798	0						431	
	m2	4988	1878		1204		1102	1330	2680		668	81						261	
	m3	4529	1552		969		813	980	2147		480	31						381	
	m4	4347	1160		342		477	698	1846		230	0						180	
	m6	4174	530		341		350	555	1504		98	0						98	
	m7	4069	77		0		210	198	930		0	0						97	
	m8	3834	28		0		0	145	727		0	0						15	
	m9	3739	49		0		0	90	530		0	0						0	
	m11	3611	0		0		0	0	31		0	0						0	
	seabed	3251	0		0		0	0	0		0	0						0	
6040	m1	5444	2248		2013		1447	2166	2802		851	48						202	
	m2	5003	1902		1286		1546	1671	2777		777	32						210	
	m3	4524	1356		702		680	819	2204		421	44						198	
	m4	4345	1080		513		525	580	1653		281	0						177	
	m6	4166	752		435		333	432	1347		98	0						131	
	m7	4053	60		0		298	198	830		24	0						31	
	m8	3822	80		0		0	134	580		0	0						0	
	m9	3740	26		0		0	166	423		0	0						0	
	m11	3607	0		0		0	0	82		0	0						0	
	seabed	3271	0		0		0	0	0		0	0						0	
6000	m1	5491	2081		2166		1547	2514	2804		580	96						130	
	m2	5018	1930		1332		1474	1843	2577		430	80						222	
	m3	4514	1378		960		899	861	1978		349	21						244	
	m4	4336	1048		426		688	625	1747		298	0						160	
	m6	4168	520		413		441	398	1447		76	0						0	
	m7	4056	45		0		250	193	960		70	0						0	
	m8	3822	127		0		0	87	681		26	0						0	
	m9	3736	138		0		0	43	445		19	0						0	
	m11	3616	0		0		0	0	0		0	0						0	
	seabed	3283	0		0		0	0	0		0	0						0	
5960	m1	5494	2201		1823		1547	2000	2627		681	0						0	
	m2	5000	1936		1352		1702	1733	2380		349	0						140	
	m3	4495	1405		813		939	988	1931		402	0						60	
	m4	4337	1078		512		751	605	1721		310	0						131	
	m6	4167	684		480		441	333	1414		161	0						0	
	m7	4047	148		77		280	98	934		30	0						0	
	m8	3808	125		0		0	81	605		25	0						0	
	m9	3742	0		0		0	66	395		23	0						0	
	m11	3605	0		0		0	0	0		0	0						0	
	seabed	3287	0		0		0	0	0		0	0						0	
5920	m1	5492	2081		1380		1700	1902	2569		580							0	
	m2	4993	1875		1227		1698	1654	2245		432							74	
	m3	4506	1374		880		1024	702	1831		381							130	
	m4	4324	1132		377		840	580	1631		129							52	
	m6	4161	786		354		569	347	1405		49							0	
	m7	4041	52		0		298	150	909		73							0	
	m8	3802	76		0		47	77	602		22							0	
	m9	3743	0		0		0	98	431		26							0	
	m11	3596	0		0		0	0	0		0							0	
	seabed	3277	0		0		0	0	0		0							0	
5880	m1	5483	2222		1412		1761	2040	2823		477							0	
	m2	4979	1911		1052		1703	1688	2504		451							0	

Continued...

			Fault heave (m)																
Inline	Hor	Depth (m)	2	3a	3b	4	5	6	7	7b	8	9	10	11	12	13	13b	14	15
	m3	4483	1132		689		1111	830	1587		469							46	
	m4	4324	1048		354		830	637	1572		330							69	
	m6	4163	1078		180		441	398	1147		280							0	
	m7	4038	45		0		204	146	680		198							0	
	m8	3804	46		0		0	44	500		98							0	
	m9	3738	0		0		0	78	289		80							0	
	m11	3601	0		0		0	0	0		24							0	
	seabed	3258	0		0		0	0	0		0							0	
5840	m1	5462	1974		1381		1624	2034	2619		598							0	
	m2	4960	1888		1126		1705	1532	2377		448							0	
	m3	4493	1152		778		1231	880	1707		480							0	
	m4	4326	1102		324		1019	630	1426		302							18	
	m6	4151	835		246		555	443	1178		222							0	
	m7	4025	96		0		330	202	754		198							0	
	m8	3804	0		0		149	132	551		150							0	
	m9	3735	0		0		0	80	398		110							0	
	m11	3597	0		0		0	0	0		32							0	
	seabed	3252	0		0		0	0	0		0							0	
5800	m1	5466	2174		1187		1789	2283	2598		444							0	
	m2	4961	1773		1181		1623	1681	2401		431							0	
	m3	4478	1078		807		1156	976	1849		451							0	
	m4	4320	998		473		880	730	1451		198							0	
	m6	4138	530		333		430	441	1253		302							0	
	m7	4019	99		0		302	234	808		177							0	
	m8	3782	0		0		80	132	560		132							0	
	m9	3723	0		0		0	110	389		98							0	
	m11	3600	0		0		0	0	0		0							0	
	seabed	3257	0		0		0	0	0		0							0	